Silesian University of Technology
Faculty of Chemistry
Department of Physical Chemistry and Technology of Polymers

DOCTORAL DISSERTATION

Thiophene polymers with tailored break of π-conjugated bond featuring tuneable electrochromic properties

Ph.D. candidate: Paulos Asefa Fufa, M.Sc.
Supervisor: Wojciech Domagała, D.Sc. Ph.D. B.Eng.

Gliwice, 2026

Acknowledgements

First and foremost, I give all glory and thanks to God Almighty, who has granted me the grace and strength to see this day and complete this journey. Without His guidance and mercy, none of this would have been possible.

I would like to express my deepest gratitude to my supervisor, Professor Wojciech Domagała, for his invaluable support, insightful guidance, and unwavering encouragement throughout this work. His mentorship has been a cornerstone of my academic growth.

To my beloved wife, Derartu Biratu Lamesa, thank you for your endless love, patience, and belief in me. Your support has been my anchor. To my dear son, Miraol Paulos Asefa, this is for your memory.

I am also profoundly grateful to my family and friends for their constant encouragement, prayers, and support. In particular, I would like to thank:

- Dr Radosław Motyka, for his significant contribution to the synthesis and NMR spectra measurements.

- Dr Przemysław Ledwoń, for his significant advice on the synthesis and measurements.

- Mr Andualem Merga Tullu, for his assistance with NMR measurements.

- Mr Damian Honisz, for his help during the measurement process and for training me with great patience and dedication.

Each of you has played a vital role in helping me reach this milestone, and I am forever thankful.

I am also grateful to the Silesian University of Technology for the financial support provided during my studies.

Abstract

This doctoral dissertation presents the design, synthesis, and comprehensive electrochemical and spectroscopic investigation of thiophene-based polymers incorporating deliberately introduced π-conjugation-break spacers. The objective of this work is to establish clear structure–property relationships and to understand how controlled interruption of π-conjugation influences redox behaviour, charge localization, and electrochromic response. Three systematic series of oligothiophene systems were synthesized: (i) alkyl-substituted methylene-bridged quaterthiophenes, (ii) oligothiophenes of varying conjugation length connected through methylene bridges, and (iii) quaterthiophene units separated by methylene, ethylene, and propylene spacers. In addition, selected model compounds were synthesized to support mechanistic interpretation and structure–redox correlation.

The molecular structures of all synthesized monomers were confirmed by ^{1}H and ^{13}C NMR spectroscopy. The UV–Vis spectroscopic properties of the monomers were investigated to evaluate the effectiveness of π-conjugation interruption in the ground state and to assess electronic communication between thiophene segments. Electrochemical behaviour was examined using cyclic voltammetry to analyse first oxidation processes and structure-dependent follow-up reactions. UV–Vis–NIR spectroelectrochemical measurements were performed on electrogenerated films across all three series to monitor electronic-state evolution during controlled doping and dedoping cycles. Electron paramagnetic resonance (EPR) spectroelectrochemical analysis was conducted for one compound to directly confirm the formation of spin-active radical species.

The results demonstrate that oxidation proceeds predominantly through stepwise one-electron processes strongly influenced by bridge substitution, thiophene conjugation length, and spacer length. Spectroelectrochemical analysis confirms the formation of localized polaronic species, with limited long-range charge delocalization due to the presence of conjugation-break spacers. Increasing spacer length progressively reduces electronic coupling between conjugated segments and modulates redox reversibility and optical response. The observed spectral changes during oxidation directly correlate spacer architecture with electrochromic behaviour, demonstrating that controlled conjugation interruption provides a molecular strategy for tuning color transitions and redox stability.

Overall, this work establishes a mechanistically coherent framework linking molecular structure, oxidation pathways, charge localization, and electrochromic properties in conjugation-broken thiophene systems. The findings provide fundamental insight into spacer-engineered organic semiconductors and contribute to the rational design of tuneable electrochromic and redox-active materials.

Abstrakt

Niniejsza rozprawa doktorska dotyczy projektowania, syntezy oraz kompleksowej analizy elektrochemicznej i spektroskopowej polimerów tiofenu zawierających celowo wprowadzone przerwy w sprzężeniu π w postaci mostków o hybrydyzacji sp^3. Celem pracy było ustalenie zależności struktura–właściwości oraz zrozumienie, w jaki sposób kontrolowane przerywanie sprzężenia π wpływa na procesy redoks, lokalizację ładunku oraz właściwości elektrochromowe badanych układów.

Zsyntetyzowano trzy systematyczne serie związków: (i) pochodne kwaterotiofenu mostkowane grupą metylenową o różnym stopniu podstawienia alkilowego, (ii) oligotiofeny o zróżnicowanej długości segmentu sprzężonego, połączone mostkiem metylenowym oraz (iii) układy kwaterotiofenowe rozdzielone mostkami metylenowym, etylenowym i propylenowym. Dodatkowo otrzymano wybrane związki modelowe, które umożliwiły pogłębioną interpretację mechanizmów utleniania oraz analizę zależności struktura–właściwości. Struktury wszystkich zsyntetyzowanych monomerów potwierdzono za pomocą spektroskopii ^{1}H i ^{13}C NMR.

Widma UV–Vis monomerów poddano analizie w celu oceny skuteczności przerwania sprzężenia π w stanie podstawowym oraz określenia stopnia komunikacji elektronowej pomiędzy segmentami tiofenowymi. Właściwości elektrochemiczne badano metodą woltamperometrii cyklicznej, analizując pierwszy etap utleniania oraz reakcje następcze zależne od budowy cząsteczki. Pomiary spektroelektrochemiczne UV–Vis–NIR przeprowadzono dla elektrochemicznie wytworzonych warstw polimerowych wszystkich trzech serii badanych związków w celu monitorowania zmian stanów elektronowych podczas procesów domieszkowania i odwracalnego oddomieszkowania. Dla jednego ze związków wykonano dodatkowo pomiary EPR w warunkach spektroelektrochemicznych, co pozwoliło bezpośrednio potwierdzić powstawanie rodnikowych, paramagnetycznych centrów ładunku.

Uzyskane wyniki wskazują, że proces utleniania przebiega etapowo, poprzez kolejne reakcje jednoelektronowe, a jego charakter silnie zależy od stopnia podstawienia mostka, długości segmentu sprzężonego oraz długości łącznika alkilenowego. Analiza spektroelektrochemiczna potwierdza powstawanie zlokalizowanych nośników ładunku typu polaronowego, przy ograniczonej delokalizacji wzdłuż całego układu wskutek obecności przerywających sprzężenie mostków sp^3. Wydłużanie łącznika prowadzi do zmniejszenia sprzężenia elektronowego między segmentami tiofenowymi oraz wpływa na odwracalność procesów redoks i charakter odpowiedzi optycznej. Zaobserwowane zmiany widmowe podczas kontrolowanego utleniania bezpośrednio korelują z właściwościami elektrochromowymi badanych materiałów, wskazując, że architektura mostka stanowi narzędzie molekularne do modulowania barwy oraz stabilności stanów utlenionych.

Przeprowadzone badania pozwoliły na sformułowanie spójnego mechanistycznie modelu łączącego budowę molekularną, ścieżki utleniania, lokalizację ładunku oraz właściwości elektrochromowe w układach tiofenowych z przerwanym sprzężeniem π. Wyniki pracy stanowią wkład w rozwój projektowania półprzewodników organicznych o regulowanych właściwościach redoks i potencjalnym zastosowaniu w urządzeniach elektrochromowych oraz elastycznej elektronice.

Table of Contents

List of Tables

List of Schemes

List of Figures

List of Figure Appendices

List of abbreviations and symbols

FETs	Field-effect transistors
CBSs	Conjugation-break spacers
OLEDs	Organic light-emitting diodes
OFETs	Organic field-effect transistors
OPVs	Organic photovoltaics
LEDs	Light emitting diodes
PEDOT	Poly(3,4-ethylenedioxythiophene)
PPV	Poly(phenylene vinylene)
MEH-PPV	Poly(2-methoxy-5-(2′-ethylhexyloxy)-*p*-Phenylene vinylene)
TFTs	Thin-film transistors
UV–Vis	Ultraviolet–Visible
^{1}H NMR	Proton Nuclear Magnetic Resonance
PA	polyacetylene
CV	Conjugation-break spacer
DCM	Dichloromethane
DDQ	2,3-dichloro-5,6-dicyano-1,4-benzoquinone
EPR	Electron paramagnetic resonance
Fc/Fc^+	Ferrocene/ferrocenium redox couple
FTIR	Fourier-transform infrared spectroscopy
ITO	Indium tin oxide
NBS	N-bromosuccinimide
PTTM	Poly[(5,5″-terthiophenediyl)-methylene]
SEC	Spectroelectrochemistry
STM	Scanning tunneling microscopy
STS	Scanning tunneling spectroscopy
UPS	Ultraviolet photoelectron spectroscopy
UV–Vis–NIR	Ultraviolet–visible–near infrared spectroscopy
A	Absorbance
E	Electrode potential (V)
E_{pa}	Anodic peak potential (V)
E_pC	Cathodic peak potential (V)
E_{onset}^{ox}	Oxidation onset potential (V)
I	Current (A)
I_p	Peak current (A)
v	Scan rate ($V \cdot s^{-1}$)
λmax	Maximum absorption wavelength (nm)
ε	Molar extinction coefficient ($M^{-1} \cdot cm^{-1}$)
E_g^{opt}	Optical band gap energy (eV)
sp^3	Tetrahedral hybridization state of carbon
π	Pi-electron system
E_{HOMO}	Highest occupied molecular orbital energy levels
λ_{onset}	Onset wavelengths

1. Introduction

Organic semiconductor materials have been extensively studied for the development of lightweight, flexible, implantable, and stretchable devices. Among these materials, conjugated polymers have attracted particular attention due to their unique combination of mechanical flexibility and functionality. They have been widely employed in optoelectronic devices such as field-effect transistors (FETs) [1], photovoltaic cells [2,3], and memory devices [4]. Conjugated polymers typically possess a one-dimensional π -conjugated backbone and exhibit high electrical conductivity upon electrochemical doping [5]. As a result, they have become a central focus of research in organic electronics.

The strong intermolecular van der Waals interactions present in conjugated polymers, particularly π–π stacking interactions, arise from their alternating single and double bond structures and play a critical role in determining their microstructure in both solution and solid state [6]. These interactions strongly influence aggregation behaviour, which is in turn affected by the chemical structure of the polymer backbone and the nature of its side chains [7]. Variations in backbone conformation and side-chain composition lead to diverse supramolecular organizations, resulting in a wide range of charge-transport and doping behaviours [8]. However, strong aggregation often compromises solubility and processability, which remain major challenges for conjugated polymers.

One effective strategy to address these limitations involves the introduction of conjugation-break spacers (CBSs) into the polymer backbone. CBSs are nonconjugated segments, commonly flexible alkyl chains, that disrupt extended π-conjugation and reduce backbone rigidity. Their incorporation increases conformational disorder and interrupts long-range π-electron delocalization, thereby improving solubility and mechanical flexibility. Numerous studies have demonstrated that conjugated polymers containing CBSs exhibit enhanced processability and improved mechanical properties compared to their fully conjugated counterparts [9–11]. For example, Chen *et al.*[12] reported improved mobility–stretchability relationships in n-type conjugated polymers incorporating functionalized CBSs. More recently, Gu*et al*.[13] investigated the effect of backbone rigidity on the thermomechanical properties of CBS-linked conjugated polymers and demonstrated the importance of spacer length in achieving stretchable materials.

While CBS incorporation offers clear structural and mechanical advantages, increasing spacer length can negatively impact electronic properties. As the length of the conjugation-break spacer increases, the effective concentration of π–π stacked units decreases, leading to reduced intermolecular charge transport. Consequently, electrical performance deteriorates at longer spacer lengths due to diminished electronic communication between conjugated segments. Despite this trade-off, CBS-containing conjugated polymers have been widely explored for improved solubility [14], melt processibility [15], and molecular weight independent optoelectronic properties [16], mechanical and electronic properties of semi-random copolymers [17] and stretchability and self-healing properties of semiconductors [18].

Despite this extensive body of work, a critical gap remains in the fundamental understanding of the electrochemical and spectroelectrochemical behaviour of CBS-containing systems. While these materials are increasingly employed in organic electronic devices, their redox processes, charge-carrier generation mechanisms, and electronic-state evolution under electrochemical bias have not been

systematically investigated. Early studies by Berlin *et al.* [19] and Benincori *et al.*[20] provided initial insights into the electrochemical properties of conjugation-broken systems. However, these investigations were largely qualitative and did not address charge-carrier identity, redox-state evolution, or structure–property relationships in detail. In particular, spectroelectrochemical techniques, which enable direct correlation between optical signatures and electrochemically generated states, were not comprehensively applied.

Early approaches toward low-bandgap materials relied primarily on chemical synthesis, in which conjugation-break spacers were introduced temporarily and later removed through oxidative elimination to restore extended conjugation [20][21]. In contrast, electrochemical synthesis and characterization have not been systematically developed as tools for constructing and probing CBS-containing materials, despite their advantages in controlled doping and in situ analysis.

Thiophene-based conjugated polymers represent an ideal platform for addressing these challenges. Polythiophenes have been extensively studied due to their favorable electronic properties and structural versatility [22][23]. Introducing nonconjugated spacers into thiophene-based systems allows systematic control of conjugation length and backbone flexibility, thereby enabling detailed investigation of structure–property relationships. Although several studies have reported alkyl-bridged thiophene monomers and their electropolymerization behaviour [24–28], comprehensive electrochemical and spectroelectrochemical analyses remain limited. Notably, Zotti et al. investigated ethylene-bridged bithiophene and terthiophene systems but reported only basic electrochemical behaviour [19]. These studies provide a benchmark for further investigation of oligothiophenes incorporating CBSs of varying length and structure.

2. Aim and scope of this dissertation.

The primary aim of this doctoral project is to design, synthesise, and investigate thiophene polymers with a tailored break of π- conjugated bond featuring tuneable electrochemical properties. Three series of oligothiophene based systems incorporating conjugation break spacers are studied.

The first series focuses on quaterthiophene derivatives bridged by alkyl-grafted methylene CBSs with systematically varied substitution patterns. These systems enable detailed investigation of redox behaviour, spectroscopic properties, and electropolymerization mechanisms of conjugation-broken oligothiophenes. The chemical structures of oligothiophenes incorporating alkyl-chain-derivatized conjugation-break spacers investigated in this work are shown in Figure 2.1.

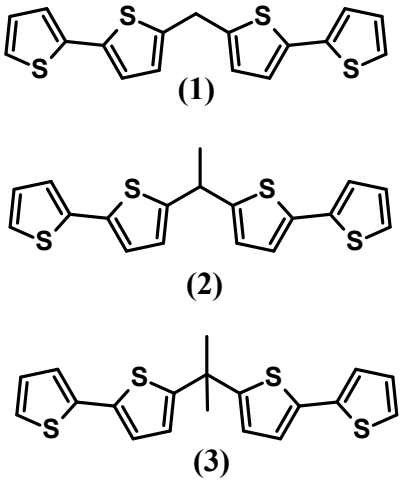

Figure 2.1 Chemical structures of oligothiophenes equipped with alkyl-chain-derivatized conjugation-break spacers: (1) no methyl substitution, (2) mono-methyl substitution, and (3) dimethyl substitution.

The second series comprises oligothiophenes of varying length, including bithiophene, quaterthiophene, and sexithiophene units, linked by α,α'-methylene conjugation-break spacers. The chemical structures of oligothiophenes with varying conjugation lengths connected through α,α'-methylene conjugation-break spacers are shown in Figure 2.2.

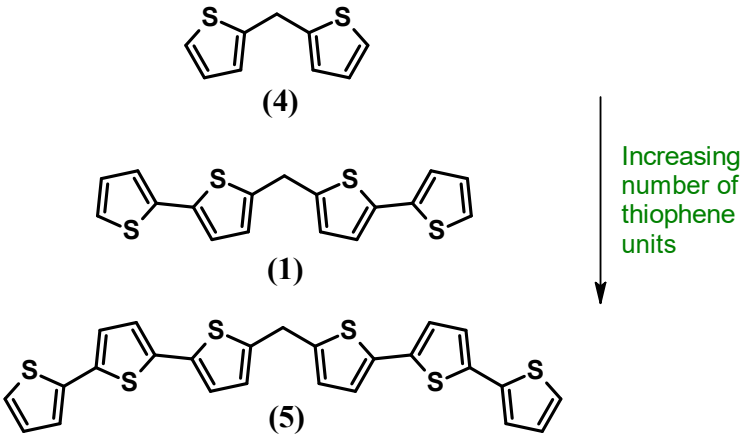

Figure 2.2 Chemical structures of oligothiophenes of varying conjugation length linked by α,α'-methylene conjugation-break spacers: (1) bithiophene, (2) quaterthiophene, and (3) sexithiophene derivatives.

The third series investigates the effect of spacer length by incorporating methylene, ethylene, and propylene linkers between fixed conjugated thiophene segments. The chemical structures of

oligothiophenes containing methylene, ethylene, and propylene conjugation-break spacers are presented in Figure 2.3.

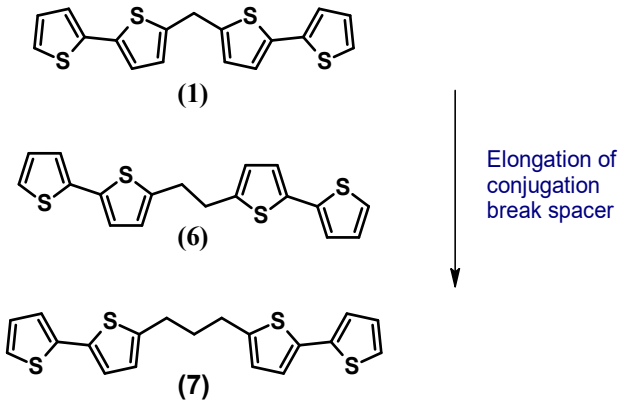

Figure 2.3 Chemical structures of oligothiophenes incorporating conjugation-break spacers of different lengths: methylene, ethylene, and propylene linkers between thiophene segments.

Several model compounds were also synthesized to support structure–property correlations. The structures of those model compounds investigated in this work are shown in Figure 2.4. Together, these studies provide a comprehensive framework for understanding how conjugation-break spacers influence the electrochemical, spectroscopic, and spectroelectrochemical behaviour of conjugated thiophene systems.

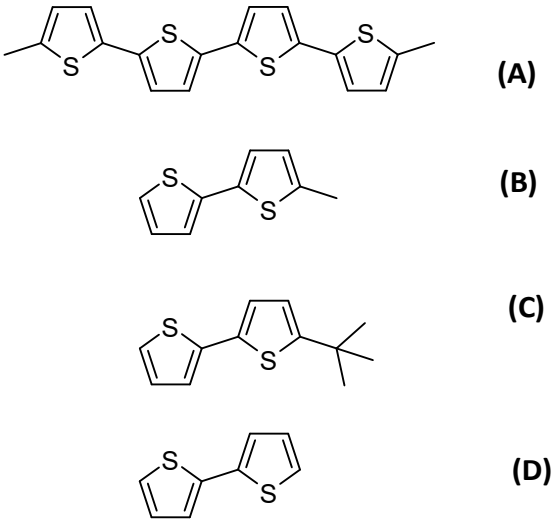

Figure 2.4 Chemical structures of model compounds synthesized to support structure–property correlation studies.

Overall, the scope of this thesis centres on the synthesis and comprehensive electrochemical and spectroscopic investigation of oligothiophene monomers and their corresponding obtained films. Spectroelectrochemical studies are conducted specifically on the electrochemically generated films to elucidate their electrochromic behaviour and charge-carrier evolution under applied potential. In addition, targeted use of electron paramagnetic resonance (EPR) spectroscopy is employed where appropriate to further clarify redox processes. Through these combined approaches, clear structure–property relationships are established in thiophene-based conducting materials incorporating conjugation-break spacers.

3. Literature review

3.1. Π-conjugated polymer materials

Ever since Heeger, MacDiarmid, and Shirakawa discovered polyacetylene in 1976 [29], scientists have been fascinated by a new and developing group of materials known as π-conjugated conducting organic polymers due to their remarkable physical and chemical characteristics. The alternating single and double carbon-carbon bonds in the polymer backbone create π-conjugation. This allows the π-electrons to extend along the polymer chain, with one unpaired π-electron per carbon atom. As a result, charge can move along the polymer chain, leading to conducting or semiconducting properties [30–37].

Conjugated polymers represent a distinct class of polymers featuring substantial Π-electron delocalization along their polymer backbones, resulting in intriguing optical and nonlinear optical properties and conferring good electrical conductivity during oxidation-reduction phenomena. Due to their unique attributes, these materials are widespread applications in optoelectronic devices such as organic light-emitting diodes (OLEDs), organic field-effect transistors (OFETs), organic photovoltaics (OPVs), and more. Furthermore, in contrast to inorganic semiconductors, organic conjugated polymers offer various advantages such as low cost, lightweight nature, solution processability, and flexibility. Moreover, conducting polymers have been extensively studied owing to their outstanding properties, including tunable electrical properties, high optical and mechanical properties, ease of synthesis and fabrication, and enhanced environmental stability compared to conventional inorganic materials [36].

Over the past 50 years, polythiophene and polyacetylene, among other π-conjugated materials, have been synthesized and investigated for their intrinsic ability to conduct electricity. Some examples of π-conjugated polymers are shown in Figure.3.1. Polythiophenes are an important representative class of conjugated polymers that form some of the most environmentally and thermally stable materials that can be used as electrical conductors, non-linear optical devices, polymer LEDs, transistors, electrochromic or smart windows, photoresists, antistatic coatings, sensors, batteries, electromagnetic shielding materials, artificial noses and muscles, solar cells, electrodes, microwave absorbing materials, new types of memory devices, batteries, nano switches, optical modulators and valves, imaging materials, polymer electronic interconnects, nanoelectronics and optical devices

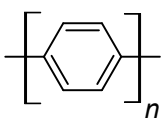

poly(p-phenylene)

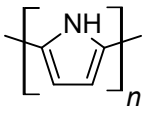

Polypyrrol

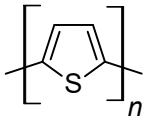

Polythiophene

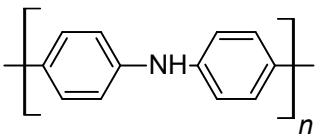

Polyaniline

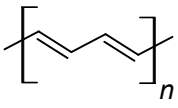

Polyacetylene

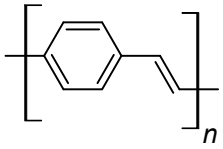

Poly(p-phynylene vinylene)

Figure 3.1 Some examples of π-conjugated polymers

3.1.1. Oligo and polythiophene

Polythiophene and its derivatives are among the most extensively investigated conjugated conducting polymers, largely due to their favorable electrical and optical properties combined with significant chemical flexibility [38,39]. In particular, α-conjugated thiophene oligomers are frequently employed as well-defined model systems for elucidating the fundamental processes of charge generation, delocalization, and transport that underpin the electrical conductivity of the corresponding polymeric materials [38,40]. Owing to their controlled molecular length and reduced structural disorder, these oligomers enable a more precise examination of structure–property relationships than is generally achievable in high-molecular-weight polymers [38,41]. Consequently, both oligo- and polythiophenes have been widely explored for applications including organic conductors, non-linear optical devices, polymer light-emitting diodes, field-effect transistors, sensors, batteries, and photovoltaic cells [41,42]. Their sustained technological relevance is commonly attributed to efficient charge transport, synthetic tunability, mechanical flexibility, and compatibility with low-cost processing on flexible substrates [41,42].

3.1.2. Structure and properties of polythiophene

Building on the discussion of oligo- and polythiophenes as model systems for charge transport, it has become increasingly evident that molecular and supramolecular structure plays a decisive role in governing the electrical and optical properties of conducting polymers. As this understanding has matured, research efforts have progressively shifted toward synthetic strategies aimed at deliberately controlling structure and function [43,44]. Consequently, a substantial body of knowledge has been established on how the optical, electronic, and redox properties of conjugated polymers can be rationally tuned through molecular design [38,43].

Among the wide range of π-conjugated materials investigated to date, polythiophenes with diverse backbone and side-chain architectures have attracted particular attention for systematic studies of structure–property relationships [38,41]. This interest arises primarily from their pronounced structural versatility, which allows, for example, color tuning via substitution at the 3-position of the thiophene ring, improved solubility through side-chain functionalization, and relatively high environmental stability compared with many other conjugated polymers [41,45].

The monomeric unit of polythiophenes is the thiophene ring, an aromatic heterocycle in which a sulfur atom replaces one carbon atom of the benzene ring. The presence of sulfur plays a crucial role in stabilizing the aromatic system and modifying its electronic structure through participation in the delocalized π-electron network, thereby facilitating efficient charge transport along the conjugated backbone [46]. Moreover, the aromatic character of the thiophene unit promotes effective π-conjugation during polymerization, a key requirement for achieving high electrical conductivity in these materials [38]. Representative molecular structures of thiophene and selected polythiophene derivatives are shown in Figure 3.2.

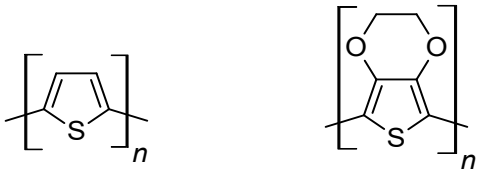

Polythiophenes PEDOT

Figure 3.2 Structures of thiohene and it's derivative

While significant effort has been devoted to optimizing the conjugated backbone and side-chain architecture of polythiophenes to enhance charge transport and optical response, it has also become evident that intentional disruption of π-conjugation can provide an additional and complementary handle for tailoring material properties [38,47]. In this context, the incorporation of conjugation-breaking spacers non-conjugated segments inserted into the polymer backbone has emerged as an effective molecular design strategy to adjust electronic communication along the chain, modulate optical band gaps, and influence mechanical behaviour without fundamentally altering the core chromophore [48,49]. Such structural modifications have proven particularly valuable for disentangling the respective roles of conjugation length, electronic coupling, and disorder in governing the optoelectronic and mechanical properties of π-conjugated polymers. Consequently, the following section focuses on conjugation-break spacers and their influence on the structure–property relationships of thiophene-based materials

3.2. Conjugation break spacers (CBS)

3.2.1. Background on Conjugation break spacers.

The use of molecular linkers as a design strategy has evolved considerably over the past several decades. Early studies in the 1970s and 1980s focused on main-chain liquid crystalline polymers[50], where linkers were introduced primarily to probe fundamental mechanical and rheological properties[51]. In these systems, the primary interest lay in understanding how chain flexibility and connectivity influenced bulk material properties rather than electronic function.

In this context, conjugation-break spacers also commonly referred to as flexible linkers can be defined as non-conjugated, typically aliphatic, chains that covalently connect π-conjugated segments along a polymer backbone[52–55]. Because these spacers are electrically insulating, they interrupt the continuous π-electron delocalization of the backbone, leading to the term 'conjugation-break' due to the disruption of electron delocalization. While such interruptions might initially be perceived as detrimental from an electronic perspective, they provide an important handle for manipulating polymer conformation and intermolecular interactions.

The strategy was further developed and applied to semiconducting polymers in the 1990s and early 2000s, particularly in poly(phenylene vinylene) (PPV) derivatives[56–59]. During this period, conjugation-break spacers were primarily employed to improve solubility and adjust the energy levels of the optical bandgap for applications such as organic light-emitting diodes (OLEDs). However, these early implementations generally resulted in compromised charge transport efficiency, as increased backbone flexibility and disrupted conjugation limited electronic coherence along the polymer chain.

Building on earlier efforts to introduce flexibility into polymer backbones, the work of Barbara and co-workers in 2011 represents an important transition from passive use of linkers toward intentional backbone engineering[60]. By synthesizing random poly(2-methoxy-5-(2'-ethylhexyloxy)-*p*-phenylene vinylene) (MEH-PPV) copolymers containing backbone-directing defects, they demonstrated that rigid and bent units reduce chain anisotropy, while saturated, non-conjugated defects introduce rotational freedom and expand the range of accessible chain conformations. These findings align closely with the emerging understanding of conjugation-break spacers as non-conjugated elements that, despite interrupting π-delocalization, offer a powerful means of controlling polymer conformation and packing.

Subsequent work by Plunkett and co-workers further advanced this concept through the introduction of flexible alkyl and glycol linkers, called flexible morphons, to connect PPV oligomers[61]. Rather than targeting electronic properties in solution which remained largely unchanged, this strategy focused on manipulating solid-state interchain interactions and effective conjugation length. In doing so, these studies reframed conjugation-breaking linkers from being merely a compromise for processability into a design tool for directing self-assembly. Although practical optoelectronic devices were not demonstrated, this body of work provided critical groundwork for modern approaches that exploit flexible linkers to engineer the mesoscale morphology of semiconducting polymers for applications such as thin-film transistors and organic photovoltaics.

In the modern era, conjugation-break spacers are recognized as a powerful tool for engineering the mesoscale organization of semiconducting polymers. Rather than serving solely to improve solubility or adjust optical properties, flexible linkers have evolved to program self-assembly pathways and optimize solid-state morphology. This approach has proven particularly valuable for applications such as thin-film transistors (TFTs) and organic photovoltaics (OPVs), where device performance is strongly governed by nanoscale ordering, interchain connectivity, and morphology-dependent charge transport [52–55].

Historically, the incorporation of non-conjugated linkers into semiconducting polymer backbones was widely assumed to be detrimental, as interruptions in conjugation were expected to introduce structural disorder and impede charge transport. Nevertheless, subsequent studies have revealed that these linkers can offer several important functional advantages when strategically implemented. Most notably, conjugation-breaking units provide a means to engineer polymer self-assembly and solid-state morphology without modifying the side chains or altering the intrinsic energetics of the π-conjugated core. In addition, the introduction of controlled backbone flexibility enables mechanical tuning by reducing chain rigidity, thereby modulating viscoelastic behaviour and improving material elasticity. From a processing standpoint, non-conjugated linkers can also enhance processability by lowering solution viscosity and enabling alternative fabrication routes, including solvent-free melt processing. Together, these findings have reshaped the perception of conjugation-break spacers from a source of disorder to a versatile design element for multifunctional polymer systems.

3.3. Π-conjugation broken systems

π-conjugation broken systems are molecules or polymers where continuous π-electron delocalization is interrupted, typically by incorporating non-conjugated molecules in the conjugated backbone.

3.3.1. Overview and classification

In conventional conjugated systems, π-electrons are delocalized across a continuous chain of alternating single and double bonds, allowing for electron movement across the entire structure. π-Conjugation-broken systems, however, feature intentional interruptions in this conjugation, resulting in isolated or segmented π-systems. In standard conjugated systems, π-electrons are delocalized along a continuous line of alternating single and double bonds, enabling electrons to move across the entire system. On the other hand, π-conjugation-broken systems purposefully interrupt this conjugation, resulting in isolated or fragmented π-systems. π-conjugation broken systems were used as two distinct categories. The first one is as a monomer, which is later polymerised to afford polymers with specific monomer segments. The second one is as a copolymer with different π-conjugated materials.

3.3.2. Preparation of π-conjugation broken systems

This section outlines the principal strategies employed to synthesize π-conjugation–broken polymer systems. Broadly, these materials can be prepared using either chemical or electrochemical approaches, each offering distinct advantages for incorporating non-conjugated units into the polymer backbone. The following subsections describe these two synthesis strategies in detail.

For clarity and consistency throughout this chapter, literature-reported structures are assigned labels **L1**, **L2**, **L3**, etc. These identifiers are used exclusively within the Literature Review to facilitate discussion and comparison of previously reported systems. They are independent of the compound numbering employed in the Synthesis Chapter, where compounds prepared in this work are assigned their own numbering scheme.

3.3.2.1. Chemical synthesis

Chemical synthesis is a fundamental strategy for constructing π-conjugation broken systems. It has been utilized to synthesize conductive and conjugated polymers across various fields, such as polymer science, chemistry, materials science, and condensed matter physics, ever since the discovery of doped conductive polyacetylene [62].

Jenekhe et al. reported the synthesis of π-conjugation-disrupted systems through a condensation polymerization approach [21]. As illustrated in Scheme 3.3.1, the synthetic strategy proceeds via a two-step methodology. In the first step, heteroaromatic building blocks (**L1**) undergo condensation with aldehydes to afford nonconjugated precursor polymers (**L2**) containing methylene (-CRH-) bridge units that interrupt π-conjugation. The heteroaromatic segments include 2,5-thiophenediyl, 5,5′-α-bithiophenediyl, and 5,5″-α-terthiophenediyl units.

In the second step, the precursor polymers (**L2**) are converted into fully conjugated narrow band-gap polymers (**L3**) through oxidative elimination of the bridging hydrogen atoms, generating alternating aromatic and quinonoid segments along the backbone. Infrared and electronic spectroscopy confirmed the elimination of bridge hydrogen, while the reduced solubility of **L3** compared to **L2** further supported formation of the extended conjugated system. The low band-gap character of these materials was attributed to stabilization of the quinonoid resonance structure within the polymer backbone.

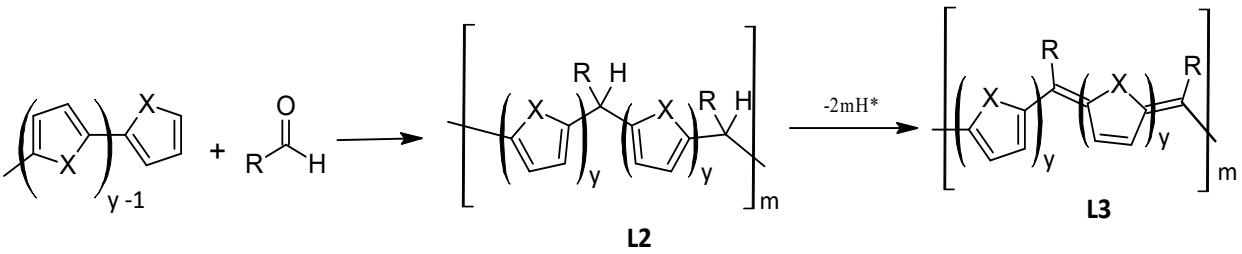

L1 **L2** **L3**

Scheme 3.3.1 Synthetic strategy reported by Jenekhe et al. [21] *for the preparation of narrow band-gap conjugated polymers: condensation of heteroaromatic units (L1) with aldehydes to afford nonconjugated precursor polymers containing methylene bridges (L2), followed by oxidative elimination of bridge hydrogen to generate fully conjugated polymers with alternating aromatic and quinonoid segments (L3).*

In 1990, Jenekhe et al. reported the chemical synthesis of polymers containing α-(5,5″-terthiophenediyl) segments separated by sp^3-hybridized carbon atoms in the main chain [63]. These materials were prepared through acid-catalyzed condensation polymerization of terthienyl derivatives with aldehydes. As illustrated in Figure 3.3, the resulting polymer **L4** consists of conjugated terthiophene segments interrupted by methylene (sp^3-carbon) bridges, thereby deliberately disrupting π-conjugation along the backboneThis approach represents a purely chemical strategy for constructing π-conjugation-broken systems, in which conjugated segments are linked through nonconjugated sp^3-carbon spacers during polymer formation. Furthermore, the methylene bridges were shown to be chemically transformable via dehydrogenation, enabling post-polymerization conversion into more extended conjugated structures [63]. These studies demonstrate that controlled interruption of conjugation can be achieved through step-growth condensation chemistry, providing a synthetic platform for designing conjugation-modulated heteroaromatic polymers.

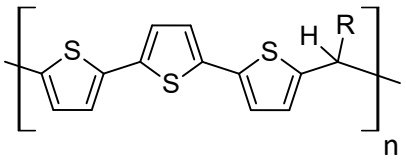

where R=H

L4

*Figure 3.3 Structures of poly[α-(5,5"-terthiophenediyl)-methylene] (PTTM, **13**) reported in* [63].

Carlsen et al. [64] reported the chemical synthesis of broken π-conjugation thiophene systems based on 2,2′-di(alkylthienyl)methane derivatives, as illustrated in Scheme 3.3.2. In their approach, 3-alkylthiophenes were subjected to chloroalkylation in the presence of zinc chloride and hydrochloric acid, affording a series of 2,2′-dialkylthienylmethane monomers (**L5**). These monomers were subsequently polymerized via oxidative coupling using iron(III) chloride to yield partially π-conjugation-broken polymers (**L6**). Although the synthetic objective was to obtain polymers with conjugation interrupted by methylene spacers, oxidative dehydrogenation at the bridge carbon during polymerization generated quinoidal segments within the backbone. Spectroscopic analysis, including UV–Vis and ^{1}H NMR measurements, confirmed the presence of these quinoidal structures. As a result, the materials exhibited measurable electrical conductivity in the range of 10^{-6} to 10^{-4} S cm^{-1}. In addition, the authors systematically varied the alkyl substituents on the thiophene rings to investigate their influence on solubility, processability, and electronic properties. This study demonstrated that alkyl chain length plays a critical role in modulating both structural organization and conductivity in chemically synthesized conjugation-break thiophene polymers.

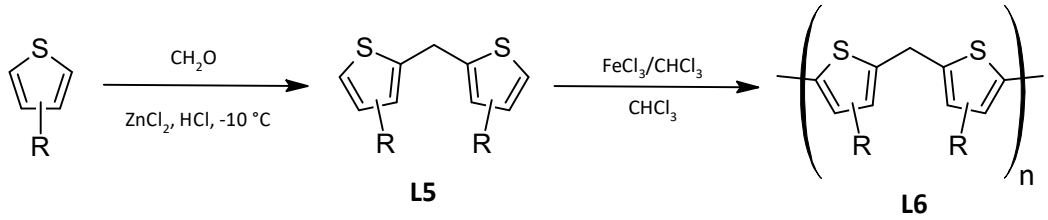

L5 **L6**

where R = H, CH_3, C_4H_9, C_8H_{17}

*Scheme 3.3.2 Synthesis of monomers (**L5**) and oxidative polymerization, and expected polymer structure (**L6**). Reported in.*[64].

Akaki et al. reported the chemical synthesis of low band-gap poly(bithienylenemethine) and poly(terthienylenemethine) derivatives incorporating arylene side chains [65]. As illustrated in Scheme 3.3.3, acid-catalyzed polycondensation afforded benzonoidal precursor polymers designated as Poly-2PB and Poly-2TB (**L7**), as well as Poly-3PB and Poly-3TB (**L8**). Subsequent oxidative dehydrogenation using (2,3-dichloro-5,6-dicyano-1,4-benzoquinone) DDQ converted these materials into their corresponding quinoidal forms, namely Poly-2PQ (**L9**) and Poly-3PQ/Poly-3TQ (**L10**).

In the original nomenclature, PB and TB denote poly(bithienylenemethine) and poly(terthienylenemethine), respectively, while the suffixes P and Q indicate benzonoidal precursor and quinoidal structures. This two-step chemical strategy enables controlled transformation from methine-interrupted systems to fully quinoidal conjugated polymers exhibiting very low optical band gaps.

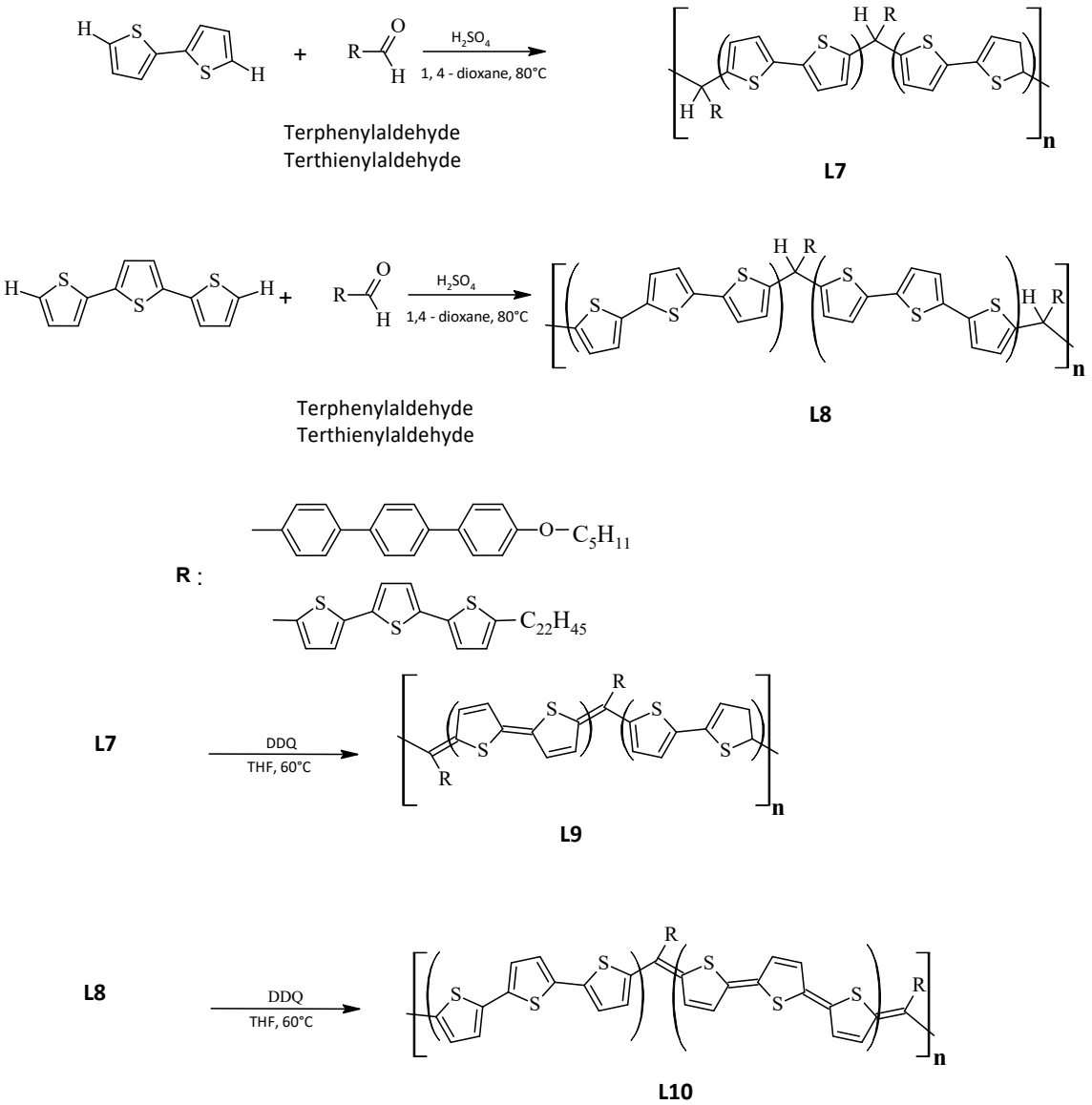

Scheme 3.3.3 Synthetic pathways for benzonoidal and quinoidal polymers with ternary phenylene or thienylene moieties in side chains. Adapted from literature [65].

Recent studies have expanded the use of conjugation-break spacers (CBSs) in thiophene- and diketopyrrolopyrrole (DPP)-based semiconducting polymers to systematically tune optical, magnetic, and charge-transport properties. Goto *et al.* [66] synthesized thiophene-based methine-bridged conjugated polymers via Migita–Kosugi–Stille polycondensation, followed by oxidative treatment to modulate the electronic structure. Optical and magnetic characterization, including UV–vis absorption, photoluminescence, iodine doping studies, and electron spin resonance spectroscopy, confirmed the generation and stabilization of charge carriers within these interrupted conjugated systems.

Complementary investigations by Mei and co-workers [67], examined DPP-based polymers incorporating pentamethylene CBSs and varied side-chain architectures. Their results demonstrated that the introduction of flexible spacers enables a balance between charge transport and improved melt processability. Similarly, Zhao *et al.* [11] systematically introduced flexible alkyl CBSs into DPP–quaterthiophene backbones, showing that controlled conjugation interruption reduces backbone rigidity, enhances conformational flexibility in solution, and significantly improves processability while preserving semiconducting functionality.

In addition, semi-random polymers prepared via Stille polycondensation with systematically varied alkyl spacer content further highlighted the structural role of CBSs in tuning material properties [10]. These studies collectively demonstrate that the deliberate incorporation of conjugation-break spacers through chemical polymerization strategies provides an effective means of modulating both mechanical behaviour and electronic performance in π-conjugated polymers.

3.3.2.2. Electrochemical synthesis

The use of electrochemical methods for the preparation of insoluble polymeric materials dates back more than 165 years. In 1862, Letheby reported the anodic oxidation of aniline in dilute sulfuric acid, describing the formation of a blue-black, insoluble material [68]. However, the modern era of conducting polymers began in 1977, when Heeger, MacDiarmid, and Shirakawa demonstrated that iodine doping of polyacetylene (PA) dramatically increased its electrical conductivity by several orders of magnitude [29][62]. This made copper-colored films and increased conductivity by 10 orders of magnitude. This discovery established the foundation for the development of organic conducting polymers.

Despite its groundbreaking significance, polyacetylene suffered from poor environmental stability and susceptibility to oxidative degradation. Consequently, significant research efforts were directed toward the development of more stable conducting polymers, including polyaniline, polyphenylene, polyphenylenevinylene, polypyrrole, and polythiophene [69][70][40][71]. Among these, polythiophene and its derivatives have attracted considerable attention due to their chemical stability, synthetic versatility, and tunable electronic properties.

Electrochemical polymerization has emerged as a powerful technique for synthesizing conjugated polymers directly onto electrode surfaces. In this approach, thiophene and substituted thiophene monomers undergo anodic oxidation to generate radical cations, which subsequently couple to form extended π-conjugated polymer chains. The process enables precise control over film thickness, doping level, and morphology. In the context of π-conjugation-broken systems, electrochemical synthesis provides an attractive platform for polymerizing monomers that incorporate predefined conjugation-break spacers. Unlike fully conjugated systems prepared solely through chemical polycondensation, this strategy allows the deliberate design of monomer structures that are subsequently assembled electrochemically into conducting polymer films. The following section discusses electrochemical approaches for the preparation of π-conjugation-modulated polymers in greater detail.

Zoti *et al.* [72] investigated the anodic coupling of oligothiophenes incorporating ethylene-based conjugation-break spacers, with the objective of producing polyconjugated polymers possessing well-defined conjugation lengths. Symmetric quaterthiophene and sexithiophene monomers were synthesized, in which conjugated thiophene segments were separated by ethylene bridges (see Figure 3.4), enabling precise control over the number of thiophene units within each conjugated domain. Electrochemical studies revealed oxidation of the broken quaterthiophene units at approximately 0.82 V, followed by the appearance of a reversible redox process attributed to polymer formation. However, upon repeated cycling, the electrochemical response progressively slowed, broadened, and shifted toward higher potentials, indicating polymer degradation associated with the relatively high oxidation potential required for coupling.

A distinct electrochemical behaviour was observed for the ethylene-bridged sexithiophene derivative. Cyclic voltammetry exhibited a partially reversible response resembling that of

polythiophene, accompanied by an irreversible oxidation process, and thin films deposited on the electrode displayed reversible redox activity. Nevertheless, infrared spectroscopic analysis of the electrosynthesized materials demonstrated that anodic coupling predominantly yielded dimeric species rather than extended polymer chains. These findings suggest that electrochemical polymerization is not well suited for symmetrically conjugation-broken oligothiophenes of this type. Importantly, the resulting dimers retained structural characteristics of both polythiophene and sexithiophene units.

Importantly, solubility limitations were also noted for the ethylene-bridged sexithiophene system. These observations establish critical design constraints for spacer-containing thiophene systems and provide an important comparative framework for our alkylene-based methylene spacer approach.

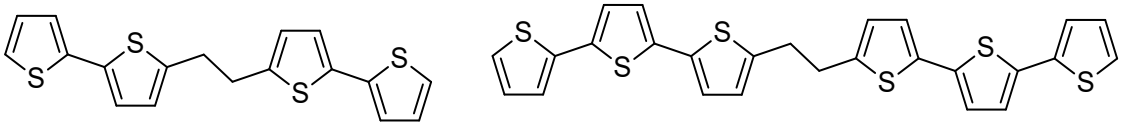

L11 **L12**

*Figure 3.4 Chemical structures of selected monomer (**3**) quaterthiophenes, and **(4**) sexithiophene, symmetrically broken by ethylene spacer.*

In 2003, Zoti *et al.* [73], reported the synthesis, characterization, and electrochemical behaviour of poly(biheteroarylidenemethine) polymers obtained via oxidative electrochemical polymerization of bis(2-thienyl)methane monomers (Figure 3.5). This approach yielded poly(dithienylenemethine) backbones characterized by exceptionally low optical band gaps. The general mechanism of the electrochemical polymerization of bis(2-thienyl)methanes, including p- and n-doping processes, is illustrated in Scheme 3.3.4. The study demonstrated that the incorporation of methine bridges as non-conjugated spacer elements between heteroaromatic units significantly influences the electronic structure and electrochemical response of the resulting polymers.

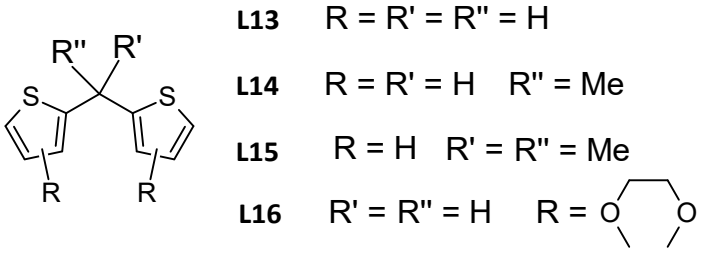

Figure 3.5 Bis(2-thienyl) methane monomers reported in [73].

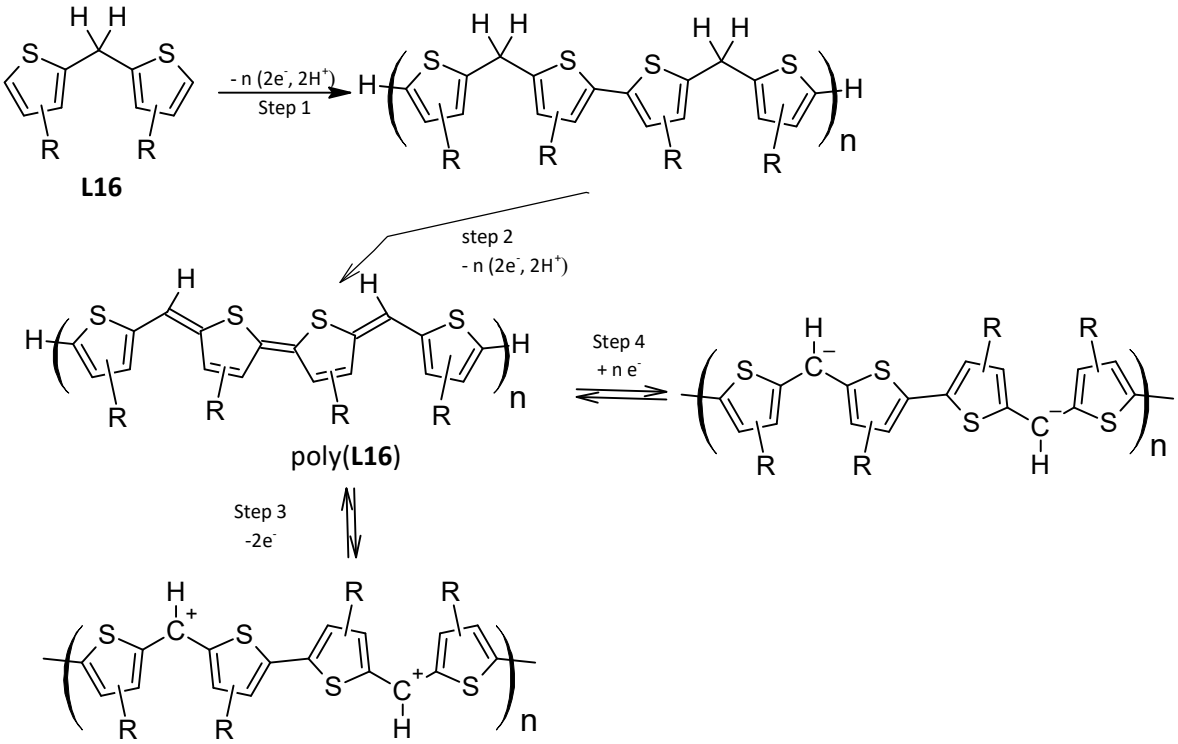

*Scheme 3.3.4 General scheme of the electrochemical polymerization of Bis(2-thienyl)methanes (**L16**) and p- and n-Doping of the Polymers reported in* [73].

According to the mechanism proposed by Zotti and co-workers, anodic polymerization proceeds initially through conventional α–α′ coupling between thiophene units (Step 1). This is followed by a two-electron oxidation process involving the methylene groups of each dimeric subunit (Step 2), accompanied by proton release from the benzylic-type carbons, whose acidity increases upon oxidation. The resulting structure exhibits an alternation of aromatic and quinoid segments along the backbone. This arrangement is twofold degenerate in the ground state and displays a narrow band gap of approximately 1.2 eV, significantly lower than that of polythiophene (2.1 eV) [73]. The oxidized polymer can undergo either a reversible two-electron oxidation process (Step 3) or a reversible one-electron reduction process (Step 4). In Scheme 3.3.4, positively and negatively doped states are depicted with charge localization primarily at the benzylic carbons, although substantial electronic delocalization occurs and multiple mesomeric structures can be envisaged.

While the primary objective of this study was to synthesize low-band-gap materials via electrochemical polymerization, our work differs in that we focus on detailed electrochemical and spectroelectrochemical characterization of structurally tailored systems, and the mechanistic scenario differs from that proposed by Zotti and co-workers.

The electrochemical behaviour of two pairs of β,β′-didodecyl-substituted quinquethiophenes incorporating trimethylene (n = 3) and tetramethylene (n = 4) spacers was investigated using cyclic voltammetry in both solution and solid films[74]. The synthetic route toward **L19** (n = 3) and **L20** (n = 4) involved the preparation of reactive intermediates **L17** and **L18**, which were subsequently coupled under Ni(dppp)Cl_2 catalysis to afford the corresponding spacer-bridged quinquethiophenes (Scheme 3.3.5). Electrochemical analysis demonstrated two sequential electron-transfer processes leading to tetracation formation. These redox processes were reversible at ambient temperature but became partially irreversible at lower temperatures. Scan-rate and concentration studies suggested preferential β-coupling near the bridging sites.

No electropolymerization was observed in solution; however, during oxidation in the solid state, intermolecular coupling between oligothiophene segments occurred. These findings further emphasize the sensitivity of electrochemical behaviour to spacer length and structural symmetry.

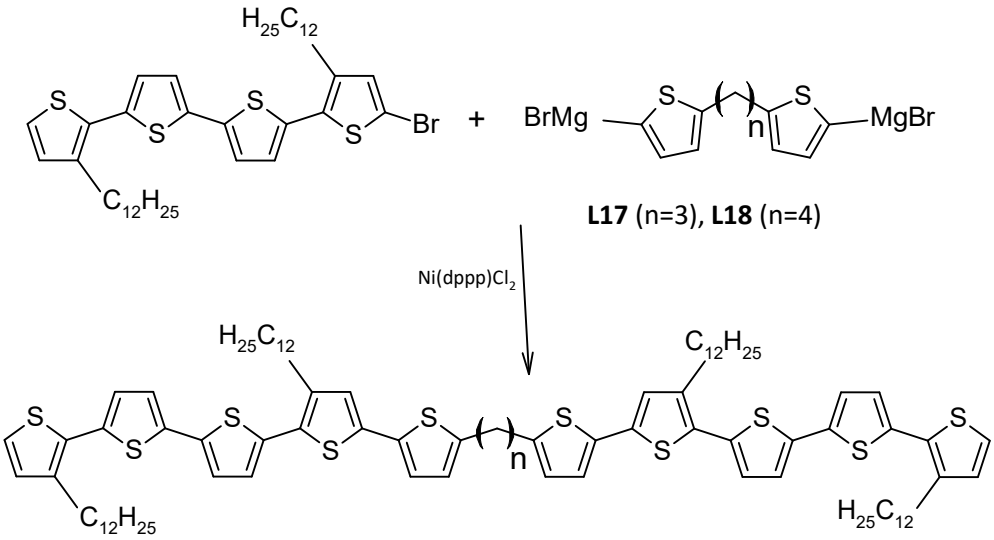

*Scheme 3.3.5 Synthesis of 1,3-bis(4_,3-didodecyl-2,2:5,2:5,2 :5,2-quinquethien-2-yl)propan **L17** and 1,4-bis(4,3-didodecyl-2,2:5,2:5,2:5,2-quinquethien-2-yl)butane **L18** reported in* [74].

3.3.3. Properties of π-conjugation broken polymers

2.1.2.1. Spectroscopic properties

Studying the spectroscopic properties of conjugated polymer is crucial to analysing their individual properties. The spectroscopic properties of materials with *π*-conjugation break spacers (CBSs) confirm that these non-conjugated linkers successfully isolate electronic segments, allowing the material to retain the optical characteristics of its individual conjugated units while enabling macro-scale processing.

The UV-vis-NIR spectrum of the oxidized blue polymer film of poly (**L16**) structure, shown in Scheme 3.3.4, revealed a high absorption peak at 1200 nm and extended into the infrared region [73]. The undoped, brownish-gray, air-sensitive version displayed a wide absorption that peaked at about 500 nm and encompassed the complete range. This shows that poly(**L16**) has a very small gap. Zotti's group also studied the FTIR properties of poly (**L16**). The FTIR spectrum of oxidized poly(5d) had four strong bands between 1490 and 1360 cm^{-1}, which were also seen in the monomer and were related to skeletal vibrational modes [73]. There was also a strong band at 1100 cm-1 that came from the perchlorate anion band (with a band at 620 cm^{-1}) and the EDOT bands (1180 and 1070 cm^{-1} in the monomer). As expected, the R-aromatic CH stretching band at 3100 cm^{-1} was not there. There were no significant bands in the 1700–1600 cm^{-1} range, which suggests that overoxidation did not transpire.

Jenekhe *et al*, [63]has also studied the infrared spectra of polymer films shown in Figure 3.3, at room temperature. The polymer film has clear bands around 790 cm^{-1}, which are caused by C-H out-of-plane vibrations and show that there are α-linkages in thiophene rings. It is thought that the band at 686–703 cm^{-1} in polymer is caused by C-H vibrations and shows that polythiophenes have β-substitution or thiophene end groups.[75][76]. The optical absorption maximum (λmax) due to the π-π* transition for the methylene-bridged polymer is shown at 367 nm [63]. To compare this result, they

did measurements for three modal compounds: α-terthiophene, α-quaterthiophene, and α-sexithiophene. These modal compounds show the λmax at 350-355, 395, and 438 nm, respectively.

The methylene and methine bridged polythiophenes are characterized by two main absorption bands in the UV (ultraviolet) region and the visible region [77]. The UV absorption bands of these polymers, except Poly[(2,5-thiophenediyl)(p-nitrobenzylidene) (2,5 thiophenequinodimethanediyl)] (PTNBQ) and Poly[(3-methylthiophene-2,5-diyl)(p nitrobenzyli-dene) (PMTNB) arise from the π- π* transition of the aromatic thiophene ring and have Amax from 230 to 245 nm. However, the UV absorption bands of PTNBQ and PMTNB, which are assigned to the π - π* transition of the p-nitrophenyl side group have a λmax that is about 30 nm larger than that of other polymers. The Visible absorption band of poly[(thienylene)- methylenes) derivatives arises from the π- π* bandgap transition and has a λmax from 366 to 485 nm, which is comparable to the λmax of P3HT (λmax = 435 nm). They also studied the solution optical absorption of poly (α-bithienylene)methylenes]; poly [(α-terthienylene)methylenes]; and poly [(α- quaterthienylene)methylenes]. The assigned λmax are 318 - 332 nm, 369 - 372 nm, and 401 - 402 nm, respectively. These results are comparable to the λmax of the corresponding thiophene oligomers α-bithiophene, α-terthiophene, and α-quaterthiophene, which have λmax at 305-310, 350-355, and 390-395 nm, respectively, depending on the solvent. It is noted that the side group at the bridged carbon shows a negligible effect on the λmax of the optical absorption spectra of the poly(heteroarylene methylenes) derivatives [77], which will be help ful in our future studies.

The solution and solid-state UV−vis−NIR spectra of diketopyrrolopyrrole (DPP) polymers reveal the impact of propyl CBS on the optical properties[49]. Goto *et al*, [66] studied the UV-vis optical absorption spectra of a thiophene-based methine-bridged type conjugated polymers **L21** and L**22** (Figure 3.6). The UV–Vis optical absorption spectra of polymers **L21** and **L22** were done in chloroform. The spectra of polymers **L21** and **L22** reveal an optical absorption attributed to π- π* transition of the main chain at 419 nm and 439 nm, respectively. The 20 nm red shift showed that effective conjugation had happened because the conjugated methine-bridged bond had formed in the polymer's main chain.

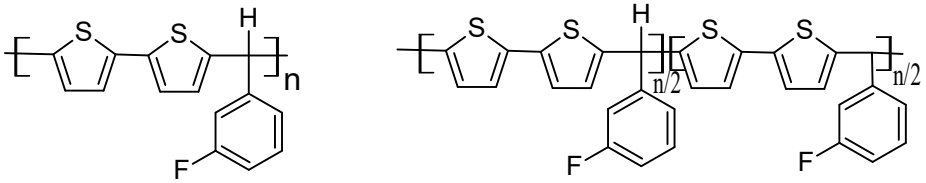

L21 **L22**

*Figure 3.6 The chemical structures of polymers **L21** and **L22** are reported in* [49].

The Mei group also studied the influence of the length of conjugation-break spacers (CBSs) on charge transport properties of the matrix polymers and their corresponding complementary polymer blends [78]. They confirmed that the UV−vis spectra and the ultraviolet photoelectron spectroscopy (UPS) measurements show that the CBS length has a marginal influence on the polymer absorption spectra, energy levels, and band gaps. The UV–Vis–NIR absorption spectroscopy was employed to directly probe how the systematic incorporation of conjugation-break spacers (CBSs) modulates π-electron delocalization in DPP-based polymers [78]. A pronounced bathochromic shift was observed as the polymer backbone transitioned from fully flexible (DPP-100) to fully rigid (DPP-0), consistent with increased effective conjugation length in both solution and thin-film states. Notably, rigid and semi-rigid polymers (DPP-0, DPP-30, and DPP-50) exhibited hypsochromic shifts upon film formation,

indicative of reduced intrachain conjugation or altered packing relative to solution. In contrast, flexible derivatives (DPP-70 and DPP-100) displayed limited red-shifting accompanied by substantial spectral broadening, reflecting increased conformational disorder and heterogeneous electronic environments. A broad absorption feature centred near 800 nm emerged in DPP-100 thin films, serving as a spectroscopic signature of strong excitonic coupling and π–π stacking, consistent with complementary structural data.

Ultraviolet photoemission spectroscopy (UPS), combined with optical absorption onsets, was used to map the evolution of frontier molecular orbitals across the DPP-x series [78]. Despite substantial changes in backbone flexibility, the absolute energy levels were only modestly affected by spacer incorporation. The HOMO level shifted gradually from −4.97 eV in the fully rigid polymer to −5.13 eV in the fully flexible analogue, while variations in LUMO energies were even smaller (ca. 0.08 eV), suggesting stronger localization of the LUMO within the conjugated core. Correspondingly, the optical band gap increased systematically with increasing spacer content, from 1.32 eV (DPP-0) to 1.40 eV (DPP-100), reflecting reduced effective conjugation length without drastic perturbation of the electronic energy landscape.

Proton NMR spectroscopy was used to confirm the chemical identity of the polymers and to quantitatively verify the incorporation of CBSs [78]. The relative spacer content was determined by comparing the integrated intensities of methylene protons adjacent to the thiophene units (ca.2.9 ppm) and those adjacent to the DPP nitrogen atoms (ca.4.0 ppm). This analysis provided direct evidence for precise control over spacer concentration, ensuring a clear structure–property correlation between CBS content, electronic structure, and solid-state organization.

Earlier work on π-conjugation-break systems, exemplified by Jenekhe's and his worker's, study, used spectroscopy primarily to confirm spacer elimination and the restoration of extended conjugation, enabling record-low band gaps near 0.75 eV [63]. In contrast, the 2015 study by Mei *et al.*[78] demonstrates that spectroscopic signatures can instead be used to verify that meaningful charge transport persists even when conjugation breaks are deliberately retained. In particular, spectral broadening and the emergence of a low-energy absorption feature near 800 nm in high-CBS polymers provide clear evidence that interchain π–π stacking can partially compensate for reduced intrachain conjugation, highlighting a fundamental shift from spacer removal to spacer-enabled electronic design.

2.1.2.2. Electrochemical properties

The electrochemical properties of materials containing *π*-conjugation break spacers (CBSs) are primarily studied to understand how isolating specific electronic segments affects oxidation potentials, polymer growth, and charge transport. As seen in the work by Berlin et al. using ethylene fragments to bridge oligothiophenes allows researchers to create systems that mimic the structural features of polyconjugated polymers while maintaining a strictly defined conjugation length [72]. Electrochemical studies revealed that oxidation potentials and polymerization behaviour are strongly dependent on the length of the isolated thiophene segments. Bithienyl-based systems exhibit an initial oxidation near 0.82 V, followed by the emergence of a reversible redox process attributed to the formation of ethylene-bridged quaterthiophene units, whereas terthienyl-based systems display an irreversible oxidative event around 0.7 V that evolves into a polythiophene-like redox response.

Despite these observations, anodic coupling of CBS-containing monomers is frequently hindered by the high potentials required for oxidation, which promote degradative processes manifested as signal broadening and anodic shifts during repeated cycling[72]. In addition, solubility plays a critical

role in limiting polymer growth: terthienyl-based systems often terminate at the dimer stage, as the low solubility of the oxidized species leads to precipitation at the electrode surface and suppresses further coupling. As a result, the electrosynthesized materials exhibit morphologies resembling polythiophene while retaining the fixed conjugation length of longer oligothiophenes. Consistent with this segmented electronic structure, the electrical conductivity of these materials is significantly reduced compared to fully conjugated polymers, with charge transport proceeding primarily via interchain hopping rather than through-bond delocalization [72]. Collectively, these electrochemical studies highlight both the promise and the inherent limitations of CBS-containing systems, underscoring the trade-offs between controlled conjugation length, processability, and charge-transport efficiency.

A high molar fraction of non-conjugated monomer units within the polymer backbone can disrupt the effective conjugation length of the π-conjugated segments[79]. This disruption leads to shifts in the ionization potential (IP) and electron affinity (EA), thereby altering the electronic properties of the resulting material. The influence of the alkylene bridging chain on the self-assembly behaviour and electronic characteristics of dual-quinquethiophenes was systematically examined using scanning tunneling microscopy (STM) and scanning tunneling spectroscopy (STS)[80]. The incorporation of different dicarboxylate linking units within the non-conjugated segments of the polymer backbone was found to have a negligible effect on the material's redox potential [55]. Electrochemical measurements indicate that variations in the chemical structure of these linkers do not significantly influence the highest occupied molecular orbital (HOMO) energy level. This suggests that the electronic properties of the conjugated domains remain largely unaffected by the nature of the non-conjugated dicarboxylate bridges, reinforcing the idea that electronic delocalization is primarily governed by the conjugated segments themselves.

2.1.2.3. Mechanical properties

The capacity to endure mechanical deformation without fracturing is essential for the application of organic electronic devices in flexible, stretchable, and portable contexts, particularly in outdoor environments where they encounter various thermomechanical stresses and during roll-to-roll manufacturing processes [81]. It has been demonstrated that conjugation-break spacers (CBS) can enhance the mechanical properties of conjugated polymers. Incorporating CBS units into semi-random polymers has proven that these materials are highly flexible and exhibit low elastic moduli. This might have resulted from the interaction between the CBS units and the semi-random structure. Thomson *et al* [82], studied the influence of acceptor side-chain length and conjugation-break spacer content on the mechanical and electronic Properties of Semi-Random Polymers. It is shown that incorporating Conjugation-break spacers (CBS) enhances the mechanical properties of conjugated polymers.

A family of semi-random polymers containing conjugation-breaking spacers was synthesized, demonstrating significant mechanical characteristics due to both the disruption of conjugation and the semi-random architecture of the polymer backbone [10]. Lipomi group also reported the effects of "conjugation-break spacers" (CBSs)aliphatic units that interrupt the sp^2 -hybridized backbone of semiconducting polymers on the mechanical and photovoltaic properties of a diketopyrrolopyrrole-based polymer [83]. Previous work has suggested that mechanical properties such as the elastic modulus (E) depend on a complex interplay between molecular structure and packing arrangement in the solid state [84]. A lower elastic modulus is generally regarded as better for flexible electronics applications, as it indicates a material that is more easily deformed and produces reduced interfacial

stresses with other layers in a device. While the elastic moduli of conjugated polymers vary widely (E = 0.1–8 GPa)[85][86][87][88], polymers with CBSs have consistently exhibited elastic moduli of less than 1 GPa [84][85].

2.1.2.4. Self-assembly and morphology properties

Numerous methodologies have been developed to regulate the solid-state morphology of semiconducting polymers by influencing their self-assembly during solution-based film formation. Extrinsic strategies; such as tuning solvent systems, employing meniscus-guided coating, and various printing techniques[89] have proven effective in directing thin-film morphology. Additionally, the incorporation of processing additives, including nucleation agents, electronically inert polymers, and post-deposition treatments, has been widely utilized[63][91][92]. However, these approaches are highly sensitive to external parameters such as substrate characteristics, solvent volatility, evaporation dynamics, and the specific processing method employed. Consequently, they often necessitate extensive empirical optimization and may lack general applicability across diverse molecular architectures[93].

In contrast, molecular engineering offers a more intrinsic route to morphology control by directly modulating the self-assembly behaviour of π-conjugated systems[94]. Structural modifications of the π-conjugated polymer backbone via the integration of planar π-extended conjugated monomers, donor–acceptor motifs, covalent conformational constraints (e.g., ladder-type polymers), or non-covalent locking mechanism[95][96][97][98][99], have demonstrated the ability to influence conjugation length and π–π stacking, thereby impacting both intra- and intermolecular charge transport[100]. Notably, while planarization typically enhances stacking, certain co-monomer configurations may induce backbone curvature, adversely affecting electronic coupling. Side-chain engineering, traditionally employed to enhance solubility, also plays a critical role in modulating intermolecular interactions [101]. Linear alkyl chains promote efficient one-dimensional stacking by minimizing steric hindrance, whereas branched chains disrupt this order [102]. Strategic placement of branching points further optimises extremely short π–π stacking distances without affecting solubility[103]. Moreover, functional side chains capable of hydrogen bonding or self-organization, such as urea-containing or fluorinated alkyl groups can significantly enhance molecular ordering[104][105]. Despite these advances, π–π interactions remain the predominant force governing supramolecular assembly in these systems.

However, a molecular design strategy has emerged for controlling the supramolecular assembly of semiconducting polymers without altering side chains or modifying the electronic structure of the π-conjugated core. This approach involves the covalent incorporation of flexible, non-conjugated spacers typically aliphatic chains between π-conjugated segments. These spacers are often referred to as conjugation-break spacers due to their disruption of continuous π-conjugation, or alternatively as flexible linkers because they introduce conformational freedom into the otherwise rigid polymer backbone. At first glance, the inclusion of such non-conjugated linkers might be expected to negatively impact charge transport by interrupting intramolecular conjugation and increasing disorder in the solid state. However, recent studies have demonstrated that this strategy can offer several advantages. By reducing backbone rigidity, flexible linkers enhance the processability of the polymer and enable unique self-assembly pathways that can lead to improved morphological control and device performance in organic field-effect transistors (OFETs) and organic photovoltaic cells (OPVs). This design paradigm represents a shift from traditional approaches that rely heavily on side-chain

engineering or backbone planarization. Instead, it leverages the interplay between molecular flexibility and supramolecular organization to achieve desirable optoelectronic properties, even in the presence of interrupted conjugation[55][106][107][108].

Generally, Conjugation break spacers are one of the tools used to control the morphology and self-assembly in π-conjugated semiconductor polymer. Moreover, polymers containing odd-numbered conjugation-breaking spacers (CBSs) exhibit enhanced solubility, lower melting transition temperatures, and reduced π–π stacking distances [109]. These structural features contribute to the formation of two-dimensional lamellar-like morphologies and result in higher overall crystallinity. Such characteristics suggest that odd-numbered CBSs promote more ordered molecular packing and improved processability, which may be advantageous for certain optoelectronic applications.

2.1.2.5. Charge transport properties

Although the incorporation of CBS often hampers charge carrier mobility by disrupting π–π stacking, recent studies have investigated ways to overcome this challenge [110]. In general, increasing the length of the conjugation-breaking spacer (CBS) leads to a reduction in π-aggregate density, thereby diminishing the likelihood of forming an efficient charge transport network within the polymer matrix. Interestingly, an odd–even effect is clearly observed in charge transport performance, with even-numbered CBS polymers consistently outperforming their adjacent odd-numbered analogues [109]. This trend is counterintuitive, as odd-numbered polymers typically exhibit shorter π–π stacking distances and higher crystallinity features that are generally favorable for charge mobility. A plausible explanation lies in the molecular conformation: even-numbered CBS units tend to adopt a Z-shaped geometry, which may facilitate the formation of a more interconnected and continuous charge transport network compared to the V-shaped configuration observed in odd-numbered counterparts. This hypothesis is supported by crystallographic data from analogous small-molecule systems.

Moreover, a primary objective in enhancing charge transport within semiconducting polymer-based devices is the optimization of intermolecular transport through controlled chain self-assembly into well-aligned domains [107]. Although short σ-covalent linkers between π-conjugated segments formally disrupt conjugation, they do not necessarily eliminate electronic communication. Under specific geometric configurations, through-bond electronic coupling can still occur, enabling charge delocalization across the interrupted segments. The incorporation of a saturated covalent bridge between two π-conjugated systems can enhance the dimensionality of charge transport by facilitating inter-segment connectivity, potentially enabling charge carriers to traverse multiple spatial directions within the material. Geerts, et al group designed and synthesized two quaterthiophene-based dimers incorporating an ethylene bridge [111]. Both experimental characterization and computational analysis indicate that these dimers exhibit promising semiconducting properties, with enhanced charge transport dimensionality relative to the parent quaterthiophene molecule.

3.4. Summary of π-conjugation break spacer research

Early work by Jenekhe [21]and Benincori [20]established CBSs as temporary synthetic elements used to access ultra-low bandgap polymers, whereas later efforts exemplified by Akagi *et al.*[65],demonstrated that permanently incorporated CBSs can act as structural stabilizers that enforce quinoidal backbone conformations and enable intrinsic band gaps in the 0.4–0.8 eV range. Beyond electronic tuning, modern research has redefined CBSs as key enablers of mechanical resilience, with

semi-random architectures developed by groups such as Thompson and Chen resolving the longstanding mobility–stretchability trade-off and yielding elastic moduli comparable to conventional elastomers. In parallel, work by Mei *et al.*[78] and Zhao *et al.*[49] introduced the tie-chain framework, showing that CBS-induced backbone segmentation can enhance processability while long-range charge transport is recovered through blending with small fractions of fully conjugated polymers. More recently, CBSs have also been exploited as functional sites for smart sensing, serving as chemical traps for proton detection or as coordination motifs in hybrid metal–organic materials. Together, these advances position conjugation breaks not as defects, but as versatile design elements for simultaneously tuning electronic, mechanical, processing, and functional properties.

Table 3.4.1 summarizes the evolution of conjugation-break spacer strategies across electronic, mechanical, and processing-focused applications

Research Context	Spacer Mechanism	Primary Application	Key Outcome / Performance	References
Low-Bandgap Precursors	sp^3 carbon bridges (–CRH–)	Record-low intrinsic gaps via oxidative elimination	Achieved intrinsic bandgaps as low as 0.75 eV (1650 nm)	[21]
Semiconductor Superlattices	Methylene and –CRH– bridges	Specified conjugation lengths independent of chain length	Solution λmax (362–379 nm) invariant with degree of polymerizatio n	[63]
Model Oligomer Systems	Ethylene fragments	Electrochemical mimics for solid-state studies	Mimicked polythiophene features; conductivity limited by interchain hopping	[19]
Small-Bandgap Platforms	EDOT–methine–EDOT	Electropolymerized small-bandgap materials	Onset-based bandgap of 0.4 eV, far lower than aryl-substituted analogues	[20]
Hybrid Materials & Sensors	Meta-substituted pyrimidines	Post-polymerization metal binding	Hybrid copolymers with tailored light harvesting and high fluorescence	[112]
Quinoidal NIR Harvesting	Methine sites + terarylene side chains	Near-infrared absorption for photovoltaics	Extended absorption to 1000 nm (Eg ≈ 0.8 eV);	[113]

			stabilized quinoidal form	
Sustainable Manufacturing	Propyl flexible units	Solvent-free mel-processed OFETs	Mobility up to 0.30 $cm^2/V·s$ without toxic solvents	[11]
Charge Transport Physics	Variable alkyl CBS (C2–C12)	Matrix/tie-chain polymer blends	Odd–even effects; 2–4 orders of magnitude mobility enhancement	[83]
Morphological Tools	Flexible non-conjugated linkers	Stabilizing morphology in crystalline small molecules	Prevented film dewetting by acting as molecular tie-ins	[114]
Mechanical Resilience	4–10 carbon alkyl spacers	Highly ductile semi-random polymers	Crack-onset strains >80% with preserved mobility	[82]
Chemical Acid Sensing	Thiophene–CH(R)–thiophene	Acid sensing via proton trapping	HCl detection limit of 3.35×10^{-5} M	[115]
Mechanical Optimization	8-carbon CBS + dtdDPP side chains	Toughness engineering	Elastic modulus reduced to 4.08 MPa; fracture strain up to 432%	[82])
Stretchable N-Type Logic	Functionalized CBS (ester, amide)	Intrinsically stretchable n-type circuits	61% mobility retention after 400 stretch cycles	[12]
Ductile OPV Ternaries	8-carbon alkyl spacers	Ductile ternary organic photovoltaics	Maintained efficiency at 25% CBS loading; fracture strain 432%	[116]
Carrier Dynamics	Bithiophene–methine bridge	Charge carrier and spin-state characterization (ESR)	Confirmed polarons and Pauli paramagnetism after iodine doping	[66]

3.5. Proposed gap statements

Despite the extensive development of conjugation-break spacer (CBS) strategies for tuning mechanical, morphological, and electronic properties of conjugated polymers, a fundamental understanding of their electrochemical oxidation mechanisms and charge-carrier evolution remains limited. Previous studies have primarily focused on synthetic strategies, band-gap engineering, or solid-state performance, while detailed investigations of first oxidation processes, follow-up reactions, and spectroelectrochemical charge-carrier dynamics in CBS-containing thiophene systems are scarce. In particular, systematic comparisons across varying bridge substitution, conjugation length, and spacer length within a unified experimental framework have not been comprehensively reported. Therefore, a mechanistically grounded electrochemical and spectroelectrochemical study is required to establish clear structure–redox–charge relationships in conjugation-broken oligothiophene systems. This dissertation addresses this gap.

4. Experimental section

4.1. Chemicals

All reagents and starting materials were purchased and used as received without further purification, unless otherwise specified. Thiophene (CAS: 110-02-1, Acros Organics, cat. No.: 138825000), Oxalyl chloride 98 % (CAS: 79-37-8, Acros Organics, cat. No.: 129611000), 1,3,5-Trioxane (CAS: 110-88-3, Switzerland cat. No.: T81108,), N-Bromosuccinimide (NBS) 99 % (CAS: 128-08-5, Acros Organics, cat. No.: 107455000), 2-Bromothiophene 98 % (CAS: 1003-09-4, Acros Organics, cat. No.: 154292500), $PdCl_2(dppf)_2$ 98 % (CAS: 72287-26-4, fluorochem), 1,3-Dibromopropane 98 % (CAS: 109-64-8, fluorochem), Potassium hydroxide (KOH) (CAS: 1310-58-3, Chempur, cat. No.: AC20607-5000), Sodium hydroxide (NaOH) (CAS: 1310-73-2, Chempur), Sodium bicarbonate ($NaHCO_3$) (CAS: 144-55-8, Chempur, cat. No.: AC217120010), Magnesium sulphate ($MgSO_4$) (CAS: 7487-88-9, Chempur, cat. No.: 005026-1KG), Sodium sulphate (Na_2SO_4) (CAS: 7757-82-6, Chempur), CuBr 98 % (CAS: 7787-70-4, Alfa Aesar), LiBr pure (CAS: 7550-35-8, Reachim), Magnesium turnings 99.9 % (CAS: 7439-95-4, Acros Organics), Boron trifluoride diethyl etherate ($BF_3{\cdot}Et_2O$) (46%) (CAS: 109-63-7, Acros Organics, cat. No.: AC17456-1000), Methyllithium 1.6M solution in Et_2O (CAS: 917-54-4, Sigma-Aldrich, cat. No.: 188751000 (100 mL)), NH_4Cl 99.5 % (CAS: 12125-02-9, Acros Organics), Hydrazine hydrate 50-60 % (CAS: 7803-57-8, Sigma Aldrich, cat. No.: AC19671-1000), Dichloromethane (DCM) (CAS: 75-09-2, Chempur), Et_2O (CAS: 60-29-7, Chempur), THF (CAS: 109-99-9, Acros Organics), Hexane fraction from naphtha (Chempur), Toluene (CAS: 108-88-3, Acros Organics), Petroleum ether (CAS: 8032-32-4, Chempur, cat. No.: 5575 / SKU 18131), Ethyl acetate (CAS: 141-78-6, Chempur), Hydrochloric acid 36-38 % (HCl) (CAS: 7647-01-0, Chempur), Acetic acid (CAS: 64-19-7, POCh, cat. No.: AC22214-0010), ethylene glycol (CAS: 107-21-1, Chempur). CuBr and LiBr were purified before being used. Both Et_2O and THF were dried before use. Magnesium turnings were activated by HCl and dried in a vacuum oven. All glassware, prior to running the Grignard reactions, was oven dried.

4.2. Measurements

4.2.1. Electrochemistry

For electrochemistry, a potentiostat, Metrohm Autolab PGSTAT302N and PGSTAT 100N, was used. Measurements were performed in a typical three-electrode cell. The platinum spiral was used as an auxiliary electrode, the silver wire was used as pseudo reference electrode (calibrated *versus* ferrocene/ferrocenium redox couple used as an external, or internal standard), and the 0.1 cm^2 platinum disk clad in PEEK (polyether ether ketone) sleeve (EDAQ, cat. no. ET075-1) as the working electrode.

In this research, electrochemical techniques have been employed:

- ✓ To investigate the redox properties of monomers and their corresponding polymers.
- ✓ To achieve direct electrochemical deposition of the polymer films onto the working electrode, facilitating the in-situ formation and characterization of conductive polymer layers under controlled conditions.
- ✓ To perform and precisely control the doping processes occurring in the investigated polymers in situ during electron paramagnetic resonance (EPR) measurements,

enabling real-time correlation between the polymer's electronic structure and its electrochemical state.

- ✓ To regulate and monitor the applied potential during spectroelectrochemical experiments, facilitating the real-time correlation between redox processes and spectral changes.

Cyclic voltammetry (CV) measurements were performed using 1.0 mM solutions of the target compounds unless specified otherwise. Electrochemical studies employed 0.1 M tetrabutylammonium hexafluoroborate (Bu_4NPF_6) as the supporting electrolyte in dichloromethane (DCM). The electrochemical cell consisted of a composite electrode comprising 0.1 cm^2 platinum disk clad in PEEK (polyether ether ketone) sleeve (EDAQ, cat. no. ET075-1) as the working electrode, a silver wire as the pseudo-reference electrode, and a platinum coil as the auxiliary electrode and handled as follows:

Working electrode preparation:

Initial polishing

- ✓ Place a small amount of coarse diamond paste onto a tissue paper, used as a polishing pad.
- ✓ Gently polish the electrode surface in a figure-eight motion.
- ✓ Repeat the polishing step using fine-grade diamond paste to achieve a smooth and active surface.

Cleaning

- ✓ Rinse and clean the electrode thoroughly with dichloromethane to remove any residual paste or contaminants.
- ✓ Immediately transfer the electrode into the electrochemical cell for measurements.

During experiments

- ✓ Periodically repolish the electrode between successive measurements, following the same coarse-to-fine polishing procedure, to remove adsorbed analytes and maintain reproducibility

Reference Electrode: This electrode was cleaned using dichloromethane prior to use to remove any surface contaminants.

Counter Electrode: This electrode required no preparation apart from flame cleaning, which was performed to eliminate residual impurities and ensure a clean surface.

CV measurements were calibrated against ferrocene/ferrocenium redox couple at room temperature at a scan rate of 0.05 $V \cdot s^{-1}$ (50 $mV \cdot s^{-1}$). Typically, the electrochemical background of the electrolyte was recorded using 1 mL of a 0.1 M NBu_4PF_6 solution in dichloromethane (DCM), at a scan rate of 100 mV/s, within the potential window of dichloromethane. The electrolyte solution was deaerated by purging it with argon before starting the measurements. Subsequently, the relative potential of the quasi-reference electrode was determined by adding a pinch of ferrocene to the electrolyte and measuring its oxidation and reduction potentials, typically within the range of 0 V to 0.55 V. This measured value was then used to define the relative potential of the quasi-reference electrode for the experiment. In all measurements, freshly prepared monomer solutions were initially used to determine the oxidation potential, followed by their use in the electropolymerization processes. After identifying the oxidation potential, polymerization was conducted within the corresponding potential range.

Electropolymerization of compounds **1** to **7** was carried out using cyclic voltammetry from 1 mM monomer solutions in dichloromethane containing 0.1 M Bu_4NPF_6 as the supporting electrolyte, at a scan rate of 100 $mV \cdot s^{-1}$. Prior to the experiments, the solutions were deaerated by purging with argon to remove any oxygen which might interfere with the polymerization process as well as to thoroughly mix the solution of the monomer, and an inert atmosphere was maintained throughout the measurements. Following polymer deposition, the resulting polymer films on the electrodes were rinsed with pure solvent to remove residual monomer and then transferred to a monomer-free electrolyte solution for further investigation. The platinum coil counter electrode was flame-cleaned before being introduced into the electrochemical cells. Additionally, the silver wire quasi-reference electrode was cleaned with pure dichloromethane to ensure cleanliness. Redox cycling was performed in the same electrolyte medium as that used for electropolymerization. After redox cycling, the working and counter electrodes were again cleaned according to the procedure used prior to electropolymerization.

4.2.2. UV-Vis-NIR Spectroelectrochemistry

UV-Vis-NIR spectroelectrochemistry is among the most widely utilized forms of spectroelectrochemical analysis, primarily due to its ease of use, cost-effectiveness, and its capacity to provide both quantitative and qualitative information about electrochemical processes. This technique focuses on monitoring the behaviour of valence electrons in species undergoing oxidation or reduction, with changes in their electronic states detected via electronic spectroscopy. It is particularly effective in elucidating the electronic transitions associated with redox processes.

UV-Vis-NIR spectroelectrochemical measurements were carried out using paired Ocean Optics QE65000 and NIRQuest512 spectrometers combined with Autolab PGSTAT 302N potentiostat. For UV-Vis spectroelectrochemistry, the cell comprised a quartz 10 mm cuvette fitted with an ITO coated glass slide as a working electrode pressed against the inner side of the cuvette window using a Teflon wedge sunk at the bottom of the cuvette in the working solution pool where the counter and reference electrodes were immersed. In order to secure a reproducibly thin (100 μm) layer of the solution studied, a Teflon gasket was placed between the ITO electrode and the wall of the quartz cuvette used. Platinum coil was used as an auxiliary (counter) electrode, and a silver wire electrode as a quasi-reference electrode. For these experiments, the concentration of a given compound and measurement conditions were identical to those used in the electrochemical studies.

Polymer films were deposited onto indium tin oxide (ITO)-coated glass electrodes under the same conditions employed during the electropolymerization experiments. Spectroelectrochemical measurements were conducted using a 10 mm quartz cuvette configured as the electrochemical cell. The polymer-coated ITO electrode served as the working electrode, a platinum mesh was used as the counter electrode, and a thin silver wire, clad in Teflon, functioned as the reference electrode. A tuning fork-shaped Teflon gasket was used to maintain separation between the working and counter electrodes. UV-Vis-NIR spectra were recorded in potentiodynamic mode by applying a series of incrementally increasing and decreasing potentials to the polymer films, thereby enabling the collection of spectral data corresponding to various oxidation states of the polymer.

Typically, this method employs a working electrode with a relatively large surface area compared to the solution volume, thereby enhancing convective mass transfer and improving the sensitivity of the measurements. Prior to the experiment, all electrodes and electrolyte solutions were placed in the

cuvette to record a blank background spectrum. Subsequently, the ITO electrode coated with the polymeric film, along with the counter and reference electrodes, was introduced into the cuvette. In all experiments, the spectroelectrochemical cell was first subjected to a potential sweep to remove any residual charged species from the polymer surface. This was achieved by stepping the potential from the open-circuit potential to a lower potential, while monitoring the spectral changes relative to those recorded at open-circuit conditions. Spectra were acquired using both potentiostatic and potentiodynamic modes, as specified in each experimental procedure.

4.2.3. UV-Vis Spectroscopy

UV-Vis-NIR spectra of solutions selected compounds were recorded by Perkin Elmer Lambda 1050 spectrometer. 10 mm path length Helma Cuvette was used.

4.2.4. NMR

NMR spectra were recorded at 300 MHz for ^{1}H-NMR and 75 MHz for ^{13}C-NMR on a Varian Unity Inova XL-300 spectrometer. All spectra were performed in $CDCl_3$ with tetramethylsilane (TMS) as an internal reference. The chemical shifts (δ) are reported in parts per million (ppm) and the coupling constants (*J*) in Hertz.

4.2.5. EPR Spectroelectrochemistry

Electron paramagnetic resonance (EPR) spectroelectrochemistry is a significant technique for the characterization of conjugated polymers and oligomers. EPR focuses on the interaction between electrons and electromagnetic radiation in a magnetic field. In this framework, the magnetic moment of an electron causes it to orient itself with the static magnetic field. This orientation impacts the energy levels of the electron spin (Em) within the magnetic field (B).

In situ EPR spectroelectrochemical experiments were performed in a custom-made glass cylindrical cell using platinum wire as a working electrode, platinum coil as counter electrode and a thin silver wire, clad in Teflon, as reference electrode. Measurements were performed using JEOL JES-FA200 EPR spectrometer, equipped with a JEOL ES-UCX2 universal cavity.

For EPR spectroelectrochemistry, polymer films were deposited on a platinum wire electrode, again using the same conditions as used during the electropolymerisation experiments. After the film was deposited on the electrode, washed with pure dichloromethane and transferred into a custom-made glass cylindrical cell. Spectra were taken in potentiostatic mode, first during oxidative doping (incrementing potentials) and then during the subsequent de-doping (decrementing potentials) of the polymer film. Double integration of the recorded first derivative EPR spectra gave the relative number of paramagnetic centres, and the abscissa axis distance between their up and down peaks was taken as the signal linewidth (ΔB_{pp}).

4.3. Synthesis

4.3.1. Synthesis strategies toward intermediate and target compounds

This section describes the synthetic strategies employed for the preparation of the target oligothiophene systems and their corresponding intermediates. Specifically, it covers:

a. the synthesis of symmetrically conjugation-broken quaterthiophene derivatives incorporating alkyl-grafted methylene spacers.

b. the synthesis of oligothiophenes symmetrically broken with methylene conjugation-break spacers; and
c. the synthesis of quaterthiophenes symmetrically interrupted by methylene, ethylene, and propylene conjugation-break spacers.

In addition, the synthesis of selected model compounds used for comparative purposes is presented. Together, this section provides a detailed and systematic account of the synthetic routes, reaction conditions, and key intermediate products leading to the target materials.

A range of synthetic strategies was employed to obtain both intermediate and target compounds, as outlined in Schemes 4.3.1 to 4.3.20.

4.3.1.1. Synthesis strategies toward target compound 1 and intermediates.

The synthesis commenced with 2,2′-methylene-bis(5-bromothiophene) (**10**), in which the terminal thiophene rings bear bromine substituents at the alpha positions. Compound **10** was prepared via a direct condensation of 2-bromothiophene with trioxane, paraformaldehyde, or dimethoxymethane under acidic conditions in acetic acid, following reported procedures [115]. Subsequent coupling of 2,2′-methylene-bis(5-bromothiophene) (**10**) with a Grignard reagent, generated from 2-bromothiophene in dry diethyl ether, afforded the target compound **1**, as shown in Scheme 4.3.1.

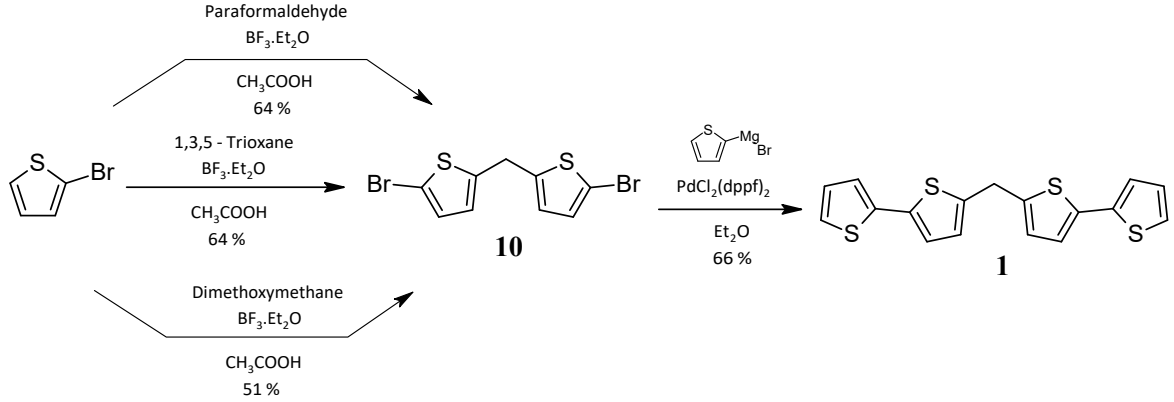

*Scheme 4.3.1 Synthesis of **1** target compound.*

In addition to this primary route, alternative synthetic approaches were also investigated. For example, the direct reaction of 5-bromo-2,2′-bithiophene with trioxane in the presence of acetic acid and $BF_3{\cdot}Et_2O$ yielded 5,5′-methylenebis(5′-bromo-2,2′-bithiophene) (**21**), as illustrated in Scheme 4.3.2.

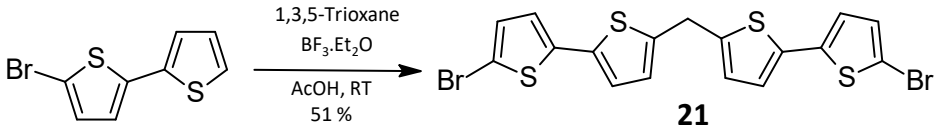

*Scheme 4.3.2 Synthesis of compound **21** intermediate product*

Subsequent debromination of compound **21** was anticipated to produce the target compound **1**, following literature procedures with minor modifications [117]. However, this approach resulted in a mixture of mono-debrominated species along with unreacted starting material, as shown in Scheme 4.3.3. The use of zinc for debromination proved ineffective, which necessitated the exploration of an alternative strategy.

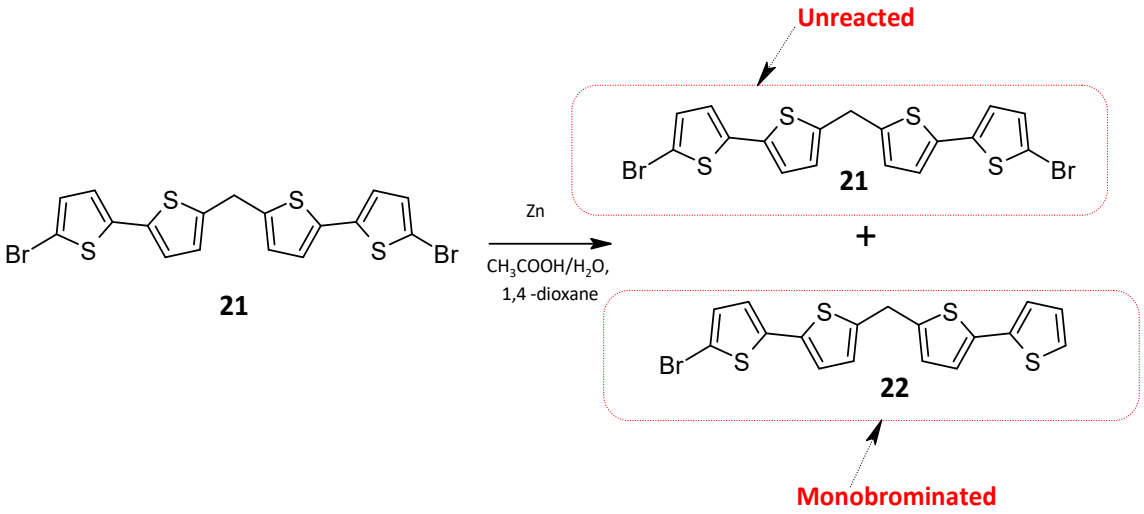

*Scheme 4.3.3 Debromination of compound **21** intermediate product*

A more controlled approach involved debromination under oxygen-free conditions, in which a mixture of compounds **21** and **22**, $NaBH_4$, and $Pd(PPh_3)_4$ in acetonitrile was stirred at 70 °C for 10 hours under an argon atmosphere [118], as depicted in Scheme 4.3.4. Purification of the resulting reaction mixture by column chromatography on silica gel afforded compound **1**, although in significantly lower yield compared to the first synthetic route.

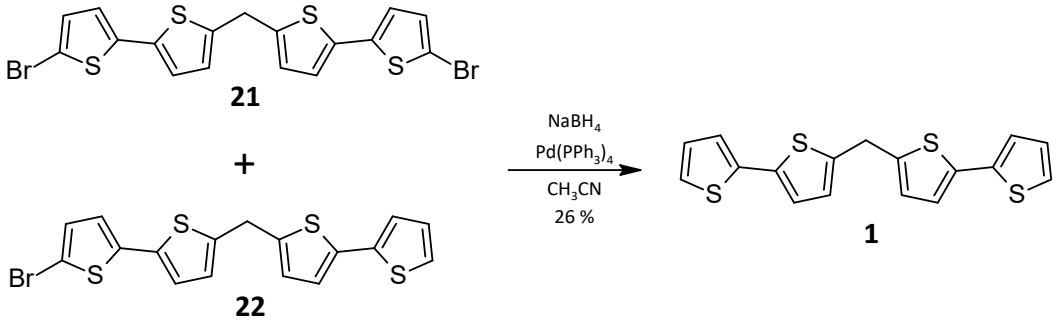

*Scheme 4.3.4 Synthesis of target compound **1** by debromination reaction*

4.3.1.2. Synthesis strategies toward target compound 2.

Target compound **2** was synthesized following a modified literature procedure, as outlined in Scheme 4.3.5. The reaction of bithiophene with paraldehyde in acetic acid, in the presence of $BF_3{\cdot}Et_2O$ at room temperature, afforded target compound **2**.

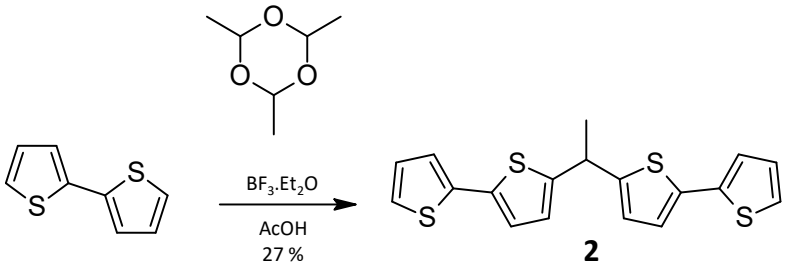

*Scheme 4.3.5 Synthesis of target compound **2**.*

4.3.1.3. Synthesis strategies toward target compound 3 and intermediate.

Target compound **3** was obtained via a two-step synthetic route adapted from reported literature procedures, with minor modifications [119], as shown in Scheme 4.3.6. In the first step, bithiophene

was lithiated in tetrahydrofuran (THF) and subsequently treated with acetone to yield the intermediate 2-([2,2'-bithiophen]-5-yl)propan-2-ol, **11**. In the second step, compound **11** was reacted with bithiophene in acetic acid with the addition of $BF_3.Et_2O$, to give the target compound **3**.

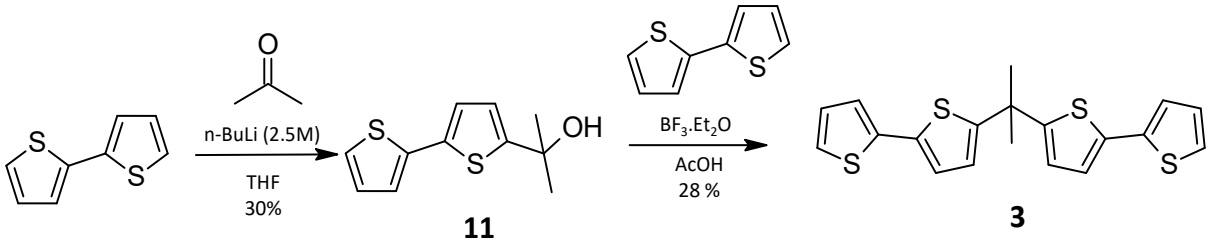

*Scheme 4.3.6 Synthesis of **3** target compound.*

4.3.1.4. Synthesis strategies toward target compound 4 and intermediates.

Different synthetic strategies were investigated for the preparation of target compound **4**. Compound **10** is obtained according to Scheme 4.3.1 described above. Debromination of compound **10** was achieved using two different methods, as shown in Scheme 4.3.7. In the first method, compound **10** was treated with sodium borohydride in the presence of a catalyst in acetonitrile. In the second method, compound **10** was lithiated in tetrahydrofuran, followed by quenching with water. Both approaches afforded compound **4** in good yields. Detailed experimental procedures for these methods are provided in the synthetic protocol section.

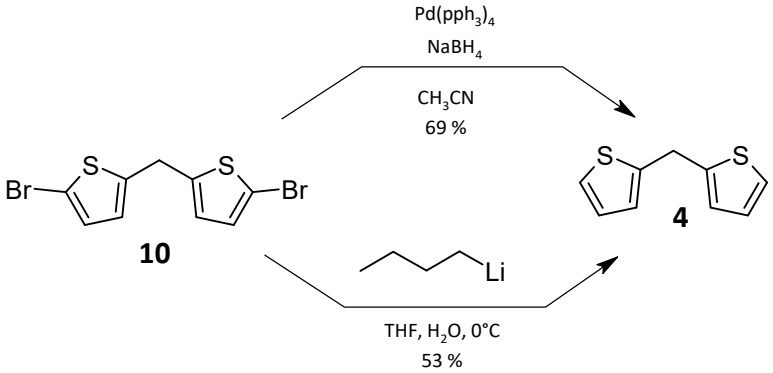

*Scheme 4.3.7 Synthesis of target compound **4**.*

An alternative synthetic route to compound **4** involved the direct reaction of thiophene with trioxane in hydrochloric acid, following established literature methods [120]. The crude product was distilled under reduced pressure; however, the resulting material consisted of a mixture of the α-α (85-90 %) and α-β (10-15 %) isomers, as shown in Scheme 4.3.8. These percentages were calculated by integrating methylene proton peaks in the ^{1}HNMR spectrum. Owing to their identical molecular weights and similar chemical affinities, the two isomers could not be separated by column chromatography. To address this limitation, compounds **4** and **23** were brominated, yielding α,α'-dibromo derivative of **4**, and α,α',α''-tribromo derivative of **23**, which enabled their separation by silica gel column chromatography using petroleum ether as the eluent. The isolated dibromo derivative of **4** was subsequently debrominated, affording the target compound **4**.

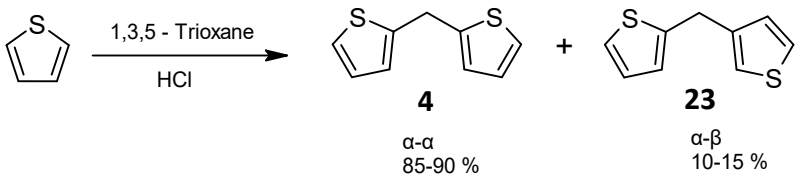

*Scheme 4.3.8 Attempted synthesis towards target compound **4**.*

4.3.1.5. Synthesis strategies toward target compound 5 and intermediates.

The synthesis of target compound **5** proved to be the most challenging among all compounds investigated in this study. Multiple synthetic strategies were explored to access compound **5** and to identify the factors limiting its formation. These approaches, along with their outcomes, are summarized in Scheme 4.3.9 to 4.3.12 and are discussed in detail below.

The first strategy involved a palladium-catalyzed cross-coupling reaction between compound **10** and 2,2′-bithiophene-5-boronic acid pinacol ester, as shown in Scheme 4.3.9. This strategy was based on Suzuki–Miyaura coupling methodologies reported for thiophene-based systems [121]. A range of catalytic systems was examined, including $Pd(OAc)_2$ with in situ generated $PtBu_3$ from the corresponding air-stable $PtBu_3{\cdot}HBF_4$ salt, as well as $Pd(PPh_3)_4$ under different solvent and base combinations. Despite extensive variation of reaction parameters, including solvent composition, base strength, and temperature, the desired target compound 5 was not obtained under any of the conditions tested.

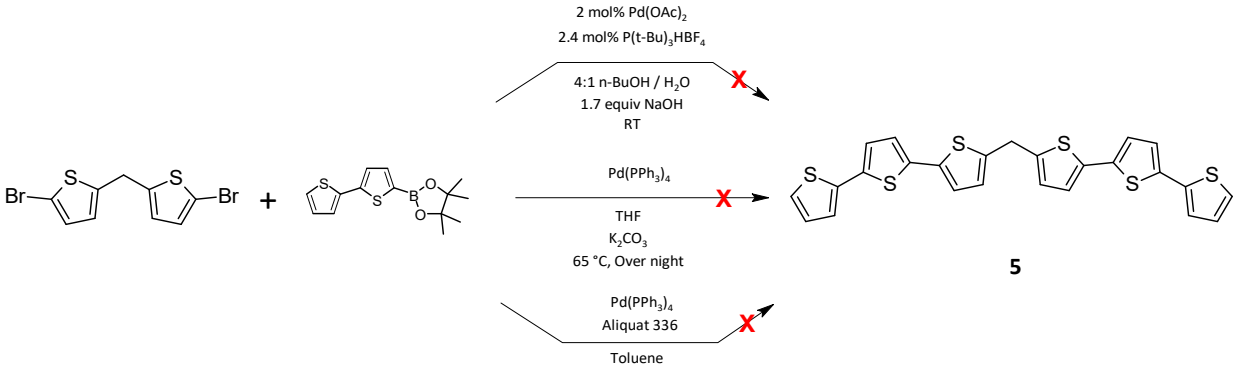

*Scheme 4.3.9 Attempted synthesis of target compound 5 via palladium-catalyzed cross-coupling of compound **10** with 2,2′-bithiophene-5-boronic acid pinacol ester under various catalytic conditions.*

As illustrated in Scheme 4.3.10, the second and third synthetic approaches were combined into a single lithiation-based strategy starting from terthiophene. Both approaches relied on treatment of terthiophene with n-butyllithium at low temperature, followed by attempted electrophilic trapping with different reagents, in accordance with literature-reported methodologies [122]. In the first pathway, the reaction mixture obtained after treatment with n-butyllithium was reacted with 5-formyl-2,2′,5′:2″-terthiophene, with the aim of forming the secondary alcohol intermediate **24** via nucleophilic addition to the aldehyde, as described in the literature [122]. However, no formation of intermediate **24** was observed under the conditions employed. In the second pathway, the reaction mixture obtained after treatment with n-butyllithium was reacted with dimethylcarbamyl chloride in an attempt to form the corresponding ketone intermediate **25**, which was intended as a precursor for Wolff–Kishner reduction to afford compound **5**, following established reduction methodologies [123]. However, this acylation step did not yield the desired ketone intermediate. The failure to obtain either intermediate **24** or **25** suggests that subsequent electrophilic trapping reactions were ineffective under the conditions employed. This outcome may be attributed to limited solubility, reduced reactivity, or

instability of the reactive species generated in situ, rendering this lithiation-based strategy unsuitable for the synthesis of compound **5**.

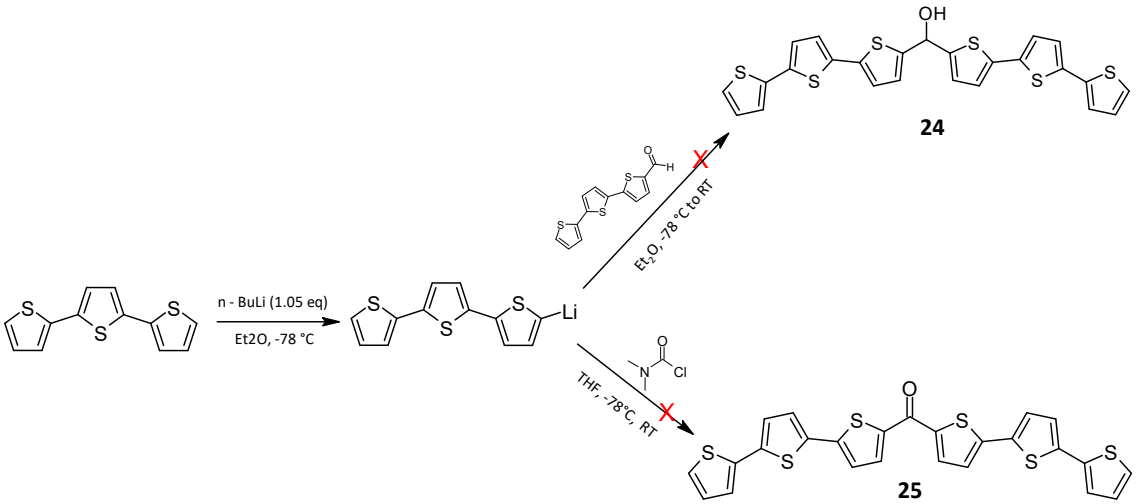

Scheme 4.3.10 Attempted synthesis of target compound 5 via lithiation of terthiophene followed by reaction with 5-formyl-2,2',5':2"-terthiophene to form intermediate 24 and dimethylcarbamyl chloride to form ketone intermediate 25.

As illustrated in Scheme 4.3.11, the fourth and fifth synthetic approaches were combined into a single acid-catalyzed methylenation strategy starting from terthiophene. Both approaches were based on literature-reported electrophilic methylenation reactions of heteroaromatic compounds using different methylene sources under acidic conditions. In the first pathway within this combined strategy, terthiophene was treated with dimethoxymethane under strongly acidic conditions in acetic acid and sulfuric acid, following reported methodologies for acid-catalyzed methylenation reactions [124]. However, this protocol also failed to yield the desired product. In the second pathway, terthiophene was reacted with trioxane as the methylene source in the presence of catalytic para-toluenesulfonic acid in dichloromethane, following previously reported procedures [115][125]. This protocol also failed to yield the desired product, and unreacted terthiophene was recovered after workup.

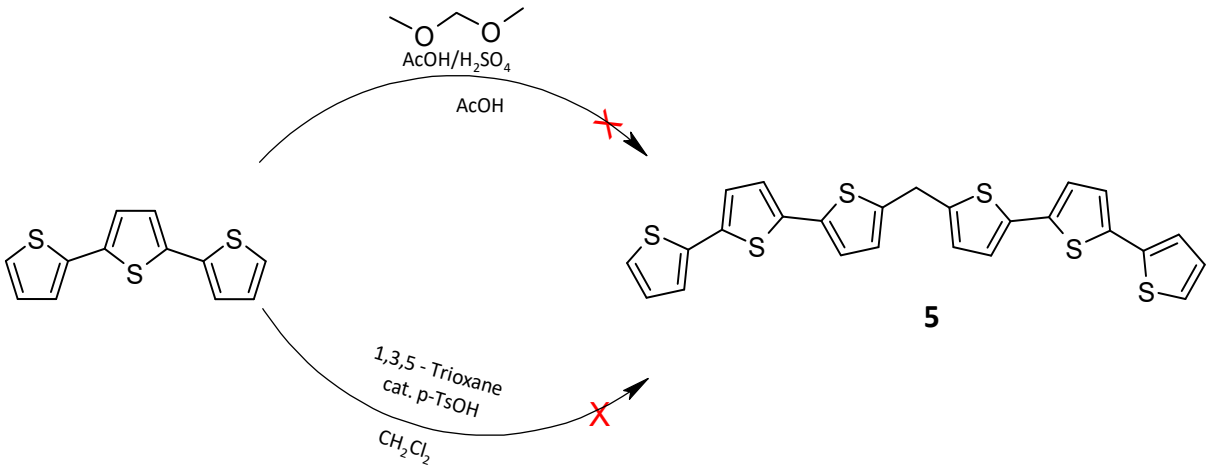

Scheme 4.3.11 Attempted synthesis of target compound 5 via acid-catalyzed reaction of terthiophene with dimethoxymethane in acetic acid and sulfuric acid, and with trioxane in dichloromethane using catalytic para-toluenesulfonic acid.

Finally, the sixth approach proved successful. As shown in Scheme 4.3.12, terthiophene was reacted with trioxane in acetic acid in the presence of $BF_3{\cdot}Et_2O$, affording the target compound **5**. Although this method successfully enabled methylene bridge formation, the isolated yield was low. Across the unsuccessful strategies, and to some extent even in the successful route, poor solubility of terthiophene-derived intermediates emerged as the primary limiting factor, significantly hindering reaction efficiency and product formation, as well as viable purification strategies.

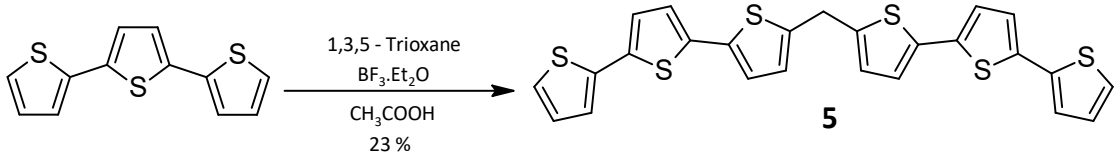

*Scheme 4.3.12 Synthesis of **5** target compound.*

4.3.1.6. Synthesis strategies toward target compound 6 and intermediates.

The target compound **6** was synthesized following a modified version of a previously reported procedure [19]. The overall synthetic route is illustrated in Scheme 4.3.13. The synthesis proceeded via a stepwise reaction. Initially, the intermediate compound **12** was synthesized, which subsequently underwent Wolff-Kishner reduction to afford intermediate product **13**. Compound **13** was then, brominated from both sides to give compound **14**, which further reacted with a Grignard reagent to yield the target compound **6**. The detailed synthetic procedures are provided in the synthetic protocol section.

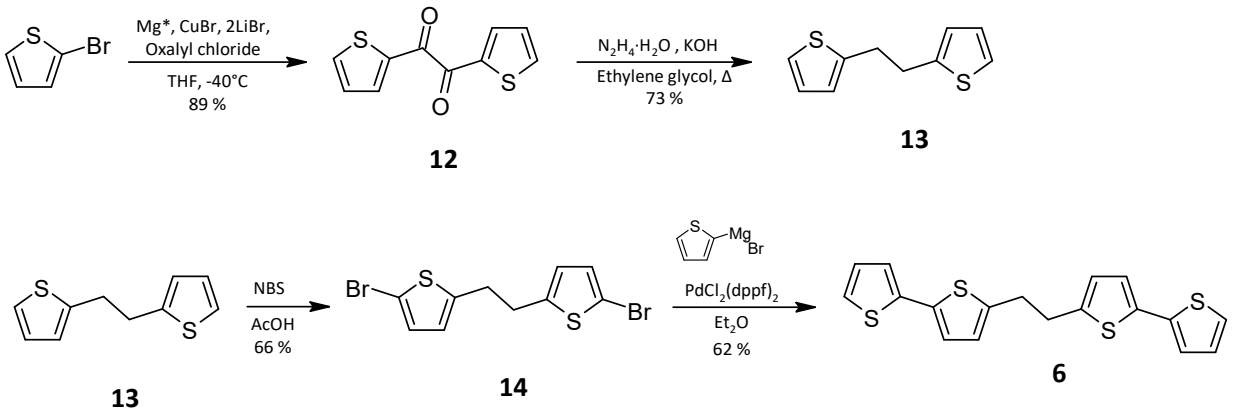

*Scheme 4.3.13 Synthesis of (**6**) target compound.*

An alternative synthetic route was also explored, as depicted in Scheme 4.3.14. The obtained intermediate compound 26, underwent Wolff-Kishner reduction [109], to afford a target compound **6**. After a purification of the crude product, a yellow stained solid product was obtained. The NMR spectra confirmed that the product corresponded to the target product **6**. However, the yellow coloration indicated contamination with quaterthiophene. This impurity likely originated during the preparation of bithiophene magnesium bromide, where a side reaction between bithiophene magnesium bromide and 5-bromo-2,2'-bithiophene produced quaterthiophene. Since quaterthiophenes are intensely yellow and tend to tail along the chromatography column, complete removal of this contamination from the target compound proved unfeasible.

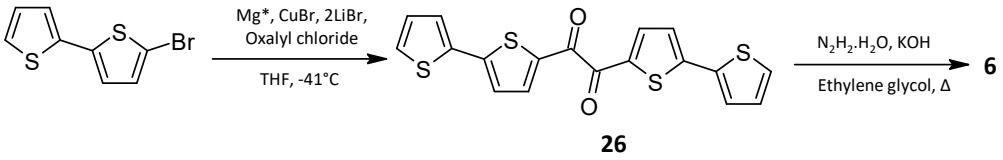

*Scheme 4.3.14 Attempted synthesis of target compound **6**.*

4.3.1.7. Synthesis strategies toward target compound 7 and intermediates.

The last target compound, **7**, was synthesized following the reported procedure in the literature, with some modifications. The overall synthetic route is illustrated in Scheme 4.3.15. The synthesis commenced with a reaction of lithiated thiophene and dibromopropane, affording the intermediate compound **15**. Subsequent bromination of compound **15** at both termini yielded the dibromo thiophene derivative **16**, which then reacted with Grignard reagent to give the target compound **7**. The detailed experimental procedure is provided in the synthesis protocol section.

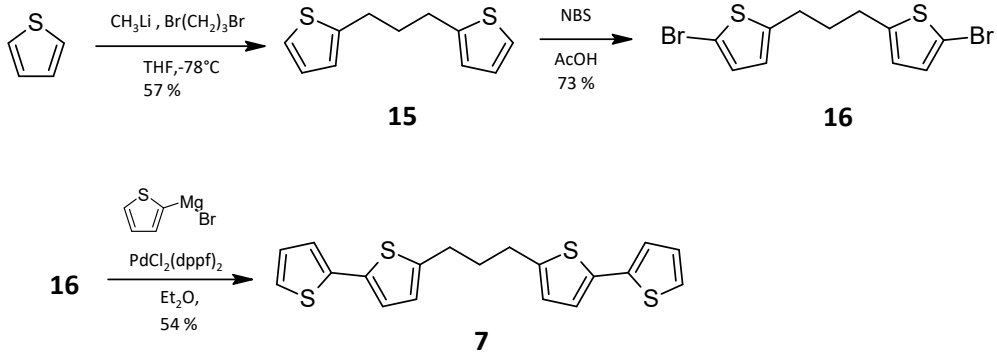

*Scheme 4.3.15 Synthesis of **7** target compound.*

4.3.1.8. Synthesis strategies toward model compound A and intermediates.

1,4-dimethylquaterthiophene (**A**) was synthesized according to the reported procedure in the literature [126]. The overall synthetic route is illustrated in Scheme 4.3.16. In this synthesis, freshly prepared Grignard solution from magnesium turnings and 2-bromo-5-methyl thiophene was treated with 5,5'-dibromo-2,2'-bithiophene in the presence of a catalyst to give a target model compound **A**.

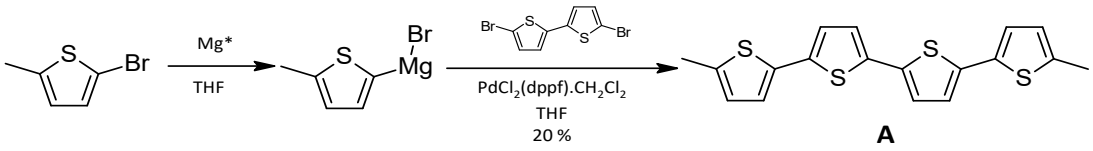

*Scheme 4.3.16 Synthesis of model compound (**A**).*

4.3.1.9. Synthesis strategies toward model compound B and intermediates.

The Synthesis of model 5-methyl-2,2'-bithiophene (**B**) was attempted via several different approaches.

The first approach is shown in Scheme 4.3.17. A Suzuki–Miyaura cross-coupling between 2-methyl-5-bromothiophene and thiophene-2-boronic acid was carried out under $Pd(PPh_3)_4$ catalysis using K_2CO_3 in THF, following a literature-reported procedure with minor modifications [127]. Although complete consumption of the starting material was observed, NMR analysis revealed a mixture of products that could not be satisfactorily separated by column chromatography. As further optimization did not improve product isolation, this route was not pursued further.

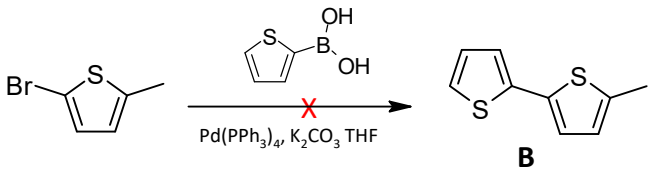

Scheme 4.3.17 Attempted Suzuki–Miyaura cross-coupling between a brominated thiophene derivative and thiophen-2-ylboronic acid for the synthesis of model compound B using $Pd(PPh_3)_4$ and K_2CO_3 in THF.

The second approach is shown in Scheme 4.3.2.18. A 5-formyl-2,2′-bithiophene (**17**) was synthesized via Vilsmeier–Haack formylation of 2,2′-bithiophene and subsequently reduced to 5-methyl-2,2′-bithiophene (B) through two Wolff–Kishner reduction routes [128]. In Procedure 2**,** Step 1, direct reduction of aldehyde **17** afforded compound B in moderate yield. In Procedure 2, Step 2, the addition of calcium oxide as a dehydrating agent significantly improved the efficiency of the Wolff–Kishner reaction, resulting in a higher isolated yield. The identity of compound B was confirmed by NMR spectroscopy and found to be consistent with literature data.

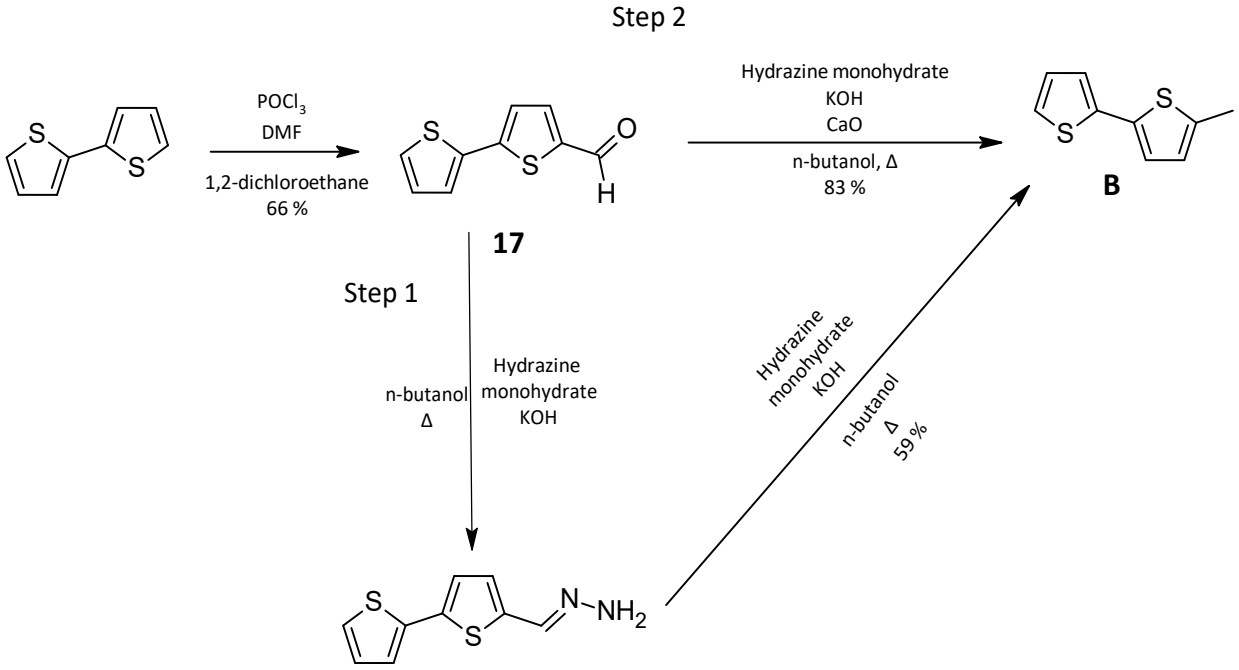

*Scheme 4.3.18 Synthesis of model compound (**B**).*

4.3.1.10. Synthesis strategies toward model compound C and intermediates.

As shown in Scheme 4.3.20, the synthetic route toward model compound **C** followed Friedel–Crafts alkylation of 2,2′-bithiophene using tert-butyl chloride in the presence of $AlCl_3$. This reaction was hoped to afford compound **C** selectively; however, under the conditions employed, a mixture of compound **C** and a doubly alkylated derivative **18** was obtained. Attempts to separate this mixture by column chromatography were unsuccessful due to similar retention factors of the two products.

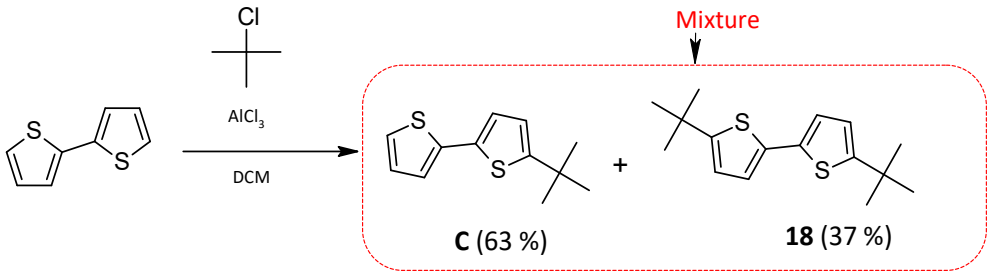

Scheme 4.3.19 Friedel–Crafts alkylation of 2,2'-bithiophene affording an inseparable mixture of model compound C and compound 18.

To resolve this issue, a selective functionalization strategy was adopted, as illustrated in Scheme 4.3.21. The crude mixture was brominated, exploiting the difference in reactivity of the α and β positions of the thiophene ring. Compound **18** did not undergo bromination due to both its α positions being blocked by the tert-butyl substituent, whereas compound C was readily brominated to afford the corresponding α-monobrominated product **19**. β-Bromination was ineffective under the reaction conditions employed. This transformation enabled effective separation of compound **19** from unreacted compound **18** by column chromatography. Subsequent lithiation of compound **19** followed by aqueous quenching regenerated compound **C**. This indirect approach thus provided an effective route to isolate model compound **C** from an otherwise inseparable mixture by leveraging selective bromination and reversible functionalization.

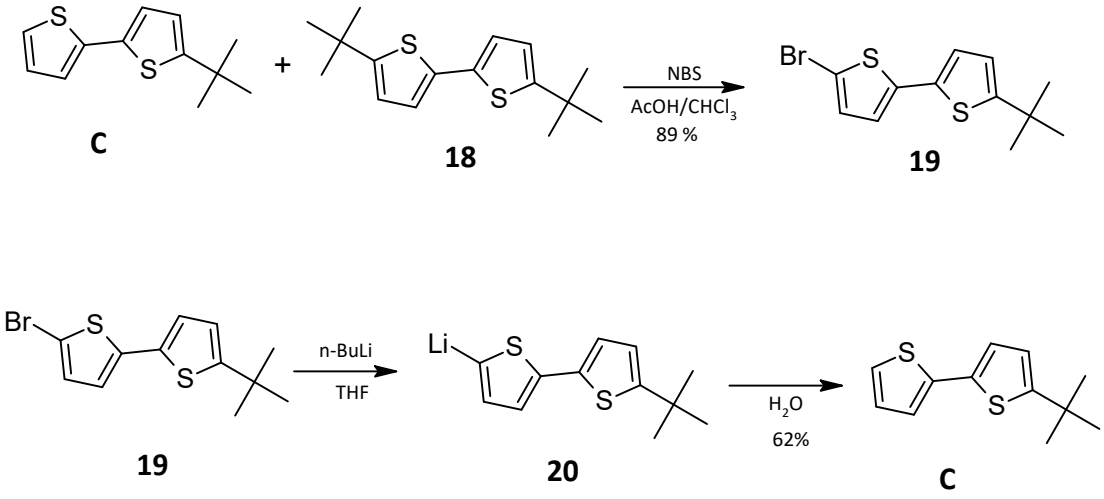

Scheme 4.3.20 Selective bromination of compound C within the mixture, followed by lithiation and hydrolysis to regenerate purified compound C.

4.3.1.11. Synthesis strategy toward model compound D.

Unlike the other model compounds, bithiophene (**D**) was not synthesized, but instead procured from a commercial supplier.

4.3.2. Synthetic protocols

This section presents detailed experimental procedures for the synthesis of all intermediate and target compounds described in this chapter.

4.3.2.1. Synthesis of 2,2'-methylenebis(5-bromothiophene) (**10**)

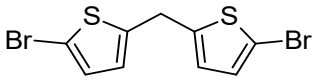

Compound **10** was prepared via the direct condensation of 2-bromothiophene with trioxane, paraformaldehyde, or dimethoxymethane under acidic conditions in acetic acid, following reported procedures [115]. The general reaction scheme is shown in Scheme 4.3.1.

Procedure 1:

To a solution of 2-bromothiophene (0.650 g, 4 mmol) and trioxane (0.030 mg, 0.33 mmol) in 10 mL of acetic acid at room temperature, 1 mL of $BF_3{\cdot}Et_2O$ was added dropwise. The colour of the solution gradually changed to dark. After stirring for 1.20 hours at room temperature, the reaction mixture was quenched with water (200 mL). The resulting mixture was washed with aqueous sodium bicarbonate (5% w/w) (100 mL) and subsequently extracted with ethyl acetate (3 × 50 mL). The combined organic layers were washed twice with water and then with saturated brine, followed by drying over anhydrous sodium sulfate overnight. The solvent was removed using a rotary evaporator, and the crude product was purified by chromatography on a silica gel column with petroleum ether as the eluent, yielding compound **10** as a colourless liquid that solidified upon standing (0.216 g, 0.639 mmol, 64%).

^{1}H-NMR (300 MHz, $CDCl_3$) δ: 6.88 (d, J = 3.6 Hz, 2H), 6.64 (dt, J = 3.6 Hz, J = 0.9 Hz, 2H), 4.18 (t, J = 0.9 Hz, 2H),

^{13}C-NMR (75 MHz, $CDCl_3$) δ: 143.96, 129.80, 125.97, 110.91, 30.99.

Procedure 2:

Same as procedure **1**, but paraformaldehyde is used instead of trioxane. The resulting yield of compound **10** is 64%.

Procedure 3:

Here, dimethoxymethane is used instead of trioxane, and the ratio of bromothiophene to dimethoxymethane is **2** molar equivalents. The procedure is adapted from Cava et.al. [124].

A mixture of acetic acid and sulfuric acid (1.2 mL, 1:1 ratio) was added dropwise to a solution of 2-bromothiophene (0.5 g, 3.12mmol) and dimethoxymethane (0.12 g, 1.53 mmol) in 3.6 mL of acetic acid. The reaction colour turned brown upon the addition of the first drops of the acid mixture and changed to a dark brown once all the acid mixture was added. Then, the reaction was stirred for 10 minutes. Afterwards, the reaction mixture was quenched with water, washed with sodium carbonate (5% w/w), and extracted with ethyl acetate. Then, the ethyl acetate extract was dried over anhydrous sodium sulphate, and the solvent was removed using a rotary evaporator to yield the crude product. The crude product was purified by chromatography on a silica gel column using petroleum ether as the eluent to obtain the target product **10** (0.264 g, 0.78 mmol, 51 %).

4.3.2.2. Synthesis of 5,5'-methylenedi(2,2'-bithiophene) (**1**)

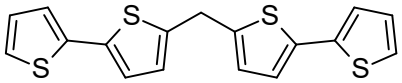

The general reaction mechanism is shown in Scheme 4.3.1. For the synthesis of compound 1, freshly prepared diethyl ether solutions of 2-thienylmagnesium bromide were used. In the initial step, a 50 mL two-neck round-bottom flask equipped with a Teflon-coated magnetic stir bar was oven-dried,

allowed to cool, and charged with activated magnesium turnings (Mg*) (0.092 g, 3.756 mmol). The flask was sealed with a septum and purged with argon. Dry diethyl ether (20 mL) was then added via syringe under an argon atmosphere, and the suspension was stirred at room temperature for 15 minutes. Subsequently, 2-bromothiophene (0.205 g, 1.252 mmol) was added dropwise by syringe, and the reaction mixture was allowed to stir for 1 hour to form the Grignard reagent. In the second step, the resulting solution was added dropwise to a precooled mixture of compound **10** (0.200 g, 0.592 mmol) and $PdCl_2$(dppf) (0.008 g) dissolved in dry diethyl ether (24 mL). This addition was carried out at 0 °C under a nitrogen atmosphere, and the reaction temperature was maintained at 0 °C throughout the addition. After completion of the addition, the reaction mixture was stirred for 1 hour at 0 °C and then allowed to warm to room temperature and stirred overnight. The reaction was quenched by the addition of aqueous ammonium chloride solution (100 mL), followed by extraction with diethyl ether (3 × 25 mL). The combined organic layers were concentrated under reduced pressure, and the resulting crude product was purified by column chromatography on silica gel using a petroleum ether to toluene mixture (4:1, v/v) as the eluent. Compound **1** was obtained as a colorless liquid that solidified upon standing (0.135 g, 0.392 mmol, 66 %).

^{1}H-NMR (300 MHz, $CDCl_3$) δ: 7.18 (dd, J = 5.1 Hz, 4J = 1.1 Hz, 2H), 7.10 (dd, J = 3.6 Hz, J = 1.1 Hz, 2H), 7.01 (d, J = 3.6 Hz, 2H), 6.98 (dd, J = 5.1 Hz, J = 3.6 Hz, 2H), 6.81 (dt, J = 3.6 Hz, J = 0.8 Hz, 2H), 4.28 (s, 2H).

^{13}C-NMR (75 MHz, $CDCl_3$) δ: 142.09, 137.66, 136.58, 127.85, 126.24, 124.27, 123.58, 30.79.

4.3.2.3. Synthesis of 5,5'-(ethane-1,1-diyl) di(2,2'-bithiophene) (**2**)

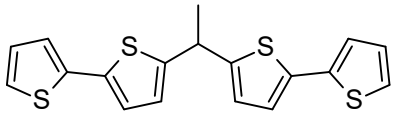

Compound **2** was synthesized following a slightly modified procedure reported by Geng et al. [119]. The general reaction mechanism is shown in Scheme 4.3.5. To a stirred solution of bithiophene (0.665 g, 4.0 mmol) and paraldehyde (0.044 g, 0.33 mmol) in acetic acid (10 mL) at room temperature, boron trifluoride diethyl etherate ($BF_3{\cdot}Et_2O$, 1.0 mL, 7.89 mmol) was added dropwise over a period of 15 minutes. During the addition, the reaction mixture became turbid and a white precipitate was observed. After completion of the addition, the reaction mixture was stirred at room temperature for an additional 6 hours. The reaction was then quenched by the addition of water (25 mL) and neutralized with aqueous sodium bicarbonate solution. The resulting mixture was extracted with ethyl acetate, and the organic layer was filtered through filter paper and dried over anhydrous magnesium sulfate. The solvent was removed under reduced pressure using a rotary evaporator, and the crude product was purified by column chromatography on silica gel using a petroleum ether to toluene mixture (4:1, v/v) as the eluent, affording compound 2 as a pure solid (0.095 g, 0.26 mmol, 27%).

^{1}H NMR (300 MHz, CDCl3) δ: 7.16 (dd, J =5.1, 1.2 Hz, 2 H,), 7.10 (dd, J=3.6, 1.2 Hz, 2 H), 7.03 – 6.94 (m, 4 H), 6.80 (dd, J= 3.6, 0.9 Hz, 2H), 4.54 (q, J= 7.2 Hz, 1H), 1.77 (d, J = 7.2 Hz , 3H).

^{13}C-NMR of compound **2** is reported elsewhere in the literature review [129].

4.3.2.4. Synthesis of 2-([2,2'-bithiophen]-5-yl) propan-2-ol (**11**)

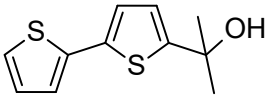

Compound **11** was synthesized following a slightly modified procedure reported by Geng *et al*.[119]. The general reaction mechanism is shown in Scheme 4.3.6. In a typical procedure, n-BuLi (2.5 M in hexane, 2.70 mL, 6.630 mmol, 1:1 equiv) was added dropwise to a stirred solution of bithiophene (1 g, 6.01 mmol, 1.0 equiv) in dry THF (15mL), at -78℃. The reaction mixture had been freeze–pump–thaw degassed four times prior to use. After the addition was complete, the mixture was gradually warmed to 0 °C and stirred for 30 minutes. Acetone (0.439 mL, 5.90 mmol) was then added dropwise at 0 °C, and the reaction mixture was stirred for an additional 60 minutes at the same temperature. The reaction was quenched by the addition of excess water, and the mixture was extracted with diethyl ether. The combined organic layers were washed with brine and dried over anhydrous magnesium sulfate. After removal of the solvent under reduced pressure using a rotary evaporator, the crude product was purified by column chromatography on silica gel using dichloromethane and ethyl acetate (19:1, v/v) as the eluent. Compound **11** was obtained as a pure product (0.782 g, 1.743 mmol, 30 %).

^{1}H NMR (300 MHz, $CDCL_3$) δ: 7.20 (dd, *J* = 5.1, 0.9 Hz,1 H), 7.13 (dd, *J* = 3.6, 0.9 Hz,1 H), 7.03 – 6.98 (m, 2 H), 6.85 (d, *J* = 3.7 Hz, 1 H), 2.05 (s,1 H), 1.68 (s, 6 H).

4.3.2.5. Synthesis of 5,5'-(propane-2,2-diyl) di(2,2'-bithiophene) (**3**)

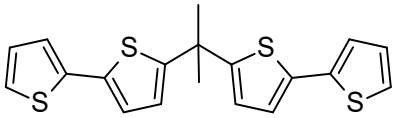

Compound **3** was synthesized following the procedure adapted from Geng et al.[119], with slight modifications. The general reaction mechanism is shown in Scheme 4.3.6. To a stirred solution of bithiophene (0.296 g, 1.783 mmol) and 2-([2,2′-bithiophen]-5-yl)propan-2-ol (**11**) (0.200 g, 0.892 mmol) in acetic acid (7 mL), boron trifluoride diethyl etherate ($BF_3{\cdot}Et_2O$), (0.12 mL, 0.892 mmol) was added in one portion via syringe at room temperature under an argon atmosphere. The reaction mixture was stirred at room temperature for 1 hour, after which it was quenched by the addition of water and neutralized with an excess of aqueous sodium carbonate solution. The resulting mixture was extracted with ethyl acetate, and the combined organic layers were dried over anhydrous sodium sulfate. The solvent was removed under reduced pressure using a rotary evaporator, and the crude product was purified by column chromatography on silica gel using a petroleum ether to toluene mixture (4:1, v/v) as the eluent. Compound **3** was obtained as a pure product (0.092 g, 0.247 mmol, 28%).

^{1}H NMR (300 MHz, $CDCL_3$) δ: 7.17 (dd, *J* = 5.0, 1.0 Hz, 2H), 7.10 (dd, *J* = 3.5, 0.8 Hz, 2H), 7.00 – 6.96 (m, *J* = 5.0, 3.6 Hz, 4H), 6.80 (d, *J* = 3.6 Hz, 2H), 1.86 (s, 6H).

^{13}C-NMR (75 MHz, CDCl3) δ 154.35, 137.82, 135.91, 127.82, 124.22, 124.01, 123.54, 123.20, 40.76, 32.87.

4.3.2.6. Synthesis of 2,2'-methylenedithiophene (**4**)

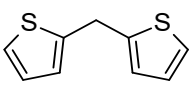

Different synthetic methods were employed for the preparation of target compound 4 via debromination of compound 10. Two distinct debromination approaches were investigated, as shown in Scheme 4.3.7.

Procedure 1. Debromination of compound **10** with sodium borohydride in the presence of a catalyst.

2,2'-Methylenedithiophene, **4**, was synthesized following the synthetic route reported by Xie *et al*.[118], with slight modifications as outlined in scheme 4.3.7. In a typical reaction, a mixture of compound **10** (0.200 g, 0.592 mmol), tetrakis(triphenylphosphine)palladium(0) (Pd (PPh_3)$_4$) (0.0684 g, 0.059 mmol), and sodium borohydride ($NaBH_4$), (0.358 g, 9.466 mmol) in dry acetonitrile (CH_3CN) (25 mL) was stirred at 70 °C under argon for 10 hours. After completion of the reaction, the mixture was extracted with diethyl ether and washed sequentially with water and brine. The organic layer was dried over anhydrous sodium sulfate, and the solvent was removed under reduced pressure using a rotary evaporator. The crude product was purified by column chromatography on silica gel using petroleum ether as the eluent, affording compound 4 as a colorless oil that solidified upon standing (0.074 g, 0.410 mmol, 69 %).

^{1}H-NMR (300 MHz, $CDCl_3$) δ: 7.16 (dd, J = 5.1, 1.3 Hz, 2H), 6.93 (dd, J = 5.1, 3.4 Hz, 2H), 6.88 (ddd, J = 3.3, 2.1, 1.0 Hz, 2H), 4.35 (t, J = 0.8 Hz, 2H).

Procedure 2: Debromination of compound **10** using lithiation.

Dry tetrahydrofuran (THF) (5 mL) was added to compound 10 (0.200 g, 0.592 mmol), and the resulting solution was purged with argon for 10 minutes. The mixture was then cooled to 0 °C and stirred for 20 minutes. Subsequently, n-butyllithium (2.5 M in hexane, 0.60 mL) was added dropwise at 0 °C. During the addition, the reaction mixture gradually turned black, indicating progression of the reaction. The mixture was stirred at 0 °C for an additional 1 hour. Deionised water (3 mL) was then added dropwise at 0 °C, and the mixture was stirred for a further 30 minutes. The reaction was quenched with water and extracted with n-hexane. The organic layer was washed successively with water and brine, then dried over anhydrous sodium sulfate. The solvent was removed under reduced pressure using a rotary evaporator to afford the crude product. Purification by column chromatography on silica gel using petroleum ether as the eluent afforded compound **4** (0.056 g, 0.311 mmol, 53 %).

4.3.2.7. Synthesis of 1^5,2^5-methylenedi(1^2,2^2:2^5,3^2-terthiophene) (**5**)

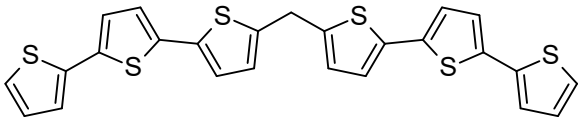

Compound **5** was synthesized following a slightly modified procedure reported by K. Peng *et al.* [115]. The general reaction scheme is shown in Scheme 4.3.12. A (0.300 g, 1.211 mmol) of terthiophene was added to 18 mL of acetic acid and sonicated for 1 hour until all terthiophene was fully dissolved. Subsequently, (0.0115 g 0.127 mmol) trioxane was added to the solution. The mixture was stirred for 1.5 hours at room temperature. Then, 0.200 mL of boron trifluoride diethyl etherate ($BF_3.Et_2O$) was added dropwise. After approximately 30 minutes of stirring, a yellowish solid began to precipitate. The reaction mixture was allowed to stir for a total of 24 hours and was then quenched by the addition of water (15 mL). The resulting solid was collected by filtration and washed three times with cold cyclohexane. To remove residual unreacted terthiophene, the solid was further washed with cyclohexane, yielding a yellowish solid. The crude product (yellowish solid) was purified by column chromatography on silica gel using a tetrahydrofuran to hexane mixture (1:4, v/v) as the eluent to remove unreacted terthiophene. The eluent was then switched to pure tetrahydrofuran to afford compound **5** as an orange solid (0.035 g, 0.069 mmol, 23%).

^{1}H NMR (300 MHz, $CDCl_3$) δ 7.21 (dd, J = 4.1, 3.0 Hz, 2H), 7.16 (dd, J = 3.6, 1.1 Hz, 2H), 7.03 (m, J = 3.7, 2.7 Hz, 8H), 6.83 (d, J = 3.7 Hz, 2H), 4.30 (s, 2H).

Due to poor solubility of compound **5**, the ^{13}C NMR spectrum could not be recorded.

4.3.2.8. Synthesis of di(thiophen-2-yl)ethane-1,2-dione (**12**)

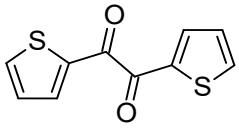

Purification of CuBr and LiBr

Prior to initiating the reaction, copper(I) bromide (CuBr, green) was purified and dried under reduced pressure. Impure CuBr was dissolved in a minimum amount of concentrated (40 wt. %) hydrobromic acid, added dropwise. A deep violet solution of CuBr complex in concentrated hydrobromic acid was then transferred to a large beaker, and distilled water, acidified with few drops of concentrated hydrobromic acid, was added until the deep violet colour disappeared and white precipitate of CuBr formed. The fine precipitate was collected by decantation and washed sequentially with water and tetrahydrofuran, with each wash performed twice, until the solid started turning orange-brown. So purified CuBr was then dried in a pistol oven under reduced pressure at 110 °C for two days. Lithium bromide (LiBr) was dried directly in a piston oven under reduced pressure at 110 °C for two days without further purification.

Activation of Magnesium

Two methods were used to activate magnesium. In the first method, magnesium was activated by treatment with hydrochloric acid. In the second method, magnesium was mechanically activated by grinding in a ceramic mortar directly prior to use.

Procedure

2-Thienylmagnesium bromide was prepared following the same procedure used for the synthesis of compound **1** and was used directly in the subsequent reaction. Compound **12** was synthesized according to previously reported methods [130][131], with some modifications. The general reaction mechanism is shown in Scheme 4.3.13. In a typical procedure, LiBr (2.084 g, 24 mmol) dissolved in 24 mL of dry THF was added to a stirred suspension of CuBr (1.721 g, 12 mmol) in 32 mL of dry THF, forming a pale green suspension. After stirring for 30 minutes, the reaction mixture was cooled to −40 °C. The freshly prepared 2-thienylmagnesium bromide solution was then added slowly to the LiBr/CuBr suspension. After an additional 30 minutes, oxalyl chloride (0.61 g, 4.8 mmol, 0.40 mL) was added dropwise via syringe while maintaining the temperature between −35 and −40 °C. The reaction mixture was stirred at −40 °C for 15 minutes and subsequently quenched by the addition of saturated aqueous ammonium chloride solution. The organic layer was separated, and the aqueous phase was extracted with ethyl acetate (3 × 50 mL). The combined organic layers were washed twice with water and once with brine, dried over anhydrous sodium sulfate, and concentrated under reduced pressure using a rotary evaporator. The crude product was purified by column chromatography on silica gel using toluene as the eluent, affording compound **12** as a yellow solid (0.744 g, 3.347 mmol, 89 %).

^{1}H-NMR (300 MHz, CDCl3) δ: 8.07 (dd, J = 3.9 Hz, J = 1.1 Hz, 2H), 7.85 (dd, J = 4.9 Hz, J = 1.1 Hz, 2H), 7.21 (dd, J = 4.9 Hz, J = 3.9 Hz, 2H).

^{13}C-NMR (75 MHz, CDCl3) δ: 182.53, 138.74, 137.58, 137.37, 128.79.

4.3.2.9. Synthesis of 2,2'-(ethane-1,2-diyl)dithiophene (**13**)

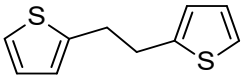

Compound **13** was synthesized according to a previously reported method [78], with some modifications. The general reaction mechanism is shown in Scheme 4.3.13. In a typical procedure, di(thiophen-2-yl) ethane-1,2-dione, **12**, (0.200 g, 0.90 mmol) and 65 % hydrazine hydrate (0.336 mL, 6.92 mmol) were dissolved in 2 mL of ethylene glycol. The reaction mixture was refluxed at 110 °C for 45 minutes and then allowed to cool to room temperature. Potassium hydroxide (0.340 g, 6.06 mmol) was subsequently added, and the mixture was refluxed again for 1.5 hours. The hot reaction mixture was poured into ice water and neutralized with HCl. The resulting mixture was extracted with dichloromethane (3 × 25 mL). The combined organic layers were washed twice with water and once with brine, then dried over anhydrous sodium sulfate. The solvent was removed under reduced pressure using a rotary evaporator to afford a crude solid. The crude product was purified by column chromatography over silica gel using a hexane: toluene (1:1 v/v) eluent. The intermediate product **13** was obtained as a colourless crystal (0.127 g, 0.654 mmol, 73 %).

^{1}H-NMR (300 MHz, CDCl3) δ: 7.13 (dd, J = 5.1 Hz, J = 1.2 Hz, 2H), 6.92 (dd, J = 5.1 Hz, J = 3.4 Hz, 2H), 6.80 (d, J = 3.4 Hz, 2H), 3.19 (s, 4H).

^{13}C-NMR (75 MHz, CDCl3) δ: 143.81, 126.86, 124.76, 123.44, 32.28.

4.3.2.10.Synthesis of 2,2'-(ethane-1,2-diyl)bis(5-bromothiophene) (**14**)

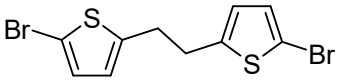

Compound **14** was synthesized according to a previously reported method[132], with modifications to the purification procedure. The general reaction mechanism is shown in Scheme 4.3.13. In a typical experiment, NBS (0.458 g, 2.572 mmol) was added to a solution of 2,2'-(ethane-1,2-diyl)dithiophene,**13**, (0.250 g, 1.286 mmol) in 5 mL of glacial acetic acid at room temperature. The addition of NBS initiated the reaction, as indicated by the consumption of NBS and the appearance of a slight orange coloration. The reaction mixture was stirred for an additional 15 minutes, then quenched with water and extracted with diethyl ether (3 x 25 mL). The combined organic layers were washed with 1 M aqueous sodium hydroxide, then with water, and finally dried over anhydrous magnesium sulphate. After filtration, the solvent was removed under reduced pressure using a rotary evaporator. The crude product was purified by column chromatography on silica gel using petroleum ether as the eluent, affording compound 14 as a colorless liquid that solidified upon standing (0.300 g, 0.852 mmol, 66%).

^{1}H-NMR (300 MHz, CDCl3) δ: 6.85 (d, J = 3.6 Hz, 2H), 6.54 (d, J = 3.6 Hz, 2H, H3,3’ Th), 3.07 (s, 4H).

The results from the ^{1}H-NMR analysis align with those previously reported in the literature. Additionally, ^{13}C-NMR findings are also documented in the literature [132].

4.3.2.11.Synthesis of 5,5'-(ethane-1,2-diyl)di(2,2'-bithiophene) (**6**)

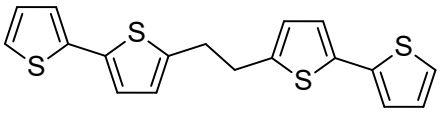

Compound **6** was synthesized following a previously reported method by Zotti et al. [19], with some modifications. The general reaction mechanism is shown in Scheme 4.3.13. In a typical experiment, a freshly prepared solution of 2-thienylmagnesium bromide (0.225 g, 1.202 mmol) in Et_2O (19.5 mL) was added dropwise to a stirred mixture of 2,2'-(ethane-1,2-diyl)bis(5-bromothiophene), **14**, (0.200 g, 0.56801 mmol) and $PdCl_2$(dppf) (0.008 g, 0.0104 mmol) in 23.5 mL of dry Et_2O. The addition was carried out under a nitrogen atmosphere while maintaining the reaction temperature at 0 °C. The reaction mixture was stirred for 1 hour at 0 °C, then warmed to room temperature and stirred overnight. After quenching with aqueous ammonium chloride solution of 100 mL, the mixture was extracted with diethyl ether (3 × 25 mL). The combined organic layers were concentrated under reduced pressure using a rotary evaporator, and the crude product was purified by column chromatography on silica gel using a petroleum ether to toluene mixture (4:1, v/v) as the eluent. Compound **6** was obtained as a white solid (0.126 g, 0.351 mmol, 62 %).

^{1}H-NMR (300 MHz, $CDCl_3$) δ: 7.17 (dd, J = 5.1 Hz, J = 1.2 Hz, 2H), 7.10 (dd, J = 3.6 Hz, J = 1.2 Hz, 2H), 6.99 (dd, J = 5.2 Hz, J = 3.6 Hz, 2H), 6.98 (d, J = 3.6 Hz, 2H), 6.70 (d, J = 3.6 Hz, 2H), 3.16 (s, 4H).

^{13}C-NMR (75 MHz, $CDCl_3$) δ: 142.90, 137.85, 135.60, 127.83, 125.68, 124.08, 123.58, 123.38, 32.30.

4.3.2.12.Synthesis of 2,2'-(propane-1,3-diyl)dithiophene (**15**)

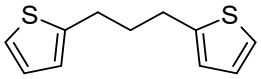

Compound **15** was synthesized following a previously reported method with some modifications [133]. The general reaction mechanism is shown in Scheme 4.3.15. In a typical experiment, thiophene (1.0 g, 11.885 mmol) was dissolved in anhydrous THF (6 mL) and cooled to −78 °C. A solution of methyl lithium (8.944 mmol, 1.6 M) in diethyl ether was added dropwise under stirring. The reaction mixture was then allowed to warm to 0 °C and stirred for 1 hour. Subsequently, 1,3-dibromopropane (0.594 g, 2.940 mmol) was added via syringe through a septum. The cooling bath was removed, and the reaction mixture was gradually warmed to room temperature and stirred for an additional 2 hours. The reaction was quenched with 200 mL of water and extracted with a hexane fraction (3 × 50 mL). The combined organic layers were dried over anhydrous $MgSO_4$, and the solvent was removed under reduced pressure using a rotary evaporator. The crude product was purified by column chromatography on silica gel, eluting with petroleum ether, yielding the desired product **15** as a white crystalline solid (1.050 g, 5.039 mmol, 57 %).

^{1}H-NMR (300 MHz, $CDCl_3$) δ: 7.12 (dd, *J* = 5.1 Hz, *J* = 1.2 Hz, 2H), 6.92 (dd, *J* = 5.1 Hz, *J* = 3.4 Hz, 2H), 6.84 – 6.76 (m, 2H), 2.98 – 2.81 (m, 4H), 2.06 (p, *J* = 7.5 Hz, 2H).

^{13}C-NMR (75 MHz, $CDCl_3$) δ: 144.81, 126.87, 124.48, 123.19, 33.66, 29.22.

4.3.2.13.Synthesis of 2,2'-(propane-1,3-diyl)bis(5 bromothiophene) (**16**)

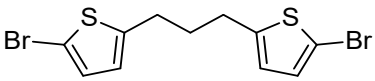

Compound **16** was synthesized following a procedure analogous to that described above for compound **14**. The general reaction mechanism is shown in Scheme 4.3.15. In a typical experiment, (0.851 g, 4.780 mmol) of NBS was added to a solution of 2,2'-(propane-1,3-diyl)dithiophene (0.500 g, 2.400 mmol) in 5 mL of glacial acetic acid at room temperature. The reaction mixture was stirred for an additional 15 minutes. The reaction was then quenched with water and extracted with diethyl ether

(3 x 25). The combined organic layers were washed with 1 M aqueous sodium hydroxide followed by water, dried over anhydrous magnesium sulphate, filtered, and concentrated under reduced pressure using a rotary evaporator. The crude product was purified by column chromatography on silica gel using petroleum ether as the eluent, affording compound **16** as a colourless liquid (0.639 g, 1.745 mmol, 73 %).

^{1}H-NMR (300 MHz, $CDCl_3$) δ: 6.86 (d, *J* = 3.6 Hz, 2H), 6.55 (dt, *J* = 3.6, J= 0.8 Hz, 2H), 2.79 (td, *J* = 7.5 Hz, *J* = 0.8 Hz, 4H), 1.96 (p, *J* = 7.5 Hz, 2H).

^{13}C-NMR (75 MHz, $CDCl_3$) δ: 146.21, 129.68, 125.06, 109.24, 32.92, 29.38.

4.3.2.14.Synthesis of 5,5'-(propane-1,3-diyl)di(2,2'-bithiophene) (**7**)

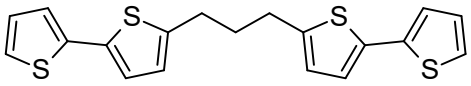

Compound **7** was synthesized following a procedure analogous to those described above for compounds **1** and **6**. The general reaction mechanism is shown in Scheme 4.3.15. In a typical experiment, a freshly prepared solution of 2-thienylmagnesium bromide (0.225 g, 1.202 mmol) in Et_2O (19.5 mL) was added dropwise to a stirred mixture of 2,2'-(propane-1,3-diyl)bis(5 bromothiophene) (0.200g, 0.546 mmol) and $PdCl_2$(dppf) (0.007 g, 0.0100 mmol) in 23.5 mL of dried Et_2O, under a nitrogen atmosphere, while maintaining the temperature at 0°C. The reaction mixture was stirred for 1 hour at 0 °C and then allowed to warm to room temperature and stirred overnight. After quenching with 100 mL of aqueous NH_4Cl solution, the mixture was extracted with Et_2O. The organic layer was dried over anhydrous magnesium sulphate, filtered and concentrated under reduced pressure using a rotary evaporator. The crude product was purified by column chromatography on silica gel using a petroleum ether to toluene mixture (4:1, v/v) as the eluent, affording compound **7** as a white crystalline solid (0.110 g, 0.295 mmol, 54 %).

^{1}H-NMR (300 MHz, $CDCl_3$) δ: 7.17 (dd, *J* = 5.1 Hz, *J* = 1.2 Hz, 2H), 7.11 (dd, *J* = 3.6 Hz, *J* = 1.1 Hz, 2H), 7.05 – 6.95 (m, 2H), 6.71 (d, *J* = 3.6 Hz, 2H), 2.88 (t, *J* = 7.5 Hz, 4H), 2.07 (p, *J* = 7.5 Hz, 2H).

^{13}C-NMR (75 MHz, $CDCl_3$) δ: 144.08, 137.93, 135.34, 127.83, 125.37, 124.00, 123.61, 123.29, 33.26, 29.36.

4.3.2.15.Synthesis of 1,4-dimethyl-quaterthiophene (model A)

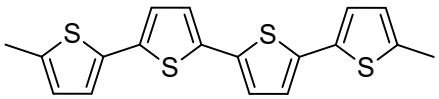

1,4-dimethylquaterthiophene (model **A**) was synthesized according to the reported procedure [126]. The general reaction mechanism is shown in Scheme 4.3.16. In a typical experiment, a Grignard reagent is prepared from magnesium turnings (0.055 g, 2.26 mmol) in dry THF (2.5 mL) by the dropwise addition of 2-bromo-5-methyl thiophene (0.300 g, 1.69 mmol) at room temperature. A freshly prepared Grignard solution (0.217 g, 1.156 mmol) was then added dropwise to a stirred mixture of 5,5'-dibromo-2,2'-bithiophene (0.229 g, 0.70 mmol), [Pd(dppf)Cl_2] ·CH_2Cl_2 (0.017 g, 0.021 mmol) in dry THF (2 mL) at 0 °C. The reaction mixture was stirred for 2.5 hours at 0°C. Then, 0.2 mL of MeOH is added to quench the reaction, resulting in precipitation of a yellow solid. The solid was collected by filtration and washed with ice-cold THF. It was then dissolved in hot toluene and recrystallized from the same solvent to afford model compound A as a golden-yellow solid (0.059 g, 0.164 mmol, 24%). The ^{1}H and ^{13}C NMR spectrum is consistent with reported literature values [126].

^{1}H -NMR (300 MHz, $CDCL_3$) δ: 7.03 (d, *J* = 3.8 Hz, 2H), 6.97 (d, *J* = 3.6 Hz, 4H), 6.67 (dq, *J* = 3.6, 1.2 Hz, 2H), 2.49 (d, *J* = 1.2 Hz, 6H).

4.3.2.16.Synthesis of [2,2'-bithiophene]-5-carbaldehyde (**17**)

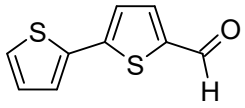

Compound **17** was synthesized following the general reaction mechanism illustrated in Scheme 4.3.18. in a typical experiment, phosphorus oxychloride ($POCl_3$), (0.18 mL, 1.9 mmol) was added dropwise to a stirred solution of 2,2'-bithiophene (0.300 g, 1.8 mmol) and anhydrous N,N-dimethylformamide (DMF), (0.15 mL, 1.9 mmol) in anhydrous 1,2-dichloroethane (4.5 mL) at 0 °C under an argon atmosphere. The reaction mixture was then allowed to warm to room temperature and subsequently refluxed at 85 °C for 2 hours. After cooling to room temperature, the reaction mixture was poured into an aqueous sodium acetate solution (1 M, 30 mL) and stirred vigorously for 2 hours to complete hydrolysis. The organic phase was separated by decantation, and the aqueous phase was extracted with dichloromethane (2 × 11.25 mL). The combined organic layers were dried over anhydrous magnesium sulfate and concentrated under reduced pressure using a rotary evaporator. The crude product was purified by column chromatography on silica gel using dichloromethane as the eluent, affording compound **17** as a yellow solid (0.232 g, 1.2 mmol, 66% yield). The purified product was subsequently used in the Wolff–Kishner reduction without further modification.

^{1}H -NMR (300 MHz, $CDCL_3$) δ: 9.86 (s, 1H), 7.67 (d, *J* = 3.9 Hz, 1H), 7.37 (dd, *J* = 3.0, 1.8 Hz, 2H), 7.26 (d, *J* = 3.9 Hz, 1H), 7.08 (dd, *J* = 5.4, 3.4 Hz, 1H).

4.3.2.17.Synthesis of 5-methyl-2,2'-bithiophene (**B**)

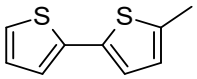

Compound model **B** was synthesized from Compound 17, via a Wolff–Kishner reaction, following the procedure reported by Roncali et al.[128]. As illustrated in Scheme 4.3.18, two Wolff–Kishner reduction routes were investigated: Step 1, which proceeds through hydrazone formation followed by reduction, and Step 2, in which the use of calcium oxide as a drying agent significantly enhanced the reaction efficiency and afforded higher isolated yields.

Reduction of Formyl-2,2'-bithiophene (17) to 5-methyl-2,2'-bithiophene (B). Step 1: The reaction was carried out following a published Wolff–Kishner procedure [128]. In a typical experiment, a mixture of (0.03 g, 0.55 mmol) of 100% hydrazine monohydrate (containing 63% hydrazine), (0.1 g, 0.51 mmol) of 5-formyl-2,2'-bithiophene, 28.3 mL of n-butanol, and (0.014 g, 0.255 mmol) of pulverized KOH was placed in a 100 mL round-bottom flask. The flask was fitted with a drying tube containing freshly dried calcium chloride and capped with an argon balloon. The reaction mixture was stirred at room temperature under argon for 5 minutes and then refluxed at 110 °C for 3 hours, during which the solution turned deep yellow. After reflux, the reaction mixture was allowed to cool to room temperature and stirred for an additional 15 hours, maintaining the yellow coloration. Saturated aqueous ammonium chloride solution (3 mL) was then added, and the mixture was extracted with

chloroform. The organic layer was dried over anhydrous magnesium sulfate, filtered, and concentrated under reduced pressure using a rotary evaporator. ^{1}H NMR analysis of the crude product indicated a mixture of intermediates (crude hydrazone) rather than the desired compound. Therefore, the crude product was used directly in the subsequent reduction step to convert the hydrazone into the target compound (**B**).

Reduction of crude Hydrazone: The overall synthesis procedure is shown in Scheme 4.3.18. Specifically, (0.10 g, 0.48 mmol) of crude hydrazone of 5-formyl-2,2'-bithiophene (orange/red), 10 mL of n-butanol, and 0.337 g (6.0 mmol) of pulverized KOH were combined in a 25 mL round-bottom flask equipped with a water condenser. The apparatus was stoppered and purged with argon gas. The n-butanol suspension was sparged with argon for 15 minutes. Subsequently, 0.036 g (0.72 mmol) of hydrazine monohydrate (containing 63% hydrazine) was added to the mixture. A sample was withdrawn for TLC analysis as a reference. The mixture was refluxed at 90°C with stirring for 3 hours. After this period, another sample was taken and analyzed by TLC, which indicated incomplete hydrazone conversion. Therefore, stirring was extended for an additional 3 hours. A final sample was collected after 6 hours, and TLC showed no hydrazone. The reaction mixture was then cooled, water was added, and the product was extracted with chloroform ($CHCl_3$). The organic layer was dried over magnesium sulphate ($MgSO_4$), filtered, and the solvent was evaporated under reduced pressure. The crude product was purified by column chromatography on dehydrated silica gel (preheated at 150°C under 1 mbar). The purified, colorless liquid target compound was obtained using petroleum ether as the eluent. (**B**) (0.055 g, 0.3 mmol, 59%).

In accordance with Scheme 4.3.2.19, step 2, calcium oxide (CaO) is employed as a drying agent during the Wolff-Kishner reaction to absorb the generated moisture. All steps are like those in procedure 1, except for the addition of CaO and some parameter adjustments. Specifically, (0.11 g, 0.57 mmol) of 5-formyl-2,2'-bithiophene (**17**), 35 mL of n-butanol, and (0.57 g, 10.2 mmol) of pulverized potassium hydroxide (KOH) were placed in a 25 mL round-bottom flask fitted with a water condenser. The apparatus was then flushed with argon gas, and the n-butanol suspension was bubbled with argon for 15 minutes. Subsequently, (0.072 g, 1.44 mmol) of 100% hydrazine monohydrate (containing 63% hydrazine) was added to the mixture. A small sample was taken for thin-layer chromatography (TLC) analysis. The mixture was refluxed at 90°C for 18 hours with stirring. After refluxing, another TLC sample was taken to confirm the complete reaction of the hydrazone. The reaction mixture was cooled, water was added, and the mixture was neutralized with 1 M hydrochloric acid (HCl). The resulting pale-yellow crude product was extracted with dichloromethane (DCM), dried over magnesium sulphate ($MgSO_4$), filtered, and the solvent was removed under reduced pressure. The crude product was purified by column chromatography on dehydrated silica gel (heated at 150°C under 1 mbar) using petroleum ether as the eluent, yielding a colorless liquid target product. (**B**) (0.075 g, 0.4 mmol, 84%). The NMR spectra agree with those reported in the literature [134].

^{1}H -NMR (300 MHz, $CDCL_3$) δ: 7.15 (dd, J = 5.1, 1.1 Hz, 1H), 7.08 (dd, *J* = 3.6, 1.1 Hz, 1H), 7.00-6.94 (m, 2H), 6.65 (dd, 1H), 2.47 (s, 3H).

The addition of CaO to the Wolff-Kishner reaction enhances product yield through several mechanisms: (i) Moisture Removal: CaO helps maintain a dry environment, preventing water-induced side reactions and increasing overall efficiency. (ii) Improved Reaction Conditions: By keeping the system moisture-free, CaO supports the high temperatures necessary for the reaction to proceed

effectively. (iii) Stabilization of the Base: CaO also boosts the performance of the strong base (KOH), contributing to a more robust reaction environment. These factors collectively lead to more efficient and successful Wolff-Kishner reaction, resulting in higher yields.

4.3.2.18.Synthesis of 5-*tert*-butyl-2,2'-bithiophene (**C**)

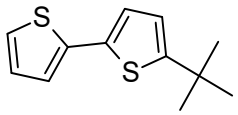

The synthesis of 5-tert-butyl-2,2′-bithiophene (model compound C) was carried out following the general reaction mechanism illustrated in Scheme 4.3.20. In a typical experiment, 2,2′-Bithiophene (0.510 g, 3.07 mmol) was completely dissolved in dichloromethane (DCM), 15 mL), after which tert-butyl chloride (0.340 g, 3.680 mmol, 0.40 mL) was added, followed by the rapid addition of anhydrous aluminum chloride ($AlCl_3$) (0.45 g, 3.375 mmol). The reaction mixture immediately turned dark brown to green and was stirred at room temperature for 30 minutes. Water (25 mL) was then added to quench the reaction, and stirring was continued for an additional 10 minutes. The organic phase was separated, extracted with DCM, and dried over anhydrous magnesium sulfate. Removal of the solvent under reduced pressure afforded a green oily crude product (0.685 g). Purification was attempted by column chromatography on dehydrated silica gel (180 °C, 2 mbar) using petroleum ether as the eluent. However, ^{1}H NMR analysis revealed that the isolated material consisted of an inseparable mixture of mono-tert-butyl-2,2′-bithiophene (model compound **C**) and di-tert-butyl-2,2′-bithiophene (**18**), present in approximate proportions of 37% and 63%, respectively (Scheme 4.3.20).

To resolve this issue, a selective bromination strategy was adopted, as illustrated in Scheme 4.3.21. Specifically, *N*-bromosuccinimide (NBS),(0.331 g, 1.86 mmol) was added to a solution containing the inseparable mixture of compound **C** and compound 18 (0.570 g) in a 1:1 (v/v) mixture of glacial acetic acid and chloroform (14 mL) at room temperature. The addition of NBS initiated a spontaneous reaction, as evidenced by the rapid disappearance of NBS and the development of a faint orange coloration. The reaction mixture was stirred for an additional 15 minutes, then quenched with water and extracted with diethyl ether. The organic layer was washed sequentially with 1 M aqueous sodium hydroxide solution and water, then dried over anhydrous magnesium sulfate. After removal of the solvent under reduced pressure, the crude product was purified by column chromatography on silica gel using petroleum ether as the eluent, affording compound 19 as a pure product (0.320 g, 1.40 mmol, 89%).

Following the selective bromination strategy, the target model compound **C** was synthesized as described in Scheme 4.3.21. In a typical procedure, a solution of *n*-butyllithium (2.5 M in hexane, 0.10 mL, 0.249 mmol) was added dropwise to a stirred solution of 2-bromo-5-tert-butylthiophene (**19**) (0.050 g, 0.166 mmol) in dry tetrahydrofuran (THF) (1.5 mL) at 0 °C. After complete addition, the reaction mixture was stirred at 0 °C for 2 hours. Water (2 mL) was then added, and the mixture was stirred for an additional 30 minutes. The reaction mixture was extracted with dichloromethane. The organic layer was washed with water, dried over anhydrous magnesium sulfate, and concentrated under reduced pressure using a rotary evaporator to afford a blue oily crude product. Purification by column chromatography on dehydrated silica gel using petroleum ether as the eluent yielded model compound **C** (0.032 g, 0.144 mmol, 62%).

^{1}H -NMR (300 MHz, $CDCL_3$) δ: 7.16 (dd, J = 5.1, 1.2 Hz, 1H), 7.10 (dd, *J* = 3.6, 1.2 Hz, 1H), 7.04-6.92 (m, 2H), 6.72 (d, J = 3.6 Hz, 1H), 1.39 (s, 9H).

^{13}C-NMR (75 MHz, $CDCl_3$) δ: 157.07, 138.12, 134.44, 127.79, 123.89, 123.30, 123.15, 122.10, 34.78, 32.54, 29.86.

5. Results

5.1. Introduction

This chapter presents the experimental results obtained from the spectroscopic, electrochemical, spectroelectrochemical, and EPR spectroelectrochemical investigations carried out in this work. The results are organized into three structural series of symmetrically conjugation-broken compounds.

Chapter 5.2 presents the data for **first series** of targets, comprising compounds **1**, **2**, and **3**, which differ in the number of methyl side groups at the methylene sp^3 carbon spacer: bearing no methyl groups (two hydrogen atoms - methylene), one methyl group (one hydrogen atom - ethylidene), and two methyl groups (no hydrogen atoms - isopropylidene), respectively (Figure 5.1, page 50).

Chapter 5.3 reports the results for the **second series** of targets, comprising compounds **4**, **1**, and **5**, in which the length of oligothiophene, symmetrically broken by a methylene spacer, varies: bithiophene, quaterthiophene, and sexithiophene, respectively (Figure 5.17, page 65).

Chapter 5.4 includes the results for the **third series** of targets, comprising compounds **1**, **6**, and **7**, which differ in the number of methylene units in the conjugation-breaking spacer: methylene, ethylene, and propylene, respectively (Figure 5.24, page 75).

In addition, comparative data from model compounds are presented where relevant. EPR spectroelectrochemical measurements were performed exclusively on Poly (**3**), as films derived from the other monomers did not exhibit sufficient stability under the experimental conditions required for this spectroscopic analysis.

5.2. Quaterthiophenes symmetrically broken with alkyl-grafted methylene

This section presents the results obtained for a series of quaterthiophenes, symmetrically broken with alkyl-grafted methylene spacer. The chemical structures of compounds **1**, **2**, and **3** are shown in Figure 5.1.

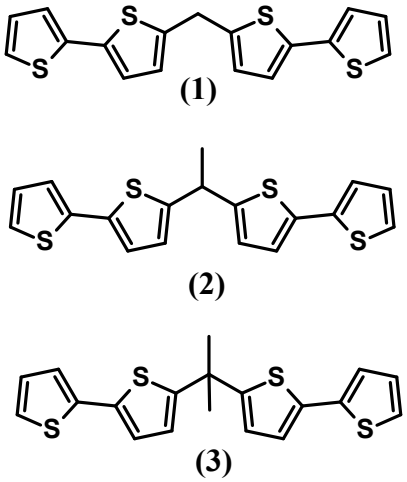

Figure 5.1 Chemical structures of compounds 1, 2, and 3.

5.2.1. UV-Visible absorption spectra

Quaterthiophene based compounds symmetrically broken with alkyl-grafted methylene unit exhibit a single dominant absorption band in their UV-Vis spectra. The absorption spectra of solutions of compounds **1**, **2**, and **3** recorded in dichloromethane are shown in Figure 5.2.

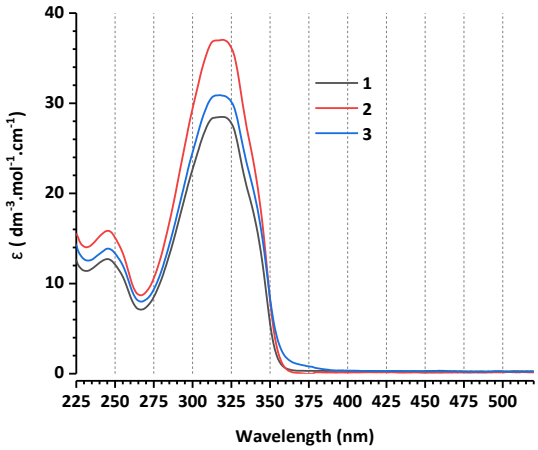

*Figure 5.2 Absorption spectra of **1, 2, and 3** registered in DCM.*

The molar absorption coefficient (ε), onset wavelength (λ_{onset}), maximum wavelength (λ_{max}), and optical band gap (E_g^{opt}) values obtained from the UV-Vis spectra are summarized in Table 5.2.1. The optical band gap energies were calculated from the absorption onset wavelength (λ_{onset}), using the relationship:

$$E_g^{opt} = 1240/\lambda_{onset}$$

where λ_{onset} is expressed in nanometers (nm), in accordance with the method reported in Ref. [135].

*Table 5.2.1 Molar absorption coefficient (ε), onset wavelength (λ_{onset}), maximum wavelength (λ_{max}),) and optical band gap (E_g^{opt}) values for compounds **1**, **2**, and **3** in dichloromethane.*

Compound	**ε** [$dm^{-3}.mol^{-1}.cm^{-1}$]	$\boldsymbol{\lambda_{onset}}$ [nm]	$\boldsymbol{\lambda_{max}}$ [nm]	$\boldsymbol{E_g^{opt}}$ [eV]
1	29	358	320	3.46
2	37	359	320	3.45
3	31	360	320	3.44

5.2.2. Electrochemistry of investigated compounds

Electrochemical characterization of targets **1**, **2**, and **3**, was carried out using cyclic voltammetry (CV). The measurements were performed on 1 mM solutions of each compound in dichloromethane containing 0.1 M Bu_4NPF_6 as the supporting electrolyte. The first cycle cyclic voltammograms recorded at a scan rate of 0.1 $V{\cdot}s^{-1}$ are shown in Figure 5.3 (a-c).

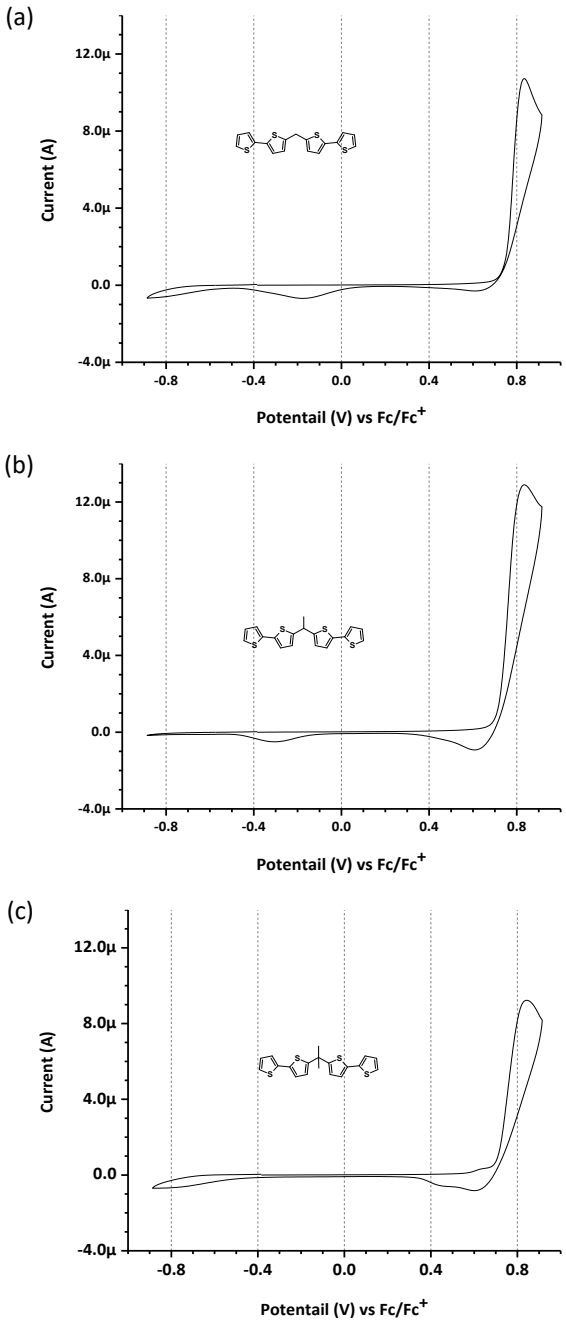

*Figure 5.3 Cyclic voltammograms of 1 mM solutions of compounds (a) **1**, (b) **2**, and (c) **3** recorded in dichloromethane containing 0.1 M Bu_4NPF_6 at a scan rate of 0.1 $V \cdot s^{-1}$.*

The cyclic voltammograms of compounds **1**, **2**, and **3** exhibit irreversible anodic oxidation processes within the investigated potential window. For compounds **1** and **2**, a cathodic current feature is observed during the reverse scan at approximately -0.2 V to -0.3 V vs Fc/Fc^+. Given the irreversible nature of the electrochemical response, this feature is not assigned to a well-defined reduction process, but it is discussed qualitatively in terms of possible chemical transformations following oxidation. In contrast, compound **3** does not display a comparable reduction feature in this potential region. In addition, during the first cyclic voltammetry scan, a cathodic peak centred at approximately −0.6 V vs Fc/Fc^+ is observed, which is more pronounced for compound **3** than for compounds **1** and **2**.

The oxidation onset potential, E_{onset}^{ox}, anodic peak potential, E_{pa}, HOMO energy levels, E_{HOMO}, and anodic peak currents, I_{pa}, derived from the cyclic voltammograms, are summarized in Table 5.2.2. The HOMO energy levels were estimated from the oxidation onset potentials using the relationship:

$$E_{HOMO} = -(4.8 + E_{onset}^{ox})$$

as described in Ref. [135].

*Table 5.2.2 The value of oxidation onset potential, E_{onset}^{ox}, anodic peak potential, E_{pa}, HOMO energy levels, E_{HOMO}, and anodic current peak, Ip, of compounds **1**, **2**, and **3** measured in dichloromethane containing 0.1 M Bu_4NPF_6 at a scan rate of 0.1V·s^{-1}*

Compounds	E_{onset}^{ox} [V] vs **Fc/Fc$^+$**	E_{pa} [V] vs **Fc/Fc$^+$**	E_{HOMO} [ev]	I_{pa} [µA]
1	0.752	0.833	-5.55	10.7
2	0.722	0.834	-5.52	12.8
3	0.709	0.843	-5.51	9.0

5.2.3. Electropolymerization

Repeated oxidative cycling of compounds **1**, **2**, and **3** leads to the formation of electroactive films on the platinum working electrode surface. Electropolymerization was carried out by cycling the applied potential between -0.9 V and 0.96 V vs Fc/Fc$^+$ for compounds **1** and **2**, and between -0.4 V and 0.96 V vs Fc/Fc$^+$ for compound **3**. The electropolymerization behaviour of compounds **1**, **2**, and **3** is illustrated in Figure 5.4. Cyclic voltammograms recorded over a wide potential window are shown in Figure 5.4(a), (c), and (e) for compounds **1**, **2**, and **3**, respectively, while Figure 5.4(b) and (d) present the corresponding voltammograms for compounds **1** and **2** recorded over a narrower potential range. For compounds **1** and **2**, electropolymerization was examined using both potential windows. In the narrow potential range, the applied potential excludes cathodic features observed at ca. -0.2 V and -0.3 V vs Fc/Fc$^+$ for compounds **1** and **2**, respectively.

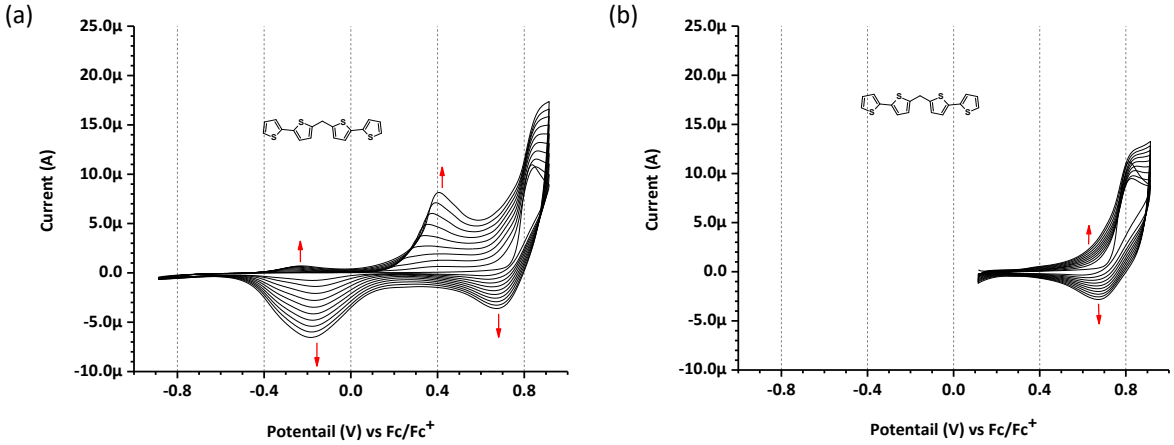

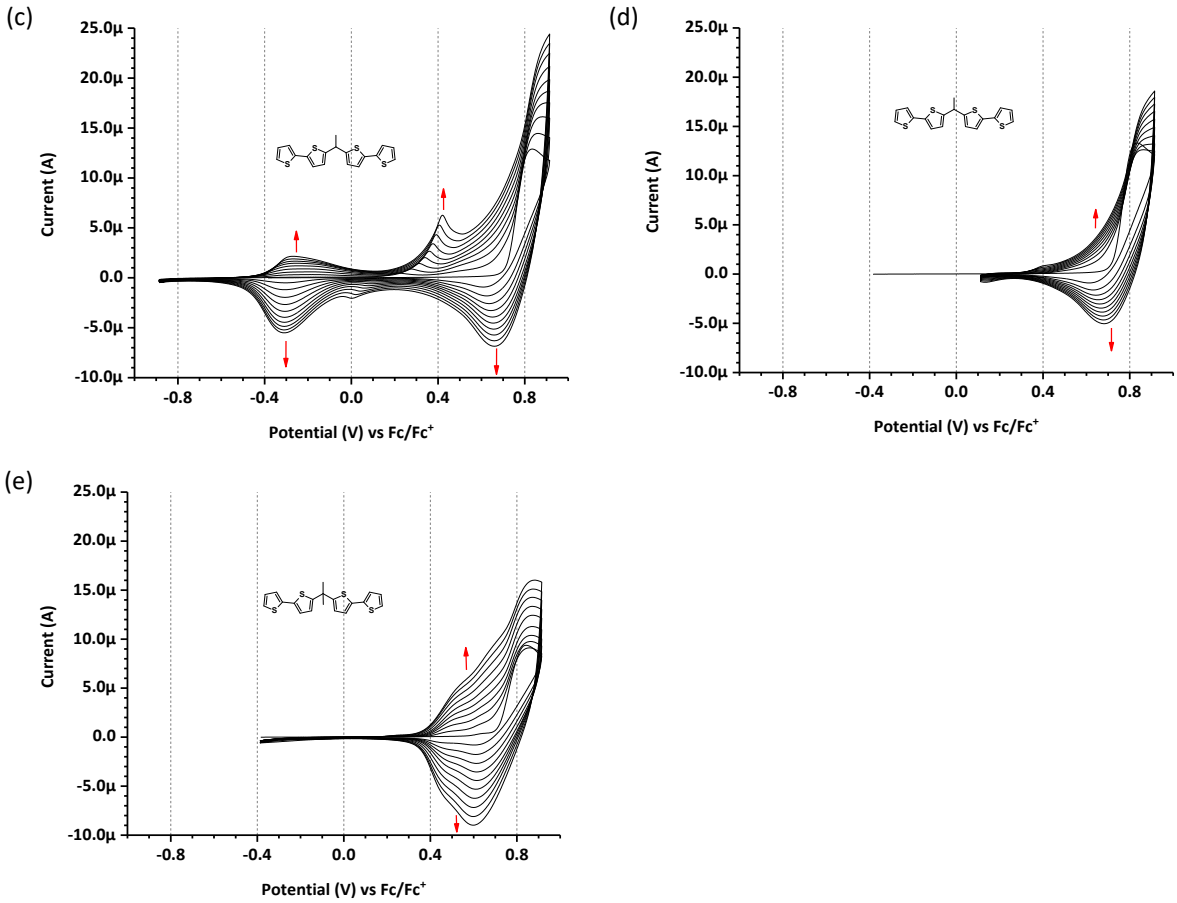

Figure 5.4 *Cyclic voltammograms recorded during the electropolymerization of quaterthiophene derivatives bearing alkyl-grafted methylene π-conjugation break spacers in dichloromethane containing 0.1 M Bu_4NPF_6 at a scan rate of 0.1 V s^{-1}. Panels (a), (c), and (e) correspond to compounds 1, 2, and 3, respectively, recorded over a wide potential window, while panels (b) and (d) show compounds 1 and 2, respectively, recorded over a narrow potential window.*

5.2.4. Electrochemistry of polymer products

Cyclic voltammograms of polymer films deposited on a platinum disc electrode are shown in Figure 5.5(a–e). Figures 5.5(a), (c), and (e) present the electrochemical responses of poly (**1**), poly (**2**), and poly(**3**), respectively, recorded over a wide potential window, while Figures. 5.5(b) and (d) show the corresponding voltammograms of poly (**1**) and poly (**2**) recorded over a narrower potential range.

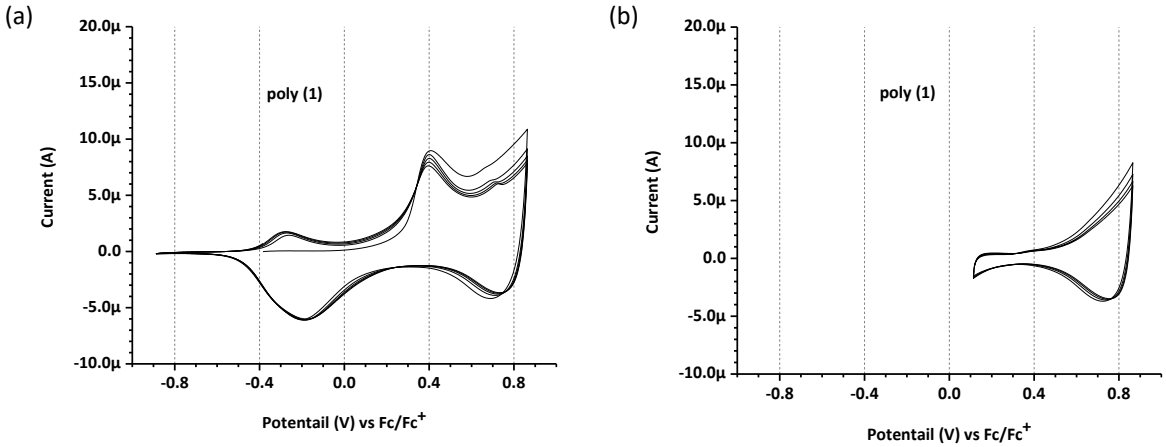

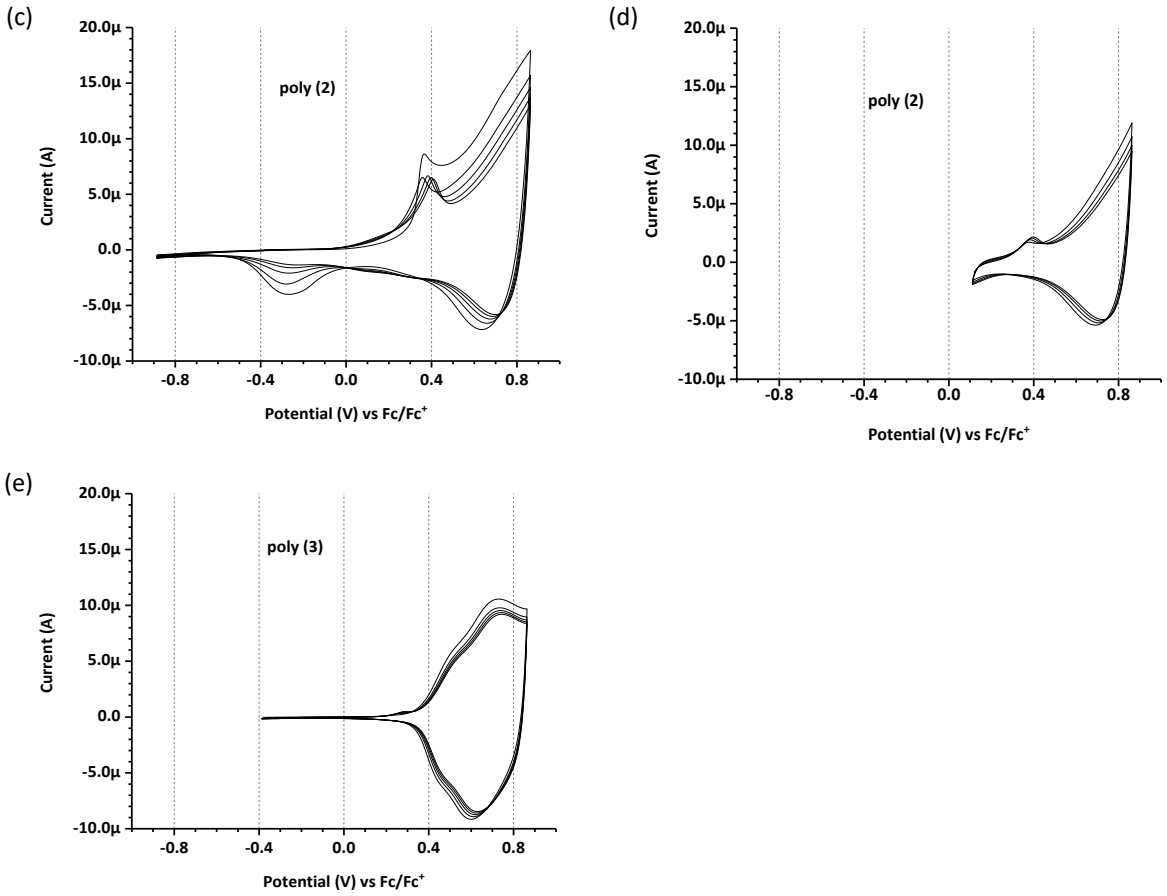

Figure 5.5 *Cyclic voltammograms of the investigated polymer films recorded in dichloromethane containing 0.1 M Bu_4NPF_6 at a scan rate of 0.1 V s^{-1}. Panels (a) and (b) show poly (1) recorded over wide and narrow potential windows, respectively; panels (c) and (d) show poly (2) under the same conditions; panel (e) shows poly (3) recorded over a wide potential window.*

For all polymer films, reversible anodic and cathodic current responses are observed within the investigated potential windows. The voltammetric profiles of poly (**3**) exhibit minimal changes in shape over successive scans, whereas more pronounced variations are observed for poly (**1**) and poly (**2**) under comparable conditions. When poly (**1**) and poly (**2**) are examined within a narrow potential window, the additional anodic and cathodic features observed under wide potential conditions are absent.

5.2.5. Spectroelectrochemistry of polymer products

UV–Vis–NIR spectroelectrochemical measurements were performed on polymer films obtained by electrochemical oxidation of the corresponding monomers. A background spectrum was collected prior to each measurement using the same electrode configuration in a monomer-free electrolyte solution. Spectroelectrochemical measurements were carried out under potentiodynamic control, and spectra were recorded during both oxidative and reductive potential sweeps. For measurements performed under wide potential conditions, the polymer films were subjected to an initial potentiostatic reduction step prior to data acquisition.

The spectroelectrochemical responses of poly (**1**), poly (**2**), and poly (**3**) are shown in Figures 5.6 – 5.9. For poly (**1**), both thick and thin films were examined, as shown in Figures 5.6 and 5.7, respectively. Polymer films of poly (**1**) and poly (**2**) were prepared using both wide and narrow potential windows, consistent with their electrochemical characterization, and their spectroelectrochemical

behaviour was examined under the corresponding conditions. Within the narrow potential window, the applied potential range excludes the cathodic features observed at approximately -0.2 V and -0.3 V vs Fc/Fc^{+} for poly (**1**) and poly (**2**), respectively.

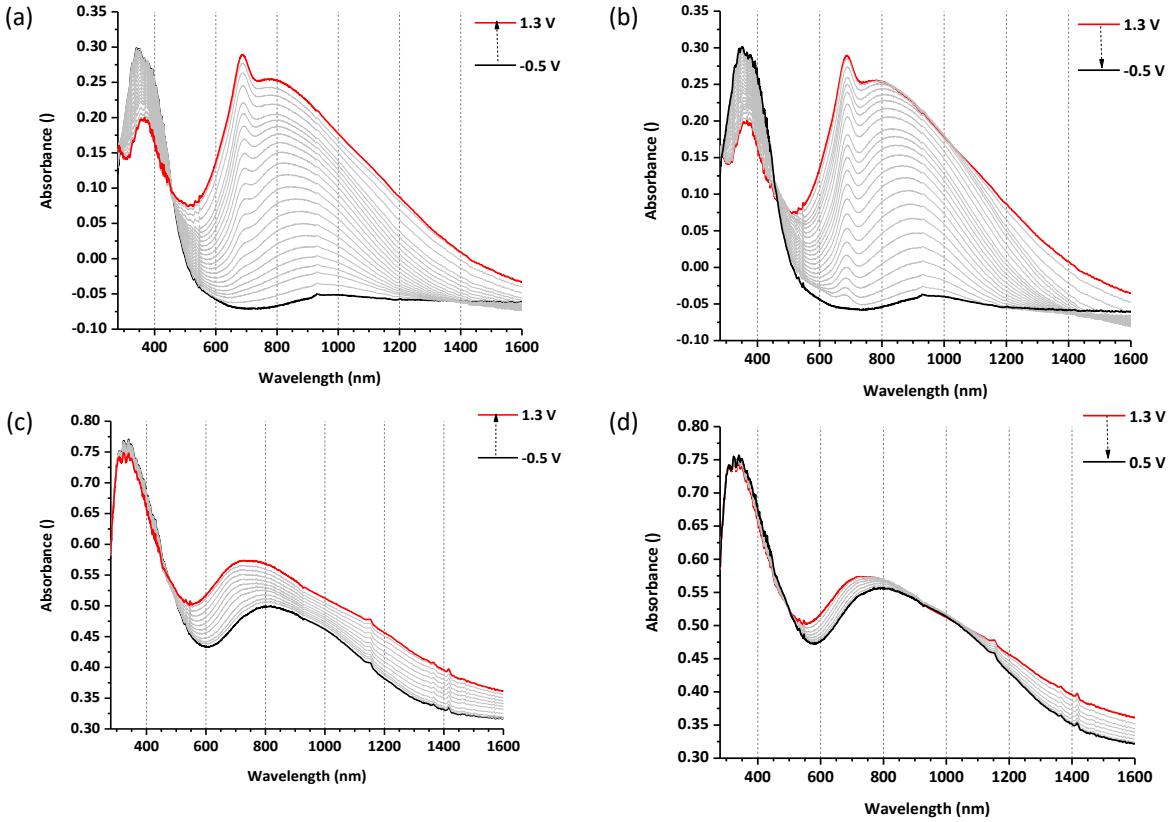

Figure 5.6 *UV–Vis–NIR spectra recorded during electrochemical oxidation of thick poly (**1**) films in dichloromethane containing 0.1 M Bu_4NPF_6 using high-speed acquisition. Panels (a) and (b) correspond to p-doping and dedoping under a wide potential window, while panels (c) and (d) show p-doping and dedoping under a narrow potential window.*

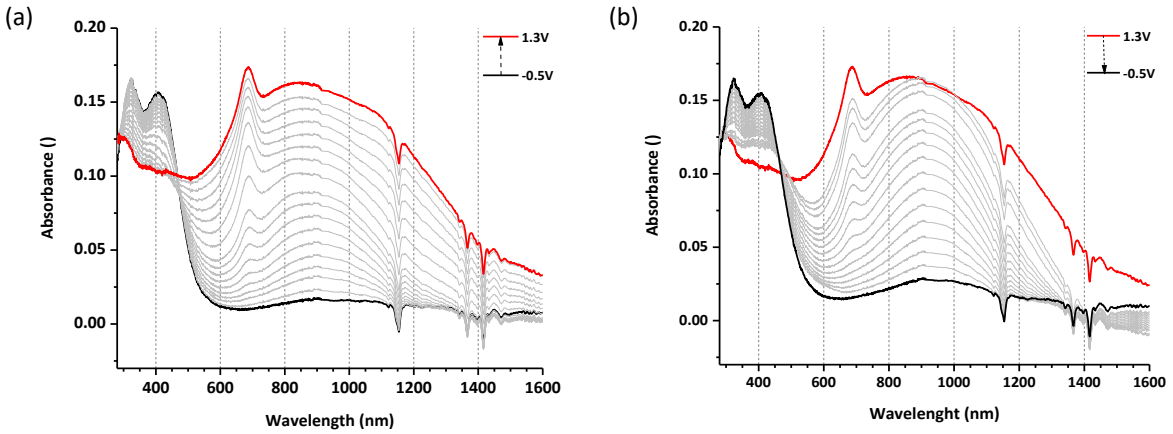

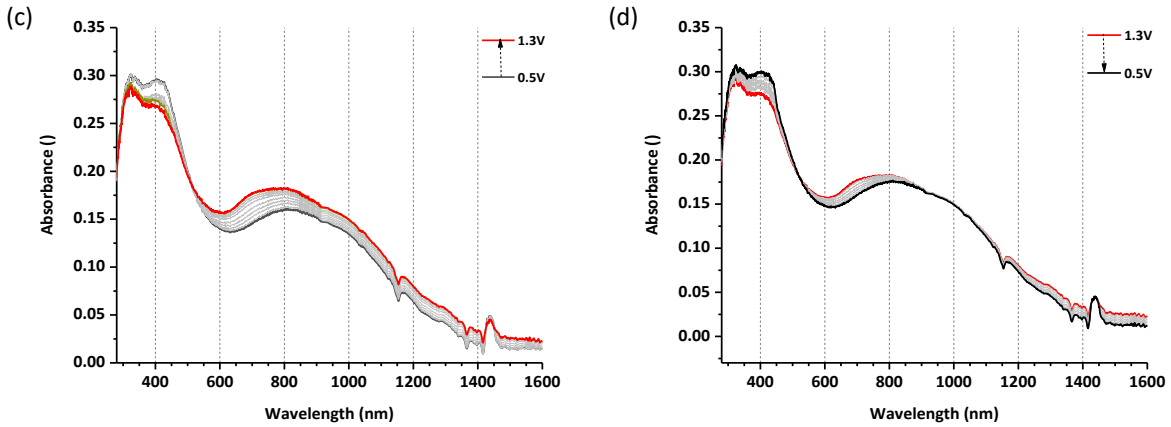

Figure 5.7 UV–Vis–NIR spectra recorded during electrochemical oxidation of thin poly(**1**) films under the same conditions as in Figure 5.6.

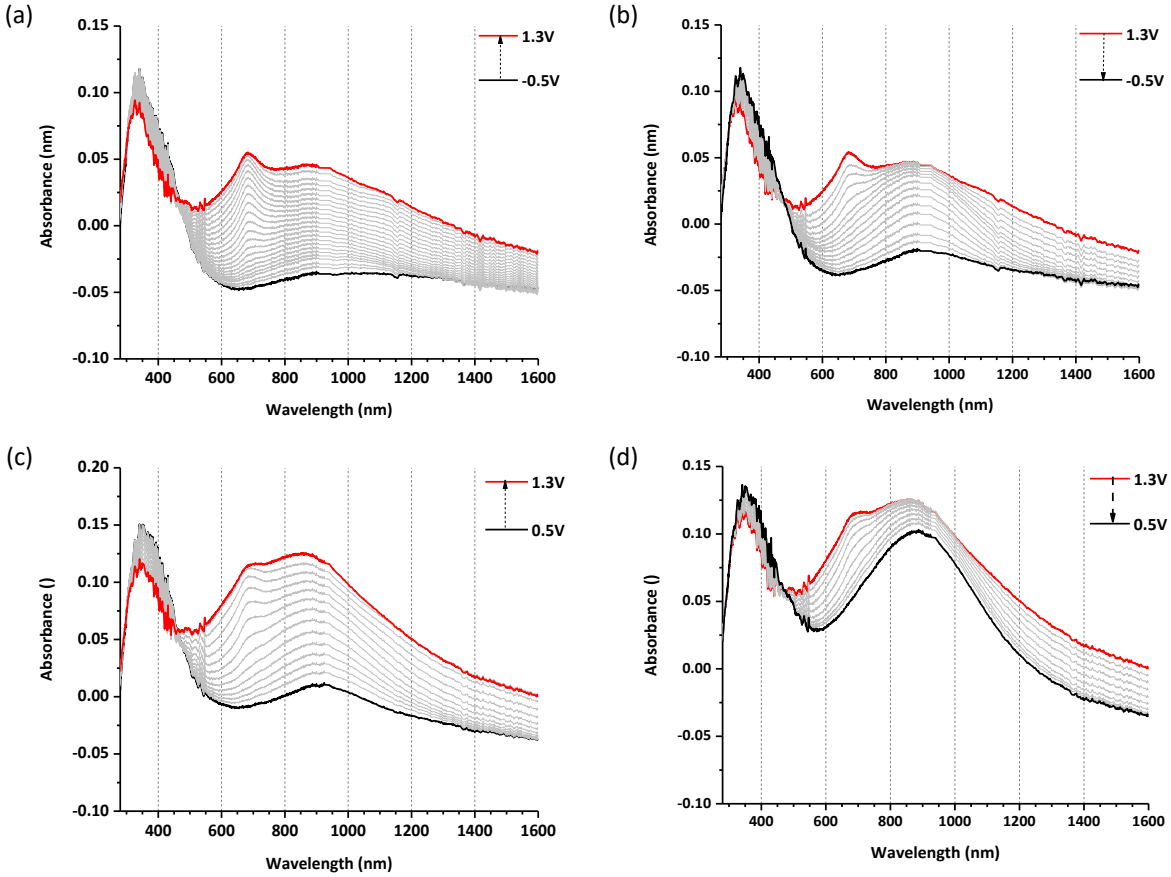

Figure 5.8 *UV–Vis–NIR spectra recorded during electrochemical oxidation of thick poly(2) films in dichloromethane containing 0.1 M Bu_4NPF_6 using high-speed acquisition. Panels (a) and (b) correspond to p-doping and dedoping under a wide potential window, while panels (c) and (d) show p-doping and dedoping under a narrow potential window.*

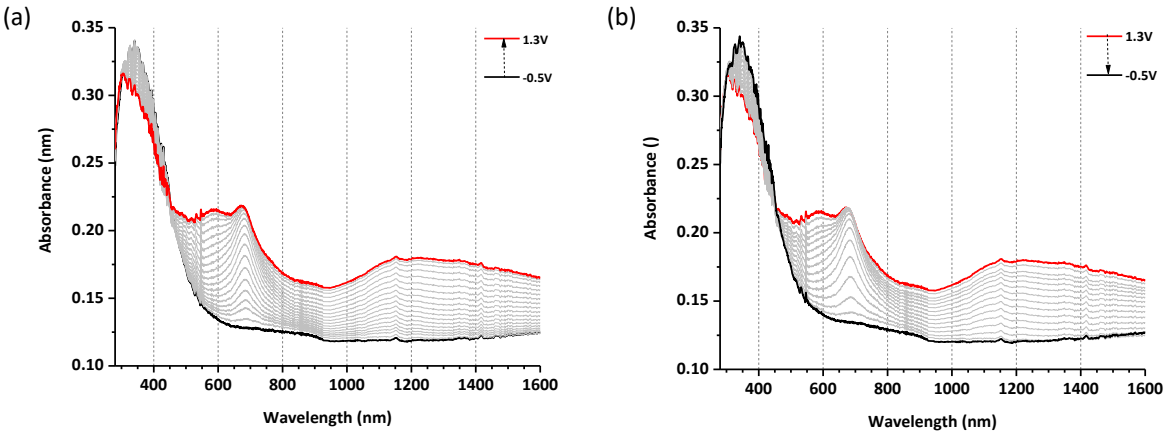

Figure 5.9 *UV–Vis–NIR spectra recorded during electrochemical oxidation of thick poly(3) films in dichloromethane containing 0.1 M Bu_4NPF_6 using high-speed acquisition. Panels (a) and (b) correspond to p-doping and dedoping under a wide potential window.*

UV–Vis–NIR spectroelectrochemical measurements were performed on both thick and thin films of poly(**1**) in order to evaluate possible charge-transport limitations arising from film thickness (Figures 5.6 and 5.7). Thicker films provided improved signal-to-noise ratios, whereas thin films were prepared to minimize potential charge-transfer hindrance. In the neutral state, poly(**1**) exhibits two main absorption bands centred at approximately 350 nm and 400 nm, attributed to π–π* transitions (Figure 5.7(a). Compared to the monomer absorption at 320 nm, these bands are red-shifted by approximately 30–80 nm. In addition to these high-energy transitions, a weak low-energy absorption band centred near 900 nm is already detectable as a residual feature in the neutral spectrum.

Upon electrochemical oxidation (p-doping), the intensities of the 350 and 400 nm bands decrease progressively, while the residual low-energy band near 900 nm increases in intensity and gradually shifts toward shorter wavelengths with increasing applied potential. Simultaneously, a broad doping-induced absorption develops between approximately 600 nm and 1400 nm. A distinct feature appears near 687 nm at higher oxidation levels. At advanced potentials, an absorption tail extending to approximately 1600 nm is observed. Comparison of wide and narrow potential windows shows that restricting the applied potential limits the growth of the near-infrared band and improves spectral reversibility, whereas the broader window produces more pronounced bleaching and stronger low-energy absorption. Upon reversal of the potential, the UV absorption bands are largely restored and the visible–NIR features diminish, indicating reversible redox behaviour. No qualitative differences in spectral evolution are observed between thick and thin films.

The spectroelectrochemical behaviour of poly (**2**) was investigated under both wide and narrow potential windows (Figure 5.8). In its neutral state, poly (**2**) exhibits a single dominant absorption band centred at approximately 340 nm. No clearly resolved secondary high-energy band is observed. In addition to this main UV band, a weak but distinct absorption feature is present in the 800–1000 nm region in the initial spectrum.

Under the wide potential window (Figure 5.8(a)), progressive oxidation leads to a steady decrease in the 340 nm band. The low-energy feature in the 800–1000 nm region increases in intensity and develops into a broad doping-induced absorption extending from approximately 900 nm to 1400 nm. In contrast to poly (**1**), this band remains largely centred in the same spectral region during oxidation and does not exhibit a noticeable wavelength shift. A distinct absorption peak near 680 nm appears during the early stages of oxidation and becomes more pronounced at higher potentials. At

advanced oxidation states, the absorption tail extends to approximately 1500–1600 nm. During the reverse scan, the low-energy absorption decreases and the UV band is substantially restored. A residual low-energy absorption remains detectable after dedoping.

Under the narrow potential window (Figure 5.8(c)), similar spectral trends are observed, although the magnitude of the changes is reduced. The growth of the visible and near-infrared absorption bands is more moderate. The doping-induced absorption centred near 680 nm still develops, although with lower amplitude compared to the wide-window experiment. The NIR band remains broad and relatively featureless. Dedoping under the narrow window also shows effective restoration of the neutral absorption profile.

The spectroelectrochemical behaviour of poly (**3**) was investigated under both wide and narrow potential windows (Figure 5.9). Poly (**3**) in its neutral state displays a strong absorption maximum at approximately 340 nm. Upon p-doping (Figure 5.9(a)), the intensity of the UV band decreases progressively. A distinct absorption peak emerges rapidly at approximately 670–690 nm during the initial stages of oxidation. With increasing potential, additional absorption features develop, including a shoulder around 550–600 nm and a broad band extending from approximately 1000 nm to beyond 1500 nm. The long-wavelength absorption tail reaches close to 1600 nm. Compared to poly (**2**), the NIR region in poly(**3**) appears more structured and shows a broader spectral distribution. During the reverse scan, the visible and NIR absorptions decrease, and the UV band recovers substantially, demonstrating good electrochemical reversibility within the examined potential window (Figure 5.9 (b)).

5.2.6. EPR spectroelectrochemistry

Electron paramagnetic resonance (EPR) spectroelectrochemical measurements were performed on polymer films deposited onto platinum wire electrodes, following the same procedures employed for the electrochemical experiments. EPR spectra were recorded under potentiostatic control, first during the oxidative p-doping process by applying progressively increasing potentials, and subsequently during the dedoping process by decreasing the applied potential. The relative concentration of paramagnetic centres was determined by double integration of the first-derivative EPR spectra. The peak-to-peak separation along the magnetic field axis was used to determine the EPR linewidth (ΔBpp). Measurements were carried out up to three applied potentials, namely 1.0 V, 1.1 V, and 1.2 V . The evolution of the paramagnetic charge-carrier concentration and the corresponding EPR linewidths (ΔBpp), together with the cyclic voltammetry traces of poly(3) recorded at each potential, are presented in Figure. 5.10 (a–c).

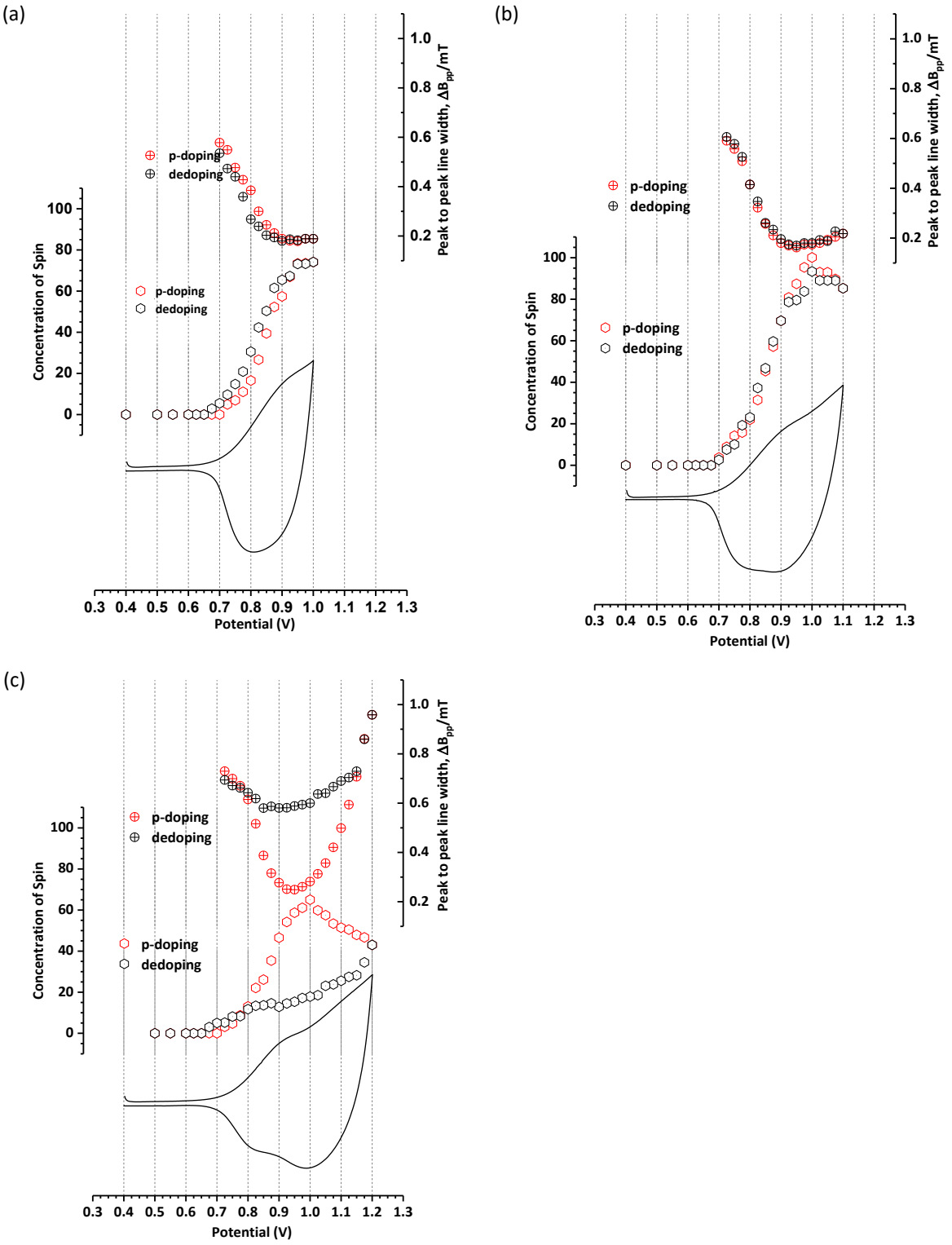

Figure 5.10 *Concentration of paramagnetic charge carriers and peak-to-peak linewidth (ΔBpp) extracted from EPR spectra of poly(3), together with the corresponding cyclic voltammetry traces, recorded during p-doping and dedoping at applied potentials of (a) 1.0 V, (b) 1.1 V, and (c) 1.2 V vs Fc/Fc⁺.*

In the neutral state, no detectable EPR signal was observed, confirming the absence of paramagnetic species prior to oxidation. Upon increasing the applied potential, the EPR signal intensity progressively increased. The onset of detectable spin concentration occurred at approximately 0.7 V, followed by a sharp rise as the potential approached 1.0 V. The spin concentration, determined by

double integration of the EPR spectra, reached a maximum near 1.0 V. Although the raw peak intensity at approximately 0.95 V appears higher than at 1.0 V, quantitative evaluation based on double integration confirms that the maximum spin concentration occurs at 1.0 V rather than at slightly lower potentials. When the upper potential limit was restricted up to 1.0 V (Figure 5.10a), the spin concentration increased during p-doping and returned close to its initial value during dedoping, indicating reversible generation and removal of paramagnetic charge carriers. A similar trend was observed when the upper limit was extended to 1.1 V (Figure 5.10b), although a gradual decrease in maximum spin concentration was observed at the highest potentials within this window. The separation between p-doping and dedoping traces indicates some hysteresis in the redox process.

Up to the upper potential limit of 1.2 V (Figure 5.10c), the spin concentration initially increased but subsequently decreased sharply at higher potentials. During the reverse scan, the spin concentration did not fully recover its original behaviour, and noticeable differences between doping and dedoping traces were observed.

The peak-to-peak linewidth (ΔBpp) shows systematic variation with applied potential. Up to upper limits of 1.0 V and 1.1 V (Figure 5.10(a,b)), the linewidth decreases as the spin concentration increases, reaching a minimum near the potential of maximum spin density. Upon dedoping, the linewidth increases again as the spin concentration decreases. In contrast, when the potential is extended up to 1.2 V (Figure 5.10(c)), linewidth broadening is observed at higher potentials, accompanying the decrease in spin concentration.

Film stability was further assessed through successive p-doping–dedoping cycles limited to oxidation thresholds of 1.0 V and 1.1 V (Figures 5.11–5.16). These controlled potential limits allow the boundary between reversible charge storage and irreversible degradation to be clearly identified. Correlating spin concentration with electrochemical response under these conditions defines the practical stability window of poly (**3**) and highlights the potential range over which reversible operation can be sustained.

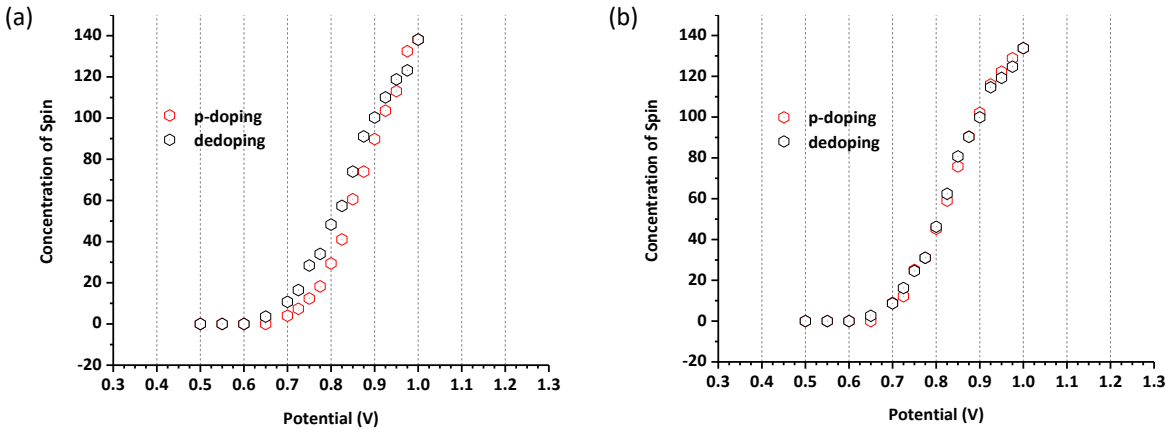

Figure 5.11 *Concentration of paramagnetic charge carriers in poly(3) recorded up to an oxidation threshold of 1.0 V during (a) the first and (b) the second p-doping–dedoping cycles.*

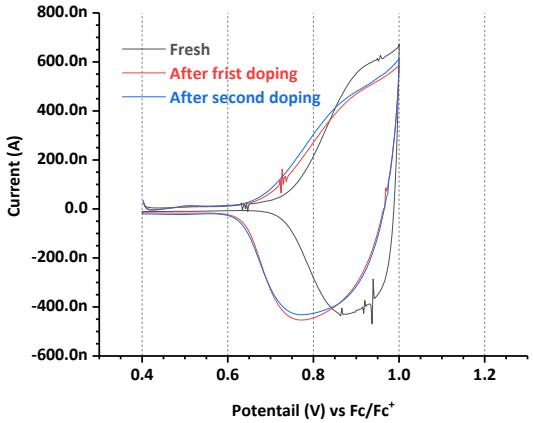

Figure 5.12 *Cyclic voltammetry of polymer films of poly (**3**) fresh (black line), trace after first doping-dedoping (red line) , and trace after second doping-dedoping (blue line) cycles up to a **1.0V** oxidation threshold potential in 0.1M of Bu_4NPF_6 in dichloromethane at 0.02 V/s.*

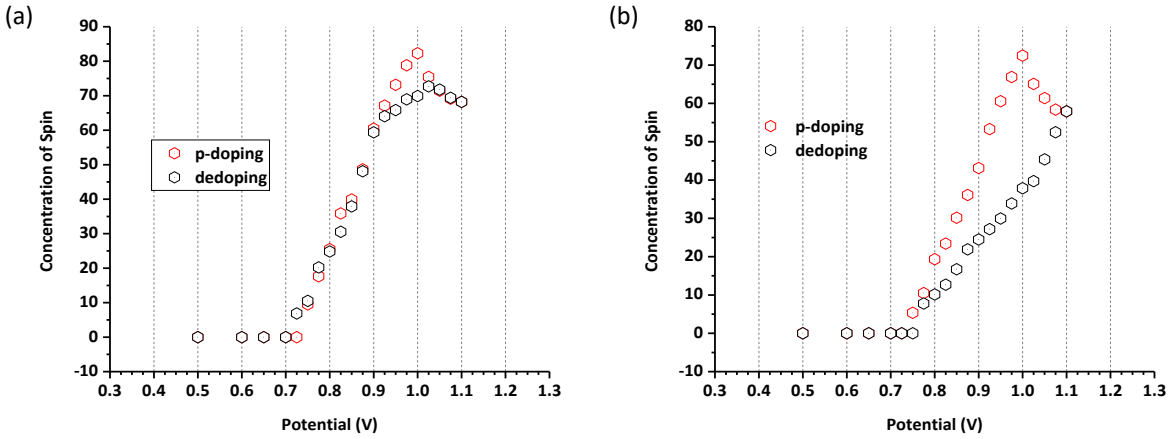

Figure 5.13 *Concentration of paramagnetic charge carriers in poly(3) recorded up to an oxidation threshold of 1.1 V during (a) the first and (b) the second p-doping–dedoping cycles.*

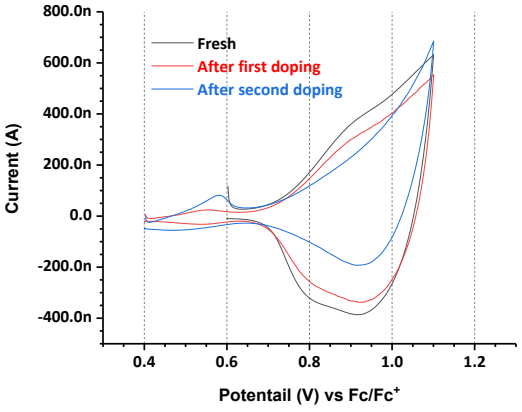

Figure 5.14 *Cyclic voltammetry of polymer films of poly (**3**) fresh (black line), trace after first doping-dedoping (red line), and trace after second doping-dedoping (blue line)cycles up to a 1.1V oxidation threshold potential in 0.1M of Bu_4NPF_6 in dichloromethane at 0.02 V/s.*

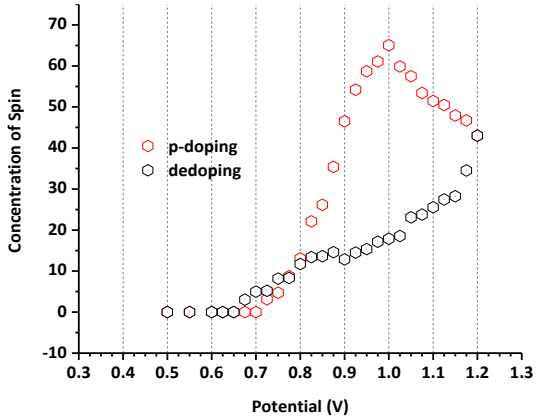

Figure 5.15 *The concentration of paramagnetic charge carriers recorded up to a 1.2V oxidation threshold potential after the first doping-dedoping for poly (**3**).*

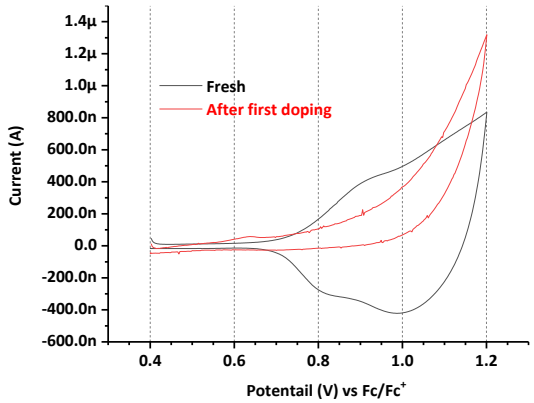

Figure 5.16 *Cyclic voltammetry of polymer films of Poly (**3**), fresh (**black line**), and (b) trace after first doping-dedoping (red line) cycles up to a 1.2V oxidation threshold potential in 0.1M of Bu_4NPF_6 in dichloromethane at 0.02 V/s.*

Figure 5.11 presents the spin concentration of poly(**3**) recorded during two successive p-doping–dedoping cycles with the oxidation threshold limited to 1.0 V. In both cycles, the spin concentration increases progressively upon oxidation and reaches comparable maximum values near the upper potential limit. During the reverse scan, the spin concentration decreases and returns close to its initial baseline value. Notably, Figure 5.11(b) shows that after the second cycle, the maximum spin concentration remains essentially unchanged compared to the first cycle.

Consistent with the EPR data, the cyclic voltammograms shown in Figure 5.12 exhibit nearly identical profiles for the fresh film and after the first and second doping–dedoping cycles at 1.0 V. No significant changes in peak position, current intensity, or overall voltammetric shape are observed, indicating preserved electrochemical behaviour within this potential window.

When the oxidation threshold is extended to 1.1 V, changes in reversibility become apparent. Figure 5.13 displays the spin concentration recorded during two successive cycles up to 1.1 V. In the first cycle (Figure 5.13a), the spin concentration increases with potential and reaches a maximum near the upper limit. During the second cycle (Figure 5.13b), the maximum spin concentration is reduced, and the dedoping branch does not fully retrace the initial path.

Correspondingly, the cyclic voltammograms recorded up to 1.1 V (Figure 5.14) show noticeable alterations after the first doping–dedoping cycle. The red and blue traces differ from the fresh film (black trace), exhibiting modified peak intensities and changes in current response, which reflect changes in the electrochemical characteristics of the film after exposure to this higher potential.

Further extension of the oxidation threshold to 1.2 V results in pronounced changes. Figure 5.15 shows that the spin concentration increases during oxidation but does not fully recover upon dedoping, indicating significant loss of reversibility. The corresponding cyclic voltammogram in Figure 5.16 reveals substantial deviation from the fresh film after the first doping–dedoping cycle. The anodic and cathodic current responses are markedly altered, demonstrating irreversible modification of the polymer film at this potential.

Overall, the combined EPR and cyclic voltammetry data show that poly(**3**) maintains reversible electrochemical behaviour when the oxidation threshold is limited to 1.0 V. Partial irreversibility appears at 1.1 V, and significant degradation is observed at 1.2 V

5.3. Alternating methylene-bridged oligothiophene polymers

This section examines the effect of increasing oligomer length on the electrochemical and spectroscopic properties of methylene-bridged oligothiophene systems. The investigated series consists of compounds 4, 1, and 5, which contain bithiophene, quaterthiophene, and sexithiophene segments, respectively, separated by a single methylene (–CH_2–) conjugation-breaking spacer. The spacer structure is kept constant across the series, enabling systematic evaluation of length-dependent trends. The chemical structures of the three compounds are presented in Figure 5.17.

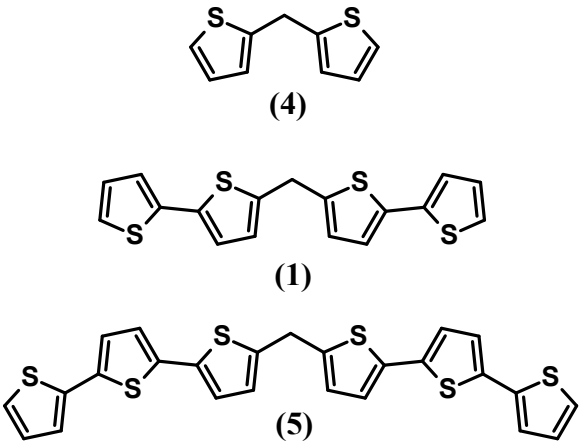

Figure 5.17 Chemical structures of methylene-bridged oligothiophenes 4, 1, and 5 with increasing oligomer length.

5.3.1. UV-vis spectra

The UV–vis absorption spectra of compounds **4**, **1**, and **5** recorded in dichloromethane are shown in Figure 5.18. All spectra were measured using a PerkinElmer UV–Vis spectrophotometer under identical conditions.

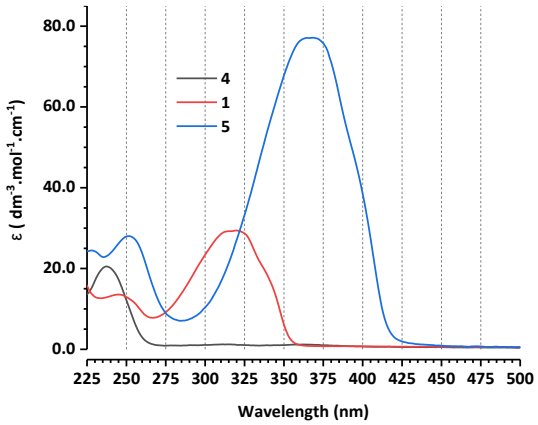

*Figure 5.18 Absorption spectra of compounds **4, 1, and 5** registered in DCM.*

Each compound exhibits a dominant absorption band in the UV–visible region, which is assigned to the π–π* electronic transition of the conjugated thiophene backbone [136]. A systematic bathochromic shift of the main absorption band is observed with increasing oligothiophene length. Compound **4** shows the highest-energy transition, while compound **1** is red-shifted relative to compound **4**. Compound **5** exhibits the most bathochromically shifted and most intense absorption band among the three compounds.

A similar trend is observed for the absorption onset, which progressively shifts toward longer wavelengths with increasing number of thiophene units. The optical band gap decreases progressively from compound **4** to **1** compound **5**. In parallel, the molar absorption coefficient increases across the series. The corresponding molar absorption coefficient (ε), absorption onset wavelengths (λ_{onset}), maximum absorption wavelengths (λ_{max}) and optical band gap energies (E_g^{opt}) are summarized in Table 5.3.1.

Table 5.3.1 The relative molar absorption coefficient (ε), onset wavelength (λ_{onset}), maximum wavelength (λ_{max}) and optical band gap (E_g^{opt}) values of compounds 4, 1, and 5 in dichloromethane.

Compounds	**ε** [$dm^{-3}.mol^{-1}.cm^{-1}$]	$\boldsymbol{\lambda_{onset}}$ [nm]	$\boldsymbol{\lambda_{max}}$ [nm]	$\boldsymbol{E_g^{opt}}$ [eV]
4	21	270	237	4.59
1	29	358	320	3.46
5	77	420	368	2.95

5.3.2. Electrochemical properties of compounds

The cyclic voltammograms of compounds **4**, **1**, and **5,** recorded in the anodic potential range, are shown in Figure 5.19 (a-c). Measurements were carried out in 0.1 M Bu_4NPF_6 in dichloromethane at a scan rate of 0.1 V s^{-1}. It should be noted that compound **5** exhibits limited solubility in dichloromethane, which resulted in reduced current response compared to compounds **1** and **4**.

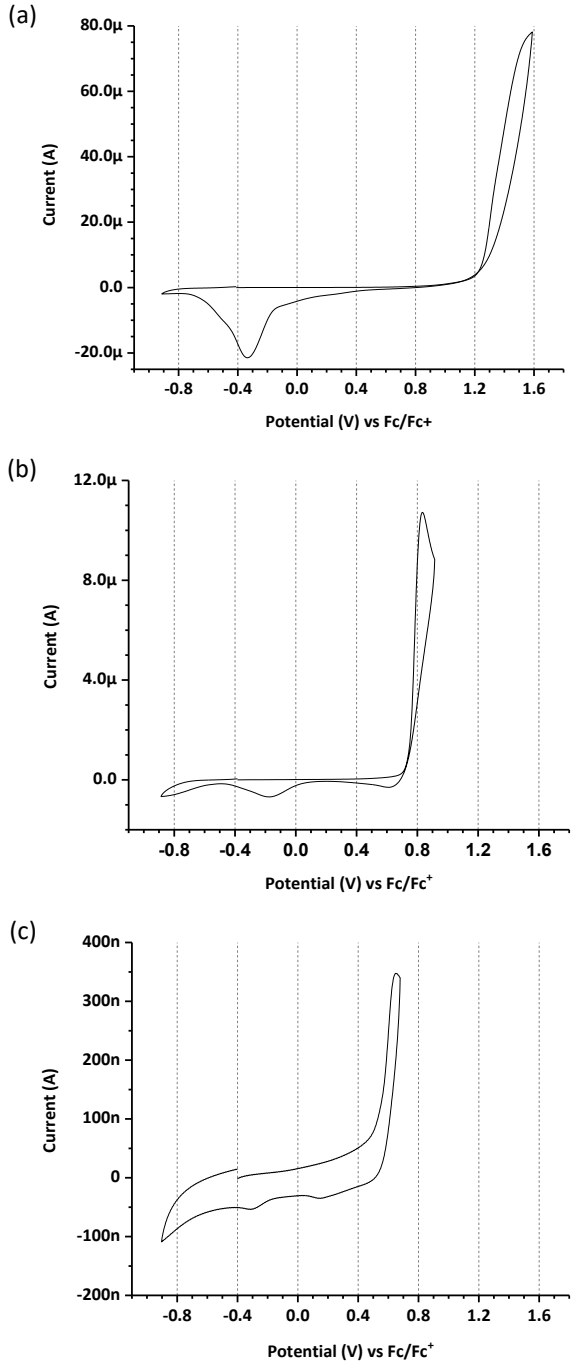

*Figure 5.19 Cyclic voltammograms of (a) 1mM **4**, (b) 1mM **1**, and (c) saturated **5**, in 0.1 M Bu_4NPF_6 dichloromethane solution, in the anodic potential range (scan rate 0.1V/s).*

Electrochemical measurements show that all investigated compounds exhibit anodic electroactivity. In the first oxidation cycle, each compound displays a single irreversible oxidation wave. The oxidation onset potentials, (E_{onset}^{ox}) and anodic peak potentials (E_{pa}) are summarized in Table 5.3.2. Compound **5** shows the lowest oxidation onset potential among the three compounds, followed by compound **1**, whereas compound **4** requires a significantly higher potential for oxidation. The same trend is observed for the anodic peak potentials. The extracted HOMO energy levels, calculated from the oxidation onset potentials, are also listed in Table 5.3.2.

The anodic peak currents (I_p) differ markedly among the compounds. Compound **4** exhibits the highest peak current, compound **1** shows a moderate current response, and compound 5 displays a

substantially lower peak current. It should be noted that compound **5** exhibits limited solubility in dichloromethane, which results in a reduced current response compared to compounds 1 and 4 under identical experimental conditions. The electrochemical parameters, including E_{onset}^{ox}, E_{pa}, E_{HOMO}, and I_p are summarized in Table 5.3.2 for direct comparison.

*Table 5.3.2 The oxidation onset potentials, E_{onset}^{ox}, anodic peak potentials, E_{pa} , HOMO energy levels, E_{HOMO}, and anodic peak currents, I_p values of compounds **1**, **4** and **5** recorded in 0.1 M Bu_4NPF_6 in dichloromethane at scan rate of 0.1 V/s.*

Compounds	E_{onset}^{ox} [V] vs **Fc/Fc⁺**	E_{pa} [V] vs **Fc/Fc⁺**	E_{HOMO} [ev]	I_{pa} [µA]
1	0.752	0.833	-5.55	10.7
4	1.221	1.587	-6.02	78.20
5	0.534	0.649	-5.33	0.35

5.3.3. Electropolymerization

Electropolymerization of compounds 4, 1, and 5 was investigated by repetitive cyclic voltammetry in dichloromethane containing 0.1 M Bu_4NPF_6. Representative voltammograms recorded over successive potential cycles are shown in Figure 5.20 (a–e).

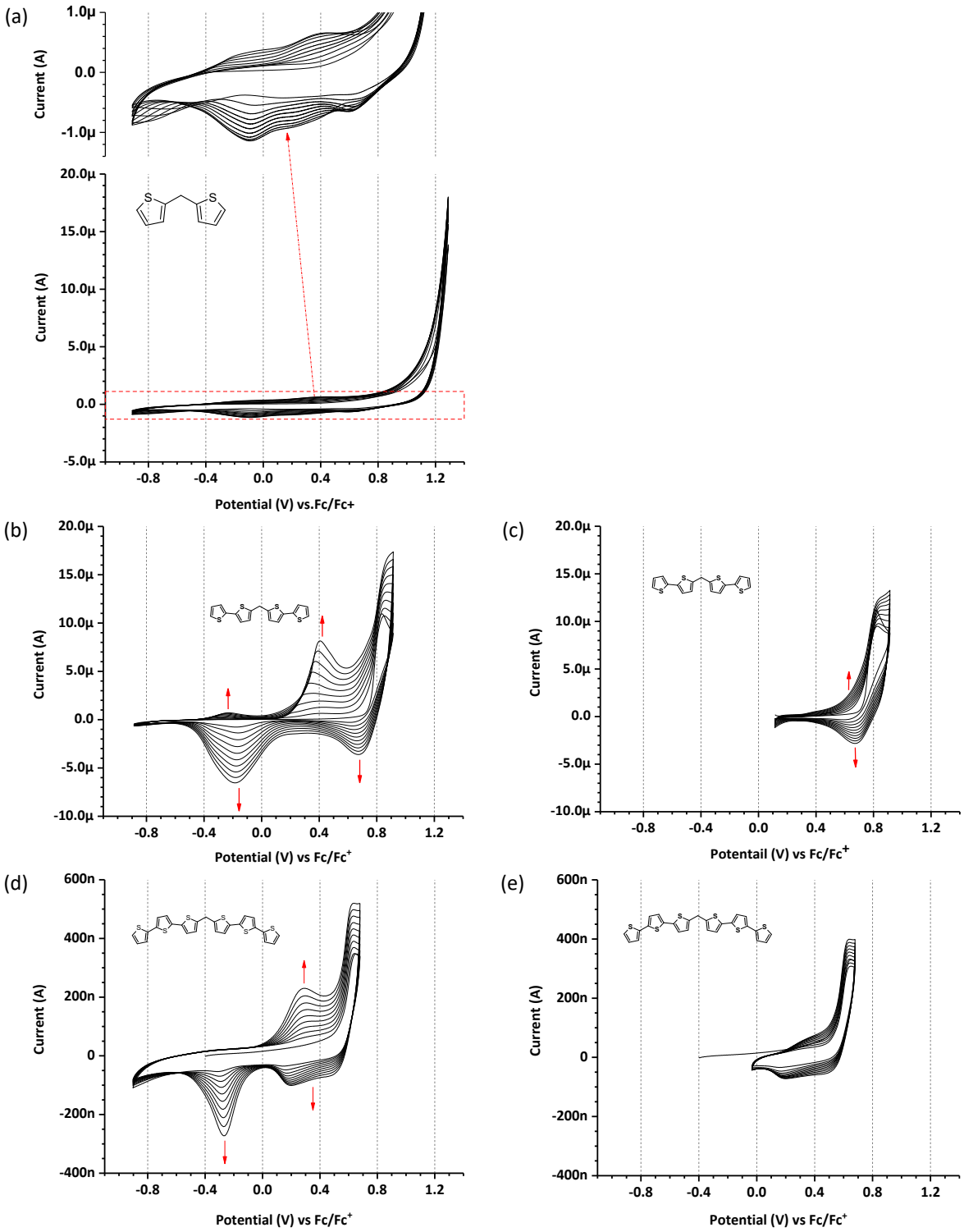

*Figure 5.20 Cyclic voltammograms of electropolymerization of bithiophene equipped with methylene π-conjugation break spacers (**4**)(a), quaterthiophene equipped with methylene π-conjugation break spacers (**1**), (b) wide and (c) narrow potential ranges, and sexithiophene equipped with methylene π-conjugation break spacers (**5**), (d) wide and (e) narrow potential range, in 0.1M of Bu_4NPF_6 in dichloromethane at 0.1V/s, demonstrating the successive accumulation of electroactive deposits during repetitive potential cycling.*

For compound **4** (Figure 5.20(a)), repeated potential cycling within the applied potential window results in only minor changes in the voltammetric response. The lower voltammogram corresponds to the full potential range, while the upper inset shows a magnified view of the region indicated by the red dashed rectangle. Both traces originate from the same dataset. A slight increase in current is

observed upon successive scans, indicating limited growth of electroactive material on the electrode surface. However, when the anodic limit is extended to higher potentials, these voltammetric features do not persist.

In contrast, compounds **1** and **5** exhibit a clear progressive increase in current response during repeated potential cycling (Figure 5.20 (b–e)). For both compounds, electropolymerization was examined under wide and narrow potential windows. Under the wide potential window (Figure 5.20(b) and 5.20(d)), successive scans show a continuous increase in anodic and cathodic currents, accompanied by the development of additional redox features. Under the narrow potential window (Figure 5.20(c) and 5.20(e)), the applied potential range excludes the cathodic region near −0.2 V vs Fc/Fc^{+}. Within this restricted range, current growth is still observed upon repetitive cycling, although the overall magnitude of the current is lower compared to the wide potential window. The current response recorded for compound **5** is smaller than that observed for compound **1** under comparable experimental conditions.

5.3.4. Electrochemical properties of polymer films

The electrochemical behaviour of the polymer films derived from compounds **4**, **1**, and **5** was investigated by cyclic voltammetry in monomer-free dichloromethane containing 0.1 M Bu_4NPF_6. The corresponding voltammograms are shown in Figure 5.21 (a-e).

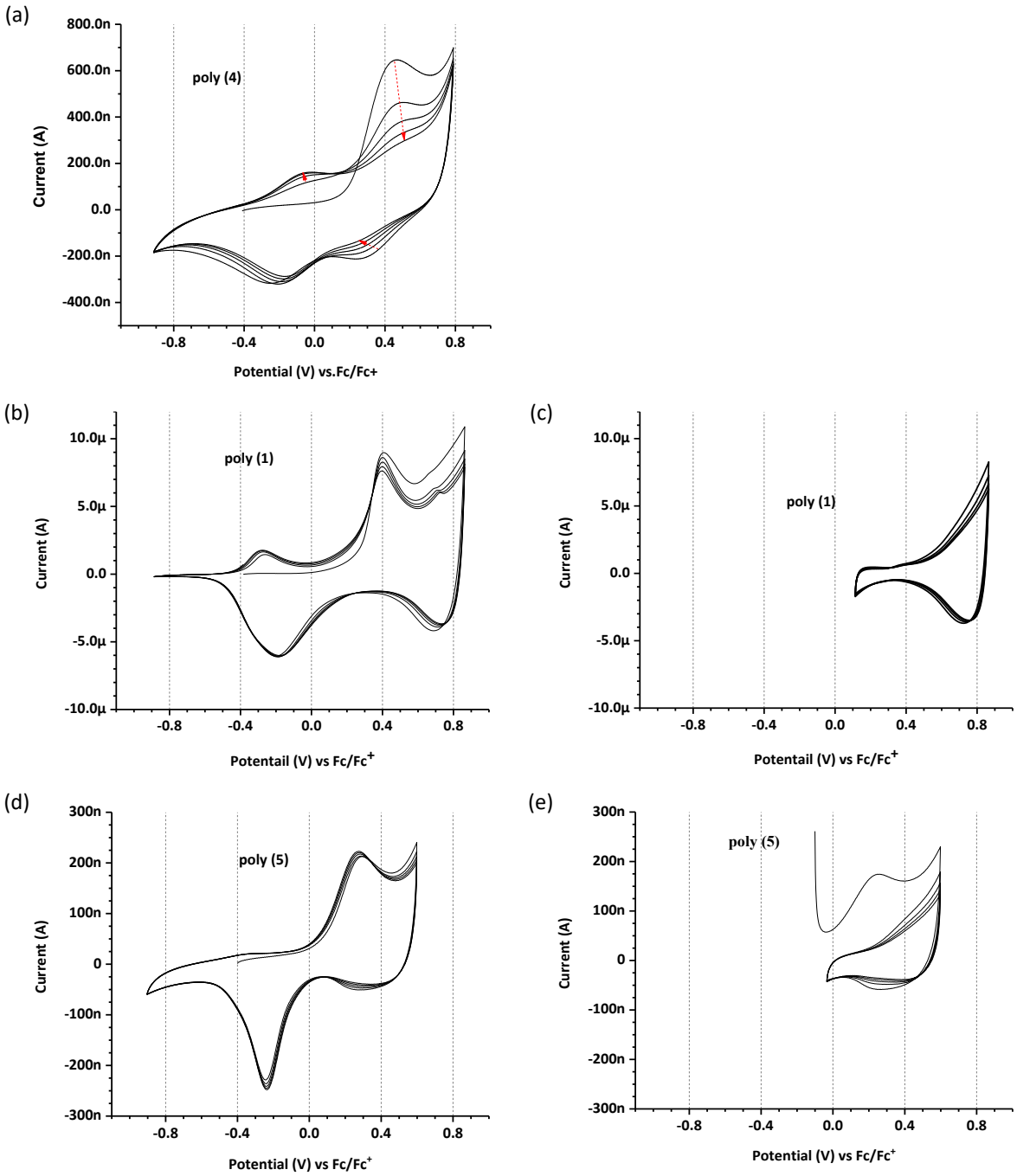

Figure 5.21 Cyclic voltammograms of polymer films recorded in monomer-free dichloromethane containing 0.1 M Bu_4NPF_6 at a scan rate of 0.1 V s^{-1}. Panels (a), (b), and (d) show the voltammetric response of poly(4), poly(1), and poly(5), respectively, recorded over a wide potential range. Panels (c) and (e) present the corresponding voltammograms of poly(1) and poly(5) recorded over a narrow potential range.

Figure 5.21(a) presents the voltammetric response of poly(**4**) recorded over a wide potential range. An anodic feature is observed in the positive potential region, with the main current increase occurring between approximately 0.6 and 0.8 V vs Fc/Fc^+, accompanied by a corresponding cathodic response during the reverse scan. The anodic wave appears relatively broad. Upon successive cycling, noticeable variations in peak shape and current intensity are observed. The current response increases during the initial scans and then shows changes in the voltammetric profile, indicating evolution of the film response under repeated polarization.

The voltammetric behaviour of poly(**1**) recorded over a wide potential window is shown in Figure 5.21(b). A defined anodic peak is observed in the positive potential region, with a corresponding cathodic peak on the reverse sweep. The separation between the anodic and cathodic features remains relatively consistent over successive cycles. The overall voltammetric profile retains a similar shape during repeated scans, with only moderate changes in peak current

When measured within a narrower potential window (Figure 5.21(c)), poly(1) exhibits a comparable redox profile with reduced overall current intensity. The voltammograms recorded in the restricted potential range display improved overlap between successive cycles, indicating stable and reproducible electrochemical response within this window.

For poly(5), the wide-range voltammogram (Figure 5.21(d)) shows a pronounced anodic process at positive potentials and a corresponding cathodic feature upon reversal of the scan direction. The peak currents are significantly higher than those observed for poly(**1**), reflecting differences in film response. During the first few scans, the current increases before reaching a relatively stable profile.

Under the narrower potential window (Figure 5.21(e)), the voltammetric response of poly(**5**) maintains a similar overall shape, with lower current magnitude compared to the wide-range measurement. Successive scans exhibit good reproducibility within the applied potential limits.

Overall, poly(**1**) and poly(**5**) display well-defined and reproducible doping–dedoping features within the examined potential windows, whereas poly(**4**) shows more pronounced scan-to-scan variations in peak shape and current intensity under wide-range polarization conditions.

5.3.5. Spectroelectrochemical properties of polymer films

Due to the limited electrochemical stability of poly(**4**), spectroelectrochemical measurements were not performed for this polymer. Spectroelectrochemical investigations were therefore carried out only for poly(**1**) and poly(**5**), as shown in Figure 5.22 and Figure 5.23, respectively. The UV–Vis–NIR spectroelectrochemical spectra of poly(**1**) films recorded during electrochemical doping and dedoping are shown in Figure 5.22. The spectroelectrochemical response of poly(**5**) films is presented in Figure 5.23. For this polymer, measurements were performed only over a wide potential range. Attempts to deposit poly(**5**) films on ITO electrodes using narrow potential windows, analogous to those employed for platinum working electrodes in electrochemical experiments, did not yield spectroscopically detectable films. As a result, spectroelectrochemical data for poly(**5**) were collected exclusively under wide-range conditions using potentiostatic control.

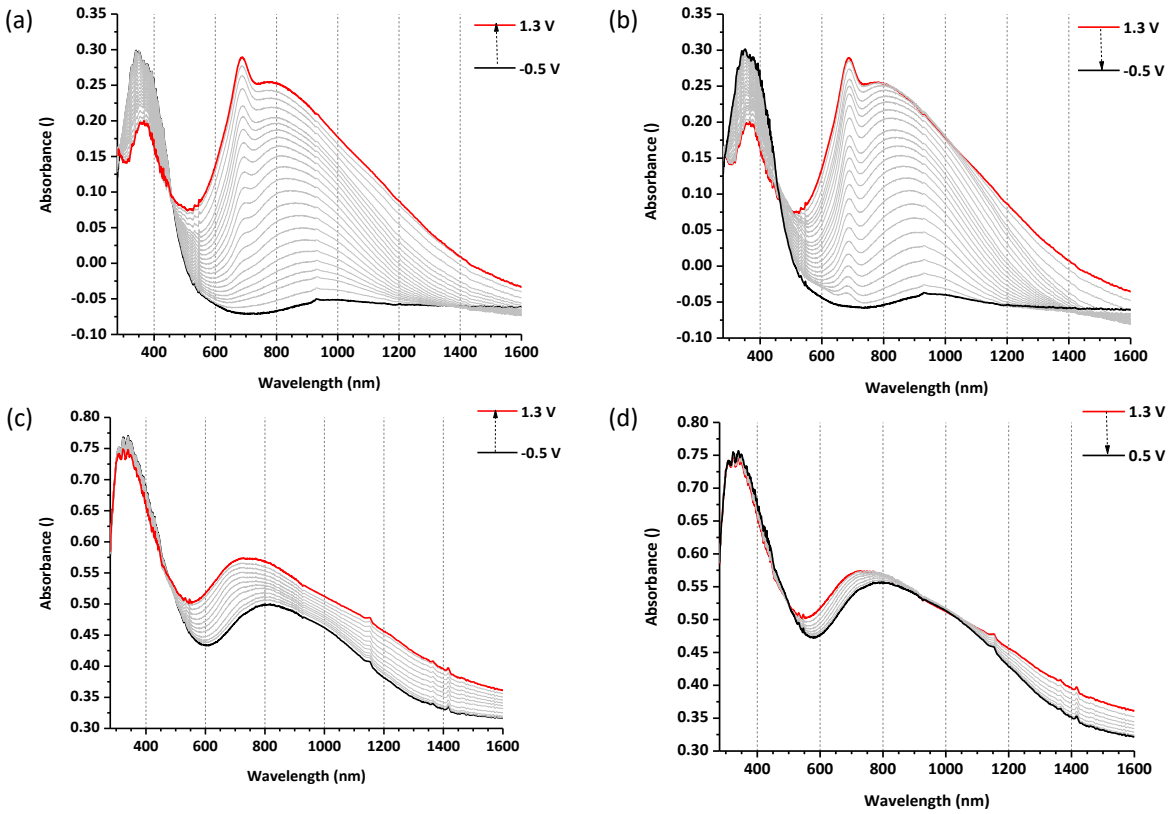

Figure 5.22 *UV–Vis–NIR spectra recorded during electrochemical oxidation and reduction of poly(1) films in dichloromethane containing 0.1 M Bu_4NPF_6. Spectra were collected during p-doping and dedoping over (a, b) a wide potential range and (c, d) a narrow potential range.*

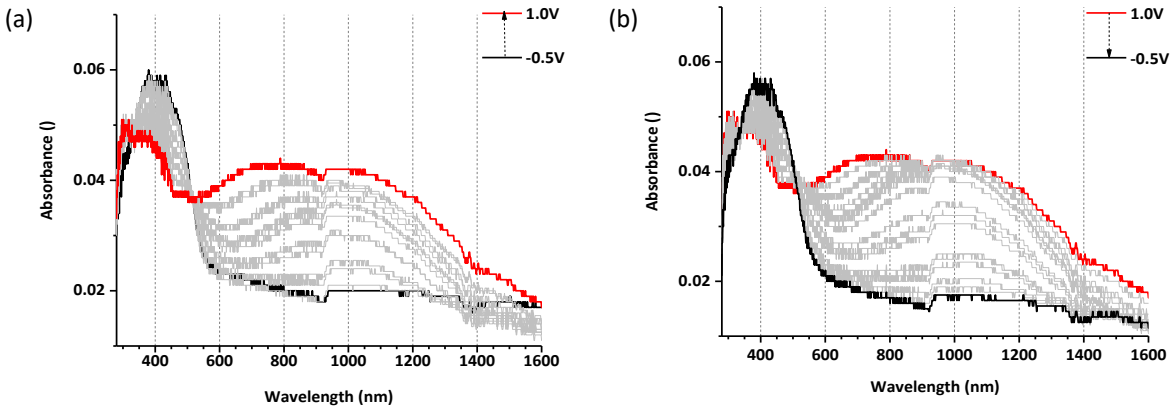

Figure 5.23 *UV–Vis–NIR spectra recorded in potentiostatic mode during electrochemical oxidation (a) and reduction (b) of poly(5) films in dichloromethane containing 0.1 M Bu_4NPF_6.*

The UV–Vis–NIR spectroelectrochemical spectra of poly(**1**) films recorded during electrochemical doping and dedoping are shown in Figure 5.22. These data are presented in detail in section 5.2.5, page 55. The UV–Vis–NIR spectroelectrochemical spectra of poly(**1**) films recorded during electrochemical doping and dedoping are shown in Figure 5.22.

The spectroelectrochemical response of poly(**5**) films is presented in Figure 5.23. For this polymer, measurements were performed exclusively over a wide potential range using potentiostatic control. Attempts to deposit poly(**5**) films on ITO electrodes under narrow potential conditions analogous to those used for platinum working electrodes did not produce films of sufficient optical density for reliable spectroscopic measurements. Consequently, spectroelectrochemical data for poly(**5**) were obtained only under wide potential window conditions.

In the neutral state, poly(**5**) exhibits a dominant absorption band centred near 400 nm (Figure 5.23 (a)). No sharp isosbestic points are observed during oxidation, and the spectral evolution proceeds continuously across the applied potential range. At higher oxidation potentials, the near-infrared absorption increases in intensity and extends toward longer wavelengths. During the subsequent reduction step (Figure 5.23(b)), the visible–NIR absorption band decreases in intensity, while the absorption in the UV region recovers toward its initial profile. The final spectrum after reduction closely resembles that of the neutral state, indicating substantial reversibility within the investigated potential range.

5.4. Alternating quaterthiophene-alkylene polymers.

This section focuses on a series of alternating quaterthiophene–alkylene compounds in which the conjugated backbone is interrupted by alkylene spacers of increasing length. The chemical structures of the investigated compounds are shown in Figure 5.24.

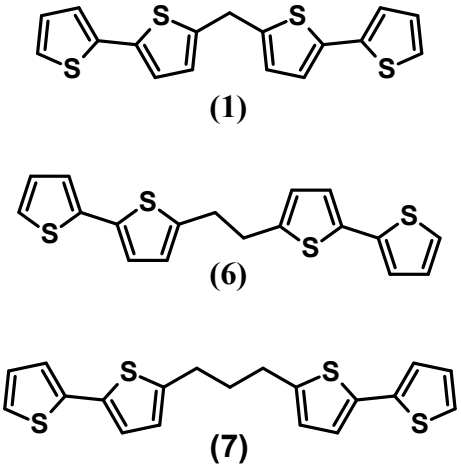

*Figure 5.24 Chemical structures of compounds **1**, **6**, and **7**.*

The series comprises compound **1**, which contains a methylene spacer, together with compounds **6** and **7**, in which the methylene bridge is extended to longer alkylene chains. This molecular design allows the systematic evaluation of the effect of alkylene spacer length on the electrochemical and spectroelectrochemical properties of the resulting polymer films, as well as spectroscopic properties of the corresponding monomer compounds.

5.4.1. UV-vis spectra

The UV–Vis absorption spectra of compounds **1**, **6**, and **7** recorded in dichloromethane are shown in Figure 5.25. All spectra were collected under identical experimental conditions. All three compounds exhibit a single absorption band in the UV region. The absorption profiles are similar in shape across the series, with well-defined maxima and relatively sharp absorption onsets

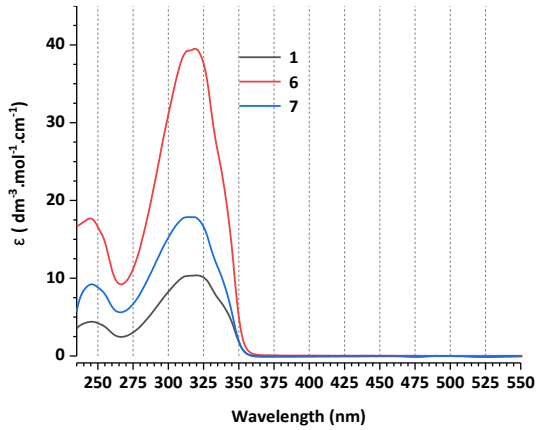

*Figure 5.25 UV–Vis absorption spectra of compounds **1**, **6**, and **7** recorded in dichloromethane.*

The molar absorption coefficients (ε), onset wavelengths, (λ_{onset}), maximum absorption wavelengths (λ_{max}), and optical band gap values (E_g^{opt}) derived from the absorption onset are summarized in Table 5.4.1.

Table 5.4.1 The relative molar absorption coefficient (ε), onset wavelength (λ_{onset}), maximum wavelength (λ_{max}), and optical band gap (E_g^{opt}) values of compounds 1, 6, and 7 in dichloromethane.

Compounds	**ε** [$dm^{-3}.mol^{-1}.cm^{-1}$]	$\boldsymbol{\lambda_{onset}}$ [nm]	$\boldsymbol{\lambda_{max}}$ [nm]	$\boldsymbol{E_g^{opt}}$ [eV]
1	10	354	320	3.51
6	39	356	319	3.49
7	18	355	318	3.50

The absorption maxima of compounds **1**, **6**, and **7** occur within a narrow wavelength range, indicating only minor variation in the position of the principal π–π* transition across the series. Likewise, the absorption onset values and corresponding optical band gaps are comparable for all three compounds. Among the investigated compounds, compound 6 exhibits the highest molar absorption coefficient, whereas compounds 1 and 7 show lower absorption intensities under identical measurement conditions. No significant shift of the absorption maximum or onset is observed as the alkylene spacer length increases from methylene (1) to ethylene (6) and propylene (7).

5.4.2. Electrochemical properties of compounds

The cyclic voltammograms of compounds **1**, **6**, and **7**, recorded in dichloromethane containing 0.1 M Bu_4NPF_6 at a scan rate of 0.1 V s^{-1}, are shown in Figure 5.26 (a–c).

(a)

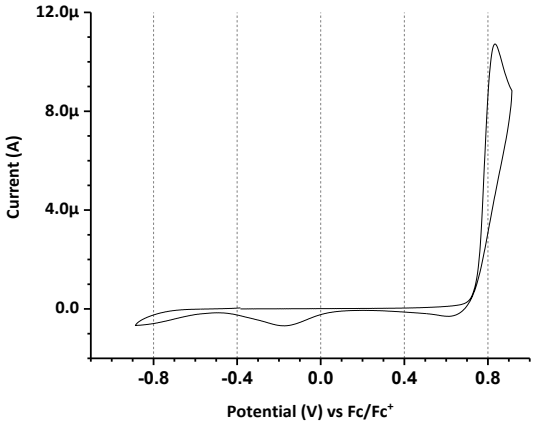

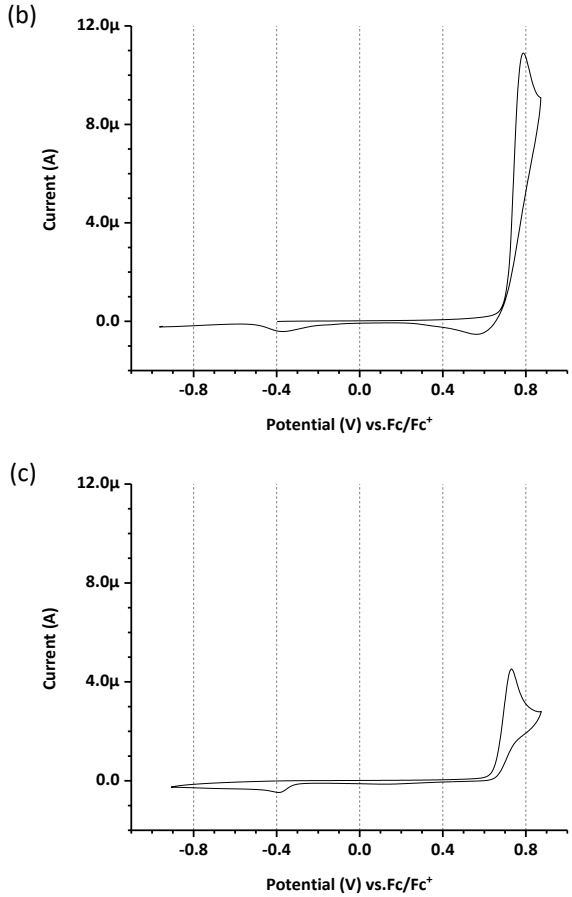

Figure 5.26 Cyclic voltammograms of compounds 1 (a), 6 (b), and 7 (c) recorded in dichloromethane containing 0.1 M Bu_4NPF_6 over the anodic potential range at a scan rate of 0.1 V s^{-1}.

Within the investigated anodic potential range, all three compounds exhibit electrochemical oxidation. During the forward scan, a single anodic oxidation peak is observed for each compound. No corresponding reversible anodic–cathodic couple is detected within the applied potential window, indicating that the oxidation process is electrochemically irreversible under these conditions.

Upon reversal of the scan direction, cathodic features are observed at negative potentials. For compound **1**, a cathodic peak appears near - 0.2 V vs Fc/Fc^+, whereas for compounds **6** and **7**, cathodic responses are detected at approximately - 0.4 V vs Fc/Fc^+ (Figure 5.26 (a–c)). The intensity of the cathodic peak decreases from compound **1** to compound **6** and **7**. The anodic peak currents also vary across the series. Compounds **1** and **6** exhibit comparable anodic peak currents, while compound **7** shows a lower peak current under identical experimental conditions.

The electrochemical parameters derived from the voltammograms, including the oxidation onset potential, E_{onset}^{ox}, the anodic peak potential, E_{pa}, HOMO energy level, E_{HOMO} , and peak current, I_p are summarized in Table 5.4.2. The oxidation onset potential decreases from compound **1** to compound **6** and **7**. A similar trend is observed for the anodic peak potential. The lowest oxidation potentials and peak current are recorded for compound **7**.

*Table 5.4.2 The value of oxidation onset potential, E_{onset}^{ox}, the anodic peak potential, E_{pa} ,HOMO energy level, E_{HOMO} and anodic current peak, I_p, of **1**, **6** and **7** recorded in 0.1 M Bu_4NPF_6 in dichloromethane at a scan rate of 0.1 V s^{-1}.*

Compounds	E_{onset}^{ox} [V] vs **Fc/Fc⁺**	E_{pa} [V] vs **Fc/Fc⁺**	E_{HOMO} [ev]	I_{pa} [µA]

1	0.752	0.833	-5.55	10.7
6	0.714	0.787	-5.51	10.90
7	0.652	0.729	-5.45	4.52

5.4.3. Electropolymerization

Electropolymerization of compounds **1**, **6**, and **7** was investigated by repetitive cyclic voltammetry in dichloromethane containing 0.1 M Bu_4NPF_6 . The cyclic voltammograms recorded during successive potential cycles are shown in Figure 5.27 (a–f).

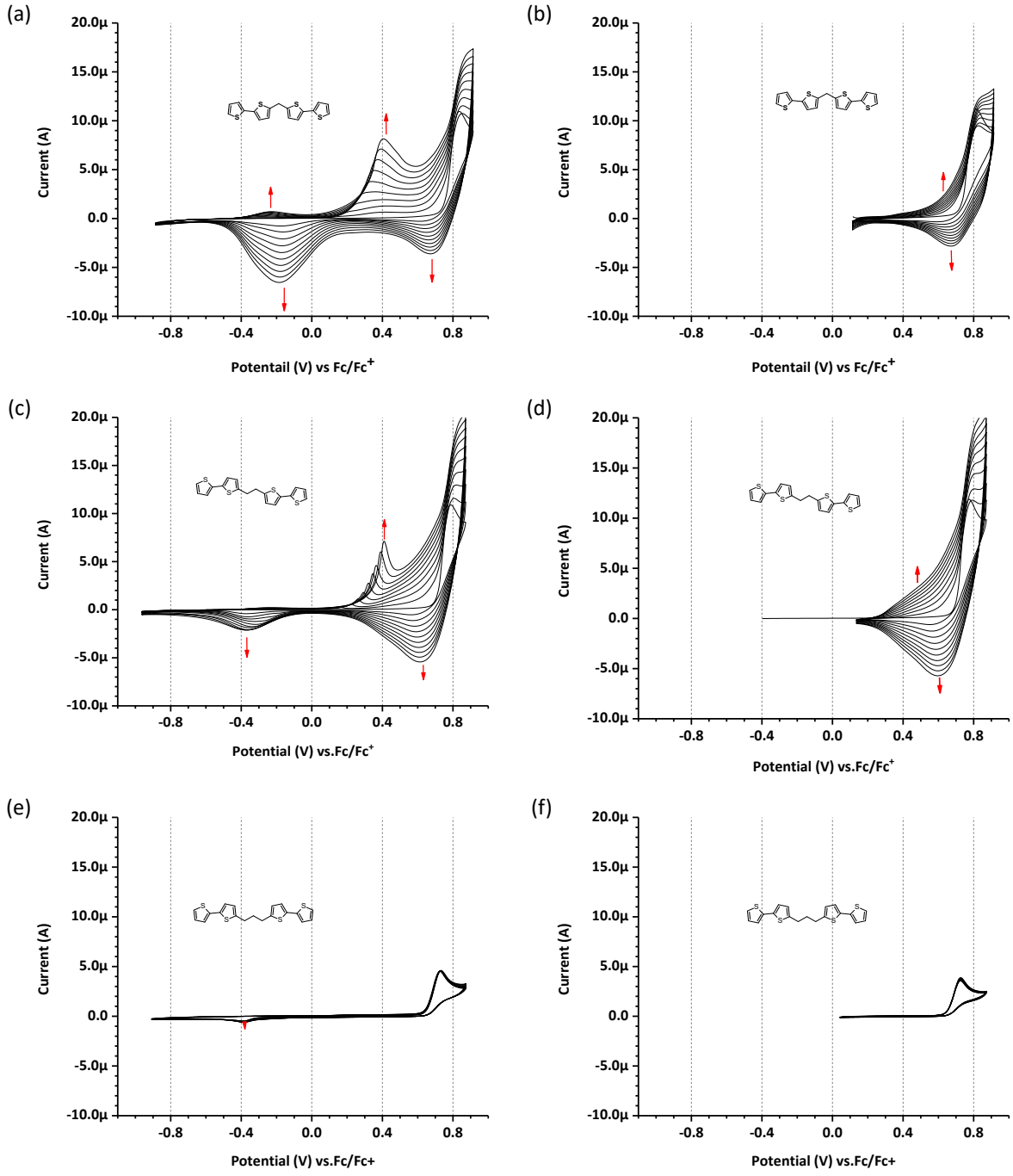

Figure 5.27 Cyclic voltammograms recorded during the electropolymerization of quaterthiophene derivatives bearing methylene (1), ethylene (6), and propylene (7) π-conjugation break spacers in dichloromethane containing 0.1 M

Bu_4NPF_6 at a scan rate of 0.1 V s^{-1}. Panels (a), (c), and (e) correspond to wide potential ranges, while panels (b), (d), and (f) show the corresponding narrow potential ranges.

For compounds **1**, **6**, and **7** measurements were performed over both wide and narrow potential windows. The wide potential range includes the cathodic feature observed between approximately -0.6 V and 0.2 V vs Fc/Fc^+, while the narrow potential range excludes this region. For compound **1**, three anodic features are observed at ca. 0.20 V, 0.40 V, and 0.80 V vs Fc/Fc^+ during successive cycles recorded over the wide potential range (Figure 5.27 (a)). Upon successive cycling, the anodic peaks at ca. 0.40 V and 0.80 V increase progressively in current intensity. Two cathodic features are observed at ca. - 0.20 V and 0.60 V vs Fc/Fc^+. The cathodic peak at ca. 0.60 V also increases, whereas the feature at ca. -0.20 V remains observable within the applied potential range. When the applied potential is restricted to exclude the cathodic feature near - 0.20 V, the voltammograms recorded in the narrow potential range show the absence of the anodic feature at ca. 0.20 V vs Fc/Fc^+, persistence and growth of the anodic feature at ca. 0.80 V vs Fc/Fc^+ and a corresponding cathodic feature at ca. 0.60V vs Fc/Fc^+(Figure 5.27 (b)).

For compound **6**, voltammograms recorded over the wide potential range (Figure 5.27 (c)) display anodic peak at ca.0.80 V vs Fc/Fc^+ and an additional anodic feature at ca. 0.40 V vs Fc/Fc^+. During successive cycles, the anodic feature at ca. 0.40 V shifts slightly toward more positive potentials and increases in current. In the cathodic scan, two features are observed: one at ca. -0.4 V and the other at ca. 0.6 V vs Fc/Fc^+. With continued cycling, the cathodic feature near 0.60 V increases in intensity, while the feature near -0.40 V decreases. Under the narrow potential window (Figure 5.27(d)), the voltammograms show: a dominant anodic feature at ca. 0.80 V, a cathodic response at ca. 0.6 V, and an absence of the cathodic feature at ca. -0.4 V vs Fc/Fc^+. The progressive increase in current with cycling remains observable under these restricted conditions.

In contrast, compound **7** exhibits a markedly different behaviour. Over a wide potential range a single anodic feature is observed near ca. 0.75–0.80 V vs Fc/Fc^+ and cathodic response appears during the reverse scan (Figure 5.27(e)). No additional anodic or cathodic features emerge during successive cycles. The current response remains comparatively low, and only minor changes in peak intensity are observed upon repeated cycling. Voltammograms recorded over the narrow potential window (Figure 5.27(f)) display similar features to those observed in the wide range, without the appearance of additional peaks or significant evolution of the voltammetric profile.

5.4.4. Electrochemistry of electrogenerated polymer films

Electrochemical doping and dedoping of the electrogenerated polymer films were examined by cyclic voltammetry in monomer-free electrolyte solution. The corresponding voltammograms recorded for poly(**1**), poly(**6**), and poly(**7**) are shown in Figure 5.28 (a–f). For each polymer, measurements were performed over both wide and narrow potential windows.

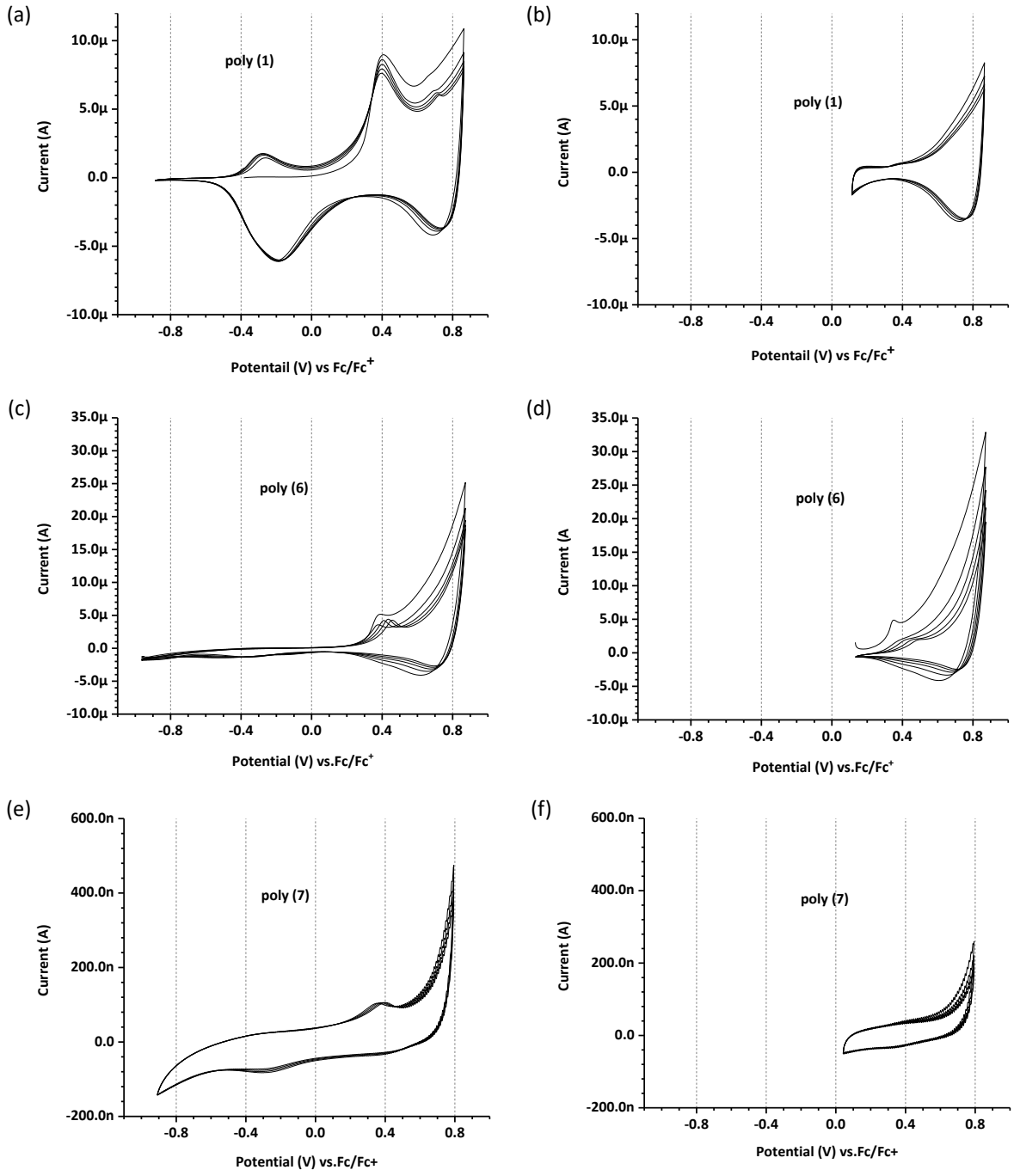

Figure 5.28 *Cyclic voltammograms recorded for electrochemically generated polymer films of poly (**1**), poly (**6**), and poly(**7**) in compound-free 0.1 M Bu_4NPF_6/dichloromethane at a scan rate of 0.1 V s^{-1}. Panels (a) and (b) correspond to poly (**1**), (c) and (d) to poly (**6**), and (e) and (f) to poly (**7**), recorded over wide and narrow potential windows, respectively.*

For poly**(1)**, voltammograms recorded over the wide potential range (Figure 5.28(a)) exhibit well-defined oxidation and reduction features that correspond to those observed during electropolymerization. These redox responses are retained during successive potential cycling, and the overall voltammetric shape remains consistent. When the potential window is restricted (Figure 5.28(b)), the lower-potential reduction feature is no longer observed, resulting in a simplified voltammetric response dominated by the higher-potential redox process.

For poly**(6)**, cyclic voltammograms recorded over the wide potential range (Figure 5.28(c)) display broader oxidation waves compared to poly(**1**), accompanied by corresponding reduction features at lower potentials. The overall current magnitude is greater than that observed for poly(**1**). Upon restricting the potential window (Figure 5.28(d)), the lower-potential reduction feature is absent, and the voltammetric response becomes more compact, with fewer distinguishable redox features.

In the case of poly**(7)**, voltammograms recorded over the wide potential range (Figure 5.28e) show a significantly lower current response compared to poly(**1**) and poly(**6**). When the potential range is restricted (Figure 5.28(f)), the voltammetric response is simplified, and only the higher-potential redox process is observed.

For poly(**6**) and poly(**7**), the reduction feature observed near -0.37 V vs Fc/Fc^{+} during electropolymerization is not detected in the compound-free electrolyte. Across all investigated polymer films, electrochemical doping and dedoping responses are observed in both wide and narrow potential ranges, with differences in current magnitude, peak definition, and number of redox features depending on polymer structure and applied potential window.

5.4.5. Spectroelectrochemistry of polymer products

The UV–Vis–NIR spectroelectrochemical spectra of poly (1), poly (6), and poly (7) are shown in Figures 5.29 (a–d), 5.30(a–d), and 5.31 (a–b), respectively. For poly(1), the spectroelectrochemical behaviour has been discussed previously in section 5.2.5 page 55 and is therefore not repeated here.

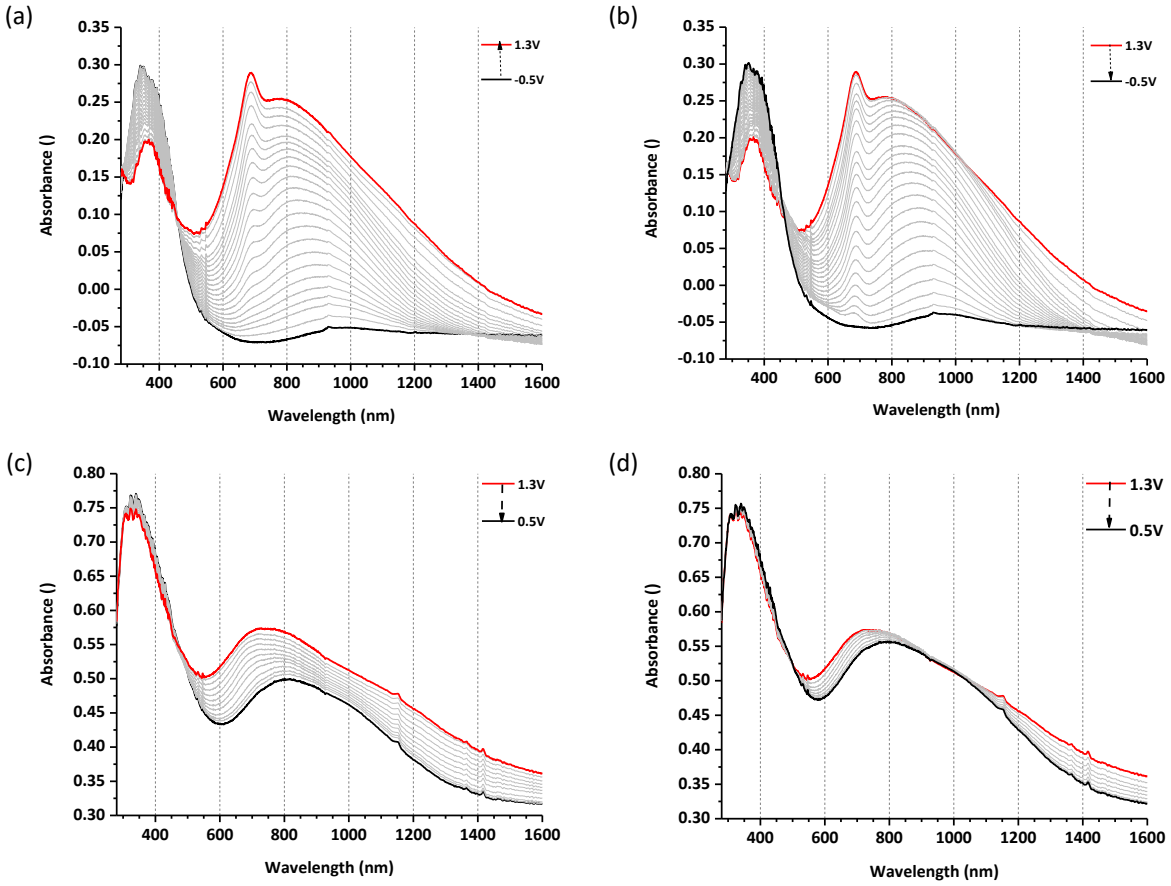

Figure 5.29 UV–Vis–NIR spectra recorded during high-speed spectroelectrochemical measurements of poly (1) films in neat 0.1 M Bu_4NPF_6 in dichloromethane. Spectra were acquired during electrochemical doping and dedoping over wide (a, b) and narrow (c, d) potential ranges.

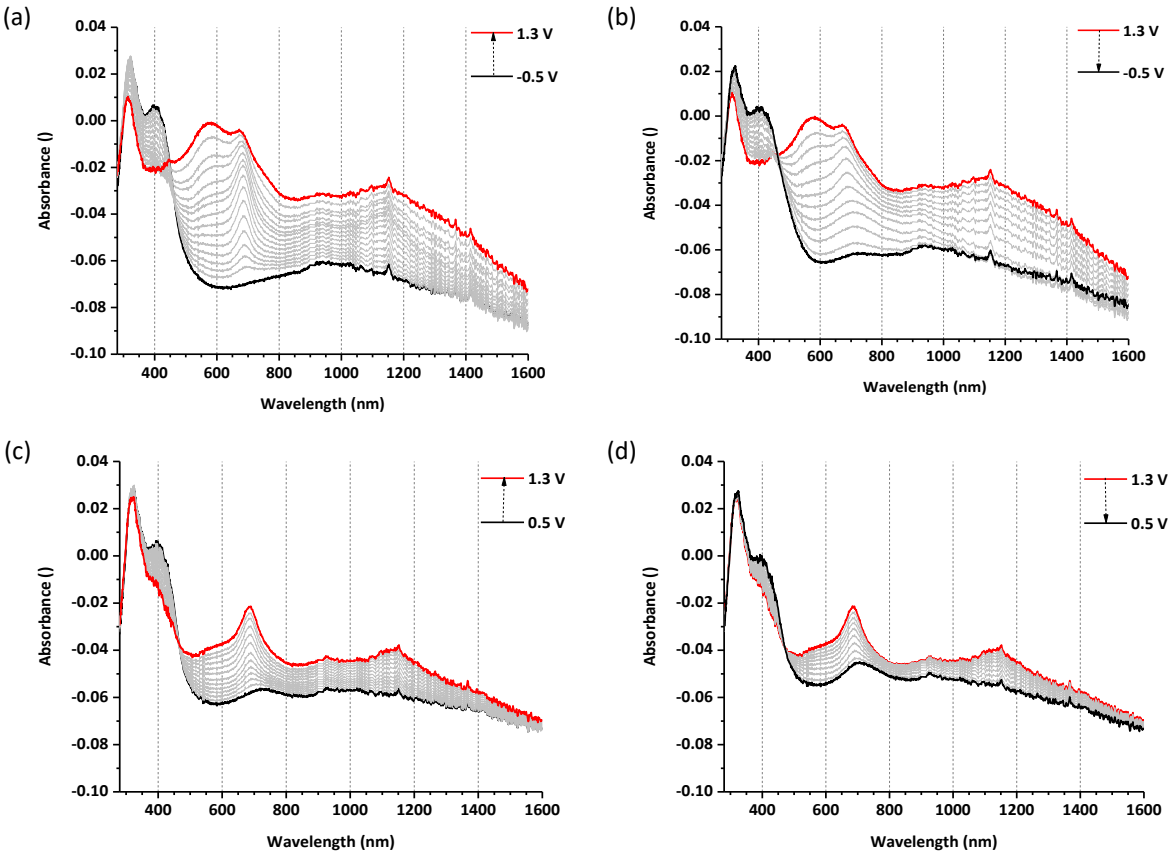

*Figure 5.30 UV–Vis–NIR spectra recorded during high-speed spectroelectrochemical measurements of poly(**6**) films in neat 0.1 M Bu_4NPF_6 in dichloromethane. Spectra were acquired during electrochemical doping and dedoping over wide (a, b) and narrow (c, d) potential ranges.*

For poly(6), spectra were recorded over both wide and narrow potential ranges. In its neutral state (black trace), poly(6) exhibits absorption bands at approximately 322 nm and 400 nm, together with a broad long wavelength extending from approximately 700 to 1000 nm, as shown in Figure 5.4.7 (a). Upon stepwise application of positive potentials (grey traces), the spectral changes occur progressively. A new absorption band develops in the visible region at approximately 580 nm and shifts slightly toward shorter wavelengths at higher applied potentials. Simultaneously, the broad band centred near 695 nm becomes sharper, decreases in intensity, and becomes more structured. At the highest applied potential (red trace), the band near 580 nm becomes the dominant spectral feature.

During the subsequent dedoping process (Figure 5.30(b)), the spectral profile gradually returns toward that of the neutral state, indicating restoration of the initial absorption features. Spectra recorded for poly(6) films prepared within a narrow potential window are presented in Figures 5.30 (c) and (d). Under these conditions, the absorption band near 695 nm appears sharper than in films prepared over the wide potential range. In contrast, the absorption feature observed near 580 nm in the wide-range experiment is not detected. During dedoping, the original spectral profile is again recovered.

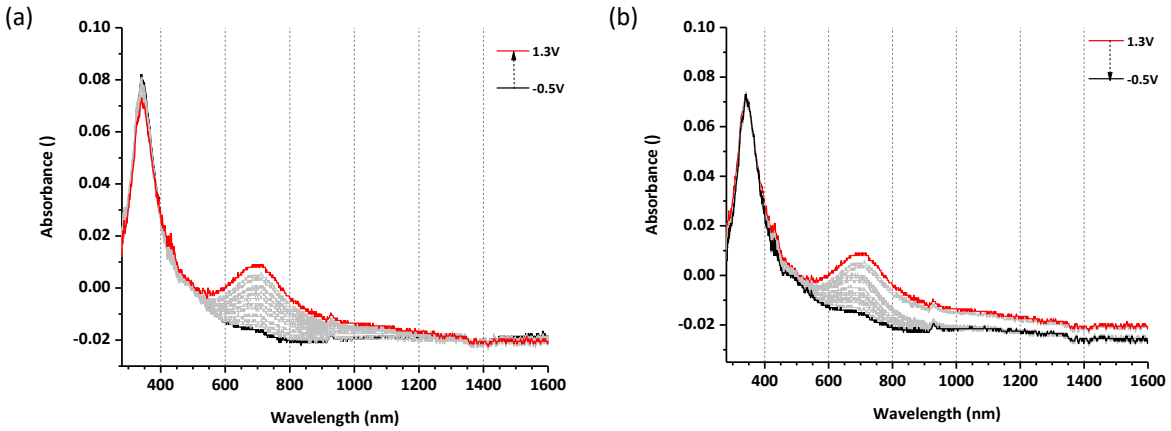

Figure 5.31 UV–Vis–NIR spectra recorded during high-speed spectroelectrochemical measurements of poly(7) films in neat 0.1 M Bu_4NPF_6 in dichloromethane. Spectra were acquired during electrochemical doping (a) and dedoping (b) over a wide potential range.

For poly(**7**), spectroelectrochemical measurements under narrow potential conditions could not be performed due to insufficient film deposition on the ITO electrode. Consequently, only spectra recorded over the wide potential range are presented (Figure 5.31). In the neutral state (black trace), poly(**7**) displays an absorption band at approximately 340 nm and a weaker feature near 680 nm (Figure 5.31(a)). Upon electrochemical oxidation, the absorption band in the UV region near 340 nm shows only minor changes in intensity and shape. In contrast, the longer-wavelength feature near 680 nm undergoes a gradual red shift, reaching approximately 700 nm at the highest applied potential (red trace). The spectral evolution in the visible–NIR region is more pronounced than in the UV region.

During the subsequent dedoping process (Figure 5.31(b)), the spectra return to the initial profile observed in the neutral state. In particular, the UV-region band remains essentially unchanged throughout the dedoping sequence, and the longer-wavelength feature recovers its original position and intensity.

5.5. UV-vis spectra, Electrochemical, and Spectroelectrochemical Properties of model compounds

This section presents the UV–Vis absorption, electrochemical, and spectroelectrochemical properties of a set of model compounds (A–D), shown in Figure 5.32. These compounds were investigated under conditions comparable to those used for the corresponding oligomeric and polymeric systems in the preceding sections.

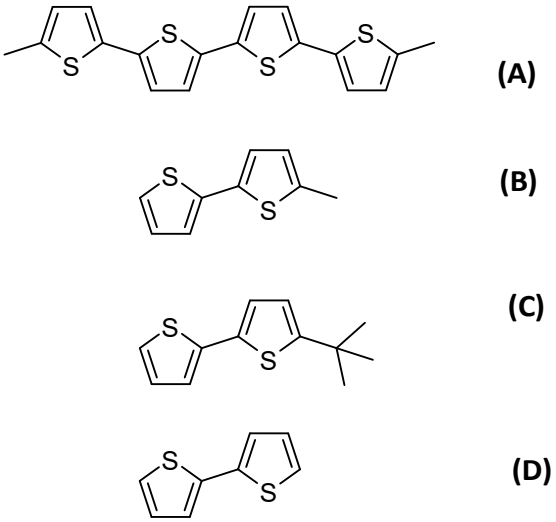

Figure 5.32 Chemical structures of model compounds A–D.

5.5.1. UV-vis spectra

The UV–Vis absorption spectra of model compounds A, B, C, and D recorded in dichloromethane are shown in Figure 5.33(a–d). All four model compounds display a single dominant absorption band in the UV–visible region.

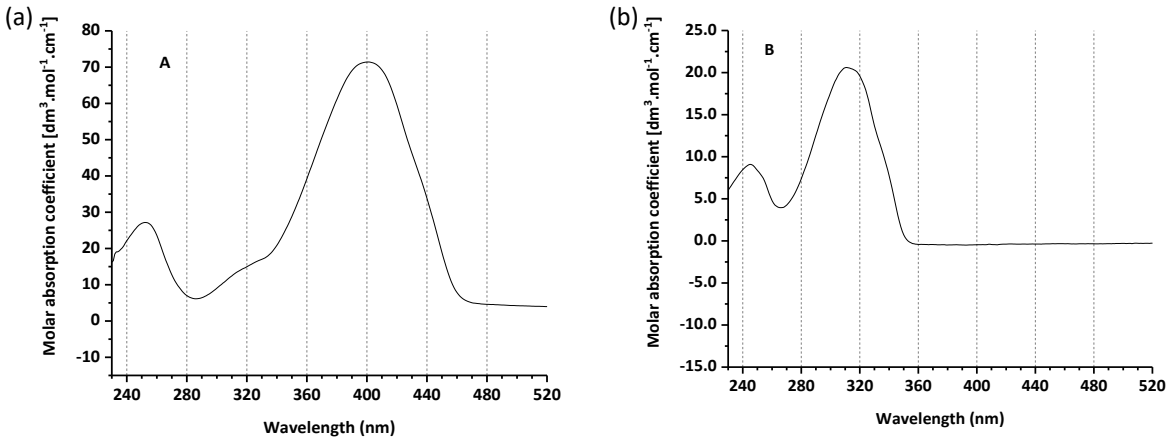

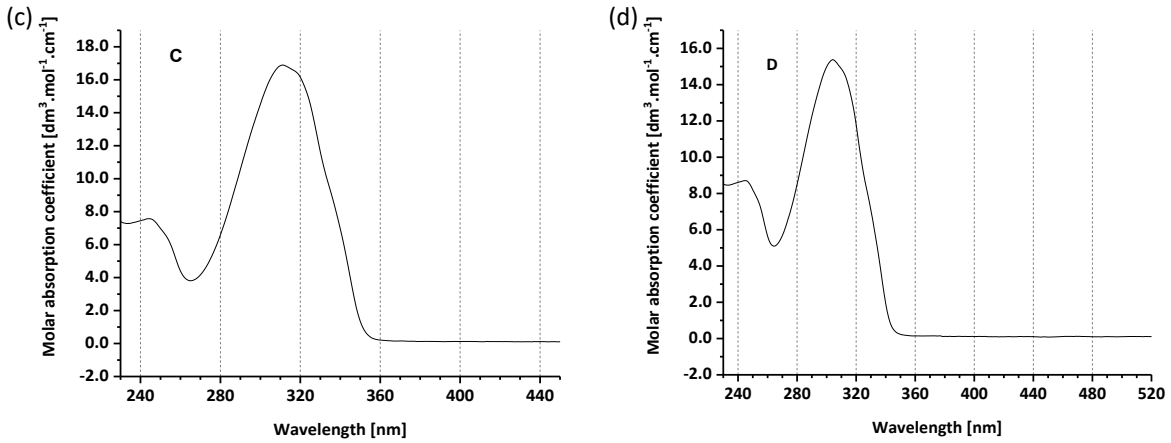

Figure 5.33 UV–Vis absorption spectra of model compounds A–D recorded in dichloromethane.

The absorption maxima (λ_{max}) and relative molar absorption coefficients (ε) extracted from these spectra are summarized in Table 5.5.1. Model compound A exhibits the most intense absorption, with a maximum at approximately 400 nm and the highest molar absorption coefficient among the series. In contrast, model compounds B, C, and D show absorption maxima at shorter wavelengths, centred around 305–312 nm, with comparatively lower absorption intensities. No additional absorption features are observed beyond the main band for any of the model compounds within the measured wavelength range.

Table 5.5.1 The relative molar absorption coefficient (ε), and absorption maxima ((λ_{max}) of modelcompounds A-D recorded in dichloromethane.

Compounds	**ε** [$dm^{-3}.mol^{-1}.cm^{-1}$]	$\boldsymbol{\lambda_{max}}$ [nm]
A	72	400
B	21	311
C	17	312
D	15	305

5.5.2. Electrochemical properties

The cyclic voltammograms of model compounds A, B, C, and D recorded over the anodic potential range are presented in Figure 5.34(a–d). Measurements were carried out in dichloromethane containing 0.1 M Bu_4NPF_6 at a scan rate of 0.1 V s^{-1}.

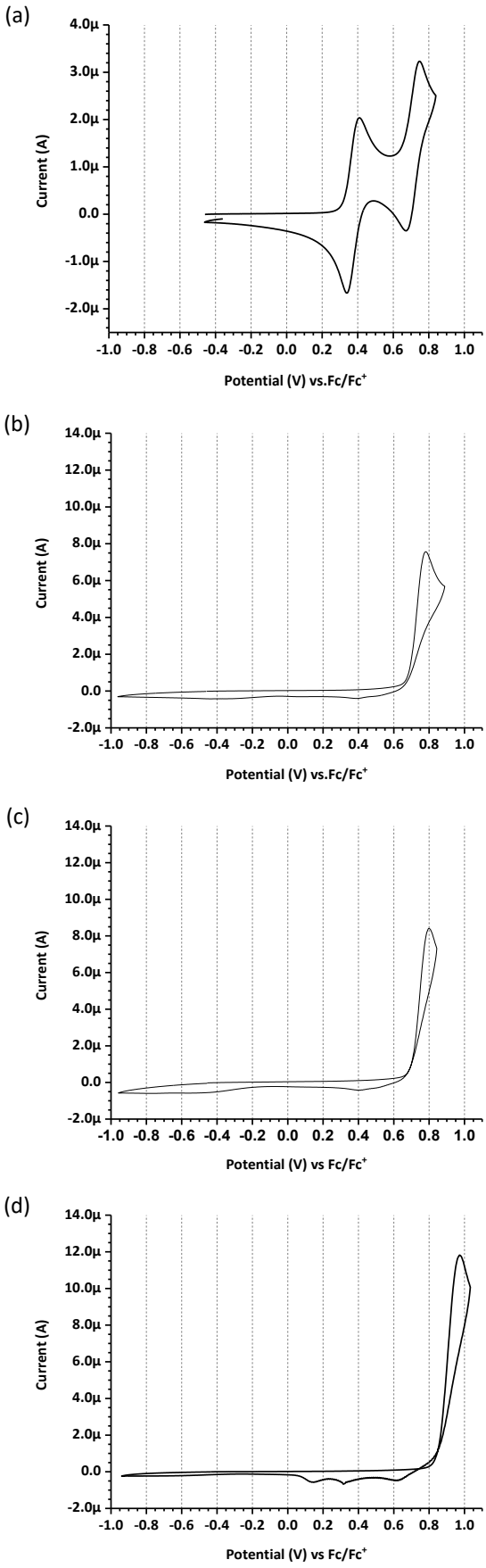

Figure 5.34 Cyclic voltammograms of the investigated model compounds (a) ***A****, (b)* ***B****, (c)* ***C*** *and (d)* ***D*** *were recorded in dichloromethane at 0.1 M Bu_4NPF_6 for the anodic potential range (scan rate, 0.1V/s).*

Model compound **A** exhibits two distinct anodic oxidation peaks located at approximately 0.40 V and 0.75 V vs Fc/Fc^+ in dichloromethane (Figure 5.34 (a)). Upon reversal of the potential scan, corresponding cathodic peaks are observed, indicating electrochemical reversibility within the investigated potential window. When the electrochemical measurements of model **A** are conducted in acetonitrile, the second anodic oxidation peak is not observed, and only a single oxidation process appears within the same potential range. In contrast, model compounds **B**, **C**, and **D** display single dominant anodic oxidation peaks at potentials above approximately 0.70 V vs Fc/Fc^+ (Figure 5.5.3 (b–d)). For these compounds, no corresponding reduction peaks are detected upon reversal of the potential scan, indicating irreversible electrochemical behaviour under the applied conditions. The current response returns close to the baseline after oxidation, and no additional redox features appear within the scanned potential range.

5.5.3. Successive oxidation

The electrochemical behaviour of model compounds **B**, **C**, and **D** during successive oxidative cycling was examined by cyclic voltammetry, as shown in Figure 5.35 (a–c). For all three compounds, repeated potential cycling results in a progressive increase in the anodic current response at higher potentials.

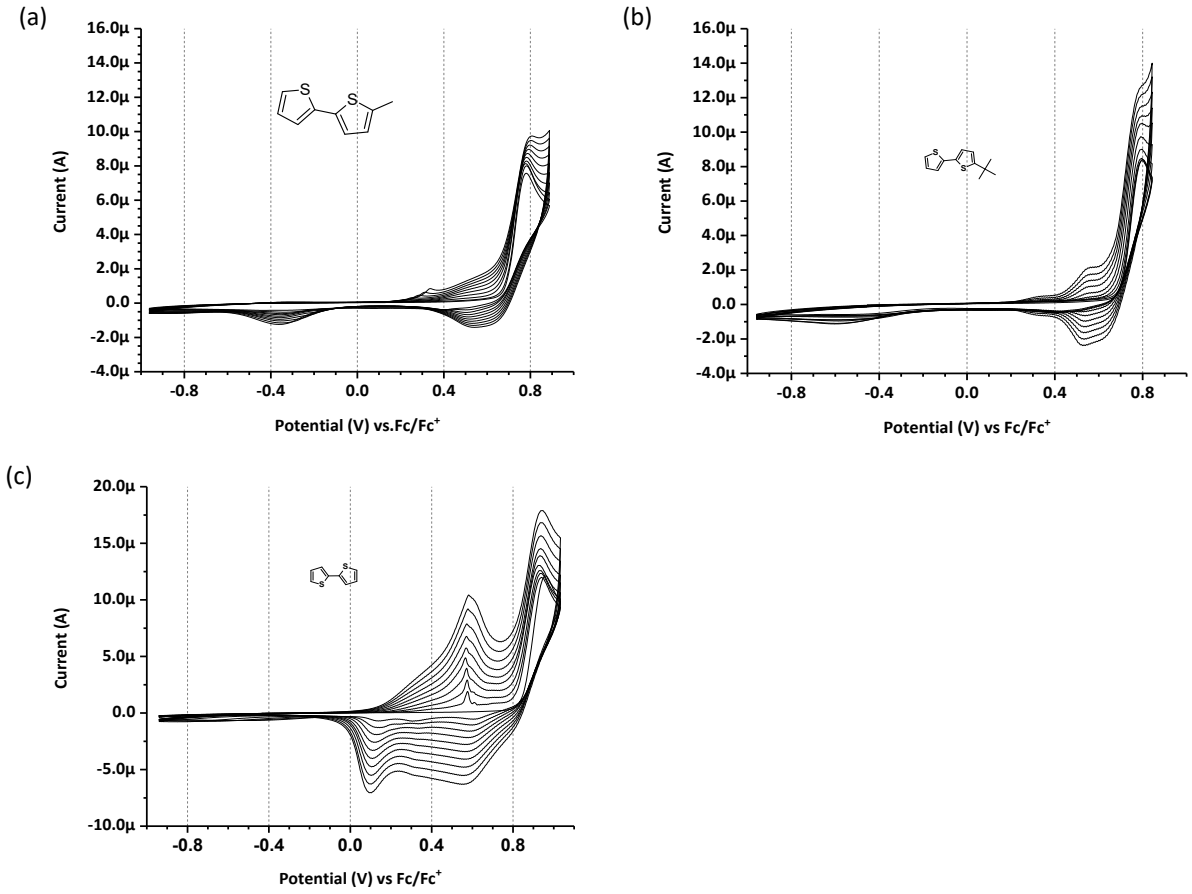

Figure 5.35 Cyclic voltammograms of successive oxidation of model compound, (a) **B***, (b)* **C***, and (c)* **D***, in 0.1M of Bu_4NPF_6 in dichloromethane at 0.1V/s, demonstrating the progressive accumulation of electroactive deposits during repetitive potential cycling.*

In the case of model **B** (Figure 5.35(a)), successive scans show a gradual increase in anodic current intensity accompanied by the emergence of additional redox features upon repeated cycling.

The current response grows predominantly at potentials above approximately 0.6 V vs Fc/Fc^+. Model compound **C** (Figure 5.35(b)) exhibits a more pronounced increase in anodic current with successive cycles. The voltammograms show the development of broad oxidation and reduction features that intensify during continued cycling, with the dominant anodic response observed near 0.8 V vs Fc/Fc^+. For model compound D (Figure 5.35(c)), successive oxidation leads to a marked increase in current response over repeated scans. The voltammograms display the gradual buildup of electroactive features across the anodic region, while the cathodic response becomes more defined with continued cycling.

Across all three model compounds, the voltammetric profiles evolve progressively with repetitive oxidation, reflecting the accumulation of electroactive material on the electrode surface during successive potential sweeps.

5.5.4. Electrochemistry of successive oxidation products

The electrochemical properties of the successive oxidation products of model compounds **B, C, and D** were investigated by cyclic voltammetry and are shown in Figure 5.36 (a–c).

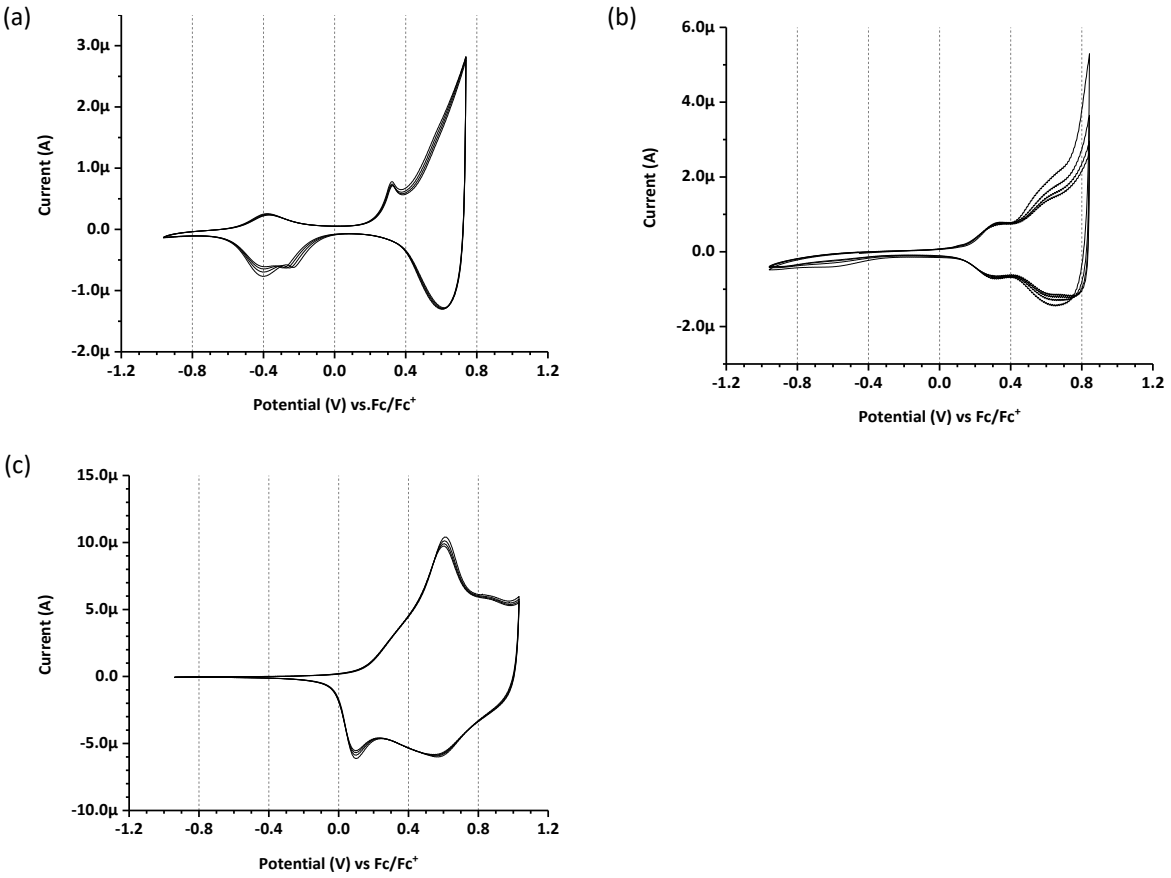

*Figure 5.36 A cyclic voltammogram of the investigated model compounds (a) **B**, (b) **C**, and (c) **D** in 0.1 M Bu_4NPF_6 in dichloromethane, with a scan rate of 0.1V/s.*

5.5.5. Spectroelectrochemical properties of model A

The UV–Vis–NIR spectra of model **A** are shown in Figure 5.37 (a–b). The spectra were recorded during the electrochemical doping–dedoping process in dichloromethane.

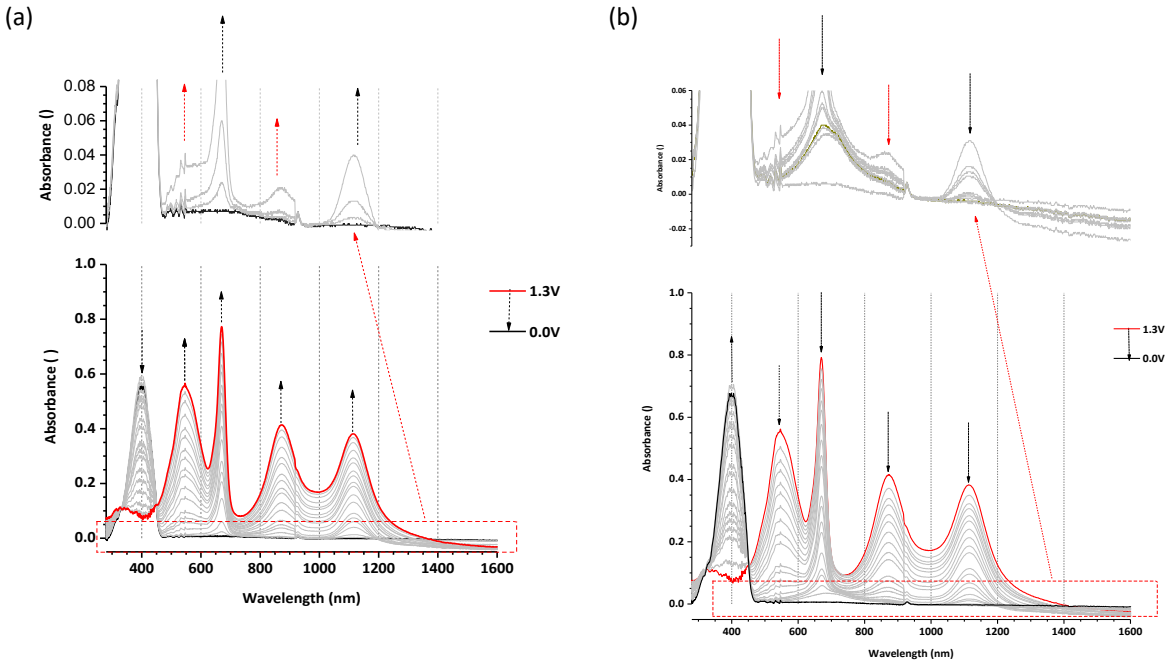

Figure 5.37 The UV-Vis-NIR spectra of model A

At low applied potentials, absorption bands appearing at approximately 650 nm and 1100 nm are attributed to the formation of radical cation species of the dimethyl quaterthiophene. As the applied potential increases, additional absorption features emerge at around 550 nm and 850 nm. These bands may be tentatively attributed to the formation of π-dimers or mixed-valence species, suggesting that increasing radical cation concentration promotes intermolecular electronic interactions. Upon reversal of the applied potential, the charge-induced absorption bands decrease and the original neutral-state spectrum is largely restored (Figure 5.37 (b)), indicating good spectroelectrochemical reversibility of model **A** under the applied experimental conditions.

6. Discussion

6.1. Introduction

This chapter discusses the spectroscopic, electrochemical, and spectroelectrochemical properties of the π-conjugation-interrupted oligothiophene systems investigated in this work. Emphasis is placed on how molecular architecture, including substitution at the sp^3-hybridized bridge, oligomer length, and alkylene spacer length, governs ground-state electronic structure, oxidation pathways, follow-up reactions, and the formation and stability of redox-generated charge-carriers in electrogenerated polymer films.

The discussion addresses features of π-conjuagtion disruption. First, the effectiveness of π-conjugation breaking is evaluated through analysis of the ground-state optical properties. Second, the electrochemical oxidation behaviour is examined, with specific focus on the first oxidation cycle, subsequent chemical transformations of oxidized species, and the stability of the resulting products. Third, spectroelectrochemical and EPR results are integrated to correlate optical transitions with the nature and evolution of redox-generated charge carriers. Throughout this chapter, interpretation is strictly grounded in the experimental observations presented in Chapter 5, without extrapolation beyond the measured data.

6.2. Effectiveness of π-Conjugation Breaking across the three Series

The effectiveness of π-conjugation breaking in symmetrically bridged oligothiophenes is evaluated by correlating systematic structural variations with the optical responses observed across three independent molecular series. Varying (i) substitution at the sp^3-hybridized bridge carbon, (ii) oligomer length at a fixed spacer, and (iii) alkylene spacer length at a fixed oligomer size, the extent of electronic communication between thiophene segments can be assessed and decoupled from secondary structural effects.

6.2.1. Effect of substitution at the sp^3 bridge (Compounds: 1, 2, 3)

In the first series, compounds **1**, **2** and **3** differ only in the degree of substitution at the sp^3-hybridized methine bridge connecting the thiophene segments. The UV–Vis absorption spectra (Figure 5.2) show that the π–π* absorption maximum remains centred at approximately 320 nm across the series. This confirms that the saturated carbon bridge effectively disrupts long-range π-conjugation along the molecular backbone, resulting in optical transitions predominantly localized on the thiophene segments. Although compound 2 exhibits a comparatively higher molar absorption coefficient, the closely clustered absorption maxima and optical band gaps summarized in Table 5.2.1 indicate that methyl substitution at the bridge does not significantly perturb the fundamental electronic structure of the conjugation-disrupted quaterthiophene framework.

Comparison with model compounds further supports this conclusion. Model compound **B** (methyl-bithiophene) and model compound **D** (α-bithiophene) exhibit absorption maxima at approximately 312 nm and 305 nm, respectively. The absorption maxima value of model D is consistent with the characteristic π–π* transitions of α-bithiophene oligomers reported elsewhere [77]. The close correspondence between these reference systems and compounds **1–3** indicates that electronic communication across the sp^3-hybridized bridge is virtually eliminated.

However, subtle differences in absorption onset and band shape suggest that substitution at the sp^3 centre modulates residual electronic interaction between thiophene units. Increased substitution reduces the availability of C–H sites and influences how charge density generated on the thiophene segments can interact across the conjugation break. Thus, conjugation breaking is effective but not absolute; rather, it is structurally tuneable.

A direct comparison between compound **1** and model compound **B** further illustrates this point (Figure 6.1). Had the methylene bridge completely interrupted conjugation, the absorption spectra would coincide. Instead, compound **1** exhibits a slight red shift relative to model **B**, indicating weak but measurable residual electronic communication across the sp^3 bridge. This suggests a limited through-space or σ*-mediated interaction between the two bithiophene arms. While subtle in the optical spectra, this residual coupling becomes more significant during electrochemical oxidation and electropolymerization.

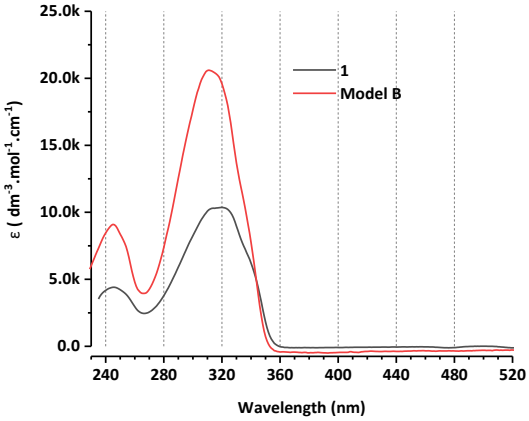

*Figure 6.1 absorption spectra of compound **1** and model **B** (methyl bithiophene).*

6.2.2. Effect of oligomer length at fixed spacer (Compounds: 4, 1, 5)

The second series isolates the influence of oligomer length by comparing methylene-bridged systems containing increasing numbers of thiophene units: compound **4** (bithiophene motif), compound **1** (quaterthiophene motif), and compound **5** (sexithiophene motif). The corresponding UV-Vis spectra are shown in Figure 5.18, and the derived parameters are summarized in Table 5.3.1

A systematic bathochromic shift of the absorption maximum is observed with increasing thiophene count. This reflects a progressive decrease in transition energy consistent with the well-established dependence of optical band gap on oligothiophene length [137]. This red shift occurs despite the presence of methylene spacers that interrupt through-bond π-conjugation.

Comparison with fully conjugated oligothiophenes [138] (thiophene, bithiophene, terthiophene, quaterthiophene, and sexithiophene exhibit absorption maxima at approximately 231 nm, 302 nm, 350 nm, 391 nm, and 429 nm respectively), demonstrates that the conjugation-broken analogues remain significantly blue-shifted relative to fully conjugated systems of comparable thiophene count. This confirms that the methylene spacer effectively suppresses extended π-delocalization.

However, the conjugation-broken systems do not behave as isolated thiophene subunits. Each broken oligomer absorbs at longer wavelength than its corresponding single thiophene segment (e.g., compound **1** vs bithiophene; compound **5** vs terthiophene) [138]. This indicates residual electronic communication between thiophene segments, likely arising from through-space interactions or partial

orbital overlap. The magnitude of this residual coupling increases with oligomer length, suggesting that larger π-systems facilitate partial inter-segment interaction even in the presence of a saturated bridge.

Thus, oligomer length modulates the degree of residual coupling despite broken through-bond conjugation.

6.2.3. Effect of spacer length at fixed oligomer (Compounds: 1, 6, 7)

The third series evaluates the effect of spacer length by comparing symmetrically broken quaterthiophenes bridged by methylene (1), ethylene (6), and propylene (7). The UV–Vis spectra are presented in Figure 5.25, and the corresponding parameters are summarized in Table 5.4.1.

All three compounds exhibit closely similar absorption maxima, with only minor variations in λ_{max} and optical band gap across the series. This indicates that increasing the alkylene spacer length imparts no additional electronic communication disruption between the thiophene units. Once π-conjugation is interrupted by a saturated bridge, further extension of the spacer primarily reinforces electronic isolation.

Comparison with 2,2'-bithiophene (λ_{max} ≈ 302 nm) [138] confirms that the conjugation-broken quaterthiophenes retain extended thiophene segments, yet the similarity of absorption energies across compounds **1**, **6**, and **7** demonstrates that spacer elongation does not promote delocalization.

Notably, compound **6** exhibits a higher molar absorption coefficient compared to compounds **1** and **7**, as summarized in Table 5.4.1. This trend is consistent with parity effects reported for conjugation-interrupted systems, where even-numbered spacers may favour more symmetric geometrical arrangements of adjacent conjugated units, enhancing transition probability without significantly altering conjugation length [109]. Importantly, this effect influences oscillator strength rather than absorption energy, reinforcing the conclusion that spacer length primarily modulates electronic coupling efficiency rather than re-establishing long-range conjugation.

6.2.4. Summary

Taken together, the systematic optical trends observed in Figure 5.2 (Series 1), Figure 5.18 (Series 2), and Figure 5.25 (Series 3), together with the quantitative data summarized in Tables 5.2.1, 5.3.1, and 5.4.1, demonstrate that π-conjugation breaking in symmetrically bridged oligothiophenes is effective, yet, to some minor degree, structurally tuneable. Substitution at the sp^3 bridge fine-tunes residual electronic communication and stabilizes the electronic framework, increasing oligomer length enhances partial coupling across a fixed conjugation break, and increasing alkylene spacer length reinforces electronic isolation while modulating transition probability through geometric effects.

These structural parameters collectively define the ground-state electronic architecture of the systems and establish the foundation for understanding their oxidation pathways, follow-up reactions, and stability of redox-generated charge carriers in electrogenerated polymer films, which are addressed in the subsequent sections of this chapter.

6.3. Electrochemical oxidation: structure-redox relationships.

The first oxidation cycle provides direct insight into how structural modification governs the redox behaviour of π-conjugation-interrupted oligothiophenes. Across all three structural series investigated in this work, oxidation is initiated on the thiophene-based π-system rather than at the sp^3-hybridized bridge, consistent with the localized nature of the π–π* transitions observed in the UV–Vis

spectra (Figures 5.2, 5.18, and 5.25), confirming that the saturated carbon functions as an electronic modulator rather than a redox-active centre. The first-cycle voltammetric responses presented in Chapter 5, therefore, reflect intrinsic structure–redox relationships prior to the follow-up chemical processes of the oxidised species.

Compounds **1–3**, which differ only in the degree of alkyl substitution at the sp^3-hybridized methylene bridge, exhibit a clear structure–property relationship in their first oxidation behaviour. As shown in Table 5.2.3 and the first-cycle voltammograms (Figure 5.3(a–c)), increasing alkyl substitution progressively lowers the oxidation onset potential while raising the HOMO energy level. This trend is consistent with the electron-donating character of methyl substituents, which increase electron density on the quaterthiophene backbone and thereby facilitate oxidation at lower potentials. Importantly, the anodic peak potentials remain nearly constant across the series. This behaviour supports the interpretation that oxidation remains localized on the quaterthiophene segments rather than involving the saturated bridge. Thus, alkyl substitution primarily modulates the thermodynamic accessibility of oxidation without altering the fundamental site of charge generation.

The influence of conjugated segment length is illustrated by compounds **4, 1,** and **5**, which contain symmetrically methylene-bridged bithiophene, quaterthiophene, and sexithiophene units, respectively. As shown in Figure 5.19 (a–c) and summarized in Table 5.3.2, both oxidation onset and anodic peak potentials decrease systematically with increasing thiophene number. This behaviour is consistent with established trends in oligothiophene systems, where extension of conjugation stabilizes the radical cation and lowers oxidation potential until the effective conjugation length is approached [139][140].

A near-linear dependence of anodic peak potential on the inverse number of thiophene units (Figure 6.2) supports this interpretation. Increasing oligomer length enhances charge delocalization over a larger π-framework, reducing the energetic cost of oxidation.

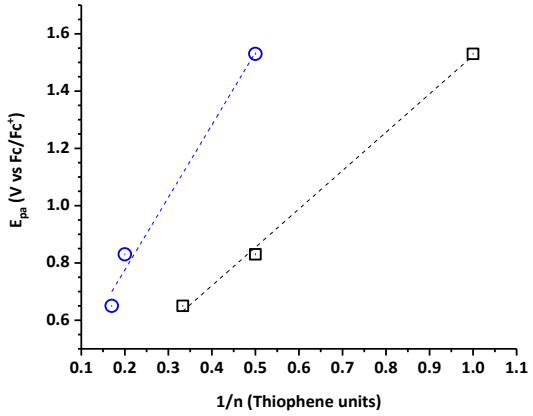

Figure 6.2 Anodic oxidation peak potential vs number of thiophene units (total and conjugation-broken)

Compound **4** exhibits the highest oxidation potential, consistent with limited delocalization. Compound **1** shows intermediate behaviour. Compound **5** undergoes oxidation at the lowest potential, reflecting its highest HOMO level. However, its anodic response is broader and less intense, which is attributable not only to increased conformational flexibility but also to its limited solubility in dichloromethane, reducing the effective electroactive concentration.

Thus, increasing conjugation length thermodynamically favours oxidation, but the electrochemical response remains sensitive to solubility and molecular organization.

Further structural control is provided by varying the alkylene spacer length while maintaining a constant quaterthiophene segment (compounds 1, 6 and 7). In this series, a gradual lowering of oxidation onset potential is observed as the spacer is extended from methylene to ethylene and propylene (Table 5.4.2 and Figure 5.26). The calculated HOMO energies increase slightly across the series, indicating that spacer elongation subtly modifies the electronic environment of the conjugated segments. The observed decrease in oxidation potential may arise from greater inductive effect of a longer alkylene chain, but also reduced steric congestion and diminished electronic repulsion between adjacent bithiophene units as the spacer length increases. However, the peak current response decreases progressively, particularly for compound 7. This reduced electrochemical response might originate from weakened electronic communication between conjugated segments and increased conformational flexibility introduced by the longer saturated spacer. Thus, while oxidation becomes energetically more accessible, electronic coupling between redox-active units becomes less efficient.

The reduced current response may arise from weakened inter-unit electronic communication and increased conformational disorder, which disrupts intramolecular charge propagation. As commonly observed in conjugation-broken systems, enhanced solubility associated with longer alkyl spacers often comes at the expense of charge-transport performance, as interruptions in conjugation impede continuous charge-transfer pathways [49].

6.3.1. Summary

Taken together, the first oxidation cycle across all three series demonstrates that oxidation is consistently thiophene-centred and that the sp^3-hybridized bridge acts as an electronic regulator rather than a charge-hosting site. Alkyl substitution at the bridge modulates oxidation energetics through inductive effects, increasing oligomer length enhances radical cation delocalization and lowers oxidation potential, and extension of the alkylene spacer lowers oxidation energy while simultaneously reducing effective electronic communication. These structure–redox relationships define the energetic landscape upon which subsequent chemical follow-up reactions and doping–dedoping behaviour occur, and they establish the mechanistic foundation for the transformations discussed in the following section.

6.4. Follow-up reactions of electrochemical oxidation

The irreversible oxidation behaviour discussed in Section 6.3 indicates that the initially generated radical cations do not persist as long-lived electroactive species but instead undergo rapid chemical follow-up reactions. These post-oxidation processes are most clearly manifested during repetitive cycling experiments, where new redox features emerge and progressive accumulation of electroactive material on the electrode surface takes place. Comparison of experiments conducted in a wide and in a narrow potential window (Figures 5.4, 5.20, and 5.27) provides direct insight into how molecular structure governs the fate of oxidized intermediates and determines the efficiency of film growth at the surface of the electrode.

6.4.1. Influence of bridge substitution on follow-up reactions (Compounds 1–3)

The influence of alkyl substitution at the sp^3-hybridized methylene bridge is clearly manifested in the electropolymerization behaviour of compounds **1**–**3**, as shown in Figure 5.4. For compounds **1** and **2**, repetitive cycling over a wide potential window results in the gradual development of additional

redox features in the negative potential region (approximately −0.2 V and −0.3 V vs Fc/Fc^+, respectively), accompanied by progressive current growth (Figures 5.4(a) and 5.4 (c). While the precise chemical nature of these follow-up pathways cannot be determined solely from cyclic voltammetry, the observed behaviour is consistent with secondary transformations of oxidized intermediates, potentially involving either deprotonation at the sp^3-hybridized carbon bridge or the formation of transient σ-dimer species arising from coupling of oxidized intermediates. The increasing intensity of these features with successive scans indicates accumulation of electroactive material at the electrode surface.

Importantly, when the potential window is restricted and the cathodic region associated with these features is excluded, the development of polymer-like redox waves is significantly slower. This comparison demonstrates that follow-up reactions accessed within the broader electrochemical window contribute directly to the redox chemistry of electroactive species.

In contrast, compound **3**, in which the sp^3 bridge is fully substituted and lacks abstractable hydrogen atoms, exhibits more rapid development of stable redox waves and film growth (Figure 5.4 (e)). The absence of reduction features around 0 V observed for compounds **1** and **2** suggests that processes taking place there are suppressed. These results indicate that increasing substitution at the bridge modifies the reactivity of oxidized intermediates and can favour more direct progression toward film-forming pathways.

Thus, bridge substitution governs the chemical fate of radical cations after the first oxidation event and modulates the efficiency of subsequent film growth.

6.4.2. Influence of thiophene chain length on follow-up reactions (Compounds 4, 1, 5)

The follow-up electrochemical behaviour of compounds 4, 1, and 5, as shown in Figures 5.20 a-c and 5.3.4, reveals a clear dependence on thiophene chain length. Although oxidation onset potentials decrease systematically from compound **4**,**1** to **5** (Table 5.3.2), the effectiveness of oxidation follow-up reactions does not increase straightforwardly.

For compound **4**, a symmetrically methylene-bridged bithiophene, follow-up reactions after oxidation are limited and highly localized. As shown in Figure 5.20 (a), repeated potential cycling within the applied potential range results only in a slow evolution of the voltammetric response, which becomes evident primarily upon magnification of a narrow anodic region highlighted in the inset graph. This behaviour indicates gradual and incipient deposition of an electroactive film rather than sustained polymer growth. Outside this restricted potential region, the voltammetric response remains largely unchanged over successive scans, demonstrating that follow-up reactions of the oxidized species are confined to a narrow electrochemical window. The short conjugation length of compound **4** limits radical cation delocalization and reduces the probability of productive σ-coupling events, resulting in weak and kinetically constrained film formation.

Compound **1**, the methylene-bridged quaterthiophene, exhibits markedly enhanced current growth and development of well-defined redox features during repetitive cycling (Figure 5.20(b–c)). In this case, radical cations appear sufficiently stabilized and delocalized to support efficient intermolecular coupling and anticipated polymer chain propagation under both wide and narrow potential conditions.

Interestingly, compound **5**, the methylene-bridged sexithiophene, although oxidized at significantly lower potential, shows comparatively sluggish film growth (Figure 5.20(d–e)). The

voltammetric response is characterized by broader features and lower peak currents. Limited solubility in dichloromethane, as noted in Chapter 5, further reduces effective charge transport and radical–radical encounters at the electrode surface. Importantly, these results demonstrate that ease of oxidation alone does not determine polymerization efficiency. Although compound **5** is thermodynamically easier to oxidize, efficient follow-up chemistry requires a balance between radical stabilization, intermolecular encounter probability (concentration of active species), and adequate charge transport. An intermediate conjugation length, as in compound **1**, appears to provide the most favourable conditions for sustained film growth.

6.4.3. Influence of alkylene spacer length on follow-up reactions (Compounds 1, 6, 7)

Systematic variation of alkylene spacer length (Figure 5.27) further clarifies the structural control of follow-up reactions. In this series, the quaterthiophene backbone is fixed, and only the spacer length increases from methylene (**1**) through ethylene (**6**) to propylene (**7**).

For compound **1**, which contains a methylene spacer, repeated potential cycling over a wide potential window results in a steady increase in both anodic and cathodic currents, indicating efficient accumulation of the electroactive material on the electrode surface (Figure 5.27 (a). Well-defined redox features develop progressively with cycling, consistent with effective follow-up reactions of the oxidized species and sustained polymer chain propagation. Even under narrow potential conditions, compound **1** exhibits continued growth of polymer-related redox waves (Figure 5.27 (b)), demonstrating that short conjugation-breaking spacers preserve sufficient electronic communication to support anticipated electropolymerization.

Compound **6** exhibits slower current evolution and broader redox waves (Figure 5.27 (c–d). The reduced current densities observed during repetitive scans indicate diminished radical coupling efficiency. Extension of the spacer weakens electronic communication between conjugated segments and likely reduces the probability of productive intermolecular encounters.

For compound **7**, the longest spacer, current responses remain small and largely unchanged over successive cycles (Figure 5.27(e–f)). Film growth is minimal, and polymer-related redox features are weak. These observations indicate that, for some reason, extending alkylene spacers suppresses follow-up reactions required for sustained electropolymerization.

Comparison of potential cycling in wide and narrow potential windows further highlights the critical role of spacer length in governing follow-up chemistry. While compounds **1** and **6** retain some capacity for polymer growth under restricted potential conditions, compound **7** shows a negligible response, indicating that extended alkylene spacers strongly suppress the post-oxidation reactions necessary for polymer formation. These results demonstrate that increasing spacer length progressively shifts the balance from efficient radical coupling toward charge localization and kinetic inhibition.

Overall, the Series **3** results establish alkylene spacer length as a decisive parameter controlling follow-up reactions after oxidation. Short spacers facilitate inter-unit electronic communication and promote effective polymer growth, whereas longer spacers introduce conformational flexibility and electronic decoupling that impede charge transport and suppress the anticipated electropolymerization.

6.4.4. Summary

The results presented in Figures 5.4, 5.20, and 5.27 collectively demonstrate that follow-up reactions after electrochemical oxidation in conjugation-broken oligothiophenes are structurally controlled. Bridge substitution (**1**–**2**–**3**) modulates the stability and reactivity of oxidized intermediates. Oligomer length (**4**–**1**–**5**) determines the degree of radical delocalization and establishes an optimal conjugation window for polymer growth. Spacer length (**1**–**6**–**7**) regulates inter-unit electronic coupling and progressively suppresses productive radical coupling with increasing alkylene length.

Together, these observations support a clear structure–reactivity relationship in which efficient electropolymerization requires simultaneous optimization of conjugation length, bridge substitution, and spacer architecture. This mechanistic framework provides the basis for understanding the subsequent doping–dedoping behaviour and charge-carrier characteristics discussed in the following section.

6.5. Doping-dedoping behaviour of follow-up products

The electrochemical and optical behaviour of the electrogenerated follow-up products provides direct insight into the stability and reversibility of oxidized species formed after electrochemical coupling. By correlating cyclic voltammetry and UV–Vis–NIR spectroelectrochemical data presented in Chapter 5, a unified structure–reactivity relationship can be established for the electroactive films.

6.5.1. Influence of bridge substitution (poly (1)-poly (3))

The cyclic voltammograms of poly(1), poly(2), and poly(3) recorded in monomer-free electrolyte (Figure 5.21) demonstrate that all three films undergo electrochemical doping and dedoping within the investigated potential ranges. However, the degree of stability differs across the series.

Poly(1) and poly(2) exhibit defined anodic and cathodic waves, but gradual changes in peak intensity and profile occur under extended potential cycling, particularly when wide potential windows are applied. When the potential window is restricted (Figure 5.2.5(b) and (d)), the voltammetric response of both poly (**1**) and poly (**2**) becomes more stable, and changes in peak shape are less pronounced. This comparison demonstrates that redox processes accessed at lower or more extreme potentials contribute significantly to the evolution of the electrochemical response across a wide range of conditions.

Poly(**3**) shows the most stable and reproducible redox behaviour. Within the optimized potential window, the anodic and cathodic waves remain well defined and consistent over successive cycles, indicating reversible insertion and removal of charge (Figure 5.5(e)).

The optical responses mirror these electrochemical trends. For poly(**1**) and poly(**2**), oxidation leads to bleaching of the neutral π–π* absorption bands and development of broad visible–near-infrared absorption features (Figures 5.6 and 5.8). The extent of these spectral changes depends on the applied potential window. Under restricted conditions, the spectral profiles are more fully restored during dedoping.

Poly(**3**) exhibits a distinct optical evolution characterized by the emergence of an absorption band near 680 nm during the initial stages of oxidation, followed by extension into the near-infrared region at higher potentials (Figure 5.9). Upon reduction within the stability window, the neutral-state spectrum is largely recovered. The close correspondence between stable voltammetric profiles and

reversible spectral modulation indicates that full substitution at the sp^3 bridge promotes controlled and reversible charge accommodation.

6.5.2. Influence of thiophene chain length (Poly (4), Poly (1), Poly (5))

The effect of conjugation length is evident in both electrochemical and optical behaviour. Poly (4), derived from the shortest oligomer, shows weak and unstable voltammetric features (Figure 5.21a). Successive scans reveal noticeable variations in current response. Spectroelectrochemical measurements could not be performed due to limited film stability, consistent with its restricted electrochemical performance.

Poly(1) displays well-defined and reproducible redox waves (Figure 5.21b–c), accompanied by pronounced optical modulation during doping (Figure 5.22). Oxidation results in bleaching of the UV absorption and growth of broad visible–NIR bands, which are largely reversed upon dedoping. Poly(5) exhibits redox activity (Figure 5.21d–e), but the current magnitude is lower than that of poly(1), and the voltammetric features are broader. Spectroelectrochemical data (Figure 5.23) show development of a broad absorption band between approximately 600 and 1400 nm during oxidation; however, the overall spectral modulation is less intense than in poly (1). These observations indicate that increasing thiophene chain length beyond the quaterthiophene framework does not enhance reversible electrochemical response in the electrogenerated film. These features may arise from the combined effects of conjugation interruption, increased conformational flexibility, and the poor solubility of the precursor monomer, as established during the electropolymerization studies.

6.5.3. Influence of spacer length (Poly(1), Poly(6), Poly(7))

Systematic variation of alkylene spacer length further clarifies the structural control of doping–dedoping behaviour (Figure 5.28). Poly(1), containing a methylene spacer, exhibits microampere-scale current responses and well-defined redox waves. Correspondingly, spectroelectrochemical measurements (Figure 5.29) show clear optical modulation during oxidation, including development of visible and near-infrared absorption bands.

Poly(6), incorporating an ethylene spacer, displays reduced current magnitude and broader voltammetric features relative to poly(1) (Figure 5.28c–d). Spectral changes during oxidation (Figure 5.30) include emergence of bands near 580 nm and 695 nm; however, the overall intensity of optical modulation is lower than in poly(1). The decrease in electrochemical and optical response indicates diminished efficiency of charge accommodation as spacer length increases.

Poly(7), bearing the longest propylene spacer, exhibits nanoampere-scale current responses (Figure 5.28e–f). The redox features are weak and less pronounced. Consistently, spectroelectrochemical measurements (Figure 5.31) reveal moderate and localised spectral evolution during oxidation. The UV-region absorption remains largely unchanged, and only modest shifts in the visible region are observed. The limited optical response parallels the weak electrochemical activity.

6.5.4. General structure–property relationships

Across all three series, the electrochemical and optical data demonstrate consistent trends governed by molecular architecture: Increasing substitution at the sp^3 bridge improves stability and reversibility of redox processes, an intermediate thiophene chain length (poly(**1**)) provides the most

balanced electrochemical and optical response and increasing alkylene spacer length progressively reduces current magnitude and optical modulation.

The cyclic voltammetry data establish the magnitude and reversibility of electrochemical doping, while the UV–Vis–NIR measurements confirm the associated formation and removal of oxidized species. In each case, systems exhibiting stable voltammetric behaviour show corresponding reversible spectral changes, whereas films with weak or unstable electrochemical responses display limited optical evolution.

6.6. Charge carrier evolution and electrochemical stability of poly (3).

The combined UV–Vis–NIR spectroelectrochemical (Figure 5.9), EPR spectroelectrochemical (Figures 5.10 and 5.11), and cyclic voltammetry (Figures 5.12, 5.14, and 5.16) provide a comprehensive description of the charge-carrier evolution and electrochemical stability of poly(3). The integration of these complementary techniques enables direct correlation between optical transitions, spin population, and electrochemical response.

In the neutral state, poly(3) exhibits no detectable EPR signal (Figure 5.10), confirming the absence of paramagnetic species prior to oxidation. Upon electrochemical oxidation, a pronounced absorption band appears at approximately 670–690 nm, together with a broad near-infrared absorption extending beyond 1500 nm (Figure 5.9(a)). Concurrently, the EPR spin concentration increases sharply, with onset near 0.7 V and reaches a maximum close to 1.0 V, as shown in Figure 5.10 (a) and quantified in Figure 5.11 9a). The close correlation between the growth of visible/NIR absorption bands (Figure 5.9 9(a)), maximum spin concentration determined by double integration of the EPR spectra (Figure 5.11), and peak anodic current response in cyclic voltammetry (Figure 5.12) confirms that the initial oxidation regime is dominated by the formation of spin-active radical cations (polarons) localized on the thiophene segments of the backbone. The initial spin growth and linewidth narrowing below 1.0 V are consistent with thiophene radical cation formation and exchange interactions reported for oligothiophenes under electrochemical oxidation [141].

When the applied potential exceeds approximately 1.0 V, divergence between optical and spin responses becomes evident. Although the near-infrared absorption continues to intensify and broaden toward longer wavelengths (Figure 5.9), the EPR spin concentration decreases progressively (Figure 5.10 (b, c), and Figure 5.11(b)). This behaviour indicates a transition from spin-active polarons to spinless charge carriers. Such a transformation is consistent with the formation of bipolarons or strongly exchange-coupled polaron pairs, as commonly reported for oxidized polythiophene derivatives [142]. The evolution of the EPR peak-to-peak linewidth (Figure 5.10, upper panels) further supports this interpretation: linewidth narrowing at intermediate doping levels reflects increasing exchange interactions among neighbouring spins [141], whereas linewidth broadening at higher potentials accompanies decreasing spin concentration, indicating increased localization and restricted charge mobility.

Systematic variation of the upper oxidation limit allows clear identification of the electrochemical stability window. When oxidation is limited to 1.0 V, the spin concentration recorded during the second p-doping–dedoping cycle (Figure 5.11b) remains comparable to that of the first cycle, and the cyclic voltammograms (Figure 5.12) show no significant change in peak shape or current intensity. This confirms fully reversible polaron formation and removal within this potential range.

Extending the oxidation threshold to 1.1 V introduces partial irreversibility. As shown in Figure 5.13, the maximum spin concentration during the second cycle is reduced compared to the first, and the dedoping curve does not fully retrace the doping branch. Correspondingly, the cyclic voltammogram recorded after cycling to 1.1 V (Figure 5.14) displays altered features relative to the fresh film, indicating the onset of charge trapping or structural rearrangement.

When the oxidation limit is increased to 1.2 V, irreversible behaviour becomes dominant. The spin concentration decreases sharply at higher potentials and does not fully recover upon dedoping (Figure 5.15). In parallel, the cyclic voltammogram recorded after the first doping–dedoping cycle to 1.2 V (Figure 5.16) shows substantial deviation from the original profile, confirming permanent electrochemical modification of the film. These results define 1.0 V as the stability threshold of poly (3) under the present experimental conditions. This is consistent with characteristic of overoxidation and backbone degradation in polythiophene systems [143].

Taken together, the combined evidence from Figures 5.9–5.16 establishes a sequential charge evolution mechanism for poly (3):

Neutral polymer → spin-active polaron (reversible regime, ≤ 1.0 V) → spinless charge carrier (transition regime, 1.0–1.1 V) → overoxidized/degraded structure (≥ 1.2 V).

The agreement between optical absorption changes (Figure 5.9), spin concentration trends (Figures 5.10–5.13), and cyclic voltammetric behaviour (Figures 5.12, 5.14, 5.16) provides a consistent mechanistic framework linking charge carrier evolution to the electrochemical stability limits of poly (3).

6.7. Proposed Oxidative electrochemical Pathways

The electrochemical behaviour of the π-conjugation-interrupted oligothiophenes investigated in this work is governed by a sequence of primary electron-transfer events followed by structurally dependent chemical transformations. Based on the cyclic voltammetry, spectroelectrochemical, and EPR results presented in Chapter 5, a mechanistic framework can be proposed that rationalizes (i) the first oxidation cycle, (ii) the nature of follow-up reactions, and (iii) the formation and evolution of electroactive polymer films.

The oxidative pathways proposed in this section are hypothesised from cyclic voltammetry, spectroelectrochemical analysis, and model-compound comparison. These mechanisms represent chemically consistent interpretations of the experimental data and are not direct structural identification of discrete intermediates. Due to the transient nature of radical species generated under electrochemical conditions, the proposed intermediates should be understood as plausible mechanistic models consistent with the observed redox behaviour.

6.7.1. Oxidative pathways of compound 3

Notably, the oxidation behaviour of compound **3** differs from that of compounds **1** and **2**. This difference is consistent with the absence of abstractable hydrogen atoms at the sp^3-hybridized bridge in compound **3**. In contrast to compounds **1** and **2**, monomer **3** exhibits more rapid development of polymer-related redox features during repetitive cycling (Chapter 5, Figure 5.2.4(e)), indicating that elimination of bridge C–H functionality suppresses competing follow-up processes and facilitates more direct progression toward film formation.

To rationalize this behaviour, a fully conjugated reference compound, dimethyl quaterthiophene (model A), lacking a conjugation-breaking spacer, was synthesized and investigated. The cyclic voltammogram of model **A** recorded in CH_2Cl_2 containing 0.1 M $(n\text{-}Bu)_4NPF_6$ (Chapter 5, Figure 5.5.3(a)) exhibits two reversible one-electron oxidation processes and does not show evidence of electropolymerization under the applied conditions. The electrochemical oxidation mechanism of model **A** is presented in Scheme 6.7.1 following the classical electrochemical oxidation of oligothiophene [144]. The absence of polymer formation suggests that the radical cations generated in model **A** remain sufficiently stabilized and do not undergo productive intermolecular α–α coupling under these conditions. Steric blocking at terminal α-positions or preferential charge localization within the conjugated backbone may reduce the probability of coupling reactions, although direct structural evidence (in this work) for charge localization is not available.

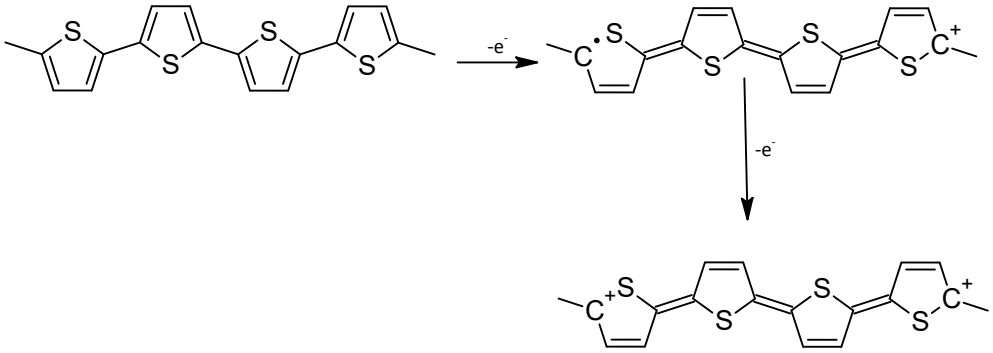

Scheme 6.7.1 Possible mechanisms for electrochemical oxidation of model A.

A comparison of peak currents provides additional qualitative insight. The current peak observed for model **A** is roughly 2 μA for a single electron oxidation process. This compound undergoes a two-electron oxidation at a potential of approximately 0.8 V versus Fc/Fc^+, as shown in Figure 5.5.3(a). This value should be compared with the peak current of monomer **3**, which is approximately 9 μA. Figure 6.3 (a-b) shows the comparison between the electrochemical oxidation of monomer **3** and model **A**.

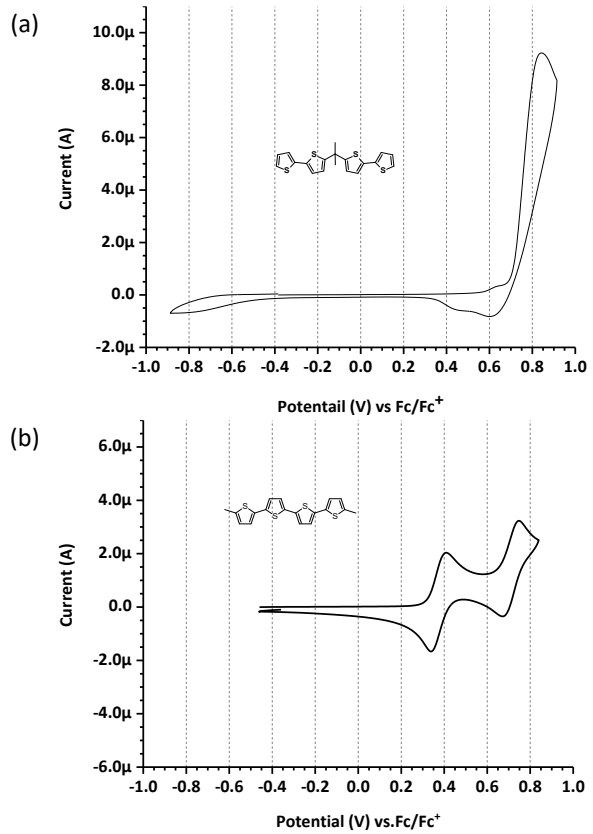

*Figure 6.3 Cyclic voltammograms of the investigated monomer 3 (a) and model **A** were recorded in dichloromethane at 0.1 M Bu_4NPF_6 for the anodic potential range (scan rate, 0.1V.s^{-1}).*

Because monomer **3** and model **A** possess comparable quaterthiophene cores, qualitative comparison of their electrochemical responses provides useful mechanistic insight. However, no quantitative electron stoichiometry is inferred from peak current magnitude alone. On this basis, a mechanistic pathway for the electrochemical oxidation of monomer **3** is proposed (Scheme 6.7.2). The process begins with a one-electron oxidation of the neutral monomer to generate a thiophene-centred radical cation (Step I), consistent with the anodic peak observed in Figure 6.3(a). The radical cations may subsequently undergo intermolecular α–α coupling to form σ-bonded dicationic intermediates (Step II). No discrete σ-dimer wave is resolved in the cyclic voltammogram; therefore, any such intermediate is not seen. Following C–C bond formation, rearomatization via proton loss yields a more stable conjugated dimeric structure (Step III). This process is consistent with the emergence of polymer-related redox features during repetitive cycling (Chapter 5, Figure 5.4(e)).

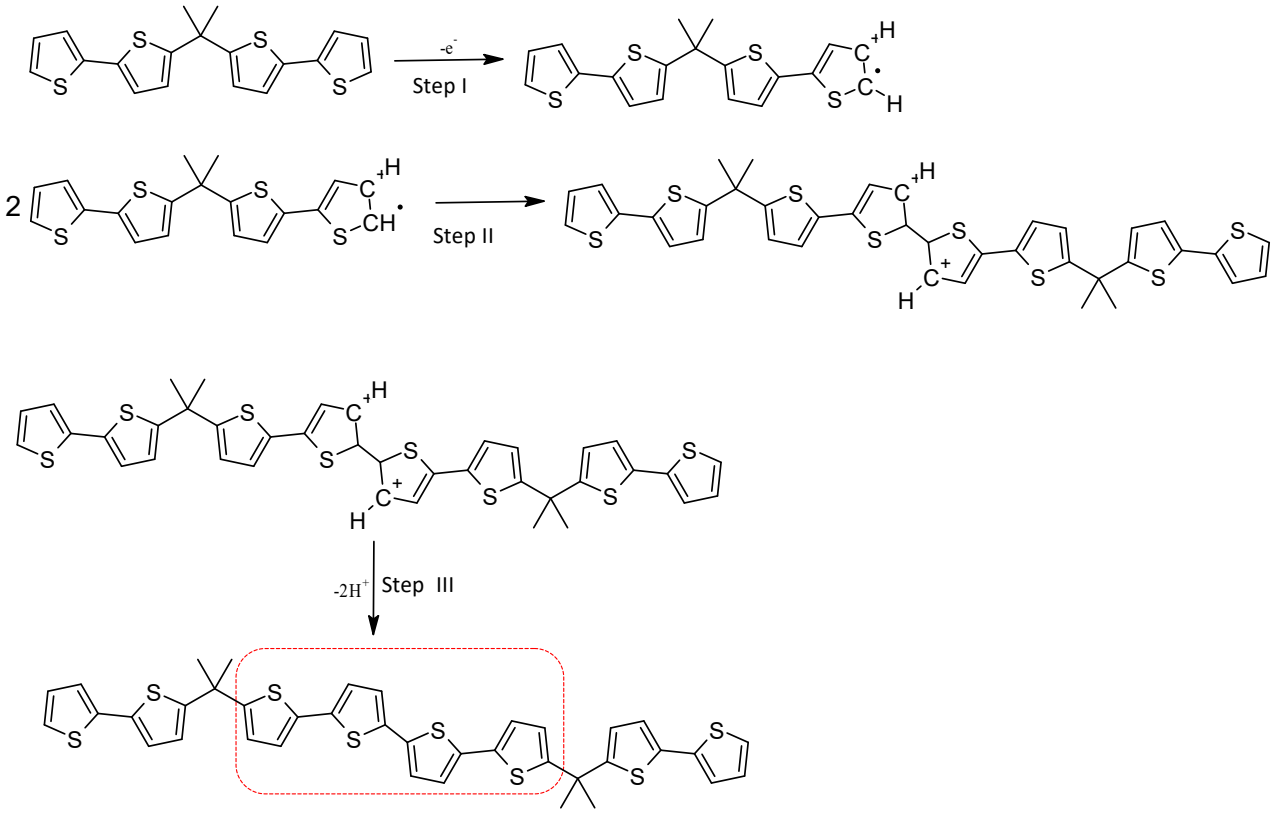

Scheme 6.7.2 Possible proposed mechanism for monomer 3.

Because model **A** undergoes two sequential reversible one-electron oxidations at approximately 0.8 V vs Fc/Fc^+ (Figure 6.3(b)), further oxidation of the coupled product derived from monomer **3** is chemically plausible at similar potentials, leading to higher oxidation states of the growing oligomeric framework (Scheme 6.7.3). This sequence of transformations involves a total of four electrons. Based on the electrochemical data for model **A**, a single-electron oxidation corresponds to a current of 2 µA. Therefore, a four-electron process would theoretically produce a current of 8 µA ($4e^- \times 2$ µA = 8 µA), which closely aligns with the observed peak current of 9 µA for monomer **3**. This correspondence supports the plausibility of the proposed mechanism and suggests that the electrochemical behaviour of monomer **3** is consistent with theoretical expectations, thereby reinforcing the mechanistic interpretation.

The deposited film can undergo stepwise redox activity as shown in Scheme 6.7.3. This might be associated with two oxidation and reduction peaks observed in the cyclic voltammogram of poly (**3**) (see Figure 5.5(e)).

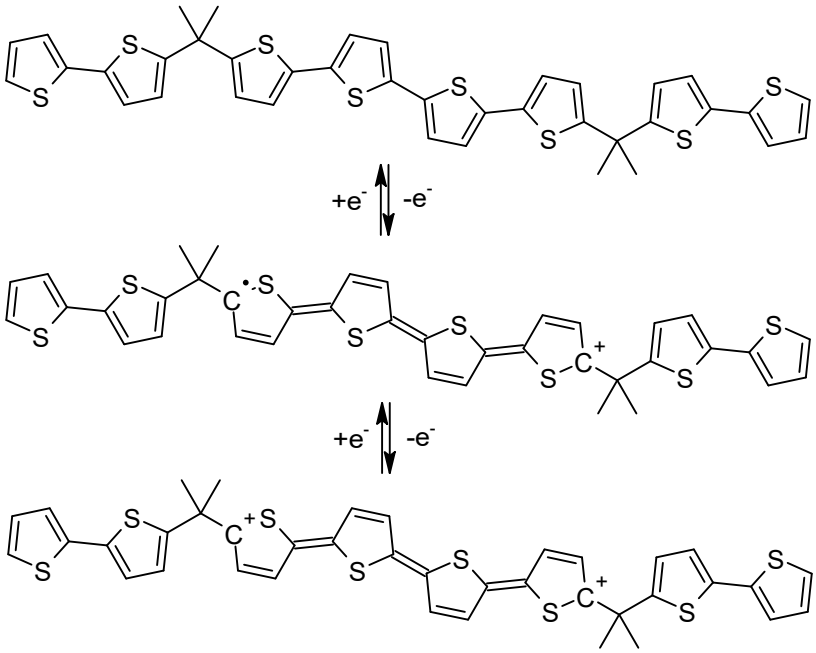

Scheme 6.7.3 Possible redox activities of the dimer product of compound 3.

As discussed in Section 5.2.6, the EPR spectroelectrochemical measurements of poly(3) reveal a non-monotonic evolution of spin concentration with applied potential. The number of paramagnetic centres increases progressively upon oxidation, reaching a maximum at approximately 1.0 V vs Fc/Fc^+, and subsequently decreases at higher potentials. Importantly, this decrease in spin concentration occurs within a potential range where the cyclic voltammetric response remains largely reversible. This observation indicates that the reduction in EPR intensity between approximately 1.0 and 1.1 V is unlikely to arise from immediate chemical degradation of the polymer backbone. Instead, it is consistent with a transformation of spin-active polarons into spin-compensated charge-carrier states.

To rationalize this behaviour, possible π-dimer stacking motifs are proposed (Scheme 6.7.4). These structures are presented as conceptual representations consistent with the combined EPR, spectroelectrochemical, and electrochemical observations, rather than as structurally confirmed species. In conjugated thiophene-based systems, oxidized segments are known to undergo intermolecular or intramolecular π–π interactions that can result in the formation of spin-paired species, such as bipolarons, polaron pairs, or π-dimers. Formation of such states leads to partial or complete pairing of unpaired spins, thereby decreasing the EPR signal intensity despite continued charge injection.

The proposed π-dimer motifs provide a coherent explanation for several experimental observations. First, the decline in spin concentration beyond 1.0 V occurs without immediate loss of electrochemical reversibility, supporting assignment of this regime to charge-carrier reorganization rather than direct irreversible structural change. Second, the accompanying evolution of EPR linewidth including narrowing at intermediate oxidation levels is consistent with increased electronic coupling and exchange interactions between neighbouring charge carriers. Third, the growth of broad, low-energy absorption features in the UV–Vis–NIR spectra of poly(3) at elevated doping levels (Section 5.2.5) indicates the presence of increasingly delocalized and interacting oxidized states.

At higher applied potentials (approximately 1.2 V vs Fc/Fc^+), the behaviour changes markedly. A sharp decrease in spin concentration is accompanied by irreversible alterations in both EPR linewidth

and the post-experiment cyclic voltammogram. In this regime, the data are consistent with the onset of chemical degradation rather than further reversible charge-carrier transformation. Thus, while the decrease in spin concentration between 1.0 and 1.1 V reflects more or less reversible conversion of polarons into spin-paired states, the loss of electrochemical reversibility at 1.2 V defines the definite degradation onset of poly(3).

Taken together, these findings indicate that poly(3) accommodates increasing oxidative charge density through a sequence of stages: (i) formation of spin-active polarons, (ii) conversion into spin-compensated or aggregated charge-carrier states at higher but still reversible doping levels, and (iii) irreversible degradation beyond a critical oxidation threshold. The π-dimer stacking motifs illustrated in Scheme 6.7.4 therefore provide a chemically reasonable framework for interpreting the reversible suppression of EPR intensity at elevated potentials and highlight the role of interchain or intrachain electronic interactions in stabilizing oxidized states prior to degradation.

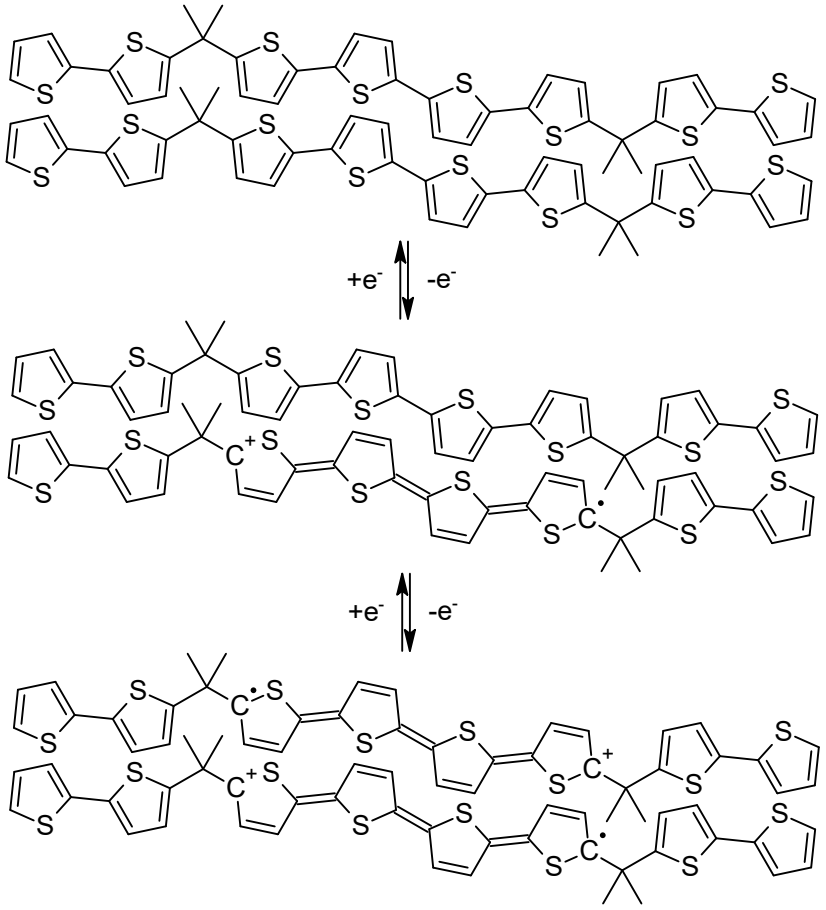

*Scheme 6.7.4 possible molecular structures of π-dimer stacks mechanism contained in poly (**3**).*

To evaluate whether oxidative alkyl cleavage could contribute to the electrochemical behaviour of monomer **3**, alternative pathways involving loss of an alkyl substituent were considered using tert-butyl–substituted model **C** as a comparative reference (Schemes 6.7.5 and 6.7.6).

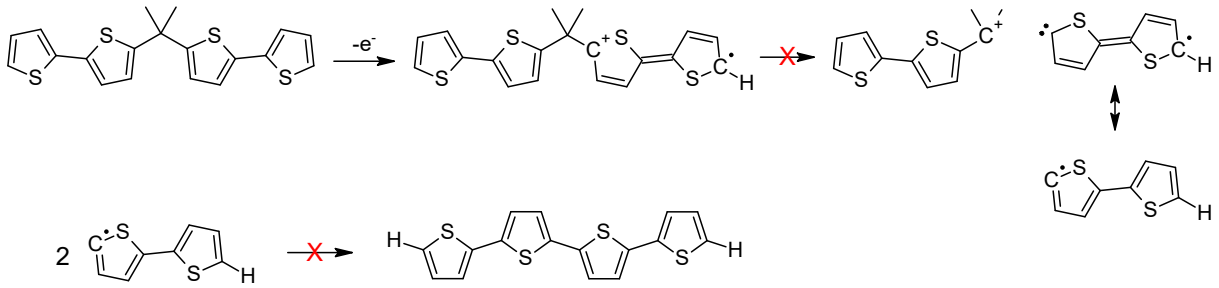

Scheme 6.7.5 *Comparison between the electrochemical oxidation of monomer 3 and a bithiophene radical species hypothetically generated via alkyl cleavage of tert-butyl-substituted model C. The distinct voltammetric responses observed experimentally demonstrate that alkyl cleavage does not occur in monomer 3 under the applied electrochemical conditions, thereby excluding this pathway.*

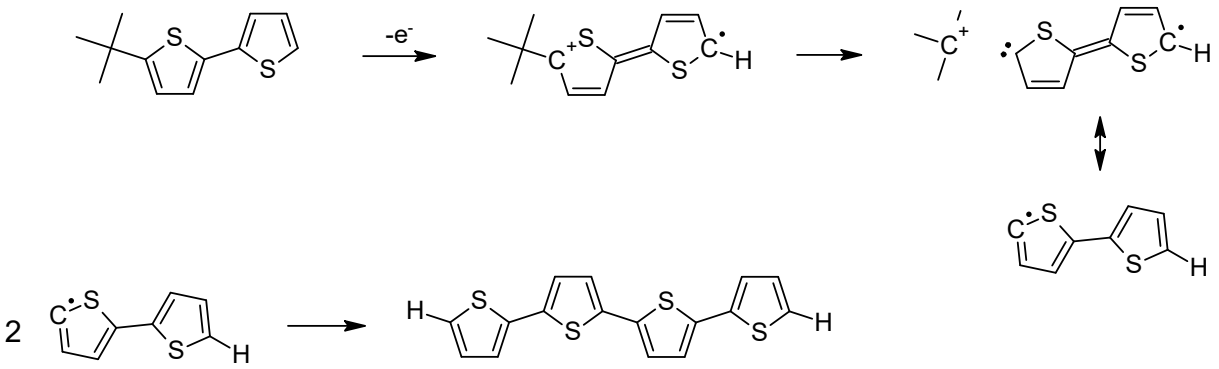

Scheme 6.7.6 *Hypothetical oxidative alkyl-cleavage pathway considered for tert-butyl-substituted model C, illustrating a possible loss of a bulky alkyl group upon electrochemical oxidation. This scheme is presented as a comparative control to evaluate whether alkyl cleavage could contribute to the electrochemical behaviour observed for monomer 3.*

Tert-butyl groups are known, under certain oxidative conditions, to undergo cleavage, generating radical intermediates that can subsequently participate in coupling reactions. Model **C** therefore provides a useful benchmark for assessing whether analogous bridge cleavage might occur in monomer **3** during electrochemical oxidation. If oxidative cleavage of the dimethyl-substituted sp^3 carbon bridge in monomer **3** were operative, one would expect the voltammetric response to resemble that of model **C**, particularly with respect to the emergence of characteristic radical-derived features and altered film growth behaviour. However, comparison of the cyclic voltammograms recorded for monomer **3** and model **C** (Figure 6.4a–b) reveals clearly distinct electrochemical profiles. Model **C** exhibits a response consistent with oxidative fragmentation and subsequent radical processes, whereas monomer **3** displays progressive current growth and redox features associated with direct coupling and electropolymerization.

Importantly, no additional voltammetric signatures attributable to alkyl cleavage products are observed for compound **3** within the applied potential window. Instead, the electrochemical behaviour is consistent with oxidation localized on the thiophene segments, followed by radical-cation coupling and film formation as discussed in Sections 6.4 and 6.5.

These comparative results indicate that, under the applied experimental conditions, cleavage of the dimethyl-substituted sp^3 bridge in monomer 3 is not taking place. Rather, the dimethyl substitution appears to stabilize the bridge framework and direct oxidative reactivity toward productive thiophene-centred coupling processes.

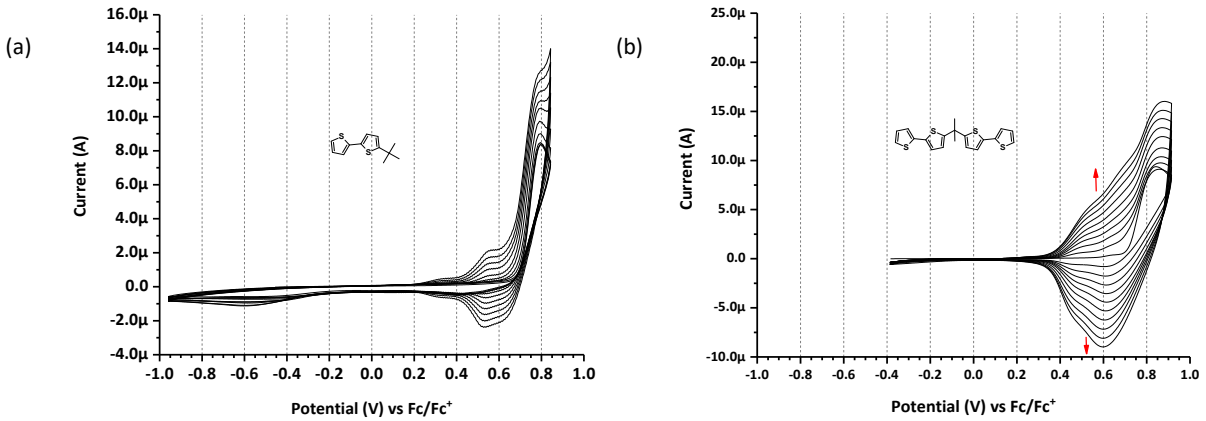

*Figure 6.4 Cyclic voltammograms of electropolymerization of monomer **3** and model **C**.*

6.7.2. Oxidative pathways of compound 1

From the UV–Vis absorption spectra of model **B** (methyl bithiophene) and compound **1** (Figure 6.1), insight can be gained into the degree of electronic communication between the two bithiophene arms of compound **1**. Model **B**, containing a single bithiophene chromophore, exhibits a characteristic localized π–π* transition. Compound **1**, which contains two bithiophene segments connected through a methylene (sp^3) bridge, displays a closely resembling absorption profile with only a minor bathochromic shift relative to model **B**. The absence of a substantial red shift or new low-energy absorption band indicates that, in the ground state, the two bithiophene arms are largely electronically decoupled. This behaviour is consistent with effective interruption of through-bond conjugation by the methylene bridge. Consequently, oxidation of compound **1** is expected to occur in a stepwise manner, involving sequential single-electron processes localized on individual thiophene segments rather than a concerted two-electron event involving both arms simultaneously. Electrochemical measurements support this interpretation.

Compound 1 undergoes an initial one-electron oxidation to generate a thiophene-centred radical cation (Scheme 6.7.7).

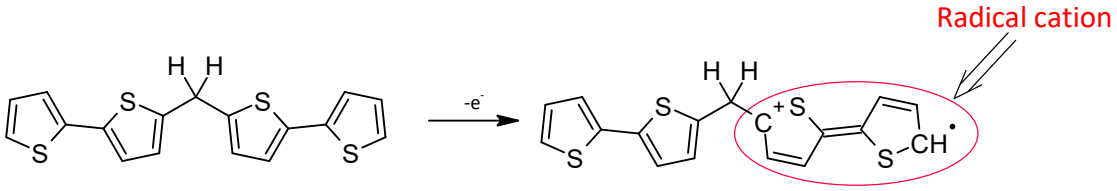

*Scheme 6.7.7 Proposed first electrochemical oxidation of compound **1** leading to the formation of radical cation.*

Following formation of the radical cation, two post-oxidation pathways can be considered (Scheme 6.7.8).

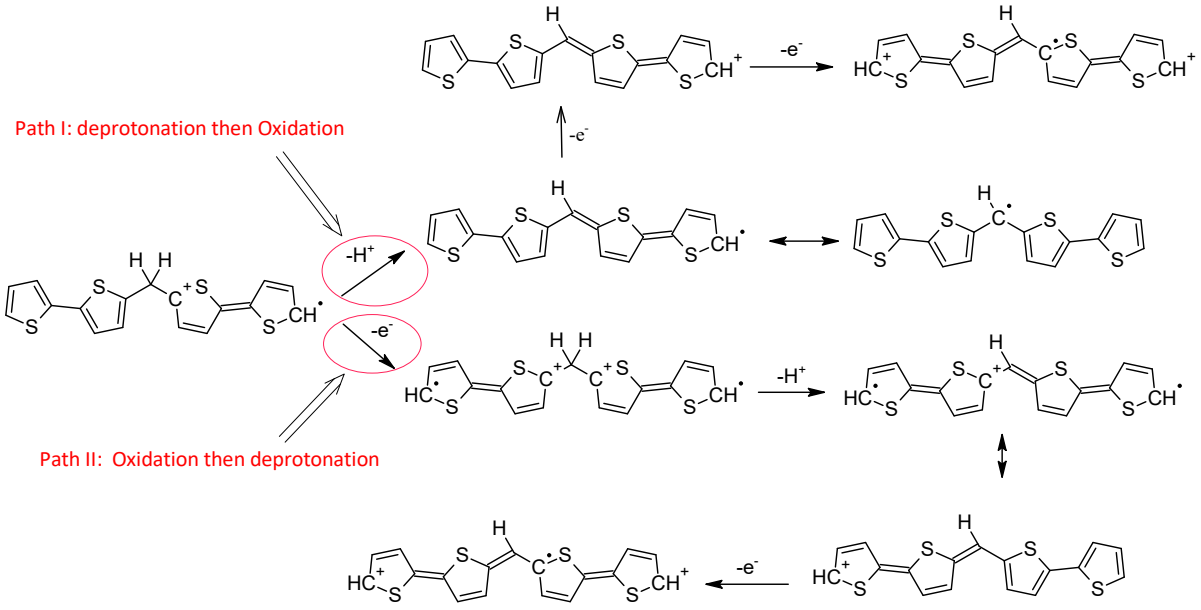

Scheme 6.7.8 Competing post-oxidation pathways of monomer 1 following formation of the radical cation: Path I involving proton loss from the sp^3-hybridized carbon bridge, and Path II involving oxidation of the second bithiophene arm.

In Path I, the radical cation undergoes deprotonation at the sp^3-hybridized carbon bridge. Removal of a proton from the methylene carbon generates a carbon-centred radical intermediate adjacent to the thiophene unit. This process modifies the electronic structure and can facilitate subsequent electrochemical steps. The appearance of a cathodic feature at approximately −0.2 V vs Fc/Fc^+ during repetitive cycling is consistent either with formation of σ-linked intermediates, or related follow-up species derived from this pathway. In Path II, oxidation proceeds at the second, initially neutral bithiophene arm prior to deprotonation, generating a doubly oxidized species. This pathway corresponds to sequential (or immediate) oxidation localized on both arms without prior proton abstraction from the bridge. Given the limited electronic coupling between the two segments, such stepwise oxidation is chemically reasonable. The relative contribution of these pathways depends on the kinetics of proton loss versus intramolecular charge redistribution; however, both routes converge toward electronically equivalent oxidized intermediates.

As illustrated in Scheme 6.7.9, possible coupling between radical cation species results in σ-dimer intermediates. Subsequent deprotonation and rearomatization would restore aromaticity to the thiophene units, yielding oxidized dimeric species. These σ-dimer-derived structures can undergo further oxidation, enabling additional coupling steps and progressive growth of polymeric chains. This sequence provides a mechanistic explanation for: the emergence of polymer-related redox features during electropolymerization (Chapter 5), the growth of current upon repetitive cycling, and the cathodic feature associated with σ-dimer-related intermediates.

Thus, the combined UV–Vis and electrochemical data indicate that oxidation of compound **1** proceeds via sequential single-electron events localized on thiophene units, followed by chemically driven coupling processes that ultimately lead to polymer chain propagation.

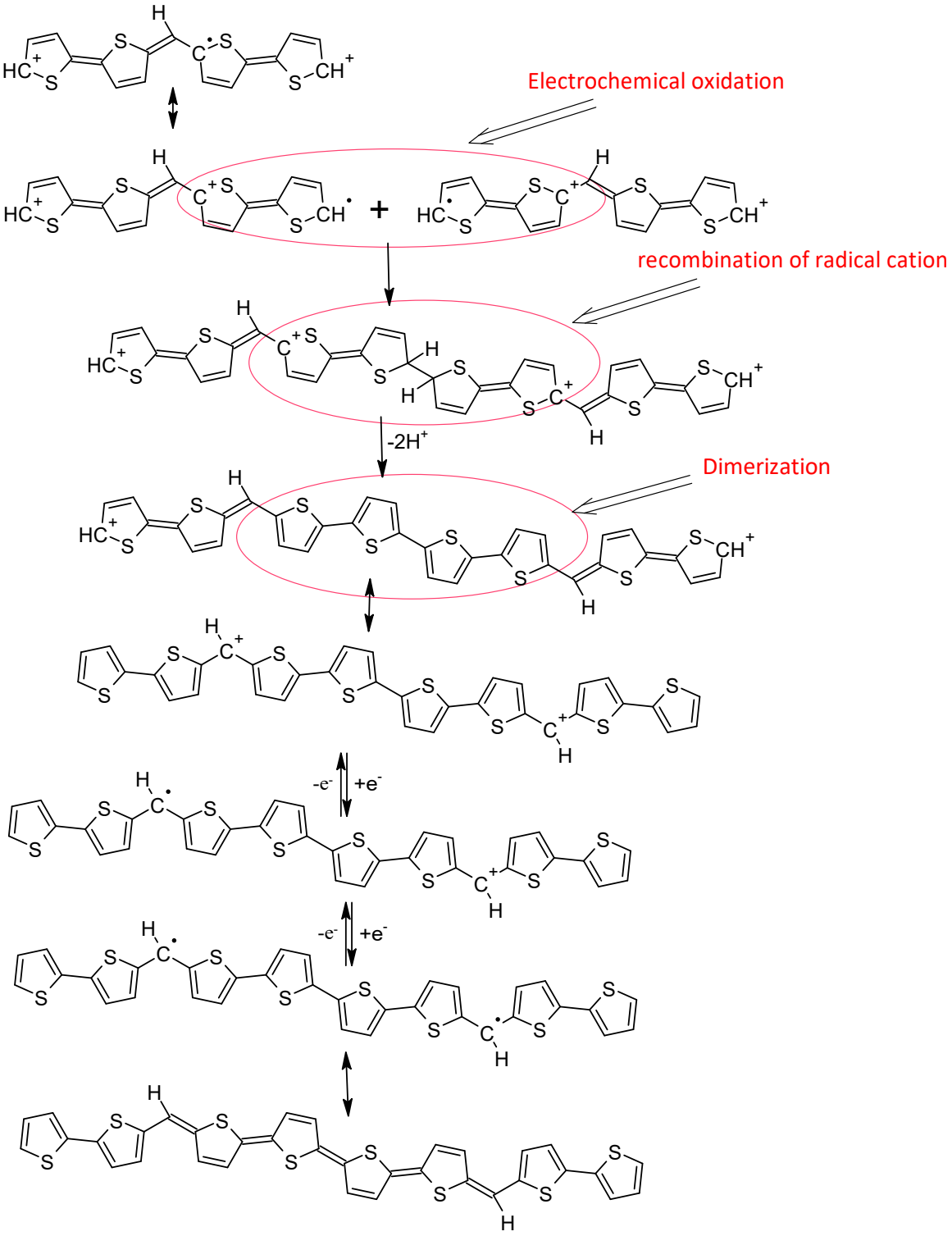

*Scheme 6.7.9 Formation of σ-dimer intermediates from dicationic species of compound **1**, followed by rearomatization and further oxidative coupling leading to polymer chain propagation.*

The dehydrogenation of sp^3-hybridized carbon atoms bridging heterocyclic units has been reported to generate multiblock conjugated structures, which can be regarded as organic semiconductor superlattices [63]. In related systems, polymer chains containing alternating sp^3 carbons and π-conjugated segments have also been shown to undergo elimination reactions under oxidative or reductive conditions, leading to the expulsion of hydrogen atoms from the bridge and the formation of new electronically active structures [145]. In the present system, such dehydrogenation processes can

be considered as a plausible mechanistic basis for the formation of σ-linked intermediates following the initial oxidation of compound **1**. Loss of hydrogen from the sp^3 carbon bridge would generate a carbon-centred radical site capable of participating in intermolecular coupling reactions. This process would effectively convert the conjugation-breaking bridge into a reactive node, enabling carbon–carbon bond formation across the spacer.

On this basis, a possible dimerization product formed via coupling across the sp^3 bridge is proposed in Scheme 6.7.10. The structure shown represents a chemically reasonable outcome of bridge-centred radical coupling. However, it is important to emphasize that this pathway is presented as a mechanistic possibility consistent with literature precedent and the observed electrochemical reactivity, rather than as a structurally confirmed intermediate.

While the voltammetric data for compound **1** primarily support thiophene-centred radical coupling as the dominant polymer growth pathway (Section 6.4), bridge-mediated dehydrogenative coupling cannot be excluded under strongly oxidative conditions. If operative, such reactions would contribute to structural diversification of the growing polymer network and could influence film morphology and electronic connectivity.

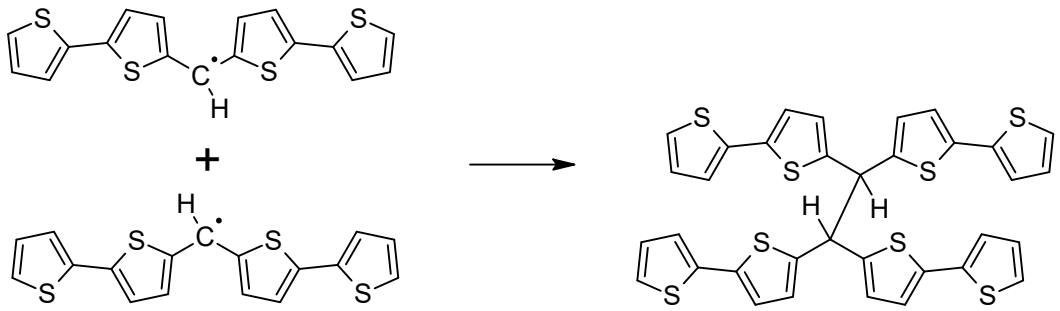

Scheme 6.7.10 Proposed dimerization product formed via coupling across the conjugation-breaking sp^3 carbon bridge of compound 1 following dehydrogenation under electrochemical oxidation conditions.

The methylene bridge in compound **1** functions as both a structural and electronic discontinuity within the oligothiophene framework. As an sp^3-hybridized carbon, it interrupts through-bond π-conjugation and limits long-range electronic communication between the two bithiophene arms. In contrast to fully conjugated thiophene backbones, where radical cations can delocalize efficiently across extended π-systems, oxidation in compound **1** is expected to generate more localized radical intermediates.

This restricted electronic communication has important mechanistic consequences. Upon electrochemical oxidation, radical cation formation occurs primarily on individual thiophene segments, and the limited delocalization across the methylene bridge promotes the formation of structurally distinct reactive intermediates. As a result, oxidative coupling may proceed through multiple localized radical sites, leading to a set of possible dimeric or oligomeric products rather than a single, fully delocalized growth pathway.

Figure 6.5 illustrates representative oxidative coupling products that may arise from this localized radical behaviour. These structures reflect the possibility of coupling at different reactive positions within the conjugation-broken framework, consistent with the electrochemical observations of progressive current growth and emergence of new redox features during repetitive cycling (Chapter 5). Importantly, these proposed products are presented as chemically reasonable outcomes of localized radical reactivity rather than as structurally confirmed species.

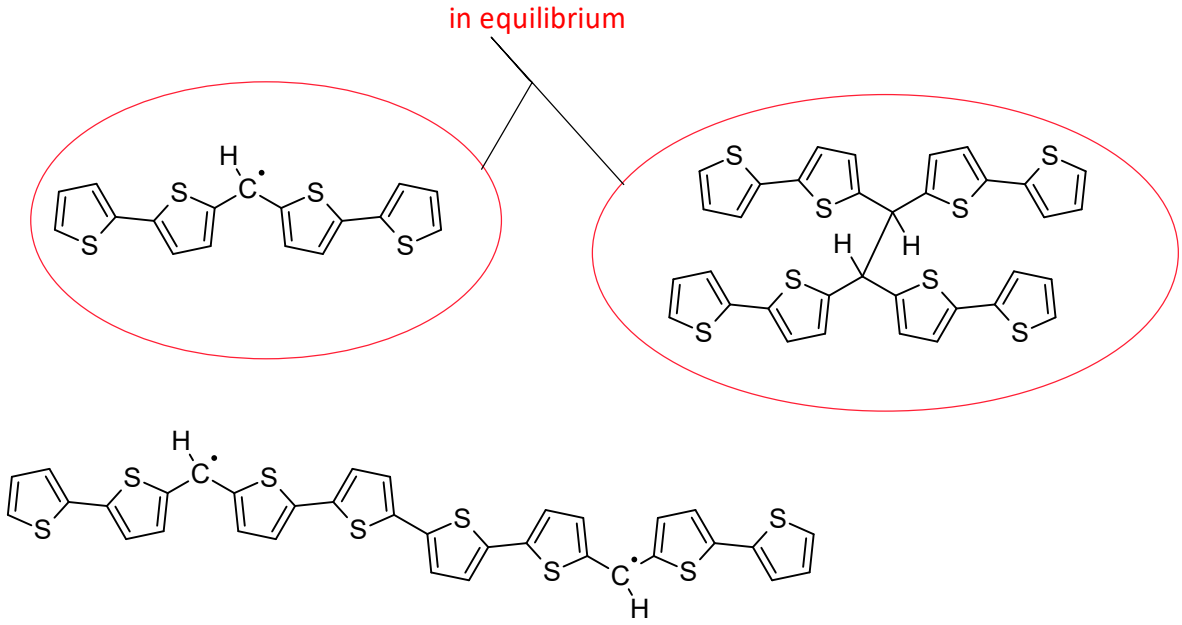

Figure 6.5 Proposed oxidative coupling products formed from compound 1 upon electrochemical oxidation.

Two distinct redox-active species may arise from the oxidative coupling products of compound **1**:

(i) a neutral radical species, and

(ii) a diradical cation species generated upon further oxidation of the coupled structure.

The first redox process could involve oxidation of a neutral radical, possible when one hydrogen atom is lost from the methylene bridge (Scheme 6.7.11).

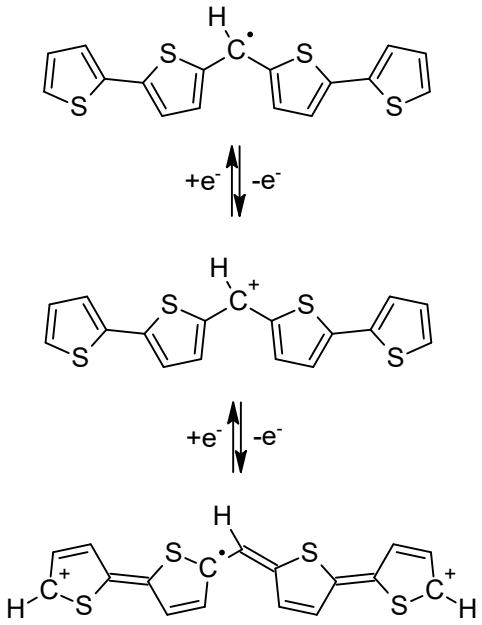

*Scheme 6.7.11 Possible redox mechanisms for radical product of monomer **1** redox transformation (neutral conjugated compound).*

Spectroelectrochemical measurements (Figure 5.6) reveal a residual absorption band centred at approximately 900 nm prior to extensive film oxidation. This low-energy feature is consistent with a localized polaron-type state or soliton-type species embedded within a partially conjugated framework. Upon further oxidation, this band shifts slightly toward shorter wavelength (higher energy),

indicating conversion of a neutral radical species into a positively charged radical cation (polaron) state. Such hypsochromic shifts are consistent with increased coulombic stabilization and altered electronic delocalization upon oxidation.

The second redox process involves further oxidation of the coupled intermediate to generate a dication species, as illustrated in Scheme 6.7.12. This transformation introduces two electronically interacting cationic centres within the conjugation-broken framework. The doping-induced absorption band observed at approximately 687 nm in Figure 5.2.6 is tentatively assigned to this higher oxidation state. The energy and growth of this feature with increasing applied potential are consistent with the formation of interacting charge carriers and increased π-delocalization across the newly formed coupling sites.

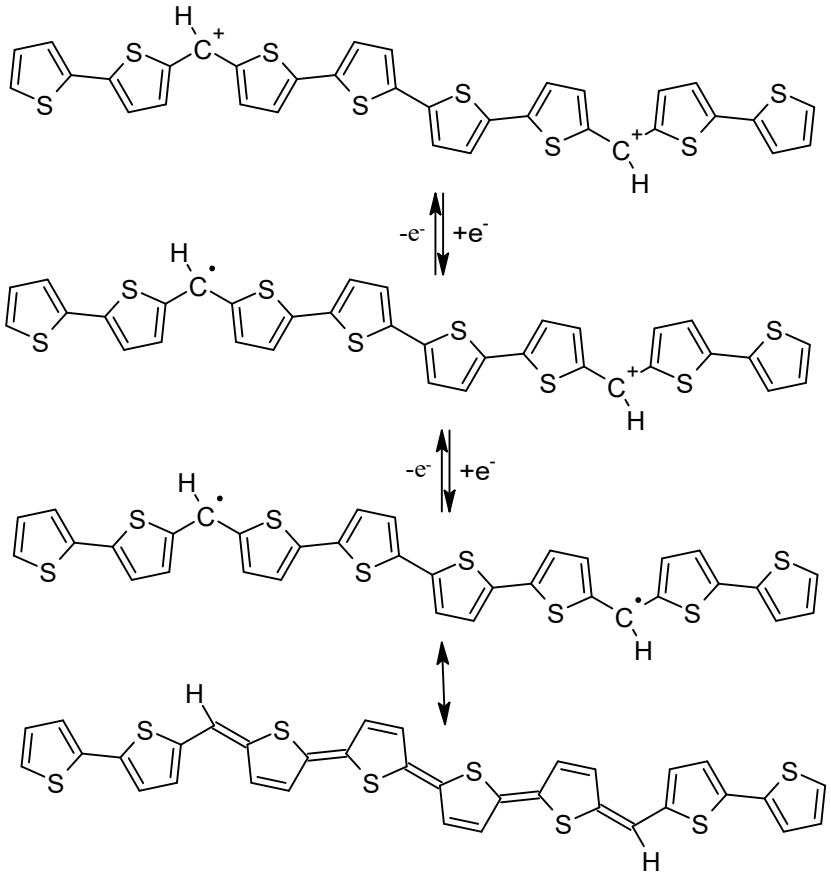

*Scheme 6.7.12 Possible redox mechanisms for diradical product of monomer **1**.*

Importantly, these assignments are supported by the electrochemical behaviour observed during cyclic voltammetry. The progressive emergence of additional redox waves upon repeated cycling indicates the formation of new electroactive species distinct from the parent monomer. The coexistence of reversible redox features and evolving optical bands suggests stepwise oxidation of structurally modified coupling products rather than direct multielectron oxidation of the original monomer framework.

Together, Schemes 6.7.11 and 6.7.12 provide a mechanistic framework in which oxidative coupling generates new conjugated segments that subsequently undergo sequential redox transformations. The spectroscopic features observed in the near-infrared and visible regions are

therefore interpreted as signatures of localized soliton-type (neutral/charged) states within the growing electropolymer film, rather than evidence of a single, fully delocalized electronic structure.

6.7.3. Oxidative pathways of compound 2

Compound **2** undergoes oxidative transformation through mechanistic pathways closely analogous to those proposed for compound **1**. Both compounds contain an sp^3-hybridized carbon bridge bearing abstractable hydrogen atoms, which enables post-oxidation deprotonation and subsequent σ-bond coupling processes. As a result, the initial electrochemical step is expected to involve formation of a thiophene-centred radical cation, followed by competing pathways involving either further oxidation of the second bithiophene arm or proton loss from the sp^3 carbon bridge.

Because hydrogen atoms remain available at the bridge position in compound **2**, dehydrogenation and radical-mediated coupling across or adjacent to the conjugation-breaking spacer remain mechanistically accessible. Consequently, the sequence of radical cation formation, σ-dimer generation, rearomatization, and further oxidative coupling described for compound **1** is also applicable to compound **2**.

However, subtle differences in substitution at the sp^3 bridge may influence the kinetics and relative contributions of these competing pathways. Increased alkyl substitution can modify the stability of intermediate radical species and alter steric accessibility for intermolecular coupling, thereby affecting the rate of follow-up reactions and film growth efficiency. Nevertheless, the fundamental oxidative framework remains consistent with that established for compound **1**.

6.7.4. Oxidative pathways of compound 4

Two competitive mechanistic pathways are proposed for the electrochemical oxidation of compound **4** (Schemes 6.7.13–6.7.15). Although the initial sequence of elementary steps differs, both pathways ultimately converge to the same oxidized coupling product.

In the first pathway (Scheme 6.7.13), electrochemical oxidation generates a thiophene-centred radical cation. Radical–radical coupling between two such species leads to formation of a σ-linked dimeric intermediate. Subsequent deprotonation ($-2H^+$) restores aromaticity within the thiophene rings, yielding a neutral conjugated dimer. This process is consistent with the established oxidative coupling behaviour of thiophene derivatives and parallels the coupling mechanisms proposed for compounds **1** and **2**.

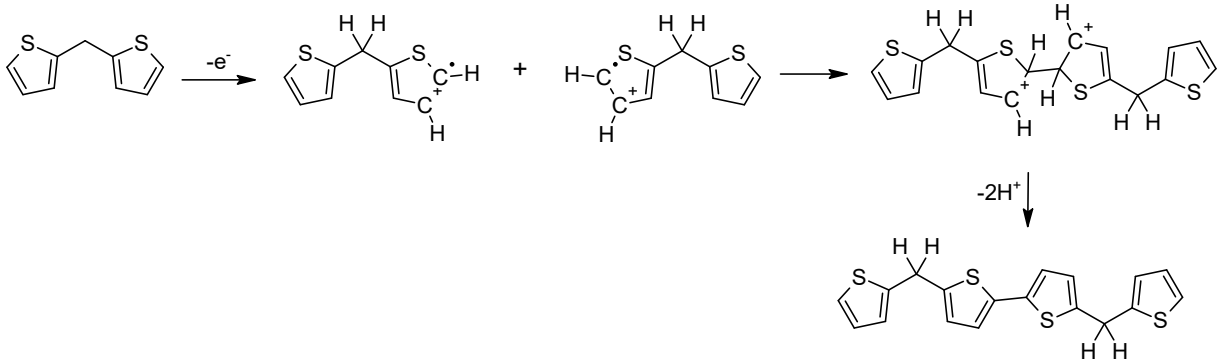

*Scheme 6.7.13 One possible pathway of electrochemical oxidation of compound **4**.*

The σ-linked dimer formed in Scheme 6.7.13 may undergo further oxidation and follow-up transformations, as illustrated in Scheme 6.7.14. Additional electron removal generates new radical cation centres within the extended framework, enabling further dehydrogenation and intramolecular rearrangement. These sequential redox steps progressively increase conjugation length and facilitate propagation toward oligomeric or polymeric structures.

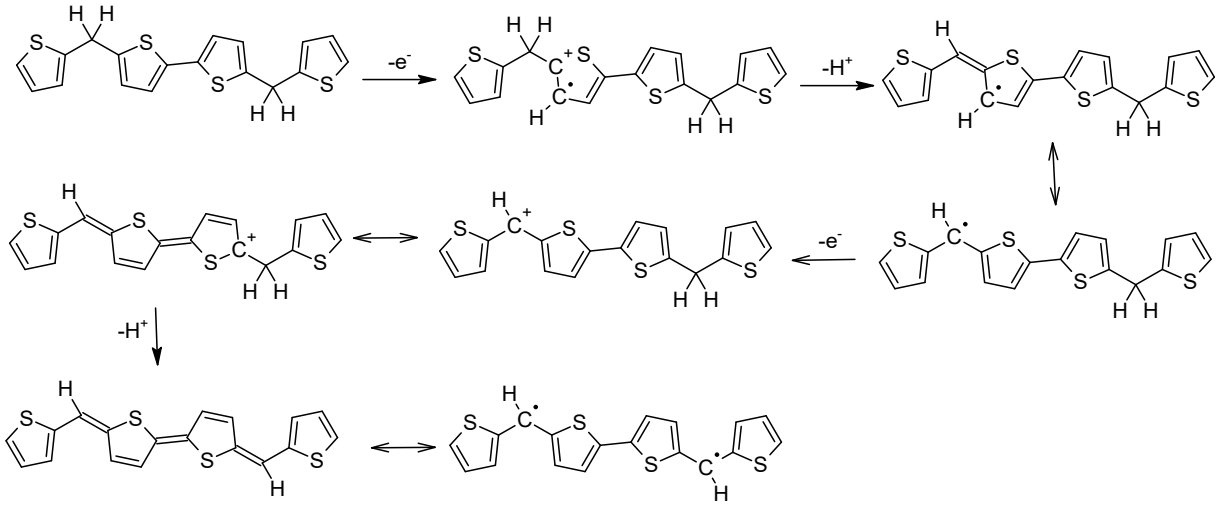

*Scheme 6.7.14 Possible follow up reaction of dimerization product of compound **4**.*

In the second pathway (Scheme 6.7.15), oxidation of compound **4** again produces a radical cation; however, in this case, dehydrogenation from the sp^3-hybridized carbon bridge occurs prior to intermolecular coupling. Proton loss from the bridge generates a carbon-centred radical intermediate.

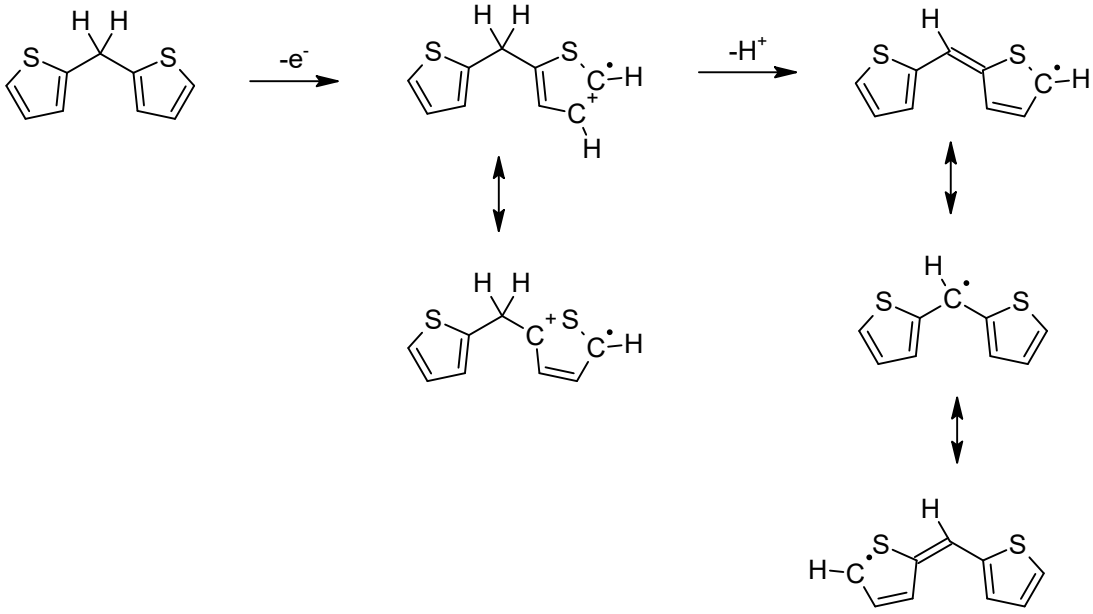

*Scheme 6.7.15 The second possible pathway of electrochemical oxidation of compound **4**.*

The radical intermediate generated in Scheme 6.7.15 is highly reactive and may undergo intermolecular coupling to form a σ-linked dimer, as illustrated in Scheme 6.7.16. In this process, two carbon-centred radical species combine through formation of a new carbon–carbon bond, yielding a

dimeric intermediate. Subsequent oxidation and deprotonation steps restore aromaticity within the thiophene rings, producing an extended conjugated structure.

This dimerization pathway is consistent with the limited conjugation length of compound **4** and the localization of radical character within the bithiophene framework. Because the π-system is relatively short, radical stabilization through long-range delocalization is restricted, increasing the likelihood of bimolecular radical coupling under electrochemical conditions. The sequential oxidation–deprotonation–coupling sequence therefore provides a plausible route toward the formation of higher oligomeric species.

Importantly, this mechanism aligns with the gradual evolution of new redox features observed during cyclic voltammetry in Chapter 5, indicating formation of electroactive products distinct from the parent monomer. Scheme 6.7.16 thus represents a chemically reasonable continuation of the bridge-dehydrogenation pathway, ultimately converging with the σ-coupling mechanism described in Schemes 6.7.13 and 6.7.14.

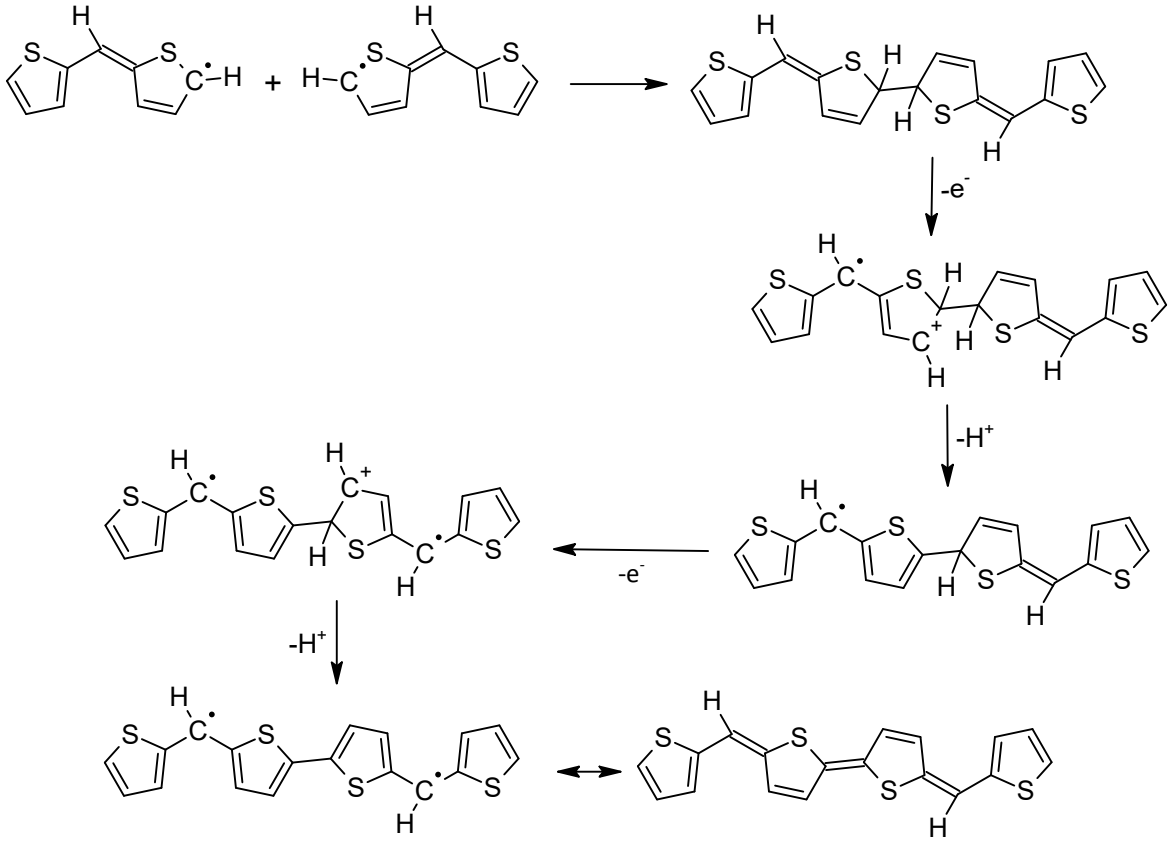

*Scheme 6.7.16 Possible dimerization process of compound **4**.*

Taken together, Schemes 6.7.13–6.7.16 demonstrate that electrochemical oxidation of compound **4** could proceed through radical-mediated processes involving either initial σ-coupling or bridge dehydrogenation, ultimately yielding a common conjugated dimeric product capable of further oxidative transformation.

An alternative oxidative pathway may involve stepwise oxidation of the two thiophene side arms, as illustrated in Scheme 6.7.17. In this mechanism, initial one-electron oxidation generates a radical cation localized on one thiophene unit. Subsequent electron removal from the second thiophene arm produces a dicationic diradical species in which both side arms bear oxidized centres. Because the

methylene bridge interrupts through-bond conjugation, the two thiophene segments are only weakly electronically coupled. As a result, oxidation of one arm does not strongly delocalize charge across the entire molecule, rendering sequential oxidation of the second arm energetically feasible. This stepwise process leads to formation of a species containing two localized radical cation centres, which can subsequently undergo intermolecular coupling or deprotonation to generate more stable conjugated products. The mechanism depicted in Scheme 6.7.17 is therefore consistent with the conjugation-broken architecture of compound **4** and provides an additional route toward dimeric or oligomeric intermediates. The progressive growth of oxidative current observed during cyclic voltammetry supports the formation of new electroactive species arising from such multistep oxidation processes.

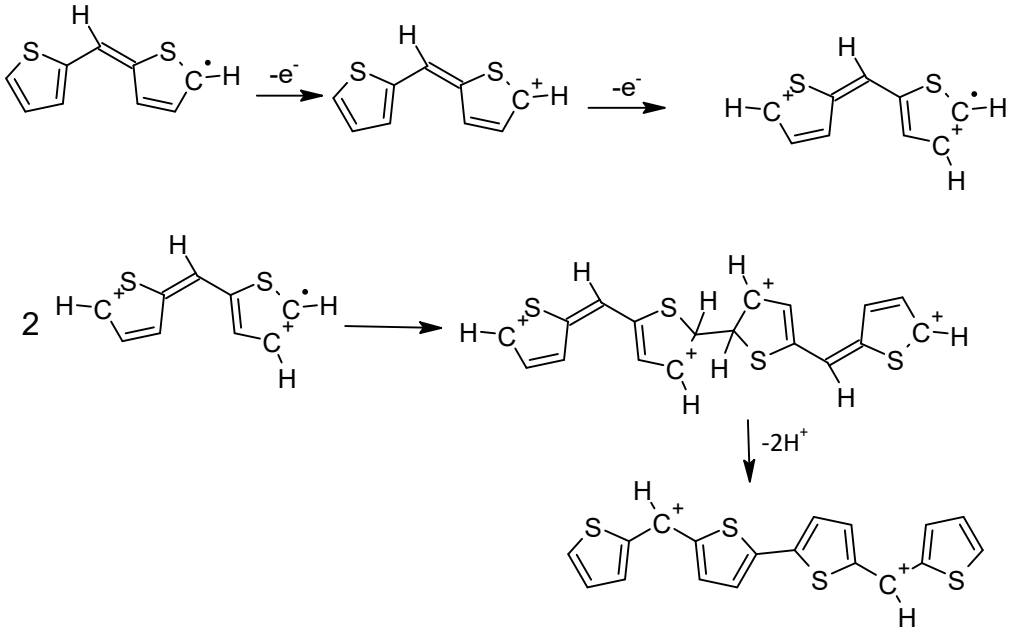

Scheme 6.7.17 Possible oxidation from the two side arms of thiophene.

The radical and diradical intermediate generated from compound **4** (Scheme 6.7.15) may undergo further redox transformations, as illustrated in Schemes 6.7.18 and 6.7.19, respectively, involving interconversion between neutral radical and cationic species. These processes represent localized redox equilibria within the short thiophene-based framework. However, because compound **4** possesses a limited π-conjugation length and a conjugation-breaking sp^3 carbon bridge, the resulting oxidized species are only weakly stabilized. The framework lacks sufficient delocalization to effectively accommodate positive charge, particularly at higher oxidation states.

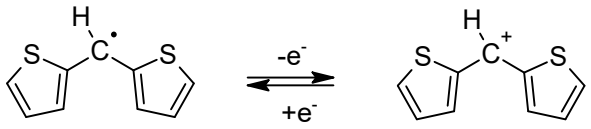

*Scheme 6.7.18 Possible redox states in dehydrogentated compound **4**.*

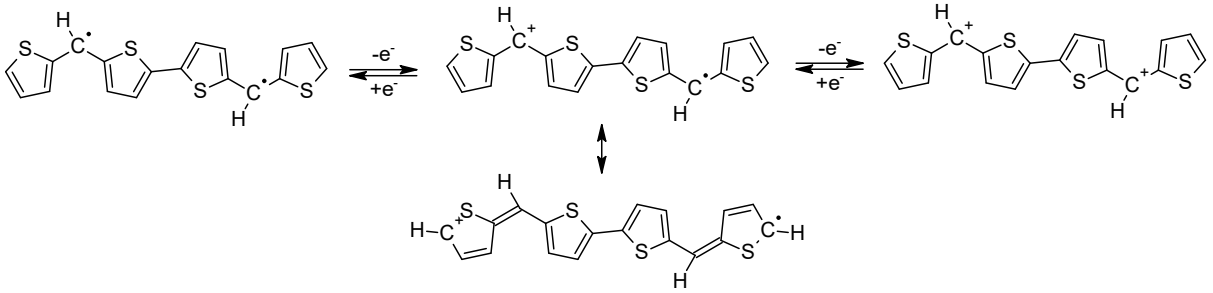

Scheme 6.7.19 Possible redox process.

This structural limitation is reflected in the electrochemical behaviour. As shown in Figure 5.3.4(a), only modest redox activity is observed in the low-potential region (highlighted in the inset), without the progressive current increase characteristic of sustained electropolymerization. The oxidized intermediates therefore remain either weakly bound to the electrode surface, soluble in the electrolyte, or poorly conducting, preventing formation of a persistent electroactive film.

The cyclic voltammogram of the electrochemically generated film (Figure 5.3.5(a)) further supports this interpretation. In the lower potential region, a broad anodic wave with a corresponding cathodic feature is observed, which can be assigned to oxidation of neutral conjugated segments to radical cation (polaron) states. The broadness of the response reflects structural heterogeneity and limited delocalization along the short, conjugated backbone. At more positive potentials, a second, poorly resolved anodic feature appears, accompanied by weak reduction signals. This response is attributed to further oxidation of polaronic sites toward higher charged (bipolaron-like) states. However, effective stabilization of fully developed dicationic species is unfavorable in such a short conjugated system. Charge localization and insufficient π-extension reduce electrochemical reversibility and promote irreversible oxidative degradation.

Consequently, compound **4** does not form a stable, long-lived electroactive film under repeated cycling. Instead, oxidation beyond the initial reversible regime leads to degradation or dissolution of the generated species, consistent with the electrochemical instability typically observed for short-chain thiophene systems under strongly oxidizing conditions [73].

6.7.5. Oxidative pathways of compound 5

The electrochemical oxidation of compound **5** is expected to proceed through mechanisms analogous to those proposed for compound **1**, owing to the presence of a conjugation-breaking sp^3-hybridized methylene bridge bearing abstractable hydrogen atoms. As in compound **1**, oxidation initially generates a thiophene-centred radical cation localized within one of the conjugated segments.

Two mechanistic scenarios may be considered. In the first pathway, stepwise oxidation occurs at one thiophene arm, followed by dehydrogenation from the methylene bridge to generate a carbon-centred radical intermediate. In the second pathway, sequential oxidation of both thiophene arms precedes dehydrogenation from the bridge. Despite differences in the order of oxidation and proton loss, both routes ultimately converge to the same neutral conjugated intermediate, as formation of the bridge-centred radical and subsequent rearomatization lead to an electronically equivalent product.

Because the final outcome of both sequences is identical, only the first pathway is illustrated in detail in Scheme 6.7.20 for clarity. This mechanism captures the essential features of oxidation in compound **5**: radical cation formation, bridge dehydrogenation, restoration of aromaticity, and generation of a neutral conjugated structure capable of further oxidative transformation.

Notably, in contrast to compound **4**, the longer conjugation length in compound **5** enhances delocalization of charge carriers within each thiophene segment. However, the presence of the sp^3 bridge still interrupts through-bond conjugation, limiting complete delocalization across the entire framework. As a result, oxidative processes remain localized within individual segments, and subsequent coupling or degradation pathways depend on the balance between charge stabilization and radical reactivity.

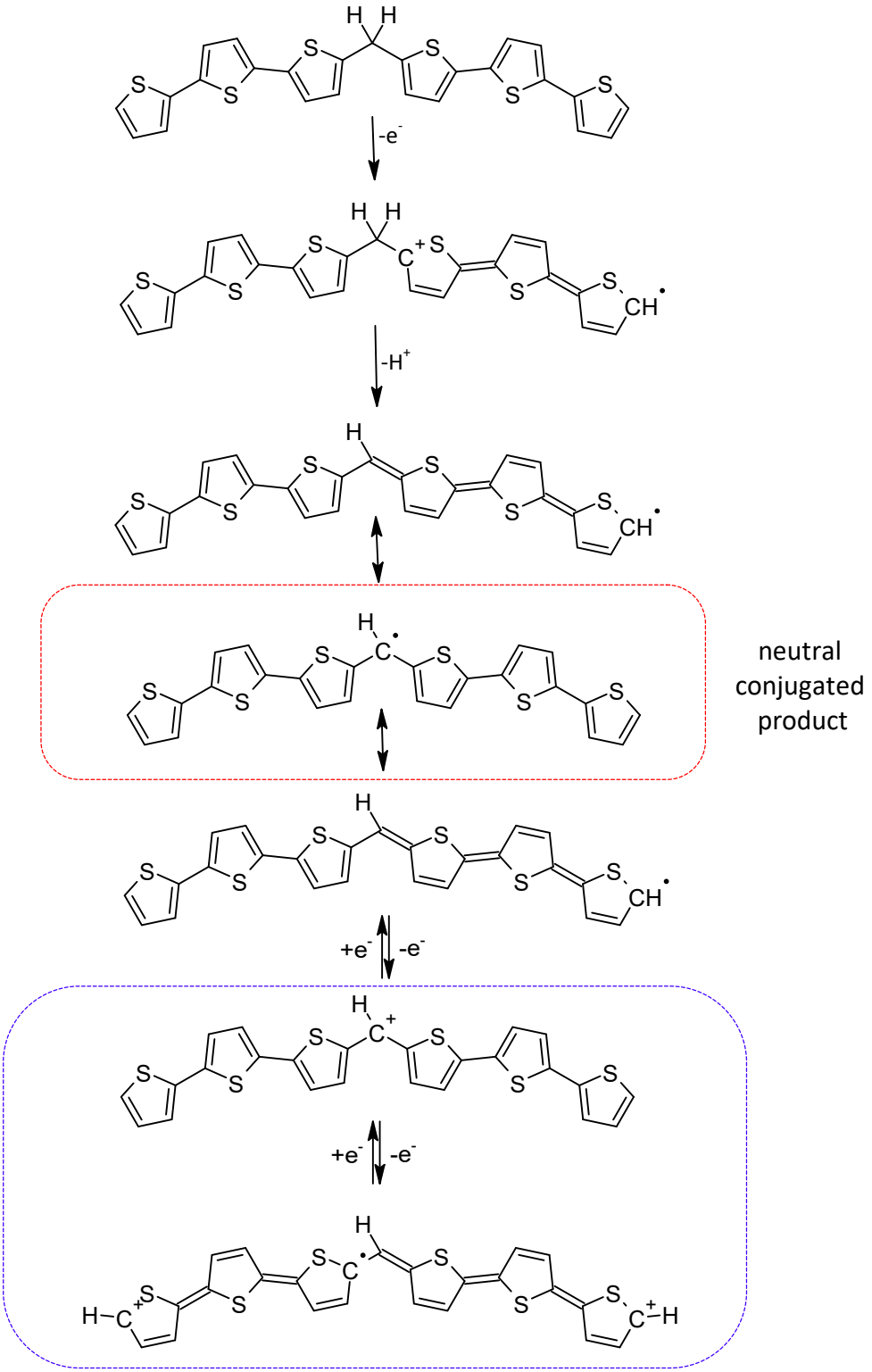

*Scheme 6.7.20 The first possible mechanism for the oxidation of compound **5**.*

The stepwise oxidation mechanism proposed in Scheme 6.7.20 is in good agreement with the cyclic voltammogram shown in Figure 5.3.4(d). The first anodic peak observed at lower positive potential corresponds to a one-electron oxidation of the neutral monomer, generating a thiophene-centred radical cation (polaron). This assignment is consistent with the typical electrochemical behaviour of oligothiophene derivatives.

Following initial oxidation, the radical cation undergoes deprotonation at the sp^3-hybridized methylene bridge. The increased acidity of the bridge hydrogen atoms arises from the positive charge density introduced upon oxidation, which stabilizes proton loss and facilitates formation of a carbon-centred neutral radical. This deprotonation step restores conjugation across the framework and generates a more electronically delocalized intermediate.

The resulting neutral radical (highlighted in the red caption of Scheme 6.7.20) undergoes intramolecular charge and spin redistribution accompanied by minor structural relaxation. This delocalization stabilizes the radical centre and opens subsequent oxidation possibility. Electrochemical oxidation of this neutral, conjugated intermediate proceeds through additional reversible one-electron steps. The first of these generates a cation species, while further oxidation at higher applied potential would produce a radical dication state. This, somewhat exotic state, is a prerequisite for radical cation coupling to take place, and higher molecular weight products to form. Under restricted potential windows, the redox processes highlighted in the blue region of Scheme 6.7.20 are favoured.

The highly oxidized species generated at elevated anodic potentials (Scheme 6.7.20), formally described as dicationic radical intermediate, may in principle undergo intermolecular coupling reactions. Such coupling processes could produce extended conjugated structures through carbon–carbon bond formation, as illustrated in Scheme 6.7.21. However, under the experimental conditions employed, this pathway is unlikely to be dominant. Methine bridge conjugated sexithiophene could well be sufficiently extended to accommodate a polaron and a soliton together, diminishing their reactivity. In addition, electrostatic repulsion between highly charged species could disfavour close approach required for bimolecular bond formation. As a result, reversible redox cycling is more probable than extensive chain growth of compound **5** at these potentials.

Consequently, although Scheme 6.7.21 represents a mechanistically feasible transformation at sufficiently high oxidation potentials, the electrochemical data hint that such intermolecular coupling plays only a minor role in the observed behaviour of compound **5**.

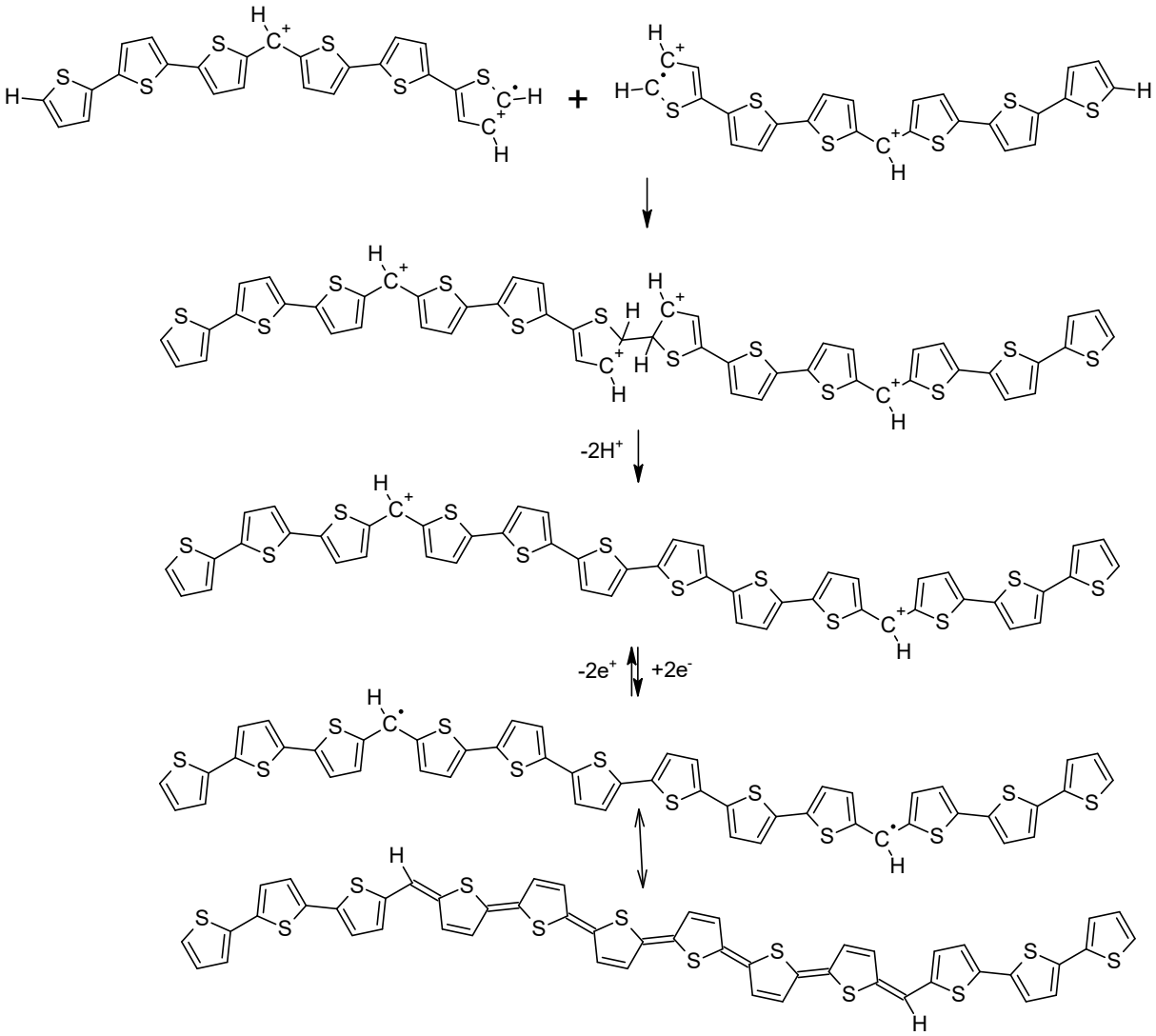

*Scheme 6.7.21 Possible coupled reaction and electrochemical transformation steps of compound **5**.*

6.7.6. Oxidative pathways of compound 6

For compound **6**, two mechanistically plausible oxidation pathways are proposed. These pathways differ in the fate of the initially generated radical cation but originate from a common first electrochemical step.

In the first pathway, electrochemical oxidation produces a thiophene-centred radical cation. Subsequent deprotonation occurs at the sp^3-hybridized ethylene spacer, where positive charge density increases the acidity of the adjacent hydrogen atoms. Proton loss generates a localized carbon-centred radical intermediate. This stepwise oxidation–dehydrogenation sequence restores partial conjugation and leads to a stabilized radical species, as illustrated in Scheme 6.7.22. The localization of spin density near the spacer limits excessive charge accumulation and reduces the likelihood of uncontrolled intermolecular reactions.

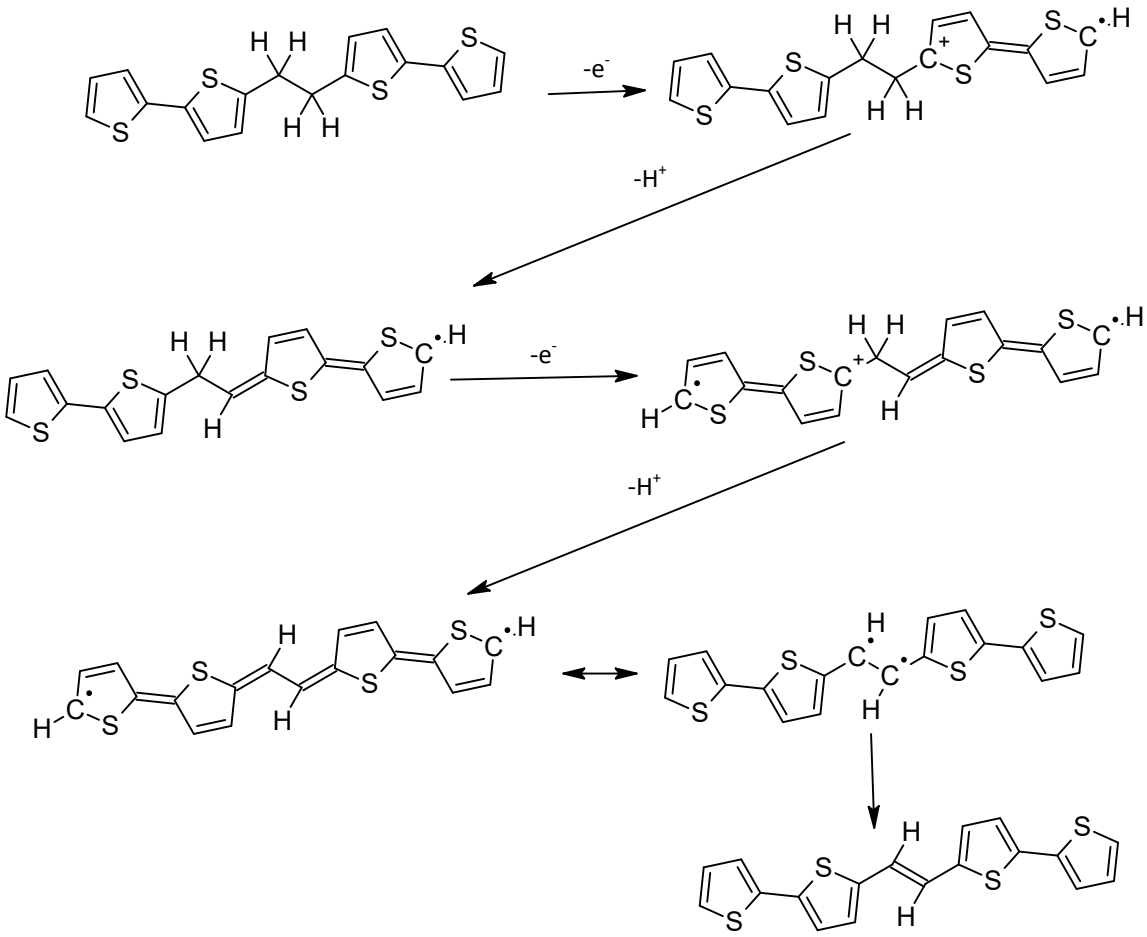

Scheme 6.7.22 Stepwise oxidation and dehydrogenation at the sp³ ethylene spacer leading to localized radical formation with ultimate collapse to a vinylene bond.

Scheme 6.7.22 illustrates the predominant stepwise electrochemical oxidation pathway of compound 6, which consists of quaterthiophene segments separated by an sp³-hybridized ethylene spacer. The oxidation process begins at the electrode surface with a one-electron transfer, generating a radical cation localized primarily on one of the terminal thiophene units. As is typical for oligothiophene systems, the highest spin and charge density reside at the α-positions of the thiophene ring, making these sites the most susceptible to oxidative activation.

Following electron removal, the oxidized intermediate undergoes rapid deprotonation. Depending on the local charge distribution, proton loss may occur either from an activated α-position of the thiophene ring or from the adjacent sp³ ethylene spacer. In the dominant pathway depicted in Scheme 6.7.22, deprotonation relieves charge accumulation and produces a neutral radical species. This step stabilizes the oxidized framework by taking away the positive charge. A subsequent one-electron oxidation may then occur on the neighbouring thiophene unit, again followed by proton loss. These consecutive oxidation–deprotonation steps generate reactive radical centres within the conjugated segments and the sp³ spacer.

The resulting radical intermediates are resonance-stabilized within each bihiophene domain. Crucially, the alkylene sp³ spacer interrupts through-bond π-conjugation and electronically isolates the two conjugated segments. As a consequence, spin density remains localized within individual thiophene domains rather than being fully delocalized across the entire molecule.

At sufficiently high oxidation levels, radical–radical coupling between activated α-positions can occur, leading to intermolecular C–C bond formation. This process generates a new conjugated -vinylene linkage between thiophene units, producing an extended conjugated structure capable of subsequent oxidation at the working electrode. However, such coupling requires adequate radical concentration and is therefore competitive only under higher anodic potentials. Overall, the stepwise oxidation–deprotonation sequence shown in Scheme 6.7.22 represents the kinetically favoured pathway for compound **6** under the experimental conditions employed. The presence of the sp^3 ethylene spacer governs charge localization, controls radical reactivity, and modulates the balance between reversible redox behaviour and productive coupling.

In the second pathway, the initially formed radical cation undergoes intermolecular coupling prior to deprotonation. This process would generate extended quaterthiophene-type segments linking two sp^3 ethylene spacers, thereby increasing effective conjugation length. However, such coupling requires sufficient radical concentration and close molecular proximity, conditions that are typically achieved only at higher anodic potentials.

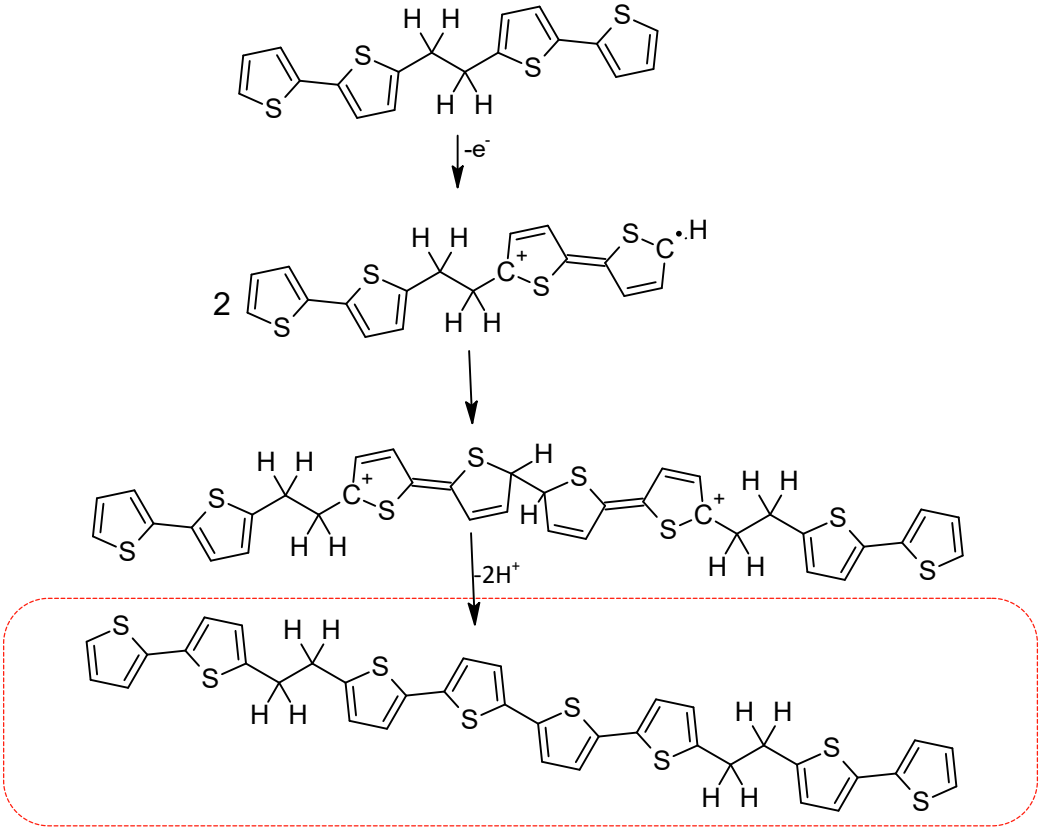

Scheme 6.7.23 Radical cation coupling pathway forming extended quaterthiophene segments between sp^3 ethylene spacers.

6.7.7. Oxidative pathways of compound 7

Compound **7** could follow oxidative pathways analogous to those described for compound **6**, but this time the crucial structural difference is the presence of an sp^3-hybridized methylene group not neighbouring any thiophene π-conjugated unit. As in compound **6**, the propylene saturated spacer interrupts through-bond π-conjugation and electronically separates the two bithiophene segments.

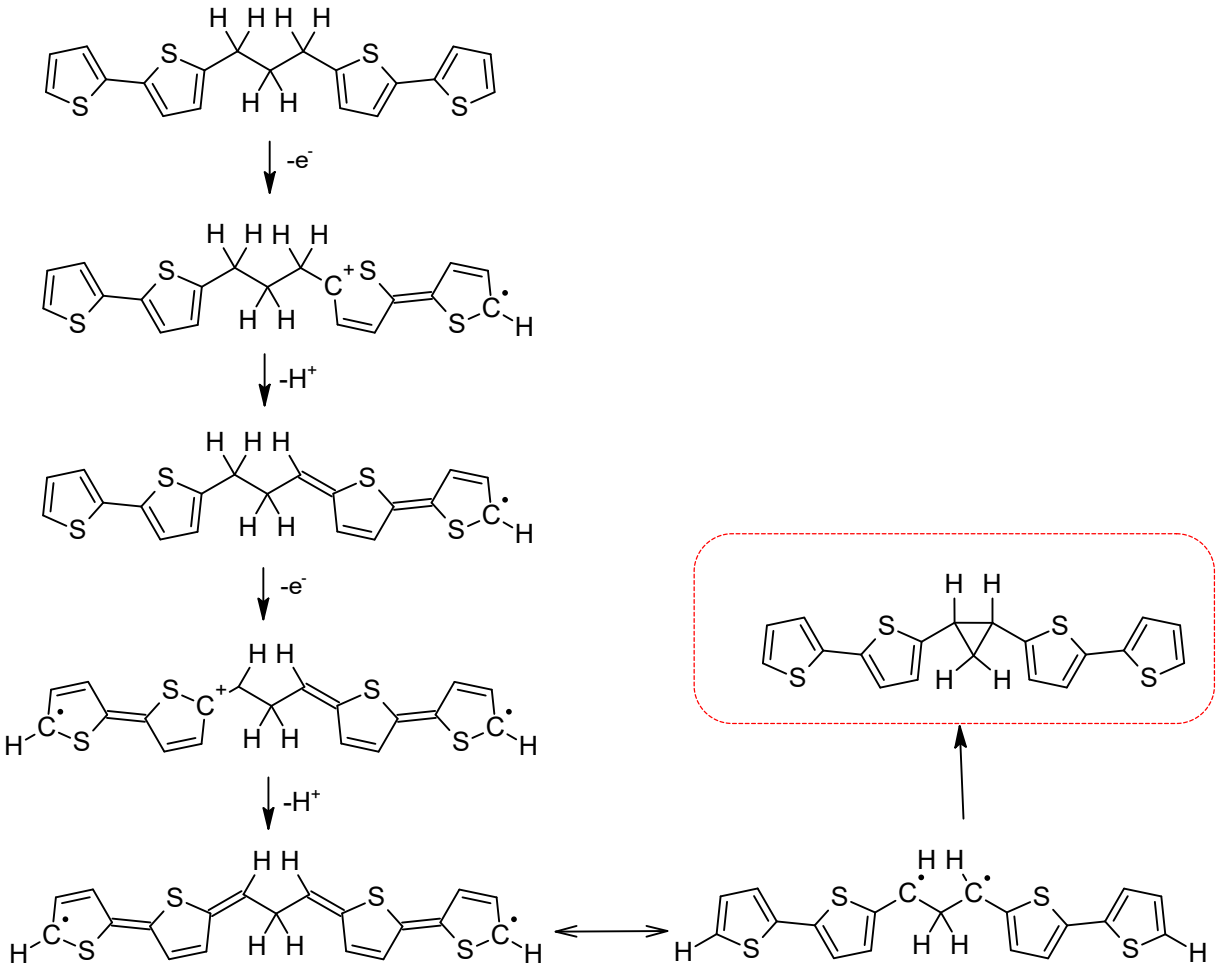

Scheme 6.7.24 Stepwise oxidation and dehydrogenation at the sp³ propylene spacer leading to localized radical formation.

The mechanism depicted in Scheme 6.7.24 describes the possible stepwise electrochemical oxidation and subsequent intramolecular transformation of compound **7**. The process begins with a one-electron oxidation at the electrode surface, generating a radical cation localized predominantly on a terminal thiophene unit. The highest spin and charge densities reside at the α-positions of the oxidized thiophene ring, rendering these sites most susceptible to subsequent chemical change.

Following electron removal, deprotonation occurs at the sp³ propylene spacer. The positive charge introduced during oxidation increases the acidity of the adjacent hydrogen atoms, facilitating proton loss and generating a neutral carbon-centred radical. This step relieves charge accumulation and stabilizes the oxidized framework while maintaining electronic separation between the two conjugated domains. A second one-electron oxidation may then occur on the opposite thiophene segment, again followed by proton loss. These sequential oxidation–deprotonation steps generate two spatially proximate radical centres within the same molecular framework. Because the propylene spacer has one more, central methylene unit, the radical centres remain localized within their respective thiophene domains.

At this stage, intramolecular radical coupling becomes feasible. The proximity of the two activated centres promotes C–C bond formation within the same molecule, leading to the cyclopropane motif highlighted in the red boxed structure of Scheme 6.7.24. This intramolecular coupling pathway would effectively stabilise the oxidized species and reduces the likelihood of extensive intermolecular chain propagation. The electrochemical behaviour of compound **7** presented in Chapter 5 supports this

mechanism. Compared to compound **6**, the longer propylene spacer further restricts effective conjugation and favours localized intramolecular reorganization rather than extended intermolecular growth. Consequently, compound **7** is expected to undergo controlled internal structural rearrangement upon oxidation rather than significant film-forming polymerization.

The second possible oxidation pathway is illustrated in Scheme 6.7.25.

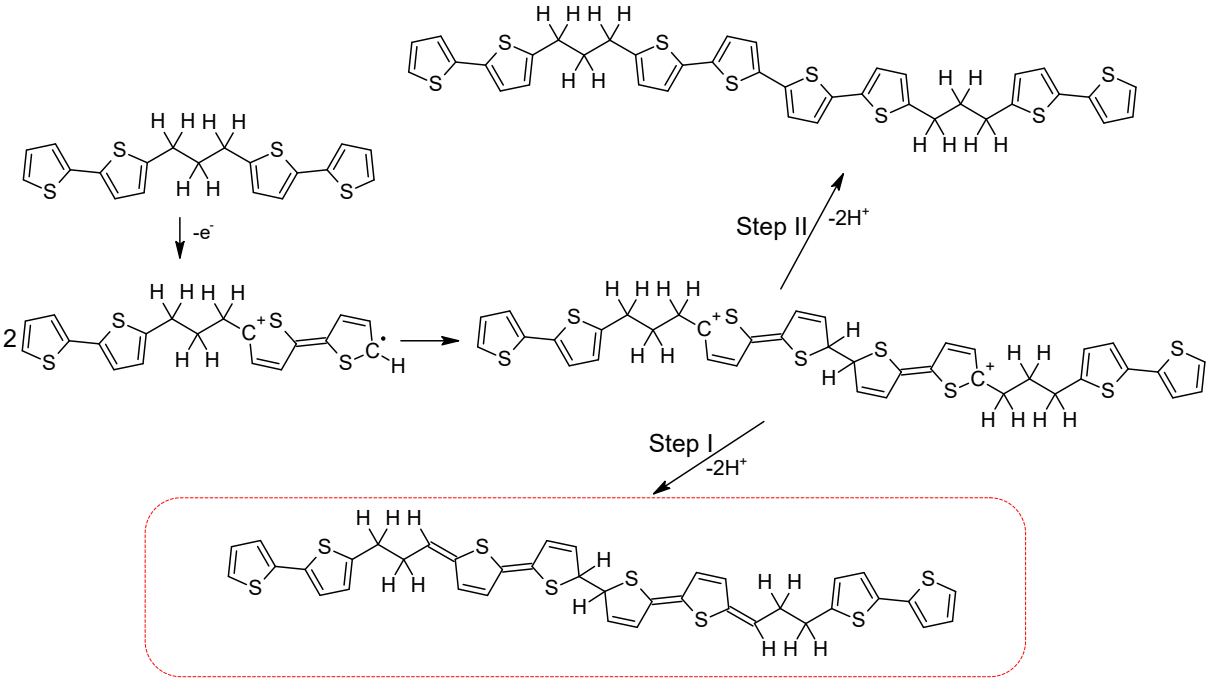

Scheme 6.7.25 Radical cation coupling pathway forming extended quaterthiophene segments between sp³ propylene spacers.

In this alternative mechanism, deprotonation at the sp³-hybridized propylene spacer does not occur following the initial electron transfer. Instead, anodic oxidation remains localized on the thiophene units, generating radical cation species that undergo coupling directly at the α-positions. Subsequent deprotonation steps then restore aromaticity after C–C bond formation, resulting in extended quaterthiophene segments bridging two sp³ propylene spacers.

Although mechanistically feasible, this pathway is unlikely to dominate under the experimental conditions. The absence of early deprotonation at the propylene spacer leads to accumulation of positive charge within the thiophene domains, increasing electrostatic repulsion and reducing intermediate stability. In contrast, the stepwise oxidation–deprotonation pathway shown in Scheme 6.7.24 provides immediate charge relief through proton loss, generating a neutral radical that is thermodynamically and kinetically more stabilized.

Furthermore, efficient intermolecular radical cation coupling requires sufficient radical concentration and favourable molecular orientation. Given the electronic isolation imposed by the propylene spacer and the lack of significant current growth observed in the cyclic voltammograms (Chapter 5), extensive radical–radical coupling to form extended quaterthiophene chains appears limited. Therefore, while Scheme 6.7.25 represents a chemically plausible pathway at higher anodic potentials, the electrochemical data suggest that it plays only a minor role compared to the dominant stepwise oxidation–dehydrogenation mechanism.

Due to the relatively long sp³ propylene spacer, compound **7** may adopt folded or partially stacked conformations in solution, absent from the other π-conjugation broken compounds of this

series. In such conformations, the two terminal bithiophene arms can approach one another and engage in intramolecular π–π interactions. This conformational flexibility introduces an alternative electrochemical pathway, illustrated in Scheme 6.7.26, in which deprotonation at the propylene spacer does not occur.

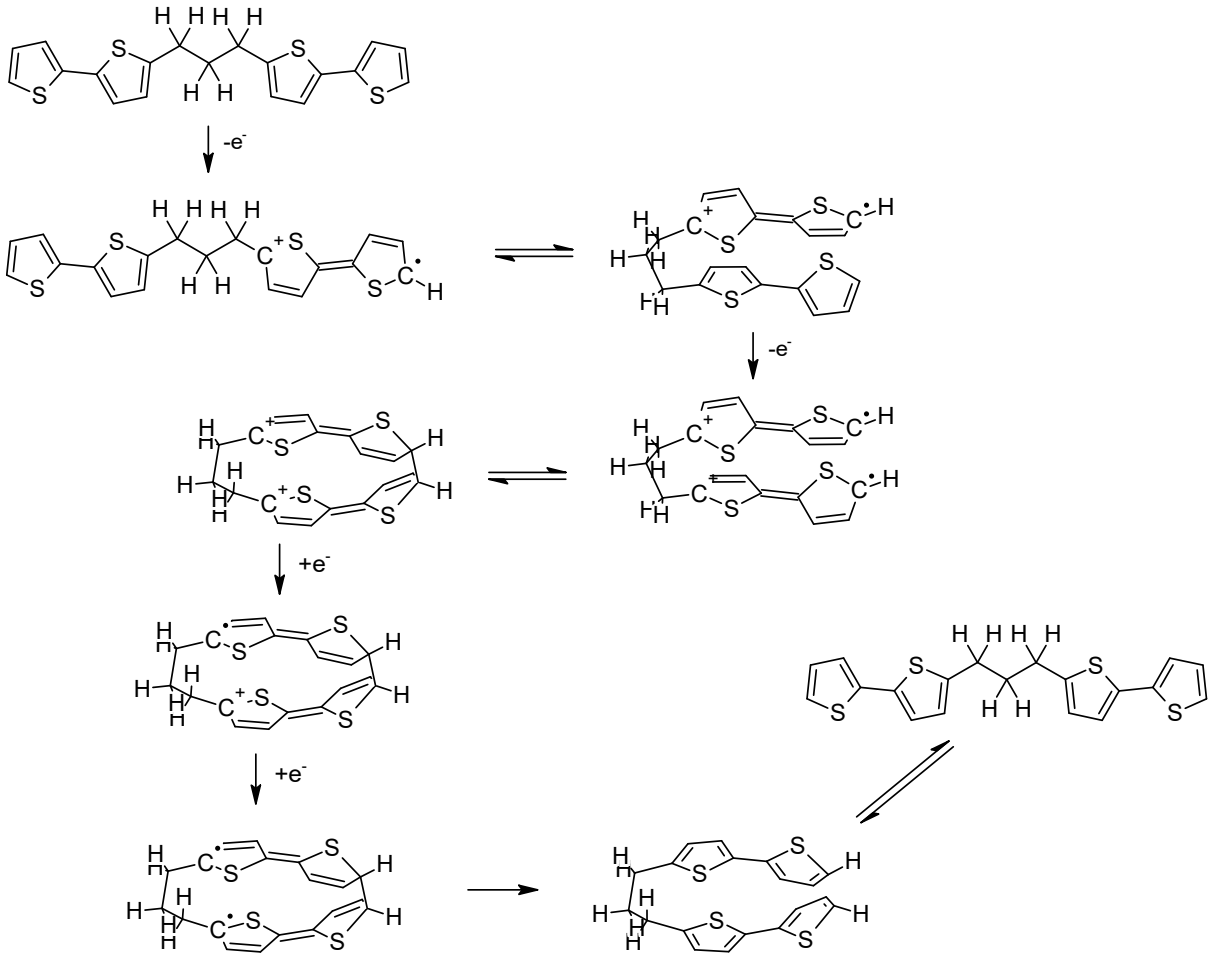

Scheme 6.7.26 Proposed oxidation pathway of compound 7 without sp³ propylene deprotonation

In this mechanism, oxidation begins with a one-electron transfer localized on a thiophene unit, generating a radical cation. Spin and charge density are redistributed within the thiophene rings through resonance, while the propylene spacer remains electronically insulating and chemically intact. Because the spacer interrupts through-bond conjugation, charge delocalization is confined to individual thiophene segments rather than extending across the entire molecular framework.

Upon further anodic polarization, a second one-electron oxidation can occur on the opposing thiophene arm. Rather than forming a fully delocalized dication, the molecule accommodates two localized polaronic sites within spatial proximity. In the folded conformation, these oxidized segments can interact through space mediated, short-range orbital overlap interactions, promoting intramolecular radical coupling. This coupling step produces the cyclic or closed motif shown in Scheme 6.7.26. Importantly, the process is intramolecular and does not require cleavage or deprotonation of the sp³ propylene spacer. The resulting folded intermediate stabilizes the oxidized state locally and effectively limits further propagation or intermolecular chain growth.

Subsequent electron exchange steps allow partial structural relaxation. The overall redox equilibrium therefore favours either regeneration of the neutral monomer or retention of locally coupled species at the electrode surface, rather than electropolymerization.

This mechanism provides a coherent explanation for the experimental observations reported in Chapter 5: the absence of significant current amplification during repeated cycling indicates limited or no long-range chain growth, the broad and localized spectroelectrochemical features are consistent with polaron formation confined to individual thiophene domains, and the lack of broad, low-energy absorption bands characteristic of highly delocalized bipolaronic states supports a localized oxidation model. Thus, the conformational flexibility introduced by the sp^3 propylene spacer allows compound **7** to access a π–π-stabilized intramolecular oxidation pathway.

An alternative oxidation pathway for compound **7** involves the formation of extended quaterthiophene segments between two sp^3 propylene spacers without deprotonation at the carbon bridge (Scheme 6.7.27).

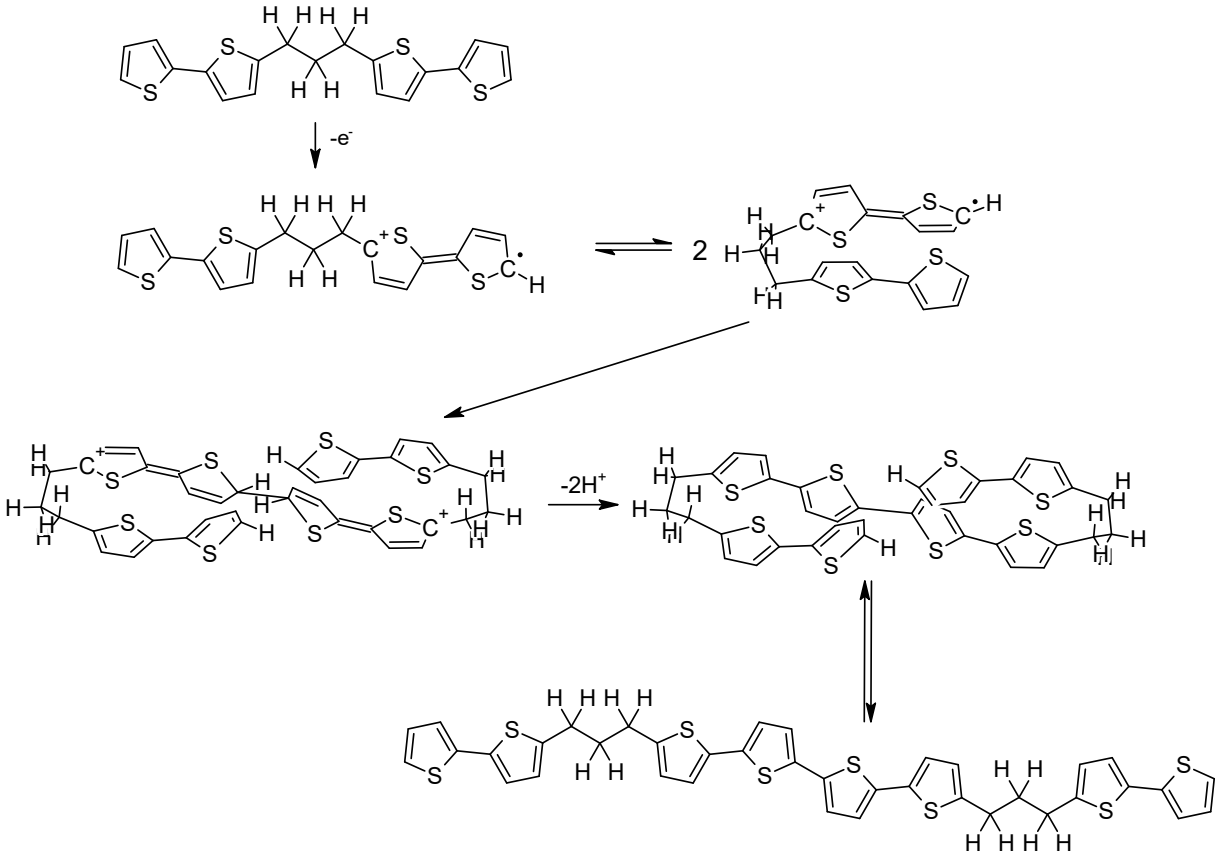

Scheme 6.7.27 Proposed oxidation pathway of radical cation coupling pathway forming extended quaterthiophene segments between sp^3 propylene spacers. without sp^3 propylene deprotonation.

In this mechanism, anodic oxidation remains localized exclusively on the thiophene α-positions, while the propylene spacer remains chemically intact and electronically insulating. The process begins with a one-electron oxidation at a terminal thiophene unit, generating a radical cation. Spin and charge density are delocalized within the thiophene segment through resonance stabilization but do not extend across the propylene spacer due to the interruption of π-conjugation. A second molecule undergoes a similar one-electron oxidation, producing another thiophene-centred radical cation.

When two such oxidized species approach each other, radical–radical coupling occurs at the activated α-positions of adjacent thiophene units. This intermolecular C–C bond formation leads to the generation of a quaterthiophene segment bridging two propylene spacers, as shown in Scheme 6.7.27. Subsequent proton loss ($-2H^+$) restores aromaticity within the newly formed thiophene units, yielding a more conjugated and thermodynamically stabilized product. When two such oxidized species approach each other, radical–radical coupling occurs at the activated α-positions of adjacent thiophene units. This intermolecular C–C bond formation leads to the generation of a quaterthiophene segment bridging two propylene spacers, as shown in Scheme 6.7.27. Subsequent proton loss ($-2H^+$) restores aromaticity within the newly formed thiophene units, yielding a more conjugated and thermodynamically stabilized product.

However, although this pathway formally produces extended conjugated segments, it is expected to be less favourable under typical experimental conditions. The relatively long and flexible propylene spacers reduce effective orbital overlap and decrease the probability of productive intermolecular alignment. Moreover, because the spacer electronically isolates each conjugated domain, stabilization of the radical cation occurs locally rather than promoting long-range delocalization required for efficient polymer growth. This mechanistic proposal is consistent with the electrochemical behaviour observed in Chapter 5. The cyclic voltammogram of compound **7** does not exhibit the progressive current increase characteristic of sustained electropolymerization. Instead, the response is dominated by localized redox processes, indicating that radical–cation coupling between molecules occurs only to a limited extent. The absence of strong film growth further supports that intermolecular quaterthiophene formation is not the dominant oxidation pathway.

7. Conclusions and perspectives

This doctoral dissertation systematically investigated the synthesis, electrochemical behaviour, and spectroelectrochemical response of thiophene-based oligomers incorporating purposely introduced π-conjugation-break spacers. Through rational molecular design, three structurally controlled series were prepared to examine the effects of bridge substitution, conjugation length, and spacer length on redox processes and electronic-state evolution. The molecular structures of all synthesized monomers were confirmed by ^{1}H and ^{13}C NMR spectroscopy, ensuring structural integrity prior to functional investigation. Spectroscopy and electrochemistry of the monomers demonstrated that the sp^3-hybridized bridges effectively interrupt long-range π-conjugation while preserving localized chromophoric behaviour within individual thiophene segments. These ground-state observations established the electronic isolation imposed by the spacer units.

Electrochemical studies revealed that oxidation proceeds predominantly via stepwise one-electron processes strongly governed by molecular architecture. Bridge substitution modulates oxidation potential and intermediate stability, increasing substitution at the sp^3 centre enhancing radical stabilization and reversibility. Extension of thiophene conjugation length lowers oxidation potential and promotes intra-segment delocalization, yet full electronic communication across the molecule remains limited by the conjugation break. Systematic elongation of the spacer from methylene to ethylene and propylene progressively reduces electronic coupling between conjugated domains, leading to increased charge localization and diminished electrochemical reactivity.

UV–Vis–NIR spectroelectrochemical analysis performed on electrogenerated films across all three series revealed the depletion of the neutral π–π* transition and the emergence of new low-energy absorption bands upon oxidation. These spectral features are consistent with the formation of localized polaronic species rather than fully delocalized bipolaronic states typical of uninterrupted polythiophene backbones. Direct evidence for spin-active radical species was obtained through EPR spectroelectrochemical analysis of compound **3**, confirming the presence and evolution of paramagnetic intermediates during oxidation of its polymer. For the remaining systems, charge-carrier assignment is supported by coherent electrochemical reversibility and characteristic spectroelectrochemical signatures.

Importantly, the observed spectral evolution during controlled doping and dedoping cycles directly correlates spacer architecture with electrochromic behaviour. The introduction of conjugation-break spacers enables modulation of optical transitions, colour change, and redox stability by controlling the degree of charge localization within the thiophene framework. Methylene-bridged systems exhibit stronger electrochromic response due to more effective electronic communication, whereas longer spacers promote localized charge states and reduced optical contrast. Thus, spacer engineering provides a molecular-level handle for tuning electrochromic properties without fundamentally altering the conjugated core.

Overall, this work establishes a mechanistically grounded framework linking molecular structure, oxidation pathways, charge localization, and electrochromic response in conjugation-broken thiophene systems. The findings demonstrate that conjugation-break spacers function not as passive defects but as deliberate electronic modulators capable of tailoring redox behaviour and optical switching characteristics. These insights contribute to the rational design of tuneable organic semiconducting materials for electrochromic devices, flexible electronics, and redox-active functional polymers.

8. References

[1] Y.C. Lin, M. Matsuda, K.I. Sato, C.K. Chen, W.C. Yang, C.C. Chueh, T. Higashihara, W.C. Chen, Intrinsically stretchable naphthalenediimide-bithiophene conjugated statistical terpolymers using branched conjugation break spacers for field-effect transistors, Polym. Chem. 12 (2021) 6167–6178. https://doi.org/10.1039/d1py01154e.

[2] J. Qin, L. Lan, S. Chen, F. Huang, H. Shi, W. Chen, H. Xia, K. Sun, C. Yang, Recent Progress in Flexible and Stretchable Organic Solar Cells, Adv. Funct. Mater. 30 (2020) 1–22. https://doi.org/10.1002/adfm.202002529.

[3] X. Xiang, W. Shao, L. Liang, X.Q. Chen, F.G. Zhao, Z. Lu, W. Wang, J. Li, W.S. Li, Photovoltaic poly(rod-coil) polymers based on benzodithiophene-centred A-D-A type conjugated segments and dicarboxylate-linked alkyl non-conjugated segments, RSC Adv. 6 (2016) 23300–23309. https://doi.org/10.1039/c6ra01200k.

[4] Q. Shi, J. Wang, I. Aziz, P.S. Lee, Stretchable and Wearable Resistive Switching Random-Access Memory, Adv. Intell. Syst. 2 (2020) 2000007. https://doi.org/10.1002/aisy.202000007.

[5] A. Facchetti, π-Conjugated polymers for organic electronics and photovoltaic cell applications, Chem. Mater. 23 (2011) 733–758. https://doi.org/10.1021/cm102419z.

[6] R. Noriega, J. Rivnay, K. Vandewal, F.P.V. Koch, N. Stingelin, P. Smith, M.F. Toney, A. Salleo, A general relationship between disorder, aggregation and charge transport in conjugated polymers, Nat. Mater. 12 (2013) 1038–1044. https://doi.org/10.1038/nmat3722.

[7] C.G. Wu, C.Y. Lai, N.L. Hsiao, Molecular engineering leading to better processability of conjugated chromophores: The optical properties of new soluble copolymers containing alternative oligo-octylthiophene and oligo-methylene blocks, Eur. Polym. J. 45 (2009) 879–887. https://doi.org/10.1016/j.eurpolymj.2008.11.037.

[8] Z.Y. Wang, Z.F. Yao, Y. Lu, L. Ding, Z. Di Yu, H.Y. You, X.Y. Wang, Y.Y. Zhou, L. Zou, J.Y. Wang, J. Pei, Precise tracking and modulating aggregation structures of conjugated copolymers in solutions, Polym. Chem. 11 (2020) 3716–3722. https://doi.org/10.1039/d0py00456a.

[9] E.L. Melenbrink, K.M. Hilby, K. Choudhary, S. Samal, N. Kazerouni, J.L. McConn, D.J. Lipomi, B.C. Thompson, Influence of Acceptor Side-Chain Length and Conjugation-Break Spacer Content on the Mechanical and Electronic Properties of Semi-Random Polymers, ACS Appl. Polym. Mater. 1 (2019) 1107–1117. https://doi.org/10.1021/acsapm.9b00115.

[10] E.L. Melenbrink, K.M. Hilby, M.A. Alkhadra, S. Samal, D.J. Lipomi, B.C. Thompson, Influence of Systematic Incorporation of Conjugation-Break Spacers into Semi-Random Polymers on Mechanical and Electronic Properties, ACS Appl. Mater. Interfaces. 10 (2018) 32426–32434. https://doi.org/10.1021/acsami.8b10608.

[11] Y. Zhao, X. Zhao, Y. Zang, C.A. Di, Y. Diao, J. Mei, Conjugation-break spacers in semiconducting polymers: Impact on polymer processability and charge transport properties, Macromolecules. 48 (2015) 2048–2053. https://doi.org/10.1021/acs.macromol.5b00194.

[12] Y.C. Lin, M. Matsuda, C.K. Chen, W.C. Yang, C.C. Chueh, T. Higashihara, W.C. Chen, Investigation of the Mobility-Stretchability Properties of Naphthalenediimide-Based Conjugated Random Terpolymers with a Functionalized Conjugation Break Spacer, Macromolecules. 54 (2021) 7388–7399. https://doi.org/10.1021/acs.macromol.1c00534.

[13] L.A. Galuska, W.W. McNutt, Z. Qian, S. Zhang, D.W. Weller, S. Dhakal, E.R. King, S.E. Morgan, J.D. Azoulay, J. Mei, X. Gu, Impact of Backbone Rigidity on the Thermomechanical Properties of Semiconducting Polymers with Conjugation Break Spacers, Macromolecules. 53 (2020) 6032–6042. https://doi.org/10.1021/acs.macromol.0c00889.

[14] G.J.N. Wang, F. Molina-Lopez, H. Zhang, J. Xu, H.C. Wu, J. Lopez, L. Shaw, J. Mun, Q. Zhang, S.

Wang, A. Ehrlich, Z. Bao, Nonhalogenated Solvent Processable and Printable High-Performance Polymer Semiconductor Enabled by Isomeric Nonconjugated Flexible Linkers, Macromolecules. 51 (2018) 4976–4985. https://doi.org/10.1021/acs.macromol.8b00971.

[15] Y. Zhao, X. Zhao, M. Roders, A. Gumyusenge, A.L. Ayzner, J. Mei, Melt-Processing of Complementary Semiconducting Polymer Blends for High Performance Organic Transistors, Adv. Mater. 29 (2017). https://doi.org/10.1002/adma.201605056.

[16] H.J. Li, J.T. Wang, C.Y. Mei, W.S. Li, A new class of organic photovoltaic materials: Poly(rod-coil) polymers having alternative conjugated and non-conjugated segments, Chem. Commun. 50 (2014) 7720–7722. https://doi.org/10.1039/c4cc03409k.

[17] E.L. Melenbrink, K.M. Hilby, M.A. Alkhadra, S. Samal, D.J. Lipomi, B.C. Thompson, Influence of Systematic Incorporation of Conjugation-Break Spacers into Semi-Random Polymers on Mechanical and Electronic Properties, ACS Appl. Mater. Interfaces. 10 (2018) 32426–32434. https://doi.org/10.1021/acsami.8b10608.

[18] J.Y. Oh, S. Rondeau-Gagné, Y.C. Chiu, A. Chortos, F. Lissel, G.J.N. Wang, B.C. Schroeder, T. Kurosawa, J. Lopez, T. Katsumata, J. Xu, C. Zhu, X. Gu, W.G. Bae, Y. Kim, L. Jin, J.W. Chung, J.B.H. Tok, Z. Bao, Intrinsically stretchable and healable semiconducting polymer for organic transistors, Nature. 539 (2016) 411–415. https://doi.org/10.1038/nature20102.

[19] A. Berlin, G. Fontana, G. Pagani, G. Schiavon, G. Zotti, Anodic coupling of oligothiophenes bridged by ethylene groups, Synth. Met. 57 (1993) 4796–4801. https://doi.org/10.1016/0379-6779(93)90819-I.

[20] T. Benincori, S. Rizzo, F. Sannicolo, G. Schiavon, S. Zecchin, G. Zotti, An Electrochemically Prepared Small-Bandgap Poly (biheteroarylidenemethine): Poly { bi [(3 , 4-ethylenedioxy) thienylene] methine }, (2003) 5114–5118.

[21] S.A. Jenekhe, A class of narrow-band-gap semiconducting polymers, Nature. 322 (1986) 345–347. https://doi.org/10.1038/322345a0.

[22] 18 (1987) 6 9 9 - 7 0 4 ~vnthetic Metals, 済無No Title No Title No Title, ~vnthetic Met. 18 6 9 9 - 7 0 4. 4 (2016) 1–23.

[23] T.P. Kaloni, P.K. Giesbrecht, G. Schreckenbach, M.S. Freund, Polythiophene: From Fundamental Perspectives to Applications, Chem. Mater. 29 (2017) 10248–10283. https://doi.org/10.1021/acs.chemmater.7b03035.

[24] G. Koßmehl, F.D. Hoppe, B. Hirsch, Liquid Crystalline Compounds in the Thiophene Series, Part 6 Synthesis and Characterization of Azomethines and Vinylenes with Two Mesogenic Groups and Different Alkylene Spacer Lengths, Zeitschrift Fur Naturforsch. - Sect. B J. Chem. Sci. 48 (1993) 826–843. https://doi.org/10.1515/znb-1993-0619.

[25] K.J. Hoffmann, E.J. Samuelsen, P.H.J. Carlsen, Broken π-conjugated thiophene systems, Synth. Met. 114 (2000) 167–172. https://doi.org/10.1016/s0379-6779(00)00243-5.

[26] K.M. Mangold, K. Morgenschweis, K. Jüttner, Relaxation of polythiophenes bridged by alkyl chains, Electrochim. Acta. 44 (1999) 1865–1869. https://doi.org/10.1016/S0013-4686(98)00327-2.

[27] K.M. Mangold, K. Jüttner, Structural modified polythiophene by cross-linking alkyl chains, Synth. Met. 101 (1999) 71–72. https://doi.org/10.1016/S0379-6779(98)01153-9.

[28] T. Satou, T. Sakai, T. Kaikawa, K. Takimiya, T. Otsubo, Y. Aso, A,Ω-Bis(Quinquethienyl)Alkanes As a Π-Dimer Model of Polythiophene, Org. Lett. 6 (2004) 997–1000. https://doi.org/10.1021/ol0499396.

[29] C.K. Chiang, C.R. Fincher, Y.W. Park, A.J. Heeger, H. Shirakawa, E.J. Louis, S.C. Gau, A.G. MacDiarmid, Electrical Conductivity in Doped Polyacetylene, Phys. Rev. Lett. 39 (1977) 1098–

1101. https://doi.org/10.1103/PhysRevLett.39.1098.

[30] D. Raichman, R. Ben-Shabat Binyamini, J.-P. Lellouche, A new polythiophene-driven coating method on an inorganic INT/IF-WS 2 nanomaterial surface, RSC Adv. 6 (2016) 4490–4504. https://doi.org/10.1039/C5RA21370C.

[31] K. Kadac, J. Nowaczyk, Polythiophene nanoparticles in aqueous media, J. Appl. Polym. Sci. 133 (2016). https://doi.org/10.1002/app.43495.

[32] J.L. Brédas, B. Thémans, J.G. Fripiat, J.M. André, R.R. Chance, Highly conducting polyparaphenylene, polypyrrole, and polythiophene chains: An ab initio study of the geometry and electronic-structure modifications upon doping, Phys. Rev. B. 29 (1984) 6761–6773. https://doi.org/10.1103/PhysRevB.29.6761.

[33] A.G. MacDiarmid, "Synthetic metals": a novel role for organic polymers, Curr. Appl. Phys. 1 (2001) 269–279. https://doi.org/10.1016/S1567-1739(01)00051-7.

[34] X. Zhao, X. Zhan, Electron transporting semiconducting polymers in organic electronics, Chem. Soc. Rev. 40 (2011) 3728. https://doi.org/10.1039/c0cs00194e.

[35] G.A. Sotzing, C.A. Thomas, J.R. Reynolds, P.J. Steel, Low Band Gap Cyanovinylene Polymers Based on Ethylenedioxythiophene, Macromolecules. 31 (1998) 3750–3752. https://doi.org/10.1021/ma971290f.

[36] X. Guo, M. Baumgarten, K. Müllen, Designing π-conjugated polymers for organic electronics, Prog. Polym. Sci. 38 (2013) 1832–1908. https://doi.org/10.1016/j.progpolymsci.2013.09.005.

[37] W. Hresko, Feature Article, Remedial Spec. Educ. 10 (1989) 8–8. https://doi.org/10.1177/074193258901000304.

[38] J. Roncali, Synthetic Principles for Bandgap Control in Linear π-Conjugated Systems, Chem. Rev. 97 (1997) 173–206. https://doi.org/10.1021/cr950257t.

[39] A.J. Heeger, S. Kivelson, J.R. Schrieffer, W.-P. Su, Solitons in conducting polymers, Rev. Mod. Phys. 60 (1988) 781–850. https://doi.org/10.1103/RevModPhys.60.781.

[40] G. Tourillon, F. Garnier, New electrochemically generated organic conducting polymers, J. Electroanal. Chem. Interfacial Electrochem. 135 (1982) 173–178. https://doi.org/10.1016/0022-0728(82)90015-8.

[41] R.D. McCullough, The Chemistry of Conducting Polythiophenes, Adv. Mater. 10 (1998) 93–116. https://doi.org/10.1002/(SICI)1521-4095(199801)10:2<93::AID-ADMA93>3.0.CO;2-F.

[42] A. Facchetti, π-Conjugated Polymers for Organic Electronics and Photovoltaic Cell Applications, Chem. Mater. 23 (2011) 733–758. https://doi.org/10.1021/cm102419z.

[43] M. Audenaert, G. Gusman, R. Deltour, Electrical conductivity of <math display="inline"> <mrow> <msub> <mrow> <mi mathvariant="normal">I</mi> </mrow> <mrow> <mn>2</mn> </mrow> </msub> </mrow> </math> -doped polyacetylene, Phys. Rev. B. 24 (1981) 7380–7382. https://doi.org/10.1103/PhysRevB.24.7380.

[44] J.L. Bredas, G.B. Street, Polarons, bipolarons, and solitons in conducting polymers, Acc. Chem. Res. 18 (1985) 309–315. https://doi.org/10.1021/ar00118a005.

[45] M. Leclerc, Optical and Electrochemical Transducers Based on Functionalized Conjugated Polymers, Adv. Mater. 11 (1999) 1491–1498. https://doi.org/10.1002/(SICI)1521-4095(199912)11:18<1491::AID-ADMA1491>3.0.CO;2-O.

[46] H. Sirringhaus, N. Tessler, R.H. Friend, Integrated Optoelectronic Devices Based on Conjugated Polymers, Science (80-.). 280 (1998) 1741–1744. https://doi.org/10.1126/science.280.5370.1741.

[47] E.L. Melenbrink, K.M. Hilby, M.A. Alkhadra, S. Samal, D.J. Lipomi, B.C. Thompson, Influence of

Systematic Incorporation of Conjugation-Break Spacers into Semi-Random Polymers on Mechanical and Electronic Properties, ACS Appl. Mater. Interfaces. 10 (2018) 32426–32434. https://doi.org/10.1021/acsami.8b10608.

[48] A. Rahmanudin, L. Yao, K. Sivula, Conjugation break spacers and flexible linkers as tools to engineer the properties of semiconducting polymers, Polym. J. 50 (2018) 725–736. https://doi.org/10.1038/s41428-018-0069-z.

[49] Y. Zhao, X. Zhao, Y. Zang, C. Di, Y. Diao, J. Mei, Conjugation-Break Spacers in Semiconducting Polymers: Impact on Polymer Processability and Charge Transport Properties, Macromolecules. 48 (2015) 2048–2053. https://doi.org/10.1021/acs.macromol.5b00194.

[50] C. Noël, P. Navard, Liquid crystal polymers, Prog. Polym. Sci. 16 (1991) 55–110. https://doi.org/10.1016/0079-6700(91)90007-8.

[51] T. Chung, The recent developments of thermotropic liquid crystalline polymers, Polym. Eng. Sci. 26 (1986) 901–919. https://doi.org/10.1002/pen.760261302.

[52] B.C. Schroeder, Z. Li, M.A. Brady, G.C. Faria, R.S. Ashraf, C.J. Takacs, J.S. Cowart, D.T. Duong, K.H. Chiu, C. Tan, J.T. Cabral, A. Salleo, M.L. Chabinyc, J.R. Durrant, I. McCulloch, Enhancing Fullerene-Based Solar Cell Lifetimes by Addition of a Fullerene Dumbbell, Angew. Chemie. 126 (2014) 13084–13089. https://doi.org/10.1002/ange.201407310.

[53] A. Gasperini, X.A. Jeanbourquin, A. Rahmanudin, X. Yu, K. Sivula, Enhancing the Thermal Stability of Solution-Processed Small-Molecule Semiconductor Thin Films Using a Flexible Linker Approach, Adv. Mater. 27 (2015) 5541–5546. https://doi.org/10.1002/adma.201501826.

[54] Z. Liang, R.A. Cormier, A.M. Nardes, B.A. Gregg, Developing perylene diimide based acceptor polymers for organic photovoltaics, Synth. Met. 161 (2011) 1014–1021. https://doi.org/10.1016/j.synthmet.2011.03.009.

[55] X. Xiang, W. Shao, L. Liang, X.-Q. Chen, F.-G. Zhao, Z. Lu, W. Wang, J. Li, W.-S. Li, Photovoltaic poly(rod-coil) polymers based on benzodithiophene-centred A–D–A type conjugated segments and dicarboxylate-linked alkyl non-conjugated segments, RSC Adv. 6 (2016) 23300–23309. https://doi.org/10.1039/C6RA01200K.

[56] I. Sokolik, Z. Yang, F.E. Karasz, D.C. Morton, Blue-light electroluminescence from p -phenylene vinylene-based copolymers, J. Appl. Phys. 74 (1993) 3584–3586. https://doi.org/10.1063/1.354539.

[57] G. Padmanaban, S. Ramakrishnan, Conjugation Length Control in Soluble Poly[2-methoxy-5-((2′-ethylhexyl)oxy)-1,4-phenylenevinylene] (MEHPPV): Synthesis, Optical Properties, and Energy Transfer, J. Am. Chem. Soc. 122 (2000) 2244–2251. https://doi.org/10.1021/ja9932481.

[58] H.C.F. Martens, P.W.M. Blom, H.F.M. Schoo, Comparative study of hole transport in poly(p -phenylene vinylene) derivatives, Phys. Rev. B. 61 (2000) 7489–7493. https://doi.org/10.1103/PhysRevB.61.7489.

[59] D. Hu, J. Yu, G. Padmanaban, S. Ramakrishnan, P.F. Barbara, Spatial Confinement of Exciton Transfer and the Role of Conformational Order in Organic Nanoparticles, Nano Lett. 2 (2002) 1121–1124. https://doi.org/10.1021/nl015661o.

[60] G. Bounos, S. Ghosh, A.K. Lee, K.N. Plunkett, K.H. DuBay, J.C. Bolinger, R. Zhang, R.A. Friesner, C. Nuckolls, D.R. Reichman, P.F. Barbara, Controlling Chain Conformation in Conjugated Polymers Using Defect Inclusion Strategies, J. Am. Chem. Soc. 133 (2011) 10155–10160. https://doi.org/10.1021/ja2006687.

[61] X. Zhu, M.C. Traub, D.A. Vanden Bout, K.N. Plunkett, Well-Defined Alternating Copolymers of Oligo(phenylenevinylene)s and Flexible Chains, Macromolecules. 45 (2012) 5051–5057. https://doi.org/10.1021/ma300430e.

[62] H. Shirakawa, E.J. Louis, A.G. MacDiarmid, C.K. Chiang, A.J. Heeger, Synthesis of electrically conducting organic polymers: halogen derivatives of polyacetylene, (CH) x, J. Chem. Soc. Chem. Commun. (1977) 578. https://doi.org/10.1039/c39770000578.

[63] S.A. Jenekhe, Synthesis and Characterization of Carbon Atom Bridged Heterocyclic Polymers of Specified Conjugation Length. 1. Novel Polyterthiophenes, Macromolecules. 23 (1990) 2848–2854. https://doi.org/10.1021/ma00213a005.

[64] K.J. Hoffmann, E.J. Samuelsen, P.H.. Carlsen, Broken π-conjugated thiophene systems, Synth. Met. 113 (2000) 161–166. https://doi.org/10.1016/S0379-6779(00)00209-5.

[65] S. Ahn, K. Yabumoto, Y. Jeong, K. Akagi, Low bandgap poly(thienylenemethine) derivatives bearing terarylene moieties in the side chains, Polym. Chem. 5 (2014) 6977–6989. https://doi.org/10.1039/C4PY00849A.

[66] M. Ichikawa, H. Goto, A new synthetic route for the production of a thiophene-based methine-bridged type conjugated polymer, Chem. Pap. 75 (2021) 5133–5138. https://doi.org/10.1007/s11696-021-01536-8.

[67] X. Zhao, G. Xue, G. Qu, V. Singhania, Y. Zhao, K. Butrouna, A. Gumyusenge, Y. Diao, K.R. Graham, H. Li, J. Mei, Complementary Semiconducting Polymer Blends: Influence of Side Chains of Matrix Polymers, Macromolecules. 50 (2017) 6202–6209. https://doi.org/10.1021/acs.macromol.7b01354.

[68] H. Letheby, XXIX.—On the production of a blue substance by the electrolysis of sulphate of aniline, J. Chem. Soc. 15 (1862) 161–163. https://doi.org/10.1039/JS8621500161.

[69] K.K. Kanazawa, A.F. Diaz, R.H. Geiss, W.D. Gill, J.F. Kwak, J.A. Logan, J.F. Rabolt, G.B. Street, 'Organic metals': polypyrrole, a stable synthetic 'metallic' polymer, J. Chem. Soc., Chem. Commun. (1979) 854–855. https://doi.org/10.1039/C39790000854.

[70] J. Guay, A. Diaz, R. Wu, J.M. Tour, L.H. Dao, Electrooxidation of soluble .alpha.,.alpha.-coupled thiophene oligomers, Chem. Mater. 4 (1992) 254–255. https://doi.org/10.1021/cm00020a006.

[71] G.E. Wnek, J.C.W. Chien, F.E. Karasz, C.P. Lillya, Electrically conducting derivative of poly(p-phenylene vinylene), Polymer (Guildf). 20 (1979) 1441–1443. https://doi.org/10.1016/0032-3861(79)90002-8.

[72] A. Berlin, G. Fontana, G. Pagani, G. Schiavon, G. Zotti, Anodic coupling of oligothiophenes bridged by ethylene groups, Synth. Met. 57 (1993) 4796–4801. https://doi.org/10.1016/0379-6779(93)90819-I.

[73] T. Benincori, S. Rizzo, F. Sannicolò, G. Schiavon, S. Zecchin, G. Zotti, An Electrochemically Prepared Small-Bandgap Poly(biheteroarylidenemethine): Poly{bi[(3,4-ethylenedioxy)thienylene]methine}, Macromolecules. 36 (2003) 5114–5118. https://doi.org/10.1021/ma025919c.

[74] M. Pagels, G. Götz, T. Fischer, P. Bäuerle, J. Heinze, Electrochemistry with alkyl-linked oligothiophenes, Electrochim. Acta. 56 (2011) 3419–3428. https://doi.org/10.1016/j.electacta.2010.12.057.

[75] J.W. Lin, L.P. Dudek, Synthesis and properties of poly(2,5-thienylene), J. Polym. Sci. Polym. Chem. Ed. 18 (1980) 2869–2873. https://doi.org/10.1002/pol.1980.170180910.

[76] T. Yamamoto, K. Sanechika, A. Yamamoto, Preparation of thermostable and electric-conducting poly(2,5-thienylene), J. Polym. Sci. Polym. Lett. Ed. 18 (1980) 9–12. https://doi.org/10.1002/pol.1980.130180103.

[77] W.C. Chen, S.A. Jenekhe, Small-Bandgap Conducting Polymers Based on Conjugated Poly(heteroarylene methines). 1. Precursor Poly(heteroarylene methylenes), Macromolecules. 28 (1995) 454–464. https://doi.org/10.1021/ma00106a008.

[78] X. Zhao, Y. Zhao, Q. Ge, K. Butrouna, Y. Diao, K.R. Graham, J. Mei, Complementary Semiconducting Polymer Blends: The Influence of Conjugation-Break Spacer Length in Matrix Polymers, Macromolecules. 49 (2016) 2601–2608. https://doi.org/10.1021/acs.macromol.6b00050.

[79] B.C. Schroeder, Y.C. Chiu, X. Gu, Y. Zhou, J. Xu, J. Lopez, C. Lu, M.F. Toney, Z. Bao, Non-Conjugated Flexible Linkers in Semiconducting Polymers: A Pathway to Improved Processability without Compromising Device Performance, Adv. Electron. Mater. 2 (2016) 1–10. https://doi.org/10.1002/aelm.201600104.

[80] Z.Y. Yang, H.M. Zhang, G.B. Pan, L.J. Wan, Effect of the bridge alkylene chain on adlayer structure and property of functional oligothiophenes studied with scanning tunneling microscopy and spectroscopy, ACS Nano. 2 (2008) 743–749. https://doi.org/10.1021/nn7004443.

[81] F.C. Krebs, N. Espinosa, M. Hösel, R.R. Søndergaard, M. Jørgensen, 25th Anniversary Article: Rise to Power – OPV-Based Solar Parks, Adv. Mater. 26 (2014) 29–39. https://doi.org/10.1002/adma.201302031.

[82] E.L. Melenbrink, K.M. Hilby, K. Choudhary, S. Samal, N. Kazerouni, J.L. McConn, D.J. Lipomi, B.C. Thompson, Influence of Acceptor Side-Chain Length and Conjugation-Break Spacer Content on the Mechanical and Electronic Properties of Semi-Random Polymers, ACS Appl. Polym. Mater. 1 (2019) 1107–1117. https://doi.org/10.1021/acsapm.9b00115.

[83] S. Savagatrup, X. Zhao, E. Chan, J. Mei, D.J. Lipomi, Effect of Broken Conjugation on the Stretchability of Semiconducting Polymers, Macromol. Rapid Commun. 37 (2016) 1623–1628. https://doi.org/10.1002/marc.201600377.

[84] S. Savagatrup, X. Zhao, E. Chan, J. Mei, D.J. Lipomi, Effect of Broken Conjugation on the Stretchability of Semiconducting Polymers, Macromol. Rapid Commun. 37 (2016) 1623–1628. https://doi.org/10.1002/marc.201600377.

[85] J.Y. Oh, S. Rondeau-Gagné, Y.-C. Chiu, A. Chortos, F. Lissel, G.-J.N. Wang, B.C. Schroeder, T. Kurosawa, J. Lopez, T. Katsumata, J. Xu, C. Zhu, X. Gu, W.-G. Bae, Y. Kim, L. Jin, J.W. Chung, J.B.-H. Tok, Z. Bao, Intrinsically stretchable and healable semiconducting polymer for organic transistors, Nature. 539 (2016) 411–415. https://doi.org/10.1038/nature20102.

[86] B. Roth, S. Savagatrup, N. V. de los Santos, O. Hagemann, J.E. Carlé, M. Helgesen, F. Livi, E. Bundgaard, R.R. Søndergaard, F.C. Krebs, D.J. Lipomi, Mechanical Properties of a Library of Low-Band-Gap Polymers, Chem. Mater. 28 (2016) 2363–2373. https://doi.org/10.1021/acs.chemmater.6b00525.

[87] A.D. Printz, S. Savagatrup, D.J. Burke, T.N. Purdy, D.J. Lipomi, Increased elasticity of a low-bandgap conjugated copolymer by random segmentation for mechanically robust solar cells, RSC Adv. 4 (2014) 13635–13643. https://doi.org/10.1039/C4RA00029C.

[88] J. Zhou, E.Q. Li, R. Li, X. Xu, I.A. Ventura, A. Moussawi, D.H. Anjum, M.N. Hedhili, D.-M. Smilgies, G. Lubineau, S.T. Thoroddsen, Semi-metallic, strong and stretchable wet-spun conjugated polymer microfibers, J. Mater. Chem. C. 3 (2015) 2528–2538. https://doi.org/10.1039/C4TC02354D.

[89] Y. Diao, L. Shaw, Z. Bao, S.C.B. Mannsfeld, Morphology control strategies for solution-processed organic semiconductor thin films, Energy Environ. Sci. 7 (2014) 2145–2159. https://doi.org/10.1039/C4EE00688G.

[90] N.D. Treat, J.A. Nekuda Malik, O. Reid, L. Yu, C.G. Shuttle, G. Rumbles, C.J. Hawker, M.L. Chabinyc, P. Smith, N. Stingelin, Microstructure formation in molecular and polymer semiconductors assisted by nucleation agents, Nat. Mater. 12 (2013) 628–633. https://doi.org/10.1038/nmat3655.

[91] A.D. Scaccabarozzi, N. Stingelin, Semiconducting:insulating polymer blends for optoelectronic applications—a review of recent advances, J. Mater. Chem. A. 2 (2014) 10818–10824. https://doi.org/10.1039/C4TA01065E.

[92] A.M. Hiszpanski, Y.-L. Loo, Directing the film structure of organic semiconductors via post-deposition processing for transistor and solar cell applications, Energy Environ. Sci. 7 (2014) 592–608. https://doi.org/10.1039/C3EE42615G.

[93] A.M. Hiszpanski, P.P. Khlyabich, Y.-L. Loo, Tuning kinetic competitions to traverse the rich structural space of organic semiconductor thin films, MRS Commun. 5 (2015) 407–421. https://doi.org/10.1557/mrc.2015.55.

[94] H.N. Tsao, K. Müllen, Improving polymer transistor performance via morphology control, Chem. Soc. Rev. 39 (2010) 2372. https://doi.org/10.1039/b918151m.

[95] W. Pisula, M. Kastler, D. Wasserfallen, M. Mondeshki, J. Piris, I. Schnell, K. Müllen, Relation between Supramolecular Order and Charge Carrier Mobility of Branched Alkyl Hexa- p eri - hexabenzocoronenes, Chem. Mater. 18 (2006) 3634–3640. https://doi.org/10.1021/cm0602343.

[96] L. Zhang, B.D. Rose, Y. Liu, M.M. Nahid, E. Gann, J. Ly, W. Zhao, S.J. Rosa, T.P. Russell, A. Facchetti, C.R. McNeill, J.-L. Brédas, A.L. Briseno, Efficient Naphthalenediimide-Based Hole Semiconducting Polymer with Vinylene Linkers between Donor and Acceptor Units, Chem. Mater. 28 (2016) 8580–8590. https://doi.org/10.1021/acs.chemmater.6b03379.

[97] T. Marszalek, M. Li, W. Pisula, Design directed self-assembly of donor–acceptor polymers, Chem. Commun. 52 (2016) 10938–10947. https://doi.org/10.1039/C6CC04523E.

[98] J. Lee, A.J. Kalin, T. Yuan, M. Al-Hashimi, L. Fang, Fully conjugated ladder polymers, Chem. Sci. 8 (2017) 2503–2521. https://doi.org/10.1039/C7SC00154A.

[99] H. Huang, L. Yang, A. Facchetti, T.J. Marks, Organic and Polymeric Semiconductors Enhanced by Noncovalent Conformational Locks, Chem. Rev. 117 (2017) 10291–10318. https://doi.org/10.1021/acs.chemrev.7b00084.

[100] T.-H. Lee, K.-Y. Wu, T.-Y. Lin, J.-S. Wu, C.-L. Wang, C.-S. Hsu, Role of the Comonomeric Units in Reaching Linear Backbone, High Solid-State Order and Charge Mobilities in Heptacyclic Arene-Based Alternating Copolymers, Macromolecules. 46 (2013) 7687–7695. https://doi.org/10.1021/ma4012973.

[101] J. Mei, Z. Bao, Side Chain Engineering in Solution-Processable Conjugated Polymers, Chem. Mater. 26 (2014) 604–615. https://doi.org/10.1021/cm4020805.

[102] B.C. Schroeder, T. Kurosawa, T. Fu, Y. Chiu, J. Mun, G.N. Wang, X. Gu, L. Shaw, J.W.E. Kneller, T. Kreouzis, M.F. Toney, Z. Bao, Taming Charge Transport in Semiconducting Polymers with Branched Alkyl Side Chains, Adv. Funct. Mater. 27 (2017). https://doi.org/10.1002/adfm.201701973.

[103] I. Kang, H.-J. Yun, D.S. Chung, S.-K. Kwon, Y.-H. Kim, Record High Hole Mobility in Polymer Semiconductors via Side-Chain Engineering, J. Am. Chem. Soc. 135 (2013) 14896–14899. https://doi.org/10.1021/ja405112s.

[104] J. Yao, C. Yu, Z. Liu, H. Luo, Y. Yang, G. Zhang, D. Zhang, Significant Improvement of Semiconducting Performance of the Diketopyrrolopyrrole–Quaterthiophene Conjugated Polymer through Side-Chain Engineering via Hydrogen-Bonding, J. Am. Chem. Soc. 138 (2016) 173–185. https://doi.org/10.1021/jacs.5b09737.

[105] B. Kang, R. Kim, S.B. Lee, S.-K. Kwon, Y.-H. Kim, K. Cho, Side-Chain-Induced Rigid Backbone Organization of Polymer Semiconductors through Semifluoroalkyl Side Chains, J. Am. Chem. Soc. 138 (2016) 3679–3686. https://doi.org/10.1021/jacs.5b10445.

[106] L. Ding, H.-B. Li, T. Lei, H.-Z. Ying, R.-B. Wang, Y. Zhou, Z.-M. Su, J. Pei, Alkylene-Chain Effect on Microwire Growth and Crystal Packing of π-Moieties, Chem. Mater. 24 (2012) 1944–1949. https://doi.org/10.1021/cm300747v.

[107] A. Gasperini, S. Bivaud, K. Sivula, Controlling conjugated polymer morphology and charge carrier transport with a flexible-linker approach, Chem. Sci. 5 (2014) 4922–4927. https://doi.org/10.1039/C4SC02073A.

[108] B.C. Schroeder, Y. Chiu, X. Gu, Y. Zhou, J. Xu, J. Lopez, C. Lu, M.F. Toney, Z. Bao, Non-Conjugated Flexible Linkers in Semiconducting Polymers: A Pathway to Improved Processability without Compromising Device Performance, Adv. Electron. Mater. 2 (2016). https://doi.org/10.1002/aelm.201600104.

[109] X. Zhao, Y. Zhao, Q. Ge, K. Butrouna, Y. Diao, K.R. Graham, J. Mei, Complementary Semiconducting Polymer Blends: The Influence of Conjugation-Break Spacer Length in Matrix Polymers, Macromolecules. 49 (2016) 2601–2608. https://doi.org/10.1021/acs.macromol.6b00050.

[110] Y. Qiang, R. Xie, B. He, C. Liu, Q. Zhou, Y. Wang, X. Gu, X. Gong, Y. Liu, X. Liu, Designer Conjugation-Break Spacer That Boosts Charge Transport in Semiconducting Terpolymers, Macromolecules. 57 (2024) 5902–5914. https://doi.org/10.1021/acs.macromol.4c00613.

[111] M. Jenart, C. Niebel, J.-Y. Balandier, J. Leroy, A. Mignolet, S. Stas, A. Van Vooren, J. Cornil, Y.H. Geerts, Quaterthiophene-based dimers containing an ethylene bridge: molecular design, synthesis, and optoelectronic properties, Tetrahedron. 68 (2012) 349–355. https://doi.org/10.1016/j.tet.2011.10.020.

[112] S. Dufresne, G.S. Hanan, W.G. Skene, Preparation, photophysics, and electrochemistry of segmented comonomers consisting of thiophene and pyrimidine units: New monomers for hybrid copolymers, J. Phys. Chem. B. 111 (2007) 11407–11418. https://doi.org/10.1021/jp075259j.

[113] S. Ahn, K. Yabumoto, Y. Jeong, K. Akagi, Low bandgap poly(thienylenemethine) derivatives bearing terarylene moieties in the side chains, Polym. Chem. 5 (2014) 6977–6989. https://doi.org/10.1039/c4py00849a.

[114] A. Rahmanudin, L. Yao, K. Sivula, Conjugation break spacers and flexible linkers as tools to engineer the properties of semiconducting polymers, Polym. J. 50 (2018) 725–736. https://doi.org/10.1038/s41428-018-0069-z.

[115] K. Peng, T. Pei, N. Huang, L. Yuan, X. Liu, J. Xia, Functionalization of poly(bis-thiophene methine)s via facile C–C bulk polymerization and their application as chemosensors for acid detection, J. Polym. Sci. Part A Polym. Chem. 56 (2018) 1676–1683. https://doi.org/10.1002/pola.29047.

[116] N. Kazerouni, E.L. Melenbrink, P. Das, B.C. Thompson, Ternary Blend Organic Solar Cells Incorporating Ductile Conjugated Polymers with Conjugation Break Spacers, ACS Appl. Polym. Mater. 3 (2021) 3028–3037. https://doi.org/10.1021/acsapm.1c00213.

[117] M. Imit, P. Imin, A. Adronov, Supramolecular interactions of fluorene-based copolymers containing 3,4-propylenedioxythiophene and phenazine units with SWNTs, Polym. Chem. 7 (2016) 5241–5248. https://doi.org/10.1039/C6PY00730A.

[118] Y. Xie, B.-M. Wu, F. Xue, S.-C. Ng, T.C.W. Mak, T.S.A. Hor, Catalytic and Stoichiometrically Directed Synthesis of Less Accessible Bromothiophenes and Bromobithiophenes. Trapping and Characterization of Catalytic Intermediates of trans -PdBr(C 4 H 4 - n Br n - 1 S- C)(PPh 3) 2 (n = 1−4), trans -PdBr(C 8 H 4 BrS, Organometallics. 17 (1998) 3988–3995. https://doi.org/10.1021/om9800142.

[119] S. Wu, Y. Sun, L. Huang, J. Wang, Y. Zhou, Y. Geng, F. Wang, Grignard Metathesis Chain-Growth

Polymerization for Poly(bithienylmethylene)s: Ni Catalyst Can Transfer across the Nonconjugated Monomer, Macromolecules. 43 (2010) 4438–4440. https://doi.org/10.1021/ma100537d.

[120] M.S. Hill, M.F. Mahon, J.M.G. McGinley, K.C. Molloy, The synthesis and characterisation of C-triorganometallated (metal=Sn, Si) bis-(thienyl)- and bis-(pyrazolyl)alkanes, including the crystal structure of [(Ph3Sn)C3N2]2CH2, Polyhedron. 20 (2001) 1995–2002. https://doi.org/10.1016/S0277-5387(01)00799-9.

[121] Y. Zou, G. Yue, J. Xu, J. (Steve) Zhou, General Suzuki Coupling of Heteroaryl Bromides by Using Tri- tert -butylphosphine as a Supporting Ligand, European J. Org. Chem. 2014 (2014) 5901–5905. https://doi.org/10.1002/ejoc.201402915.

[122] K. V. Zaitsev, K. Lam, O.K. Poleshchuk, L.G. Kuz'mina, A. V. Churakov, Oligothienyl catenated germanes and silanes: synthesis, structure, and properties, Dalt. Trans. 47 (2018) 5431–5444. https://doi.org/10.1039/C8DT00256H.

[123] H. Halvorsen, J. Skramstad, H. Hope, Oligothiophenes III: Synthesis of Tetra-thienyl-Substituted Ethylenes Including an Abnormal McMurry Coupling Result, Synth. Commun. 37 (2007) 1179–1187. https://doi.org/10.1080/00397910701199037.

[124] Z. Hu, J.L. Atwood, M.P. Cava, A Simple Route to Sulfur Bridged Annulenes, J. Org. Chem. 59 (1994) 8071–8075. https://doi.org/10.1021/jo00105a025.

[125] H. Katsuta, S. Banba, Experimental and theoretical investigation of the reaction of a 3-amidothiophene derivative with various carbonyl compounds, J. Pestic. Sci. 46 (2021) 235–241. https://doi.org/10.1584/jpestics.D21-004.

[126] A. Belhboub, P. Hermet, L. Alvarez, R. Le Parc, S. Rols, A.C. Lopes Selvati, B. Jousselme, Y. Sato, K. Suenaga, A. Rahmani, J.-L. Bantignies, Enhancing the Infrared Response of Carbon Nanotubes From Oligo-Quaterthiophene Interactions, J. Phys. Chem. C. 120 (2016) 28802–28807. https://doi.org/10.1021/acs.jpcc.6b09329.

[127] N. Xie, Y. Chen, Combination of fluorescent switch and electrochemical switch based on a photochromic diarylethene, New J. Chem. 30 (2006) 1595. https://doi.org/10.1039/b609156c.

[128] J.M. Raimundo, P. Blanchard, N. Gallego-Planas, N. Mercier, I. Ledoux-Rak, R. Hierle, J. Roncali, Design and synthesis of push-pull chromophores for second-order nonlinear optics derived from rigidified thiophene-based π-conjugating spacers, J. Org. Chem. 67 (2002) 205–218. https://doi.org/10.1021/jo010713f.

[129] T. Zhang, N.X. Wang, Y.H. Wu, Z. Yan, Y. Xing, J.L. Wen, X.W. Gao, Direct alkylation of thiophenes via bis-coupling with vinyl acetates, Tetrahedron Lett. 59 (2018) 4525–4527. https://doi.org/10.1016/j.tetlet.2018.11.027.

[130] W. Zhang, Z. Mao, N. Zheng, J. Zou, L. Wang, C. Wei, J. Huang, D. Gao, G. Yu, Highly planar cross-conjugated alternating polymers with multiple conformational locks: Synthesis, characterization and their field-effect properties, J. Mater. Chem. C. 4 (2016) 9266–9275. https://doi.org/10.1039/c6tc02891h.

[131] H. Qin, L. Li, T. Liang, X. Peng, J. Peng, Y. Cao, Donor-acceptor (donor) polymers with differently conjugated side groups at the acceptor units for photovoltaics, J. Polym. Sci. Part A Polym. Chem. 51 (2013) 1565–1572. https://doi.org/10.1002/pola.26526.

[132] K.J. Hoffmann, P.H.J. Carlsen, Study of an efficient and selective bromination reaction of substituted thiophenes, Synth. Commun. 29 (1999) 1607–1610. https://doi.org/10.1080/00397919908086142.

[133] Y. Zhao, X. Zhao, Y. Zang, C.-A. Di, Y. Diao, J. Mei, Conjugation-Break Spacers in Semiconducting Polymers: Impact on Polymer Processability and Charge Transport Properties S2-S3 Devices

fabrication and characterization methods S4 NMR, GPC, TGA and DSC characterizations S5-S7 Electrical characterization of O, (n.d.) 1–13. http://pubs.acs.org/doi/suppl/10.1021/acs.macromol.5b00194/suppl_file/ma5b00194_si_001.pdf.

[134] D.A. Bushnev, Alkylated 2,2′-bithiophenes and 2-phenylthiophenes in the composition of pyrolysis products of high-sulfur kerogen, Pet. Chem. 47 (2007) 184–192. https://doi.org/10.1134/S0965544107030061.

[135] S. Doi, T. Mikie, K. Yamanaka, Y. Sato, H. Ohkita, M. Saito, I. Osaka, A highly crystalline face-on π-conjugated polymer based on alkoxythiophene-flanked benzobisthiazole for organic photovoltaics, Polym. J. (2024). https://doi.org/10.1038/s41428-024-00906-9.

[136] X.-G. Li, J. Li, Q.-K. Meng, M.-R. Huang, Interfacial Synthesis and Widely Controllable Conductivity of Polythiophene Microparticles, J. Phys. Chem. B. 113 (2009) 9718–9727. https://doi.org/10.1021/jp901395u.

[137] J. Zak, M. Lapkowski, S. Guillerez, G. Bidan, Electrochemistry and spectroelectrochemistry of regioregular oligooctylthiophenes, Synth. Met. 152 (2005) 185–188. https://doi.org/10.1016/j.synthmet.2005.07.257.

[138] J.W. Sease, L. Zechmeister, Chromatographic and Spectral Characteristics of Some Polythienyls, J. Am. Chem. Soc. 69 (1947) 270–273. https://doi.org/10.1021/ja01194a031.

[139] H. Meier, U. Stalmach, H. Kolshorn, Effective conjugation length and UV/vis spectra of oligomers, Acta Polym. 48 (1997) 379–384. https://doi.org/10.1002/actp.1997.010480905.

[140] J. Gierschner, J. Cornil, H. -J. Egelhaaf, Optical Bandgaps of π-Conjugated Organic Materials at the Polymer Limit: Experiment and Theory, Adv. Mater. 19 (2007) 173–191. https://doi.org/10.1002/adma.200600277.

[141] G. Zotti, G. Schiavon, A. Berlin, G. Pagani, Thiophene Oligomers as Polythiophene Models. 2. Electrochemistry and in Situ ESR of End-Capped Oligothienyls in the Solid State. Evidence for π-Dimerization of Hexameric Polarons in Polythiophene, Chem. Mater. 5 (1993) 620–624. https://doi.org/10.1021/cm00029a008.

[142] R. Shomura, K. Sugiyasu, T. Yasuda, A. Sato, M. Takeuchi, Electrochemical Generation and Spectroscopic Characterization of Charge Carriers within Isolated Planar Polythiophene, Macromolecules. 45 (2012) 3759–3771. https://doi.org/10.1021/ma300373n.

[143] G. Zotti, G. Schiavon, The polythiophene puzzle. Electrochemical and spectroelectrochemical evidence for two oxidation levels, Synth. Met. 31 (1989) 347–357. https://doi.org/10.1016/0379-6779(89)90802-3.

[144] J. Heinze, B.A. Frontana-Uribe, S. Ludwigs, Electrochemistry of Conducting Polymers—Persistent Models and New Concepts, Chem. Rev. 110 (2010) 4724–4771. https://doi.org/10.1021/cr900226k.

[145] J.M. Macromolecules, B.J.P.B. Berlin, F.C. Schilling, F.A. Bovey, A.J. Lovinger, M. Hill, J.M. Zeigler, References and Notes Synthesis of Conjugated Polymers with Alternating Aromatic and Quinonoid Sequences via Elimination on Precursors The aliphatic C-H stretching vibration bands in the, (1986) 2663–2664.

9. Appendices

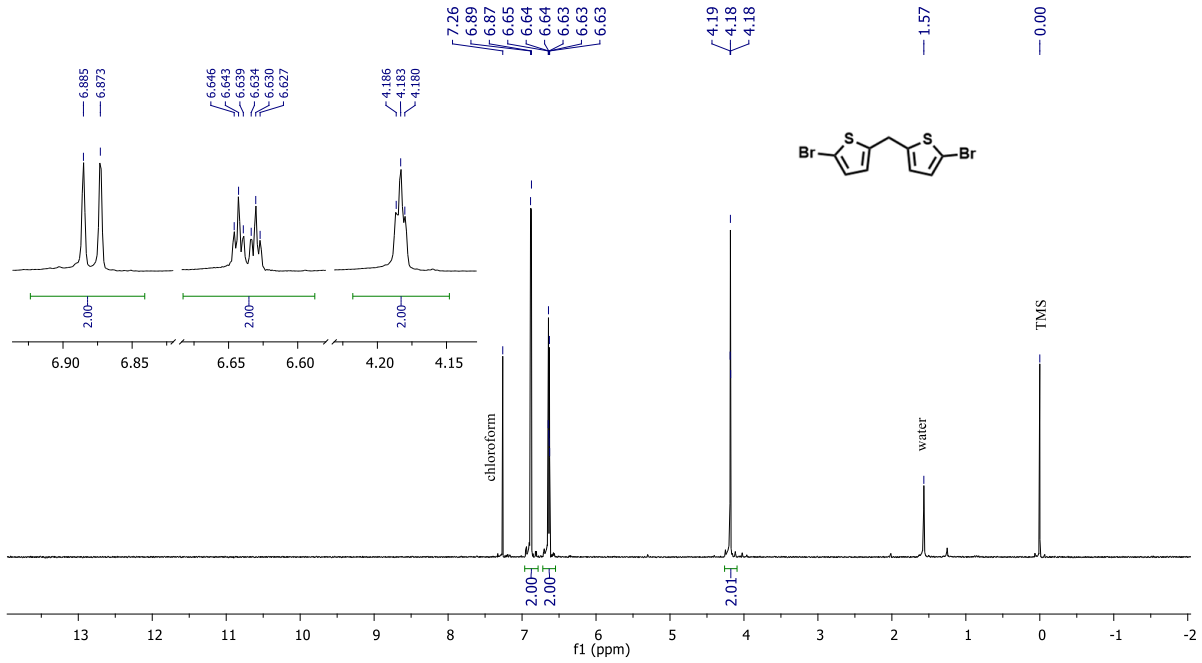

*Figure A 1. ^{1}H NMR (300 MHz) in $CDCl_3$ of the compound **10**.*

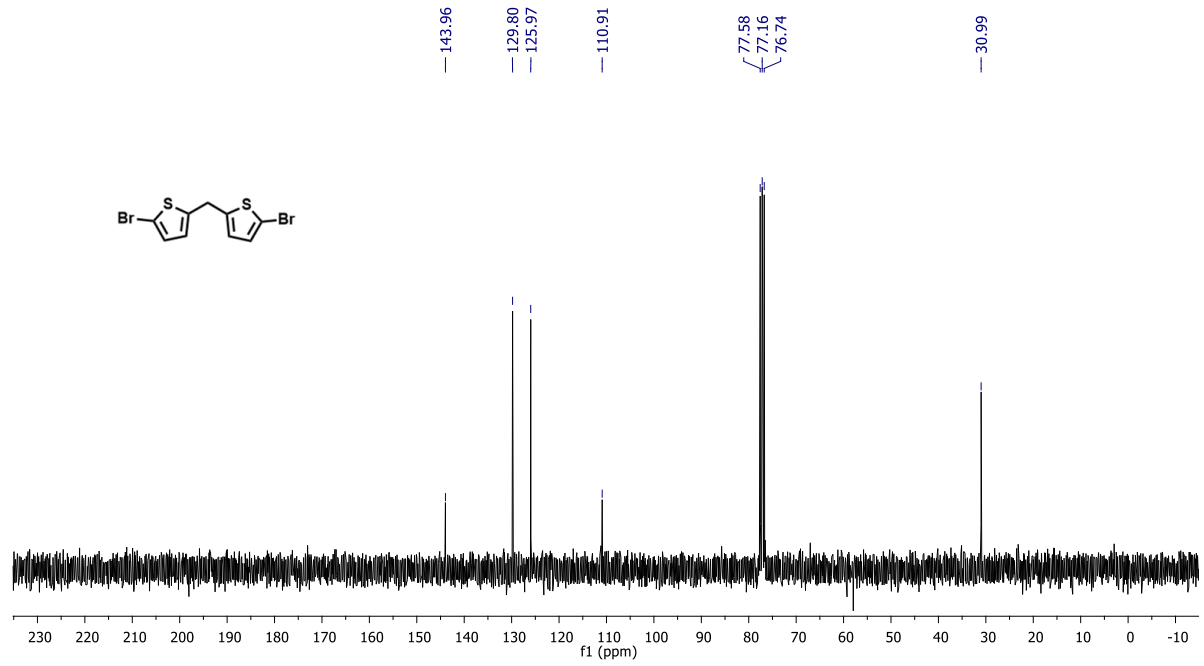

*Figure A 2. ^{13}C NMR (300 MHz) in $CDCl_3$ of the compound **1**.*

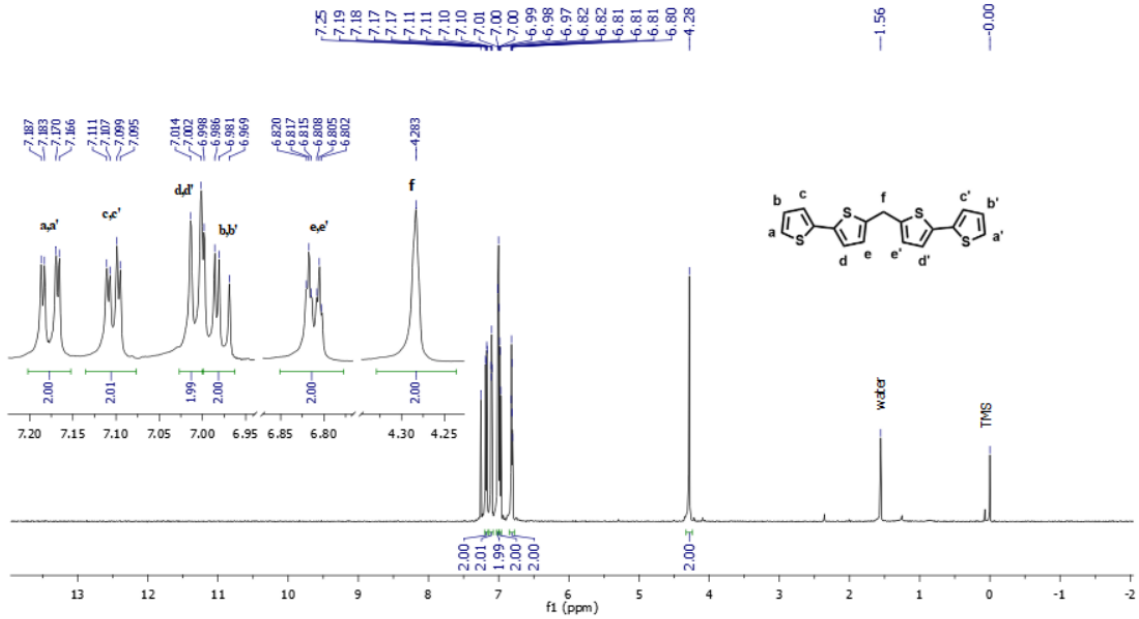

*Figure A 3. ^{1}H NMR (300 MHz) in $CDCl_3$ of the compound **1**.*

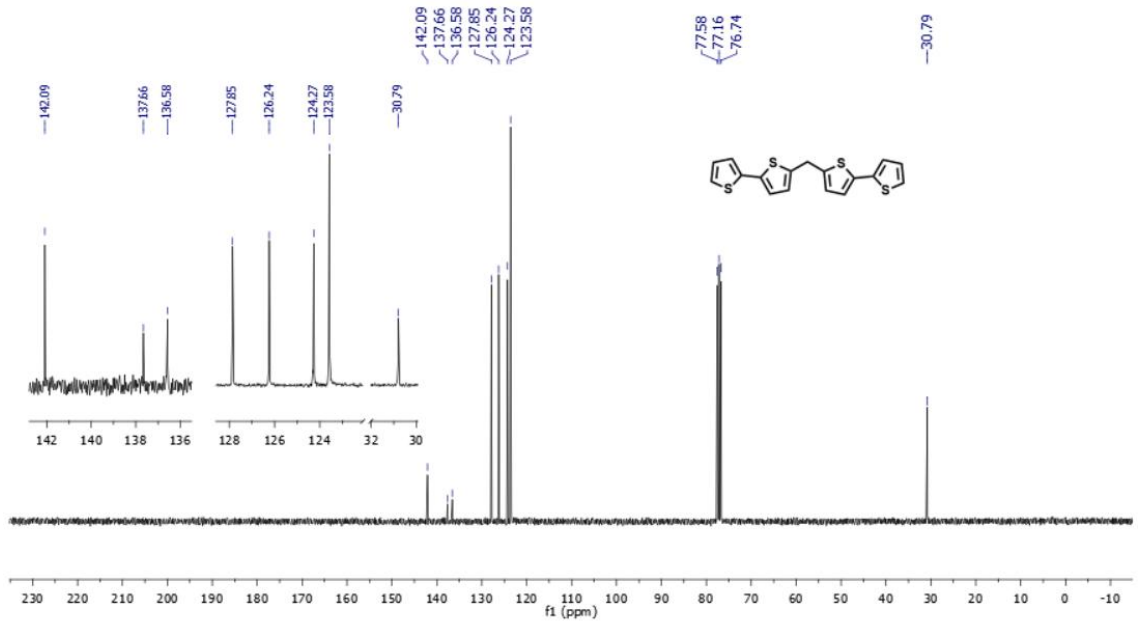

*Figure A 4. ^{13}C NMR (300 MHz) in $CDCl_3$ of the compound **1**.*

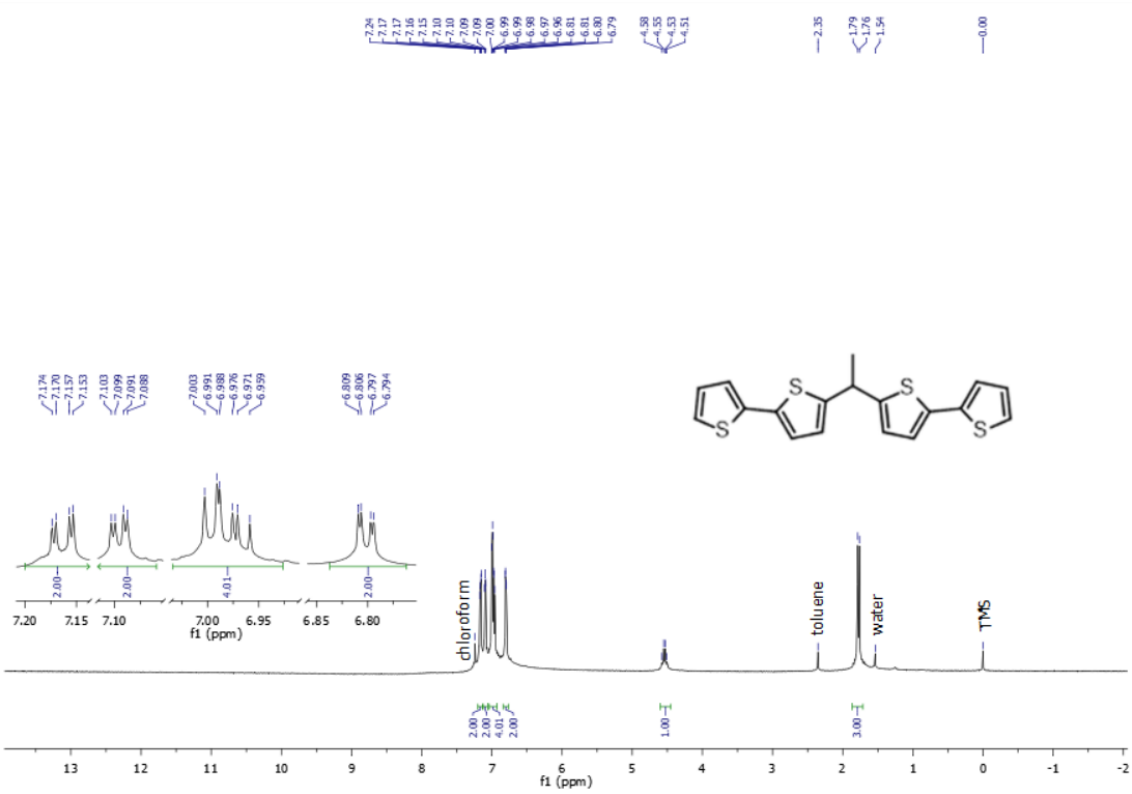

*Figure A 5. ^{1}H NMR (300 MHz) in $CDCl_3$ of the compound **2.***

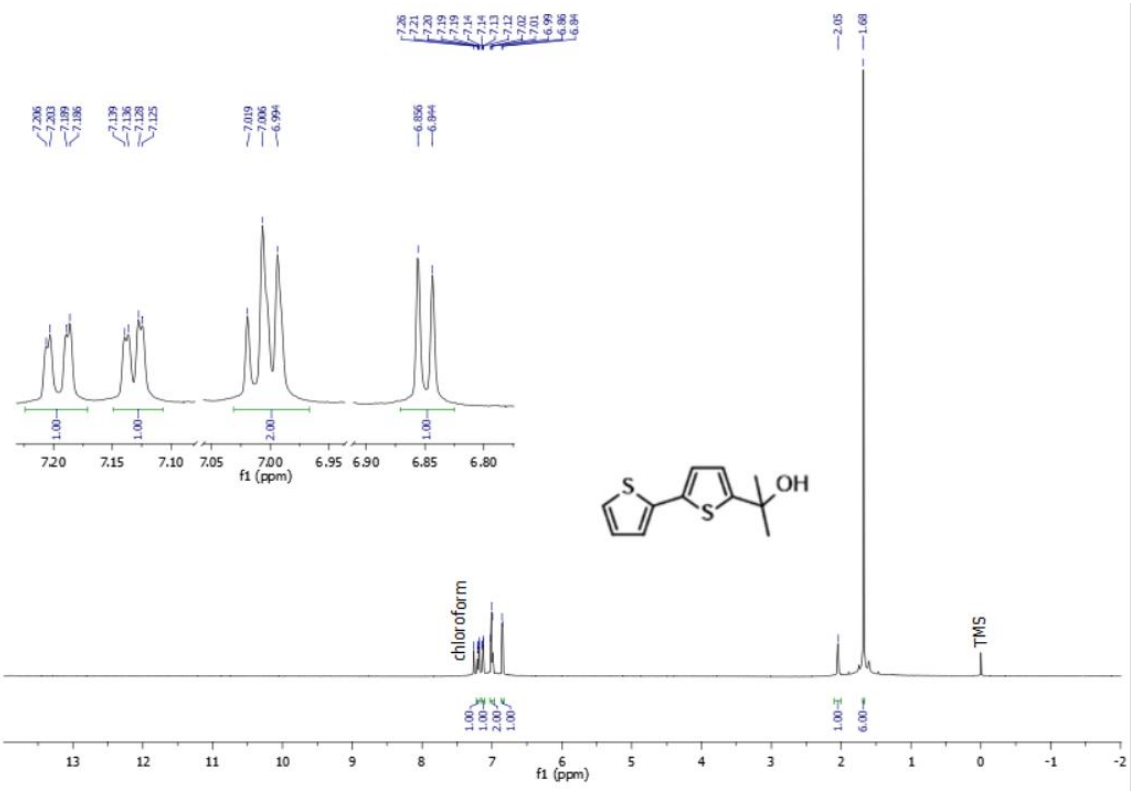

*Figure A 6. ^{1}H NMR (300 MHz) in $CDCl_3$ of the compound **11***

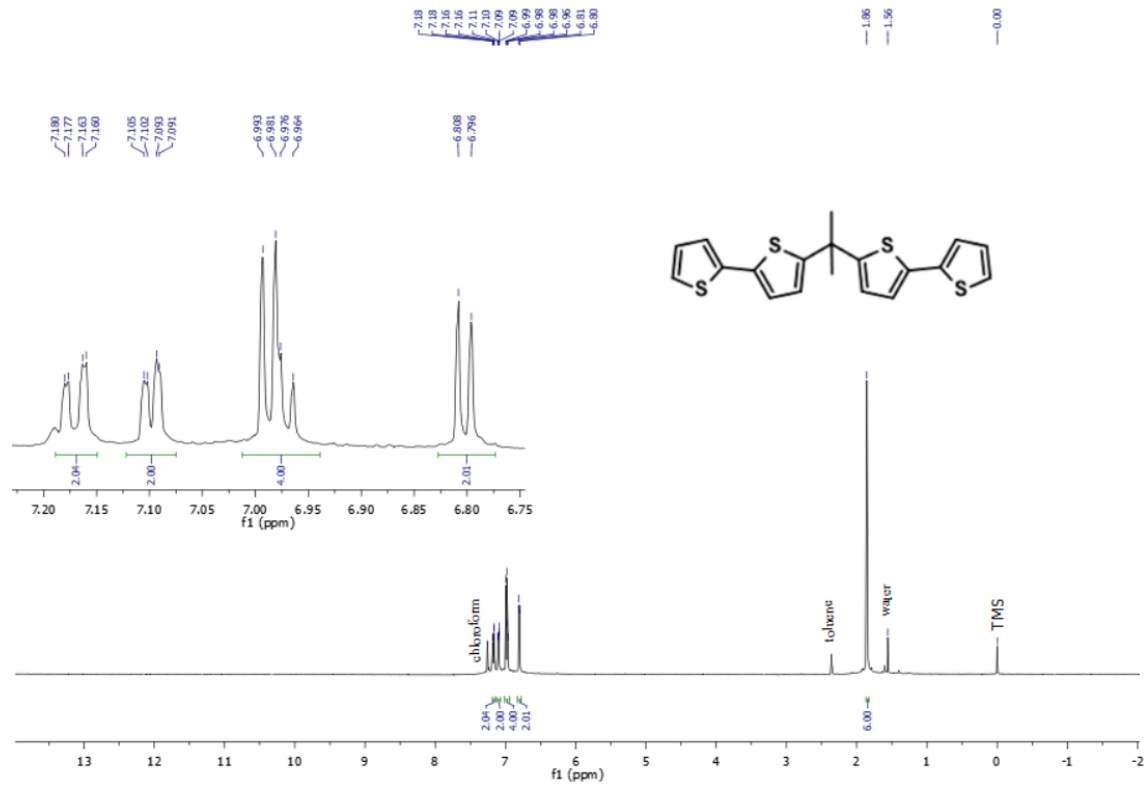

*Figure A 7. ^{1}H NMR (300 MHz) in $CDCl_3$ of the compound **3**.*

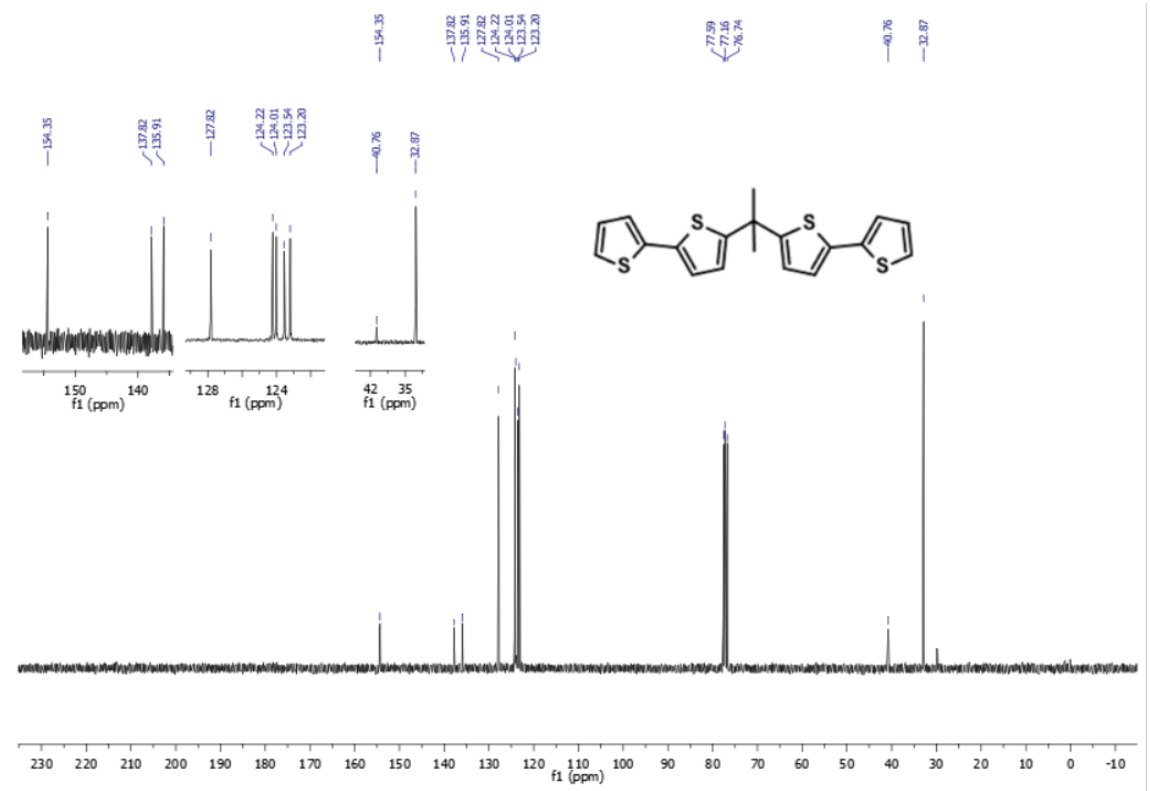

*Figure A 8. ^{13}C NMR (300 MHz) in $CDCl_3$ of the compound **3**.*

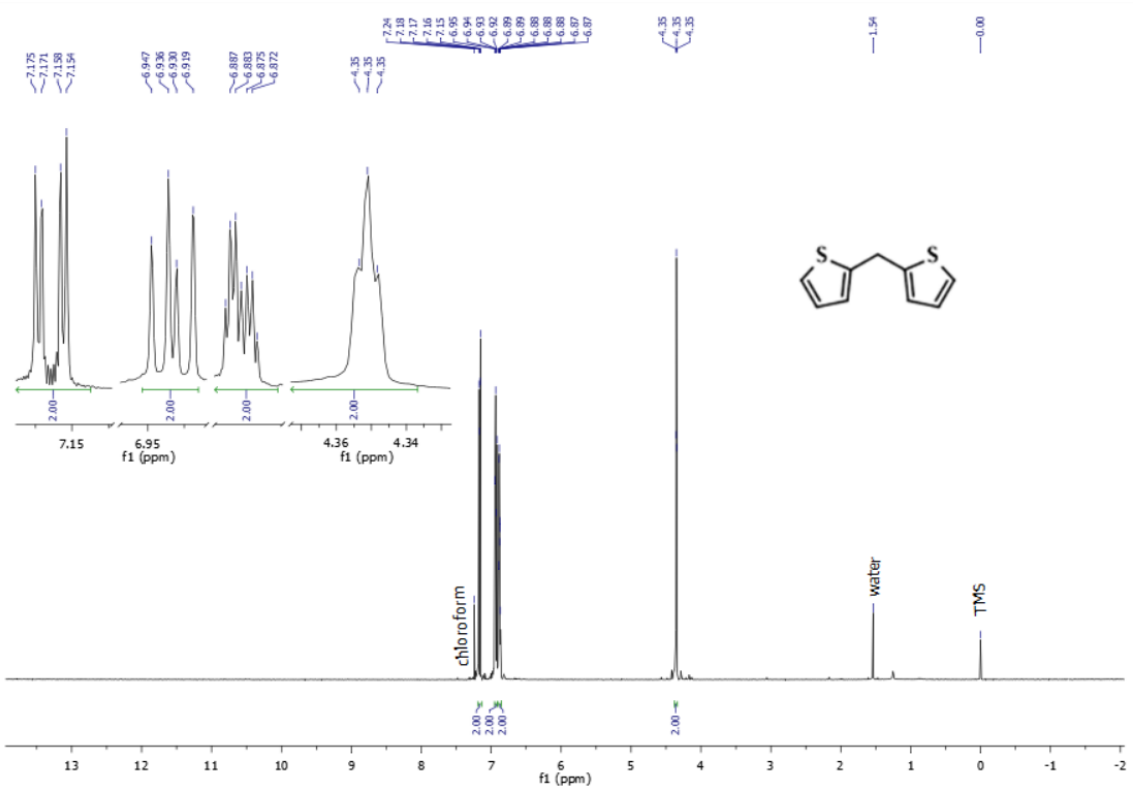

*Figure A 9. ^{1}H NMR (300 MHz) in $CDCl_3$ of the compound **4**.*

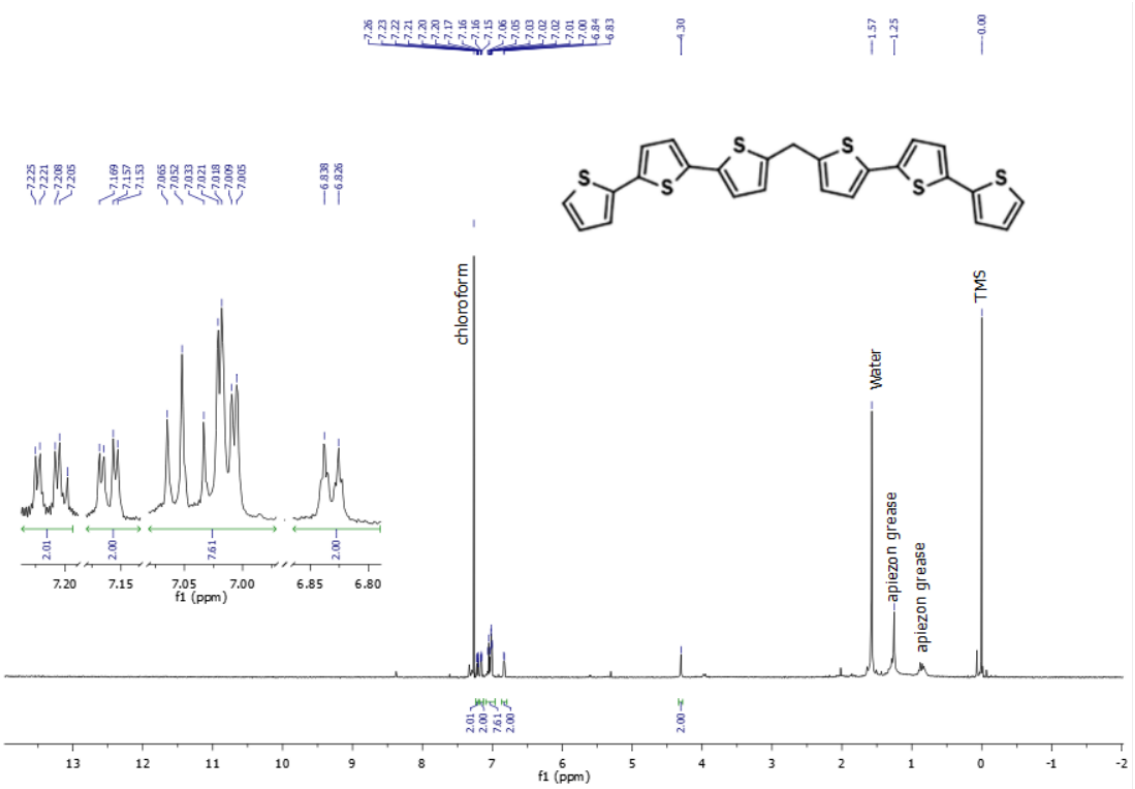

*Figure A 10. ^{1}H NMR (300 MHz) in $CDCl_3$ of the compound **5**.*

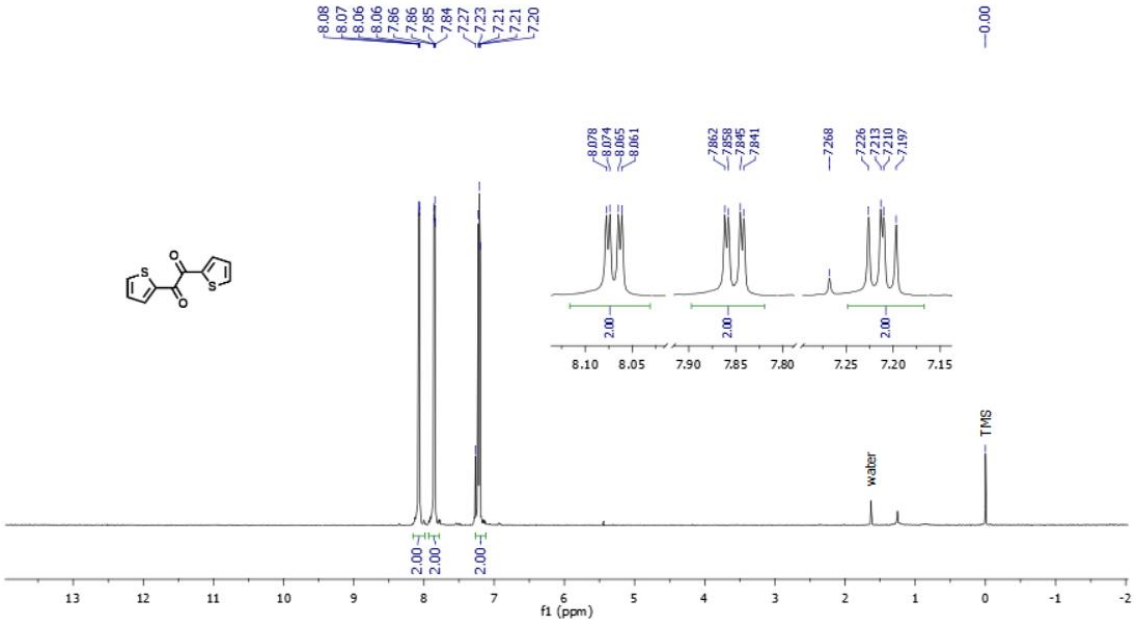

*Figure A 11. ^{1}H NMR (300 MHz) in $CDCl_3$ of the compound **12.***

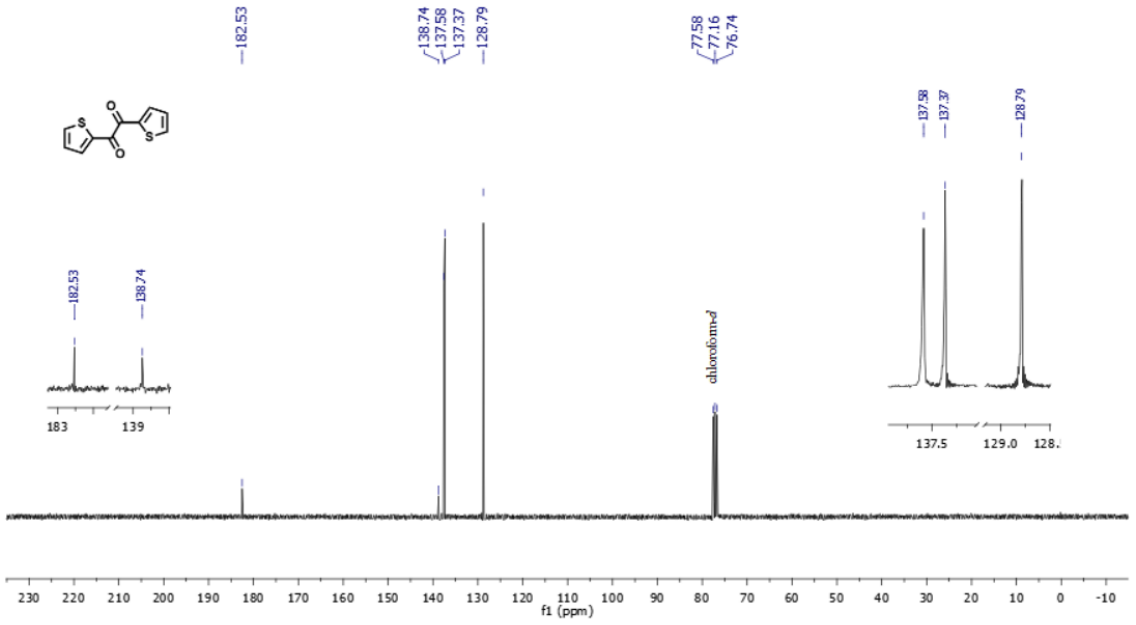

*Figure A 12. ^{13}C NMR (300 MHz) in $CDCl_3$ of the compound **12**.*

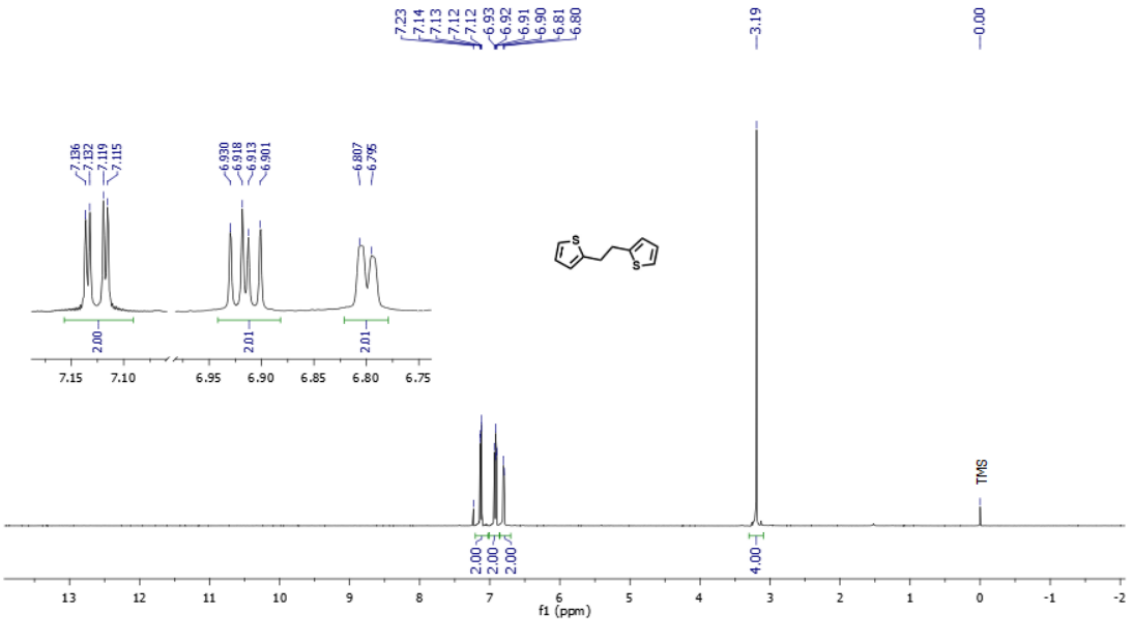

*Figure A 13. ^{1}H NMR (300 MHz) in $CDCl_3$ of the compound **13.***

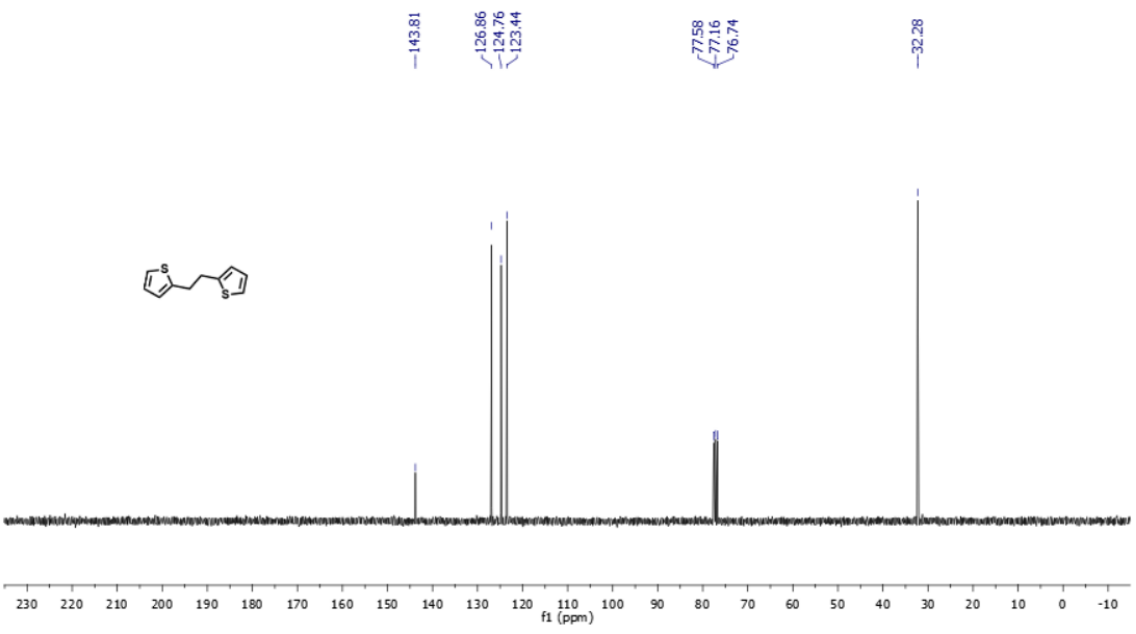

*Figure A 14. ^{13}C NMR (300 MHz) in $CDCl_3$ of the compound **13**.*

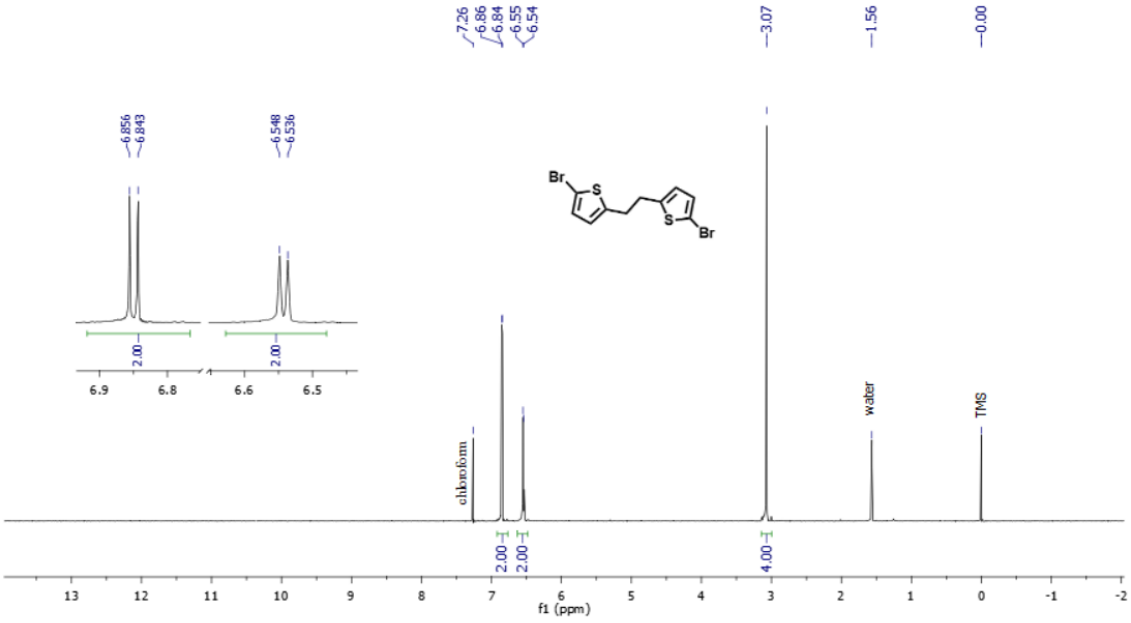

*Figure A 15. ^{1}H NMR (300 MHz) in $CDCl_3$ of the compound **14.***

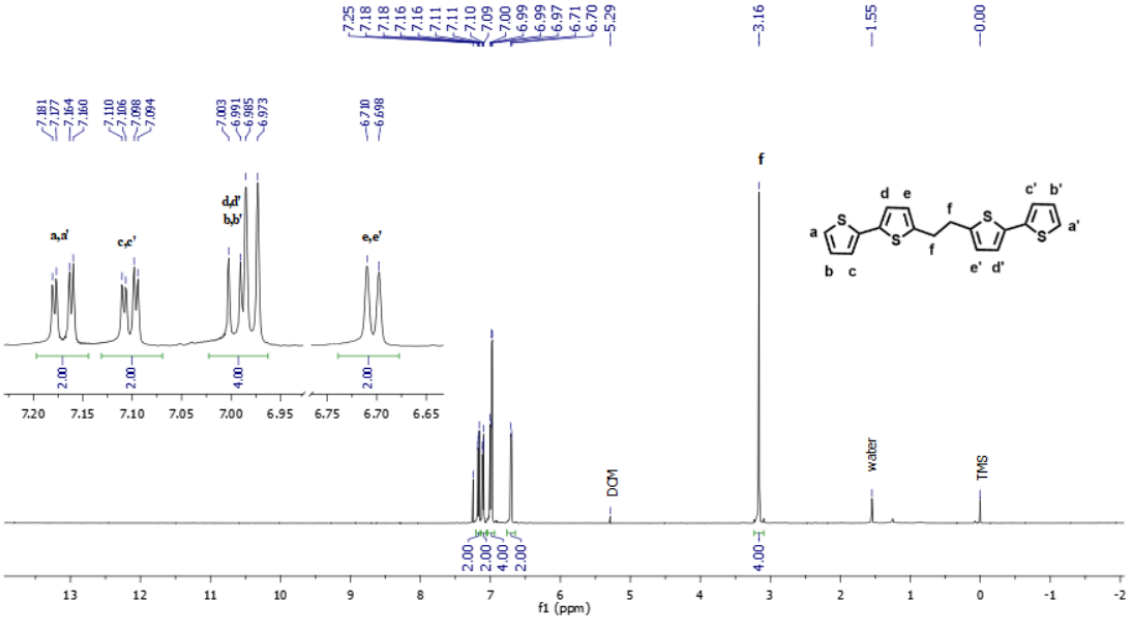

*Figure A 16. ^{1}H NMR (300 MHz) in $CDCl_3$ of the compound **6.***

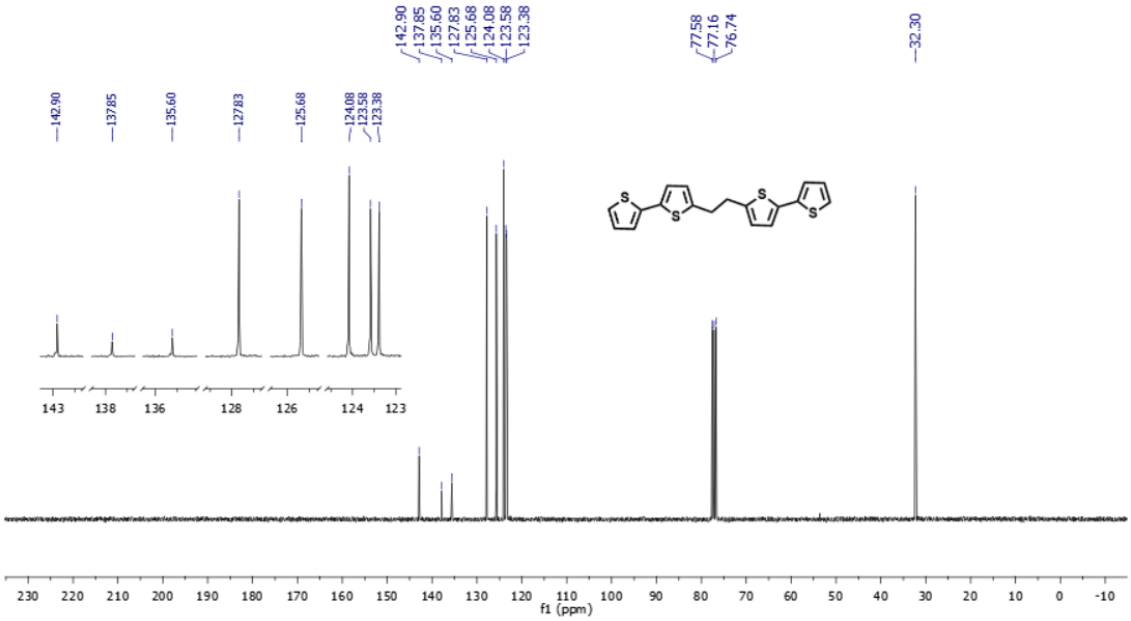

*Figure A 17. ^{13}C NMR (300 MHz) in $CDCl_3$ of the compound **6***

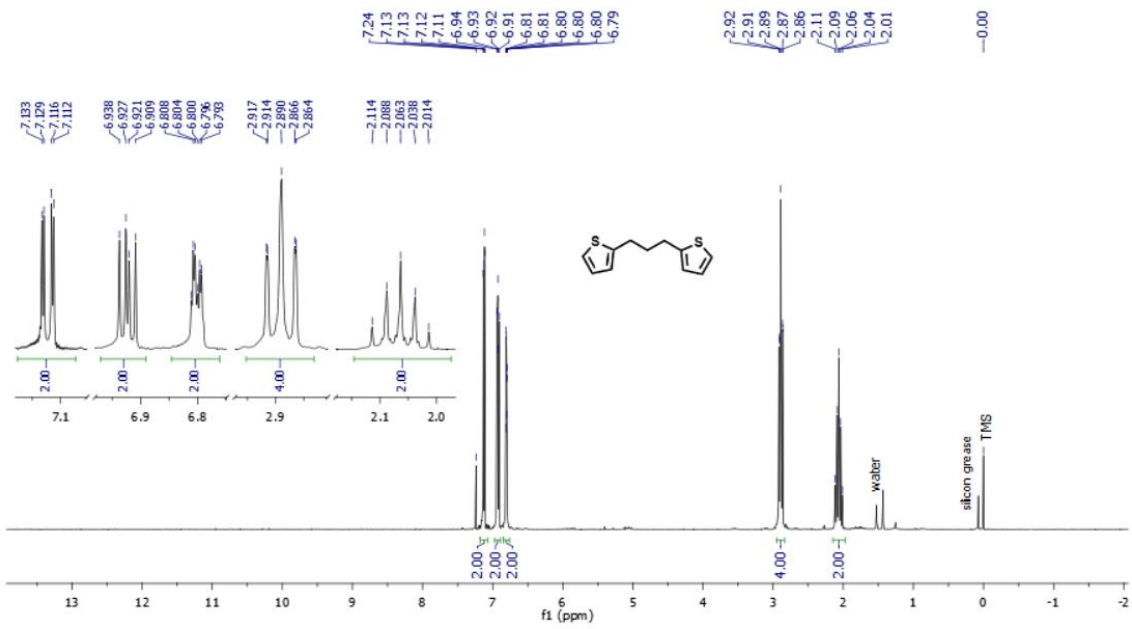

*Figure A 18. ^{1}H NMR (300 MHz) in $CDCl_3$ of the compound **15.***

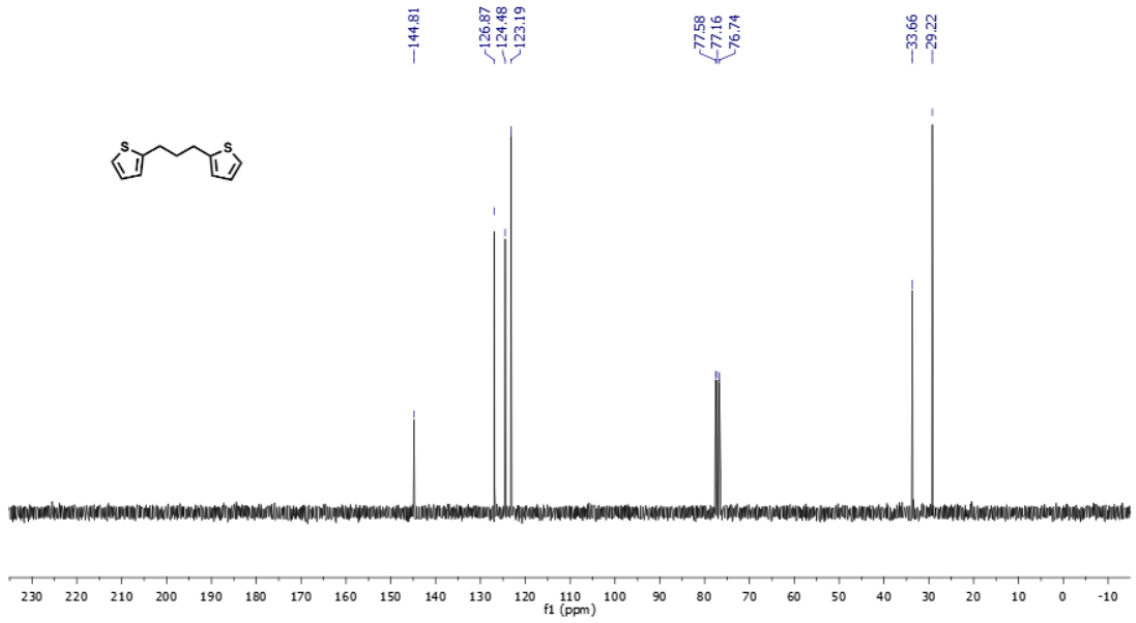

*Figure A 19. ^{13}C NMR (300 MHz) in $CDCl_3$ of the compound **15**.*

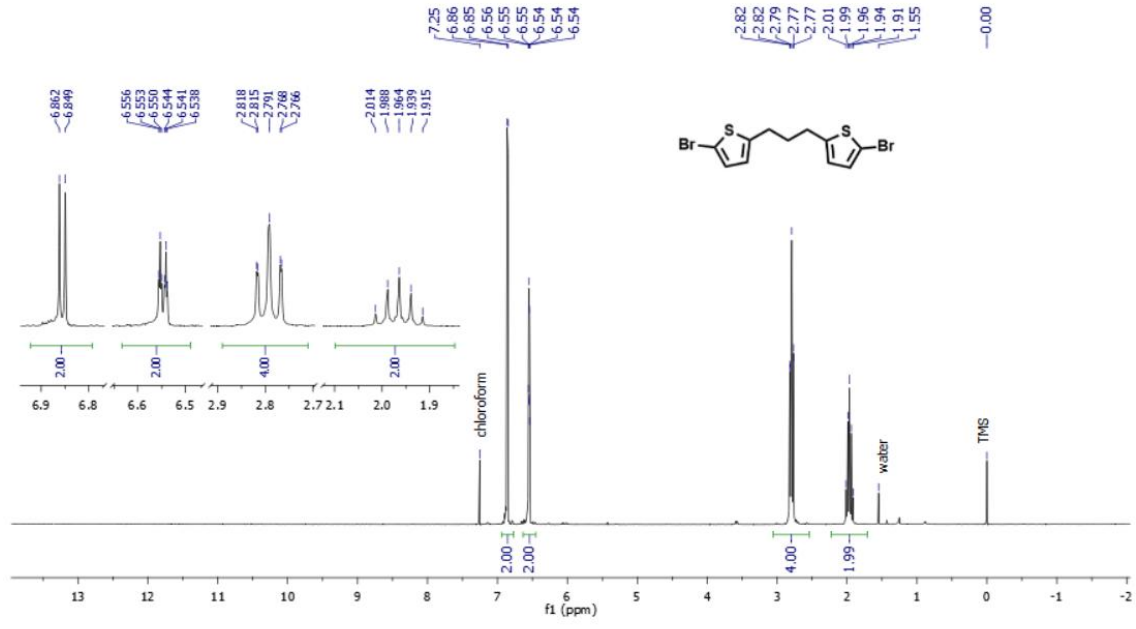

*Figure A 20. ^{1}H NMR (300 MHz) in $CDCl_3$ of the compound **16.***

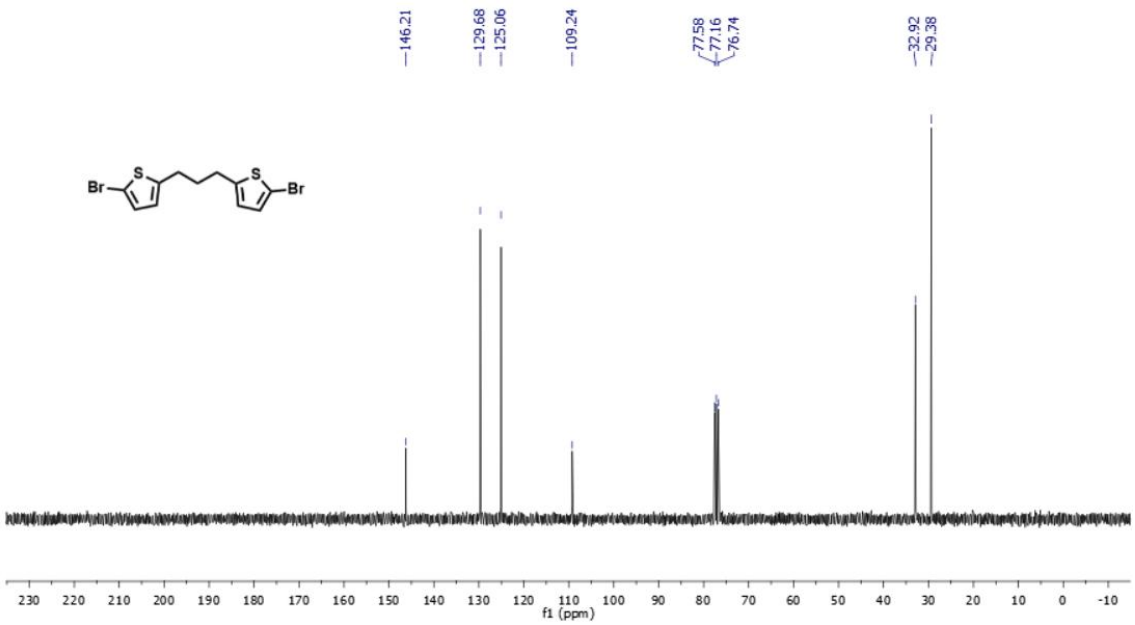

*Figure A 21. ^{13}C NMR (300 MHz) in $CDCl_3$ of the compound **16**.*

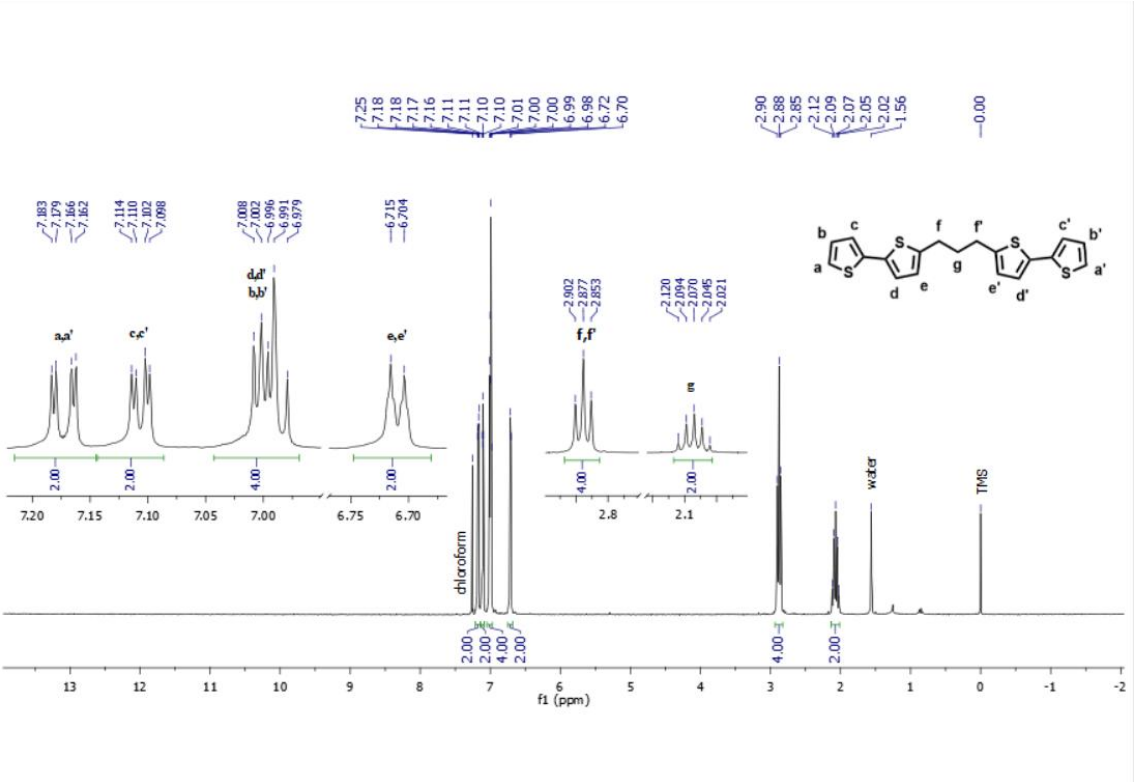

*Figure A 22. ^{1}H NMR (300 MHz) in $CDCl_3$ of the compound **7.***

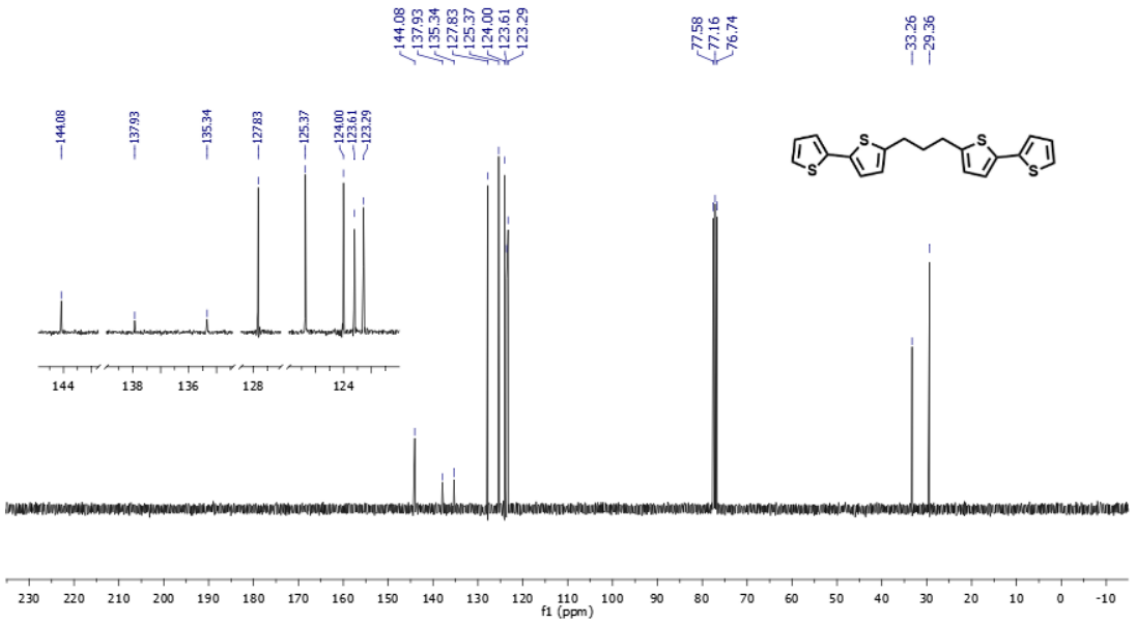

*Figure A 23. ^{13}C NMR (300 MHz) in $CDCl_3$ of the compound **7.***

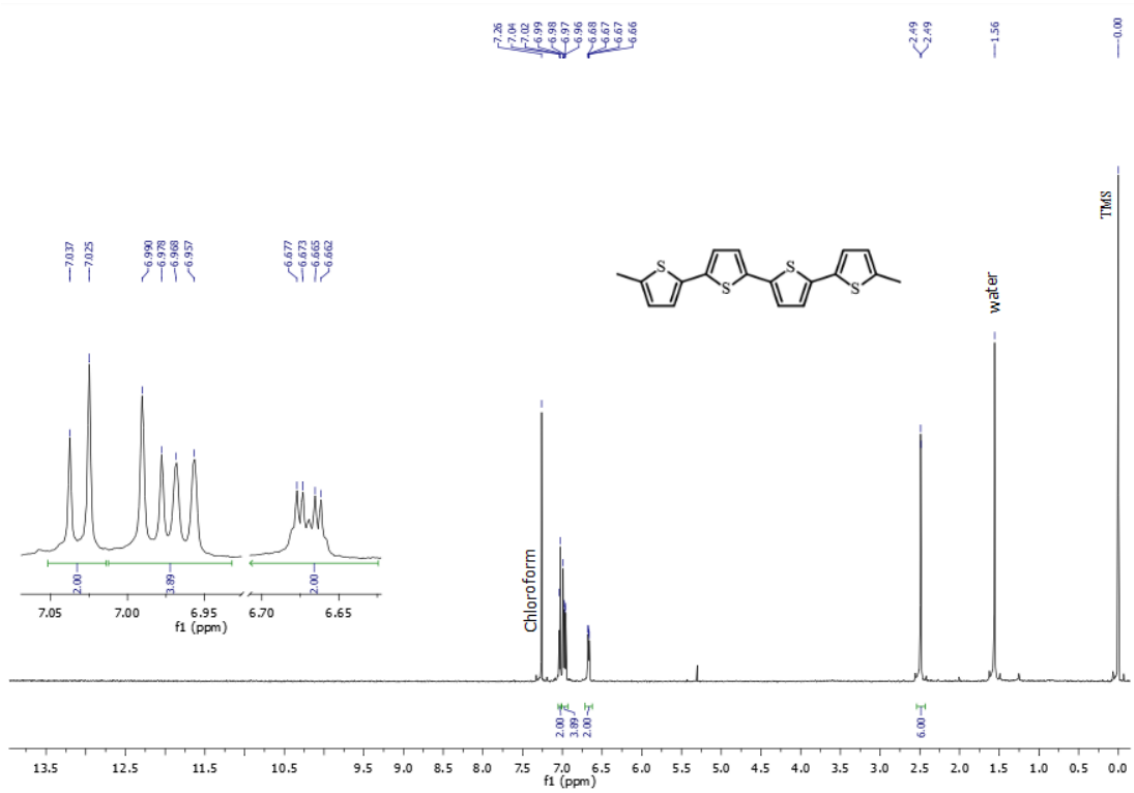

*Figure A 24. ^{1}H NMR (300 MHz) in $CDCl_3$ of the model compound **A.***

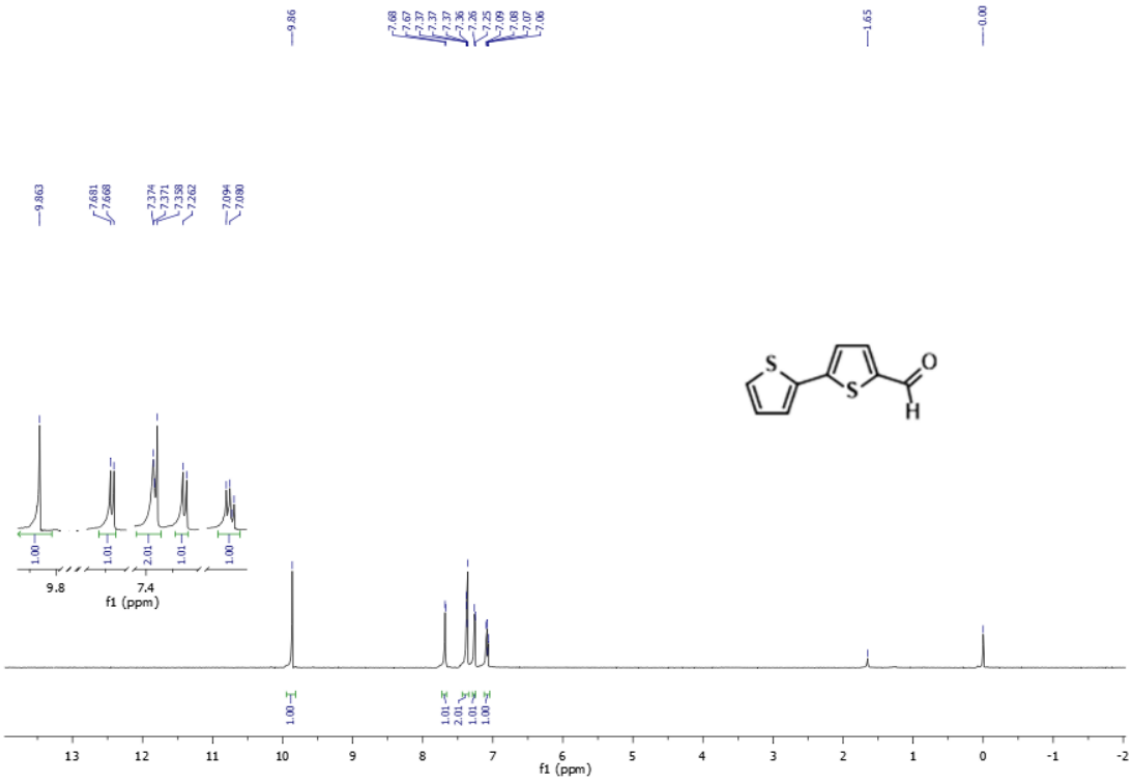

*Figure A 25. ^{1}H NMR (300 MHz) in $CDCl_3$ of the model compound intermediate **17**.*

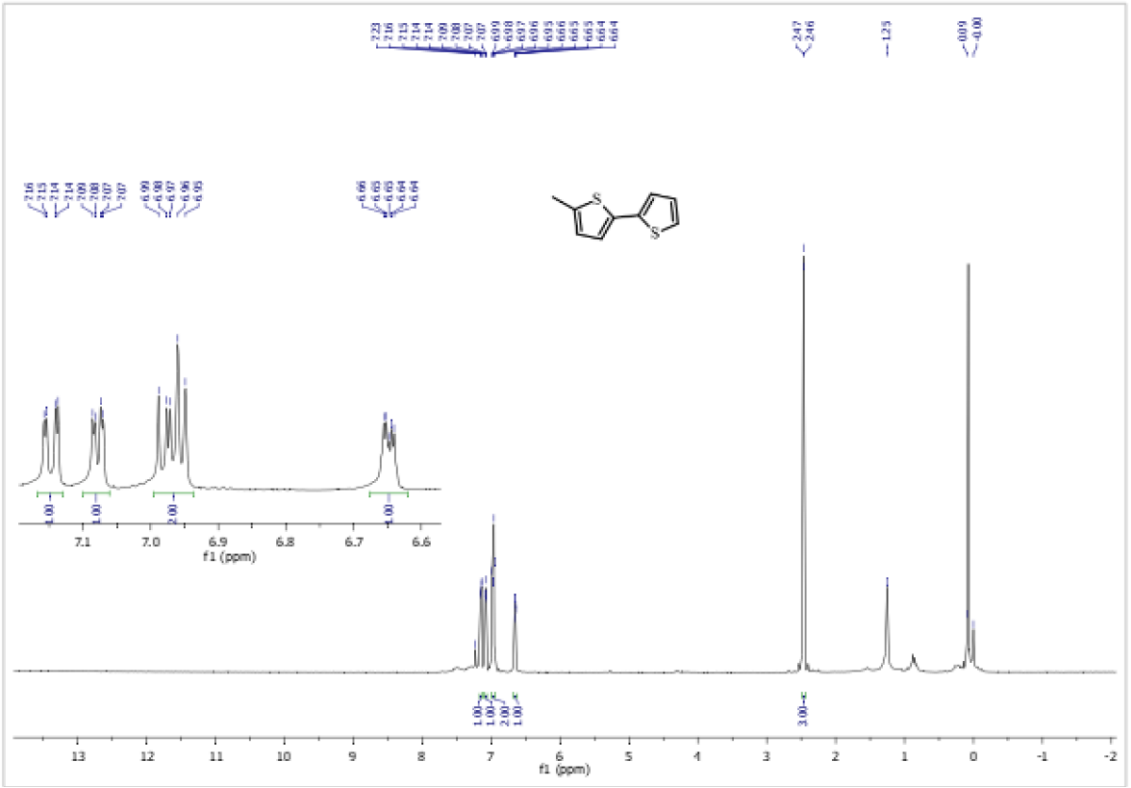

Figure A 26. ^{1}H NMR (300 MHz) in $CDCl_3$ of the model compound B.

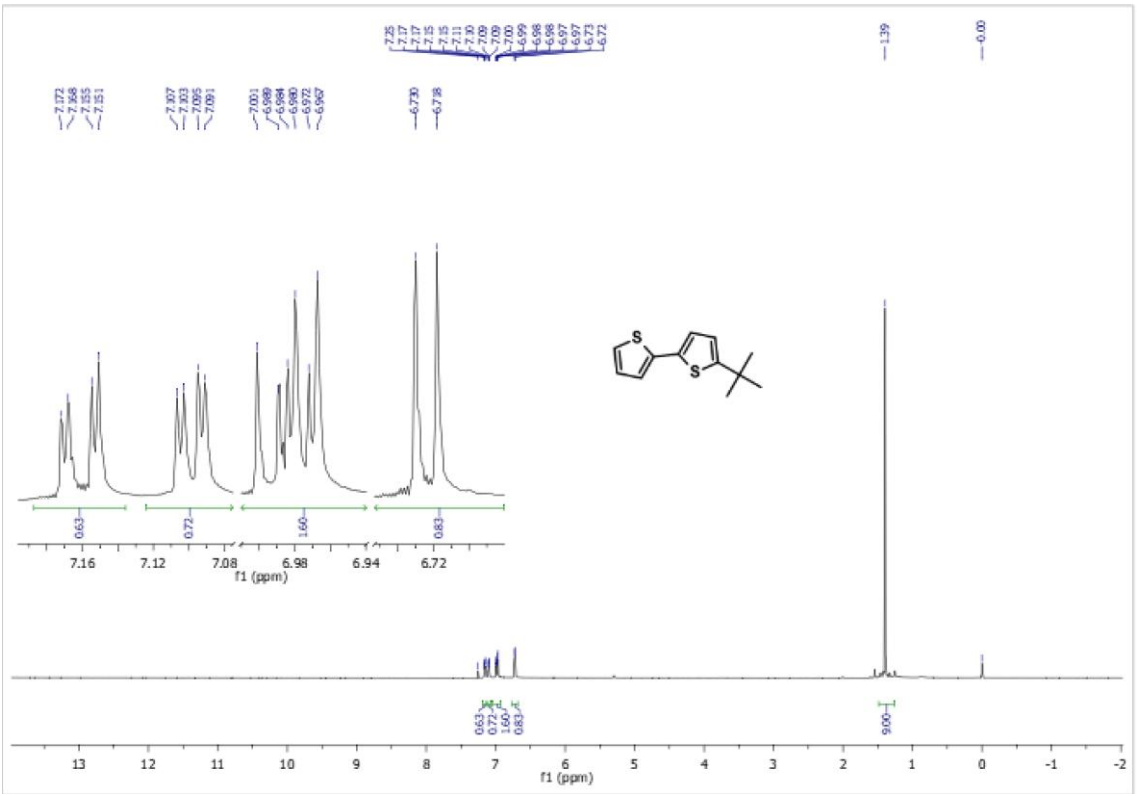

Figure A 27. ^{1}H NMR (300 MHz) in $CDCl_3$ of the model compound C.

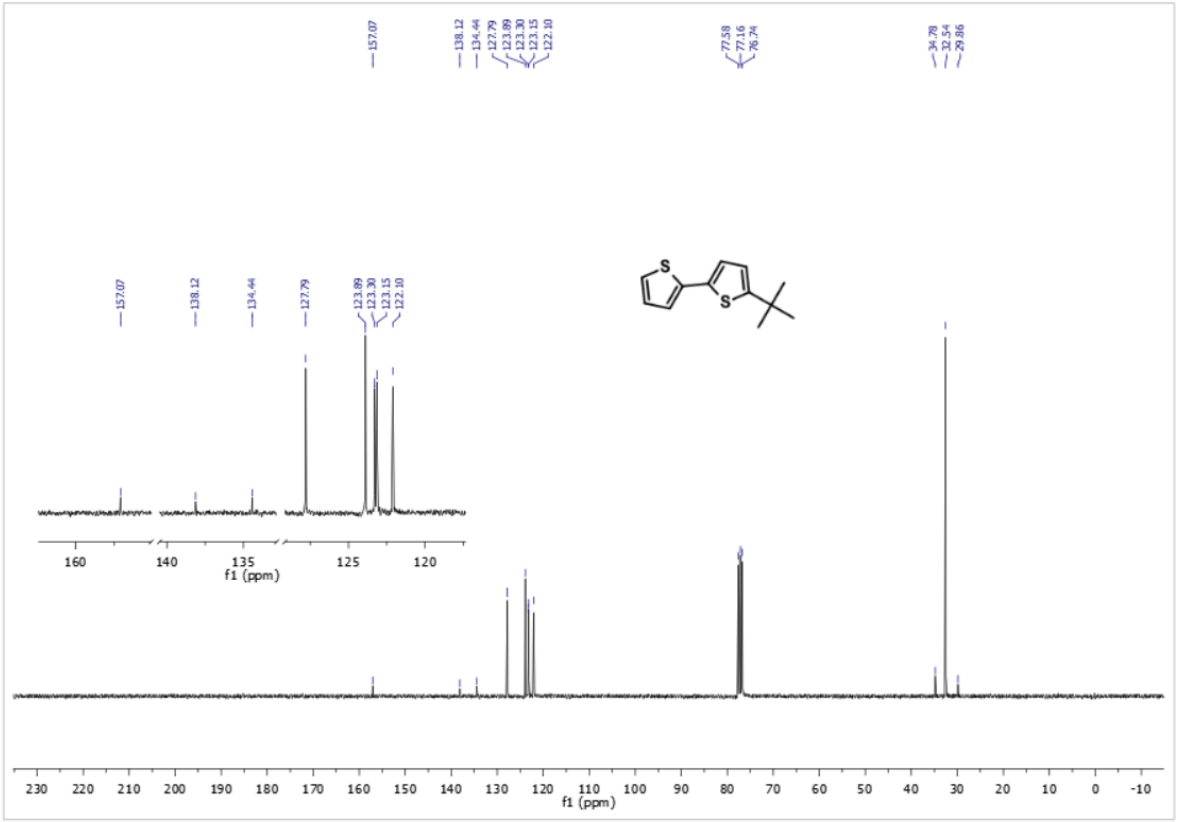

Figure A 28. ^{13}C NMR (300 MHz) in $CDCl_3$ of the model compound C.

10. Student Achievements

A. Published articles in Scientific Journals

1. Marcin Landrat, Mamo Abawalo1, Krzysztof Pikoń, **Paulos Asefa Fufa**, Semira Seyid: Assessing the potential of teff husk for biochar production through slow pyrolysis: effect of pyrolysis temperature on biochar yield, Energies, 2024, vol. 17, no. 9, pp.1-17, Article number:1988; 140 MniSW points; IF 3.2.
2. **Fufa Paulos Asefa,** Feyisa Gebisa Bekele, Gultom Noto Susanto, Kuo Dong-Hau, Xiaoyun Chen, Kabtamu Daniel Manaye , and Zelekew Osman Ahmed Zelekew: Visible light-driven photocatalytic activity of Cu_2O/ZnO/Kaolinite-based composite catalyst for the degradation of organic pollutant, Nanotechnology, 2022, vol. 33, no. 31, pp.1-30 ; 100 MNiSW points; IF: 3.5
3. Osman Ahmed Zelekew, **Paulos Asefa Fufa,** Fedlu Kedir Sabir, Dinsefa Mensur Andoshe, Noto Susanto Gultom, Hairus Abdellah, Dong-Hau Kuo, Xiaoyun Chen, Gopal Krishna Devulapalli, Chromium Ion Accumulations from Aqueous Solution by the Eichorinia crassipes Plant and Reusing in the Synthesis of Cr-Doped ZnO Photocatalyst, Journal of Nanomaterials, 2022, Volume 2022, Issue 1 4943844; 70 MniSW points; IF: 3.791
4. Osman Ahmed Zelekewa, **Paulos Asefa Fufa**, Fedlu Kedir Sabir · Alemayehu Dubale Duma, Water hyacinth plant extract mediated green synthesis of Cr_2O_3/ZnO composite photocatalyst for the degradation of organic dye, Heliyon, 2021, Volume 7, Issue 7e07652, 40 MniSW points; IF: 3.776

B. Chapters in scientific monographs

1. **Paulos Asefa FUFA**, Wojciech DOMAGALA; CONJUGATION BREAK SPACER STRUCTURAL MOTIFS AND THEIR EFFECTS ON THE PHYSICAL AND CHEMICAL PROPERTIES OF π-CONJUGATED POLYMERS; in: Materials of the Future, Vol. 2, eds. M. Czichy, A. Kazek-Kęsik, Silesian University of Technology Press, UIW 48600, Gliwice 2025, ISBN 978-83-68390-42-1; 20 MNiSW points
2. **Fufa Paulos Asefa**, Domagała Wojciech, Is methyl a universal inert protecting group? The curious case of α-methylbithiophene. In: Zjazd Zimowy Sekcji Młodych Polskiego Towarzystwa Chemicznego 2024. Lublin,14.12.2024. Książka abstraktów / Jaworska-Krych Daria, Siwiak Agnieszka (eds.), 2024, pp.55-55
3. **Paulos Asefa Fufa***, Wojciech Domagala; Electrochemistry and spectroelectrochemistry of alternating alkyl grafted methylene bridged oligothiophene polymers.; EPAE 2023;
4. **Fufa Paulos Asefa**, Motyka Radosław, Domagała Wojciech, Electrochemistry and spectroelectrochemistry of alternating methylene-bridged oligothiophene polymers, In: Nowe wyzwania dla polskiej nauki. Edycja XI. Materiały konferencyjne - streszczenia wystąpień, 2022, Kraków, Creativetime, pp.95-95, ISBN 978-83-66772-17-5
5. **Fufa Paulos Asefa**, Motyka Radosław, Domagała Wojciech, Electrochemistry and spectroelectrochemistry of alternating oligothiophene alkylene-polymers, In: 63. Zjazd Naukowy Polskiego Towarzystwa Chemicznego, Łódź, 13-17 września 2021 : Książka abstraktów 2020/2021, 2021, Polskie Towarzystwo Chemiczne, pp.552, ISBN 978-83-60988-32-9

C. Grants obtained

1. Grant supporting academics starting their scientific activity in a new research field: Synthesis and Investigations of new ternary thiophene based alternating donor-acceptor bridged alkylene polymers for OPVs applications. Amount: 12000 PLN.
2. Research tasks carried out by young scientists SBM (BKM)- Electrochemistry and spectroelectrochemistry of alternating alkyl- grafted methylene bridged oligothiophene polymers. Project no. 04/040/BKM23/0261. Amount: 12000 PLN.
3. Research tasks carried out by young scientists SBM (BKM)- Electrochemistry and spectroelectrochemistry of alternating methylene-bridged oligothiophene polymers. Project number: BKM-596/RCH4/2022 (04/040/BKM22/0208). Amount: 5000 PLN.
4. Research tasks carried out by young scientists SBM (BKM)- Electrochemistry and spectroelectrochemistry of alternating oligothiophene alkylene polymers. Project number: 04/040/BKM21/0163 (BKM-531/RCH4/2021). Amount: 11000 PLN.